frontiers | Research Topics

Rock physics of unconventional reservoirs

Edited by
Qiaomu Qi, Lidong Dai, Maxim Lebedev,
Tobias Mueller and Junfang Zhang

Published in
Frontiers in Earth Science

ISSN 1664-8714
ISBN 978-2-8325-3002-3
DOI 10.3389/978-2-8325-3002-3

About Frontiers

Frontiers is more than just an open access publisher of scholarly articles: it is a pioneering approach to the world of academia, radically improving the way scholarly research is managed. The grand vision of Frontiers is a world where all people have an equal opportunity to seek, share and generate knowledge. Frontiers provides immediate and permanent online open access to all its publications, but this alone is not enough to realize our grand goals.

Frontiers journal series

The Frontiers journal series is a multi-tier and interdisciplinary set of open-access, online journals, promising a paradigm shift from the current review, selection and dissemination processes in academic publishing. All Frontiers journals are driven by researchers for researchers; therefore, they constitute a service to the scholarly community. At the same time, the *Frontiers journal series* operates on a revolutionary invention, the tiered publishing system, initially addressing specific communities of scholars, and gradually climbing up to broader public understanding, thus serving the interests of the lay society, too.

Dedication to quality

Each Frontiers article is a landmark of the highest quality, thanks to genuinely collaborative interactions between authors and review editors, who include some of the world's best academicians. Research must be certified by peers before entering a stream of knowledge that may eventually reach the public - and shape society; therefore, Frontiers only applies the most rigorous and unbiased reviews. Frontiers revolutionizes research publishing by freely delivering the most outstanding research, evaluated with no bias from both the academic and social point of view. By applying the most advanced information technologies, Frontiers is catapulting scholarly publishing into a new generation.

What are Frontiers Research Topics?

Frontiers Research Topics are very popular trademarks of the *Frontiers journals series*: they are collections of at least ten articles, all centered on a particular subject. With their unique mix of varied contributions from Original Research to Review Articles, Frontiers Research Topics unify the most influential researchers, the latest key findings and historical advances in a hot research area.

Find out more on how to host your own Frontiers Research Topic or contribute to one as an author by contacting the Frontiers editorial office: frontiersin.org/about/contact

Rock physics of unconventional reservoirs

Topic editors

Qiaomu Qi — Chengdu University of Technology, China

Lidong Dai — Institute of geochemistry, Chinese Academy of Sciences, China

Maxim Lebedev — Edith Cowan University, Australia

Tobias Mueller — Center for Scientific Research and Higher Education in Ensenada (CICESE), Mexico

Junfang Zhang — Commonwealth Scientific and Industrial Research Organisation (CSIRO), Australia

Citation

Qi, Q., Dai, L., Lebedev, M., Mueller, T., Zhang, J., eds. (2023). *Rock physics of unconventional reservoirs*. Lausanne: Frontiers Media SA.

doi: 10.3389/978-2-8325-3002-3

Table of contents

frontiers | Frontiers in Earth Science

TYPE Editorial
PUBLISHED 30 June 2023
DOI 10.3389/feart.2023.1234699

OPEN ACCESS

EDITED AND REVIEWED BY
Jeroen Van Hunen,
Durham University, United Kingdom

*CORRESPONDENCE
Qiaomu Qi,
qiaomu_qi@163.com
Lidong Dai,
dailidong@vip.gyig.ac.cn
Maxim Lebedev,
m.lebedev@ecu.edu.au
Tobias Müller,
tobias@cicese.mx
Junfang Zhang,
junfang.zhang@csiro.au

RECEIVED 05 June 2023
ACCEPTED 19 June 2023
PUBLISHED 30 June 2023

CITATION
Qi Q, Dai L, Lebedev M, Müller T and Zhang J (2023), Editorial: Rock physics modeling and well-log practice for unconventional reservoirs.
Front. Earth Sci. 11:1234699.
doi: 10.3389/feart.2023.1234699

Editorial: Rock physics modeling and well-log practice for unconventional reservoirs

Qiaomu Qi[1,2]*, Lidong Dai[3]*, Maxim Lebedev[4]*, Tobias Müller[5]* and Junfang Zhang[6]*

[1]State Key Laboratory of Oil and Gas Reservoir Geology and Exploitation, Chengdu University of Technology, Chengdu, China , [2]College of Geophysics, Chengdu University of Technology, Chengdu, China, [3]Key Laboratory of High-Temperature and High-Pressure Study of the Earth's Interior, Institute of Geochemistry, Chinese Academy of Sciences, Guiyang, China, [4]Centre for Sustainable Energy and Resources, School of Engineering, Edith Cowan University, Joondalup, WA, Australia, [5]Department of Seismology, CICESE, Ensenada, Mexico, [6]CSIRO Energy, Perth, WA, Australia

KEYWORDS

rock physics, well-log interpretation, unconventional resources, elastic property, transport property, fluid saturation, shale, tight sand

Editorial on the Research Topic
Rock physics modeling and well-log practice for unconventional reservoirs

Unconventional resources with commercial interest in the world mainly include heavy oils, shales, coalbed methane and tight gas sands. The production and development of these resources have changed the supply pattern of global energy. Quantitative interpretation of geophysical data in the exploration, well logging and engineering development of the unconventional resources requires a comprehensive understanding of the physical properties of rocks and their relationships. The research of rock physics provides an interdisciplinary treatment of physical properties, whether it is highly related to geological, geophysical and geomechanical methodologies. The development of new rock physics methods is essential when integrating core, well-log, seismic data to improve the accuracy of formation evaluation and reservoir characterization. In this Research Topic, it includes 10 articles addressing a variety of rock physics studies on unconventional resources, highlighting fundamental theories, laboratory work and well-log interpretation.

The development of tight reservoirs is of significance to increase crude-oil production and optimize energy supply. These reservoirs have a low porosity/permeability with the high spatial heterogeneity, which requires new developments on the experimental and theoretical studies of acoustic properties. Ba et al. investigated the effects of pressure and fluid saturation on velocity and attenuation of tight sandstones. They conducted ultrasonic experiments on seven tight sandstones collected from the shale-oil strata as a function of the confining pressure. By analyzing the P-wave velocities and attenuations using the spectral-ratio method, they observed that the attenuation increases with both porosity and permeability and decreases with increasing pressure. Tight sandstones with oil saturation present higher attenuation than those of water and gas saturations. Furthermore, the dispersion and attenuation can be reasonably explained by a double-porosity theory, which takes into account mesoscopic heterogeneities of the rock frame and gas pockets. In tight gas reservoirs, the major flow channels are composed of micro/nanopores, in which the rarefaction effect is prominent and the traditional Darcy law is not appropriate for gas flow. A sound understanding of reservoir properties and gas flow mechanisms are required to effectively develop the natural gas in tight reservoirs. Zheng et al. conducted a 3D analysis of compressible gas

slip flow by combining the Maxwell fist-order slip boundary condition and Navier-Stokes equations. By analyzing the flux rate and non-linear pressure variation for gas slip flow, they proposed a new gas flux formula which is in good agreement with published experimental data. By substituting the gas flux formula into Darcy's law for compressible gas, they also presented a new apparent permeability model which considers both slippage effect and Knudsen diffusion in a tight gas reservoir. Compared to the new model, other previous models may underestimate the apparent permeability of tight reservoirs. Their results show that the apparent permeability strongly depends on the reservoir pressure and pore-throat radius.

Calcite cement is widely distributed in sandstone reservoirs and may significantly affect its elastic and electrical properties. Wang et al. quantitatively analyzed the effects of calcite cement and porosity on the P- and S-wave velocities and electrical resistivity of artificial calcite-cemented sandstones manufactured by a new method. Interpretation and analyses of the experimental results demonstrate that the elastic and electrical rock properties are a comprehensive result of porosity, the content and distribution of the calcite cement, as well as the microstructure of the samples caused by the variation in the applied consolidation stress. Their results revealed the mechanisms of how porosity and calcite cement affect the elastic and electrical properties of calcite cemented sandstones and provided a theoretical basis for the accurate characterization of sandstone reservoirs through seismic and electromagnetic surveys. On the other hand, the presence of calcium in calcareous tight sandstone reservoirs will reduce the travel time of acoustic waves, increase the compensated density, and substantially increase the resistivity of the sandstone reservoir. The logging response characteristics are influenced by the change in calcium content, leading to possible large errors in lithology identification and reservoir parameters evaluation. Yu et al. proposed a method for resistivity correction and water saturation evaluation for calcareous tight sandstone reservoirs. They analyzed the controlling factors of oil-bearing property in the calcareous tight sandstone reservoir through systematic petrophysical experiments and established the petrophysical volume model. They used optimized cross-plot to extract lithology-sensitive logging curves to calculate the calcium content. On this basis, they applied the resistivity index associated with calcium content to correct the resistivity. Finally, they calculated the water saturation by variable rock-electro parameters to eliminate the influence of calcium content and improve the evaluation accuracy of the calcareous tight sandstone reservoir.

Lacustrine shale oil is widely distributed in lacustrine lake basins and has become an important field of petroleum resource exploration and development in the world. Quantitative analysis of fluid saturation in lacustrine shale is difficult due to the complexity of diagenetic minerals and pore types. Nuclear Magnetic Resonance (NMR) technique has emerged as a key technique for characterizing the fluid components of shale oil in downhole logging and laboratory measurements. Different fluids have different T1/T2 ratio and T2 relaxation time, and different T2 relaxation time reflect different size of the pores. Based on NMR experiments, Fan et al. evaluate the fluid occurrence state and saturation of lacustrine shale oil in Fengcheng Formation. Using the T1-T2 map, they developed a 2D T1-T2 NMR quantitative calculation method for quantifying the movable oil saturation. In addition to fluid saturation, understanding the elastic properties of shales are important to seismic imaging, wellbore stability analysis and hydraulic fracturing treatment of unconventional shale reservoirs. Jiang et al. studied the elastic properties of heterogeneous Eagle Ford Formation consisting of marl and interbedded limestone layers. They extracted the relationship between the compressional and shear velocities using well-log data. The empirical equation obtained in their work can be used to estimate the shear velocity of the Eagle Ford Formation when there is insufficient well-log data. They also obtained the correlations between the elastic properties and the Gamma Ray value. They found that the lower marl layers possess the lowest averaged values of velocities and Young's modulus while the upper limestone layers have the highest averaged values of these elastic parameters. Their analysis shows that the aspect ratio of confined fractures can be significantly influenced by the contract of Young's modulus in the shale layers.

Identification of gas hydrate-bearing sediments (GHBS) in engineering applications worldwide mainly relies on seismic exploration techniques. The existence of hydrates highly affects the elastic wave velocity and attenuation. Ba et al. explored the mechanism of wave propagation in hydrate-bearing sediments by developing a triple-porosity model. The model considers combined effects of various fluid flow mechanisms including the local fluid flows between the rock frame and clay/hydrate inclusions, and the classical Biot's global flow loss. The model relates P-wave velocity and attenuation with the sediment properties such as the hydrate volume ratio, clay content, porosity, and the hydrate inclusion radii. The model predictions are in good agreement with the well-log data from ODP sites in Japan. The new model associated with the hydrate morphology could be helpful to improve the accuracy in the estimation of hydrate content from seismic and well-log data. On the other hand, understanding the effect of cement slurry penetration is important for the application of appropriate drilling techniques and wellbore stability evaluation in GHBS. Wang et al. studied the effect of cement slurry penetration during cementing in GHBS. They used TOUGH + HYDRATE software packages to simulate the cement penetration process. They investigated the effects the cementing process parameters on the cement slurry penetration process including the hydration heat of cement slurry, cementing pressure difference, holding time of cementing pressure difference. Furthermore, they analyzed physical properties responses such as hydrate saturation, hydrate phase equilibrium temperature difference, permeability and porosity. Their results penetration process is complex and can be significantly affected by environmental and physical states.

Heavy oil is an important alternative oil resource to conventional oil and gas reservoirs because of its huge availability all over the world, which is twice the conventional oil reservoirs. Current methods for characterizing the elastic properties of Fengcheng heavy oil reservoirs, the third largest sub-oilfield in the Xinjiang oilfield system, mainly involve well logs inspection without rock physics analysis and modeling. Yuan et al. performed rock physics analysis of heavy oil sands in Fengcheng Oilfield, Xinjiang. With integration of well-log and laboratory data, they investigated the consolidation status of heavy oil sands using theoretical rock physics modeling. Their results suggest that the grain contacts are scarce, and the frame is loose and poorly consolidated, which are consistent with the SEM observations. The effective evaluation of consolidation status is useful for seismic reservoir characterization and drilling risk analysis.

Apart from the above rock physics studies, earthquake-induced building damage and secondary disasters such as landslide, collapse and mud-rock flow have attracted extensive

attention because of their huge disaster causing force. The seismic response of the structure is closely related to the natural vibration frequency of the structure. It is important to determine the dynamic similarity relation in the shaking table model test. Guo et al. proposed a design method using frequency as input seismic wave similarity design control quantity. They studied the natural vibration frequencies of the prototype by means of the Gonza landslide field ground pulsation test. A new frequency compression ratio design scheme is given from the perspective of dynamic similarity.

The results of the rock physics theories and well-log practices presented in this Research Topic provide a glimpse of the challenges faced in the quantitative evaluation of physical properties in unconventional reservoirs by rock physicist, well-log analysts and geophysicists today. We hope you find this Research Topic to be a useful update on recent advances in rock physics of unconventional resources.

Author contributions

All authors listed have made a substantial, direct, and intellectual contribution to the work and approved it for submission.

Acknowledgments

The Research Topic editors would like to thank all contributing authors to this Research Topic and the editorial staff of Frontiers in Earth Science for making this Research Topic possible.

Conflict of interest

The authors declare that the research was conducted in the absence of any commercial or financial relationships that could be construed as a potential conflict of interest.

Publisher's note

frontiers | Frontiers in Earth Science

TYPE Original Research
PUBLISHED 04 January 2023
DOI 10.3389/feart.2022.1099848

OPEN ACCESS

EDITED BY
Qiaomu Qi,
Chengdu University of Technology, China

REVIEWED BY
Hongtao Wang,
Chengdu University of Technology, China
Xiaobin Li,
China National Petroleum Corporation, China

*CORRESPONDENCE
Jia Jun,
e.cruiser@163.com

SPECIALTY SECTION
This article was submitted to Structural Geology and Tectonics, a section of the journal Frontiers in Earth Science

RECEIVED 16 November 2022
ACCEPTED 05 December 2022
PUBLISHED 04 January 2023

CITATION
Yu Z, Jun J, Hua H, Yao D, Hongyi A and Shi F (2023), Resistivity correction and water saturation evaluation for calcareous tight sandstone reservoir: A case study of G oil field in Sichuan Basin. *Front. Earth Sci.* 10:1099848. doi: 10.3389/feart.2022.1099848

Resistivity correction and water saturation evaluation for calcareous tight sandstone reservoir: A case study of G oil field in Sichuan Basin

Zhang Yu[1], Jia Jun[2]*, Hu Hua[1], Du Yao[3,4], An Hongyi[1] and Fang Shi[1]

[1]Exploration Business Department of PetroChina Southwest Oil and Gas Field Company, Chengdu, China, [2]College of Resource and Environmental Engineering, Mianyang Normal University, Mianyang, China, [3]State Key Laboratory of Oil and Gas Reservoir Geology and Exploitation, Southwest Petroleum University, Chengdu, China, [4]School of Geoscience and Technology, Southwest Petroleum University, Chengdu, China

The calcareous tight sandstone reservoir of the Triassic Shaximiao Formation in the G oil field of the central Sichuan Basin has high calcium content and abnormally high resistivity, making it difficult to reveal the oil-bearing property, evaluate water saturation, and calculate geological reserves. In this work, a petrophysical volume model of calcareous tight sandstone was established through systematic petrophysics experiments and the analysis of the main control factors of oil bearing grade. A method of using conventional logging data to calculate the calcium content of the reservoir and correct the calcium content of resistivity was proposed. After resistivity correction, the water saturation of the tight calcareous sandstone reservoir was more accurately calculated based on variable rock-electro parameters. The results indicated that with the decrease in calcium content and the increase in feldspar content, the reconstructive effect of corrosion was enhanced, the physical properties and pore structure of the reservoir were improved, and the oil bearing grade increased. The calcium content of the reservoir can be continuously calculated by the volume model and the crossplot of $logRt_n/AC_n$ and V_{ca}/POR. The resistivity of the reservoir with a high calcium content can be corrected using the resistivity index of calcium content (I_{ca}). In conjunction with the water saturation calculation model using variable parameters, the accuracy of calculated water saturation was 14% and 5.8% higher than the calculation results without resistivity correction and using fixed rock-electro parameters, which can satisfy the requirements for reservoir evaluation and the calculation accuracy of hydrocarbon reserves.

KEYWORDS

Sichuan Basin, calcareous tight sandstone, petrophysics, resistivity correction, water saturation

1 Introduction

In the past decade, unconventional hydrocarbon resources represented by tight oil/gas and shale oil/gas, have played an increasingly important role in world energy structures (Roberto, 2013; Zou et al., 2014). Unconventional oil and gas accounted for 25% of global oil production in 2018 (US EIA, 2018), with tight oil contributing significantly. The tight oil production in the United States alone reached 3.29×10^8 t, pushing the oil production in the U.S. to the second-highest level (US EIA, 2019). Unlike conventional oil and gas exploitation, the exploitation in tight reservoirs has been a challenge due to the complex lithology and pore structure (Clarkson et al., 2012), strong heterogeneity (Liu, 2021), and difficulty in determining the controlling factors of oil bearing grade (Dai et al., 2012) and characterizing reservoir parameters (Li and Zhu, 2020).

Lithology identification is the foundation for tight reservoir evaluation and hydrocarbon exploitation (Zhang C. S. et al., 2019; Mateen et al., 2022). Mineral composition, structure, and cementation mode are directly related to the physical properties (Enkin et al., 2020; Bai et al., 2021), pore structure (Slatt and O'Neal, 2011), and wettability of reservoirs (Esfahani and Haghighi, 2004; Sauerer et al., 2020), and affect the distribution of reservoir fluid (Wu et al., 2016) and the evaluation accuracy of reservoir parameters (Agbasi et al., 2018). Lithology can be identified by experimental test techniques, such as Scanning Electron Microscope (SEM) (Quaid et al., 2016; Li et al., 2017), Cast Thin Section (CTS) (Borazjani et al., 2016; Dong et al., 2019), X-Ray Diffraction (XRD) (Kahle et al., 2002), and Computed Tomography Scan (CT) (Kyle and Ketcham, 2015; Ma et al., 2017). However, the experimental results are discrete, and it is difficult to obtain the continuous lithological characterization along the Well shaft. In addition, the above techniques cannot be widely used due to the excessive cost. In recent years, statistical analysis techniques have been applied to lithology identification, such as Gradient Boosting Decision Trees (Zhang G. et al., 2019; Dev and Eden, 2019), Neural Networks (Gu et al., 2018; Ahmed et al., 2021), and Machine Learning techniques (Thinesh et al., 2022). However, the identification accuracy of the above statistics methods depends on the number and significance of samples, and their application is regionally restricted. Economical, efficient, and continuous logging data with high vertical resolution have become a crucial means for lithology identification. Previous studies plotted the crosslet by lithology-sensitive logging curves (Benoit et al., 1980; Liu et al., 2016) and identified the logging lithology using Elemental Capture Spectroscopy (ECS) logging (Wu et al., 2013), imaging logging (Lai et al., 2019), and multi-mineral model (Butt and Naseem, 2022). Crossplot has been widely used to identify the lithology of conventional reservoirs; however, it is less effective in identifying the complex lithology of tight sandstone reservoirs due to the similar logging response of complicated lithological components. Therefore, it is beneficial to refine the crossplot technique and improve its performance in identifying complex lithology in tight reservoirs.

Some calcareous tight sandstone reservoirs in the Triassic Shaximiao Formation in the G oil field of the central Sichuan Basin are characterized by high calcium content (≥ 20%) and large variation in calcium content, which, together with the random distribution of calcium, complicates the lithology identification. The calcareous sandstone reservoir contains quartz and calcite, and the mineral content ratios are variables. As a result, the rock matrix value cannot be easily determined by logging evaluation. In addition, logging response characteristics are influenced by the change in calcium content, leading to large errors in lithology identification and reservoir parameters evaluation. At the same time, calcium will reduce the travel time of acoustic waves, increase the compensated density, and abnormally increase the resistivity of the sandstone reservoir (Djebbar and Erle, 2012). Consequently, the logging response characteristics between tight dry and oil reservoirs are easily confused, which further adversely affects fluid identification and hydrocarbon reserves calculation.

To address these problems, this paper analyzed the controlling factors of oil-bearing property in the calcareous tight sandstone reservoir through systematic petrophysical experiments, established the petrophysical volume model of calcareous tight sandstone, and uses optimized crossplot to extract lithology-sensitive logging curves to calculate the calcium content of the reservoir. On this basis, the resistivity index caused by calcium content (I_{ca}) was proposed to correct the resistivity, then the water saturation of the calcareous tight sandstone reservoir was calculated by variable rock-electro parameters to eliminate the influence of calcium and improve the evaluation accuracy of the calcareous tight sandstone reservoir.

2 Geological setting

G oilfield is located in the north-central Sichuan Basin, with hilly terrain and an altitude of 300–500 m (Figure 1). The northern part is higher than the southern part, and the exploration area is 1700 km^2 (Yang et al., 2016). The regional geological structure is formed in Yanshanian, which is a long stripe-shaped anticline extending in an east-west direction with NE-EW stress orientation, and its main fault lies parallel to the tectonic axis. The targeted formation, Shaximiao Formation in the Middle Jurassic, is the main productive zone of the oilfield and is widely spread in this area, with a formation thickness of 600–2200 m and a buried depth of 2100–2700 m. The sedimentary type is inland freshwater lacustrine facies clastic sediment, dividing into S_1 and S_2 sub segments from the bottom up, and the lithology is mainly aubergine and grey-green mudstone interbedded with pale grey-green and grey-green sandstone (Huang et al., 2017). In recent years, tight sandstone oil/gas reservoirs in this region have proven reserves of over 100 million tons, making it one of the hot spots for unconventional hydrocarbon exploitation in China (Yang et al., 2022).

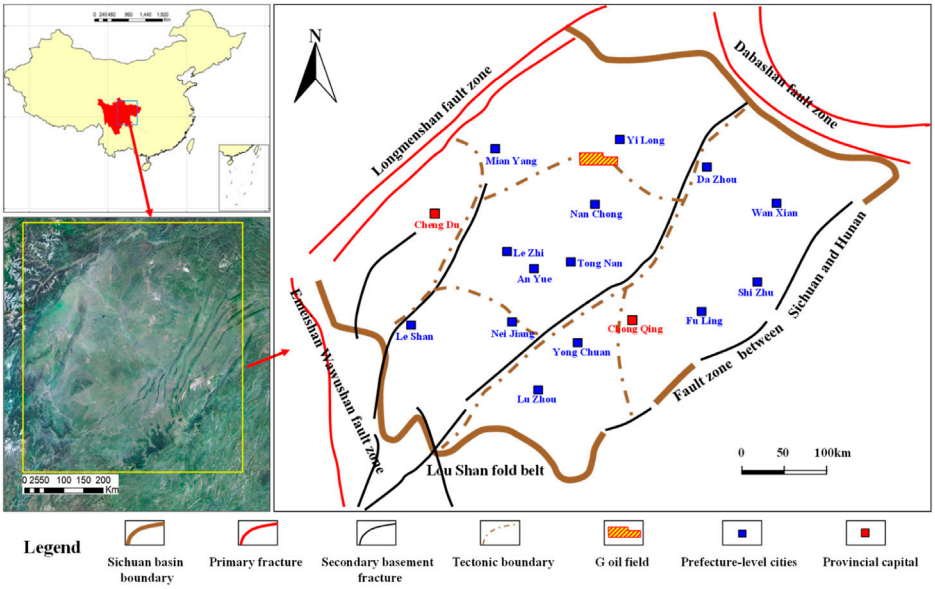

FIGURE 1
Geographical and structural location of G oilfield.

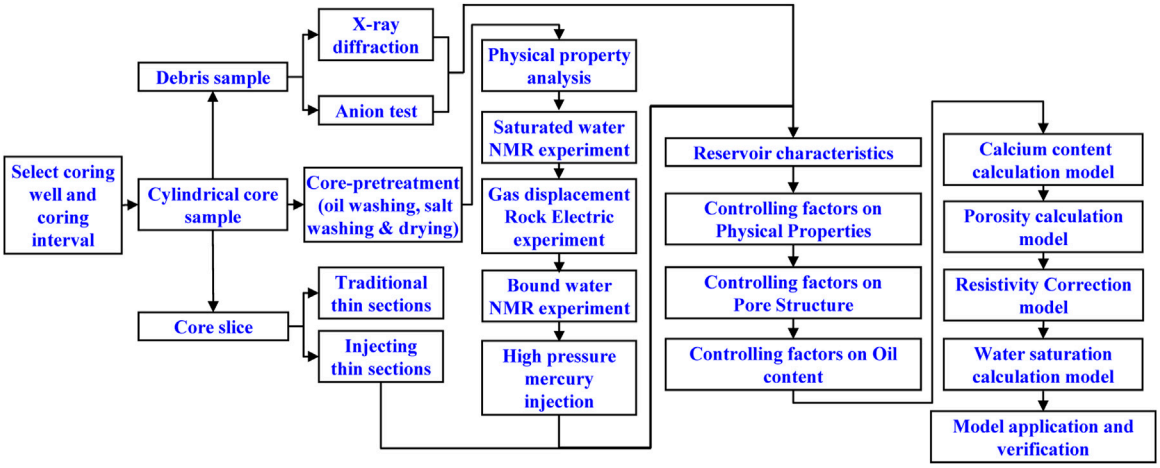

FIGURE 2
Experiment and research flow chart.

3 Methodologies

We collected core samples from 11 Wells with a high coring recovery rate and representative reservoir characteristics, prepared rock plug samples with diameters ranging from 25 to 80 mm, and performed the petrophysical experiment in steps (Figure 2).

X'Pert MPD PRO was used in the X-ray diffraction (XRD) analysis. AniMR-Hole Core was used in the nuclear magnetic resonance (NMR) experiment (maximum sample size: 150mm × 150mm × 150 mm). The automated mercury porosimeter Poremaster60 GT was applied in the High-Pressure Mercury Injection (HPMI) experiment (pore-size distribution: 0.0036–950um). The ion chromatography instrument ICS-5000

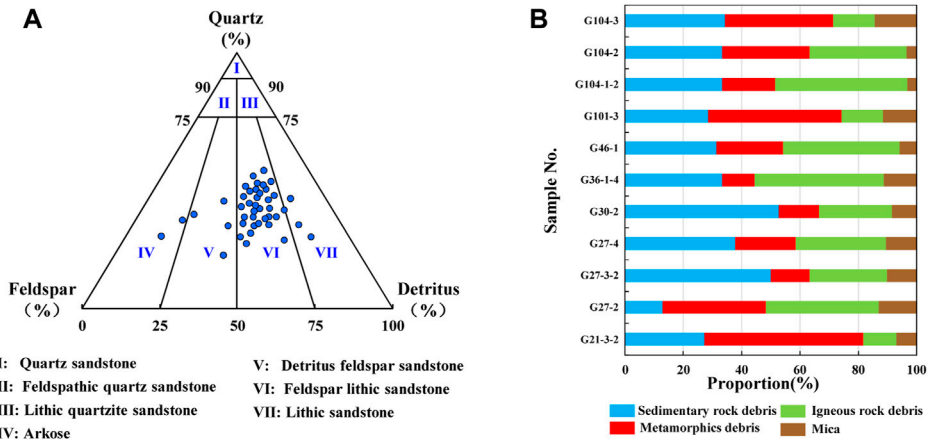

FIGURE 3
Lithology **(A)** and debris **(B)**.

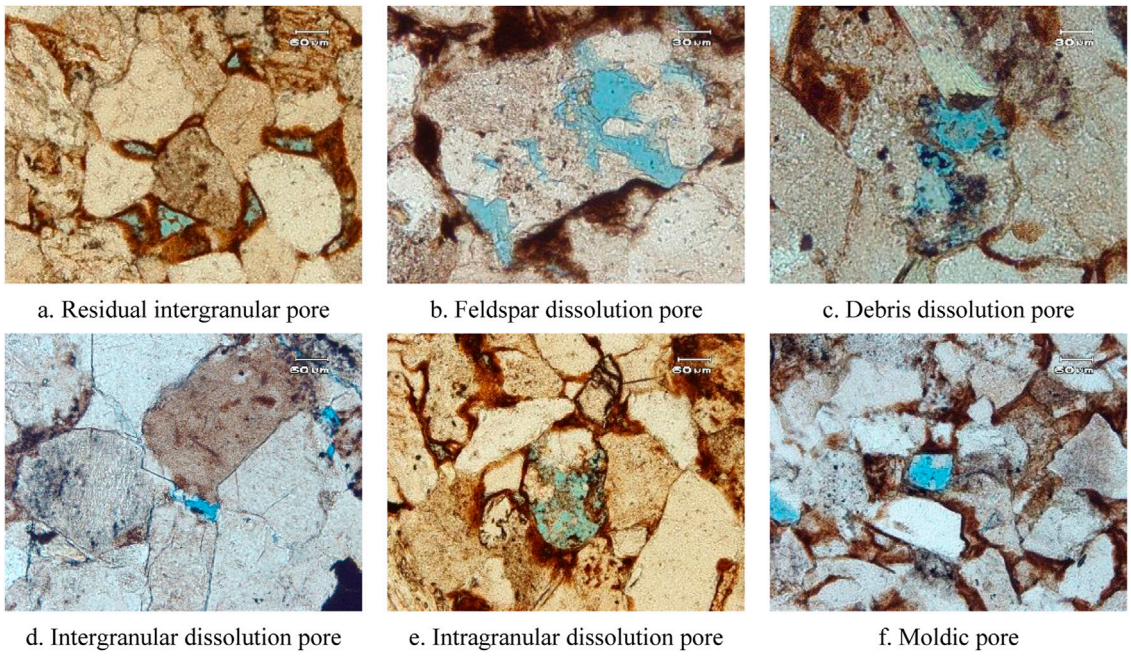

FIGURE 4
Pore types of reservoir. **(A)** Residual intergranular pore. **(B)** Feldspar dissolution pore. **(C)** Debris dissolution pore. **(D)** Intergranular dissolution pore. **(E)** Intragranular dissolution pore. **(F)** Moldic pore.

was employed in Anion Test (AT). The above experiments were completed in strict accordance with industry standards. The core samples used for the petroelectric test and conventional physical properties were pretreated beforehand by washing oil and salt using the carbon dioxide displacement method. Considering the influence of crystal water of clay minerals on pore structure, samples were dried at constant temperature and humidity (T&H: 70°C, 40%).

4 Phenomena and results

4.1 Lithologic characteristics

XRD results showed that the lithology of the Shaximiao Formation was mainly feldspar lithic sandstone and detritus feldspar sandstone (Figure 3A). The mass fraction of quartz

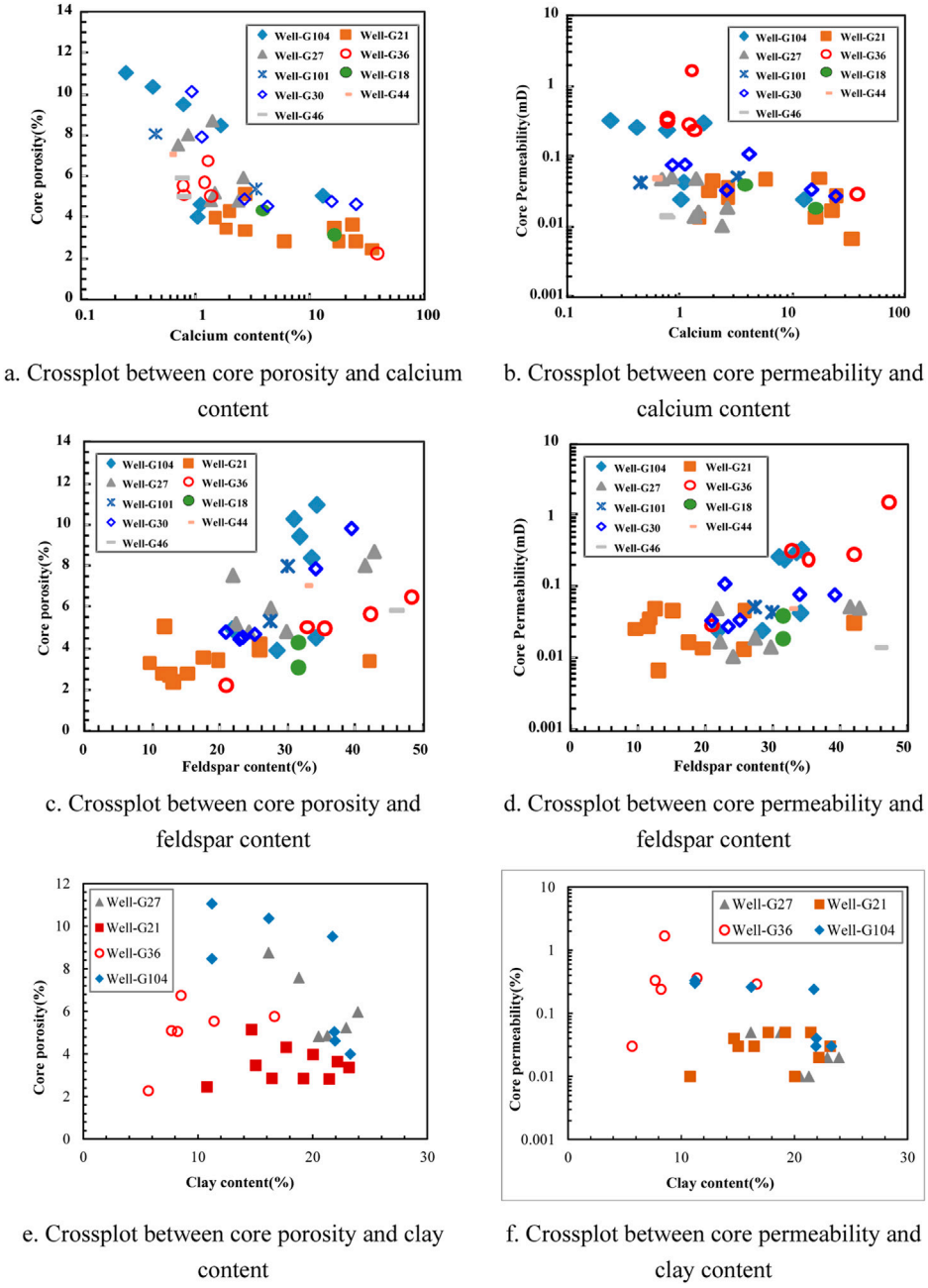

a. Crossplot between core porosity and calcium content

b. Crossplot between core permeability and calcium content

c. Crossplot between core porosity and feldspar content

d. Crossplot between core permeability and feldspar content

e. Crossplot between core porosity and clay content

f. Crossplot between core permeability and clay content

FIGURE 5
Correlation between feldspar, calcium, and clay content with porosity and permeability. **(A)** Crossplot between core porosity and calcium content. **(B)** Crossplot between core permeability and calcium content. **(C)** Crossplot between core porosity and feldspar content. **(D)** Crossplot between core permeability and feldspar content. **(E)** Crossplot between core porosity and clay content. **(F)** Crossplot between core permeability and clay content.

(w_Q) and feldspar (w_R) ranged from 22% to 72% and 4%–48%, respectively, and their average values were 45.95% and 20.4%, respectively. The composition of debris was complicated, including sedimentary rock debris, igneous rock debris, metamorphics debris, and little mica (Figure 3B). Laumontite was also found in some wells.

Laumontite is a porous silicate mineral with a water frame structure formed by the alteration of intermediate basic pyroclastic and alkaline minerals in an environment of low temperature and alkaline water medium. It has a large number of micropores and cavities (Lu et al., 2004; Chipera et al., 2008).

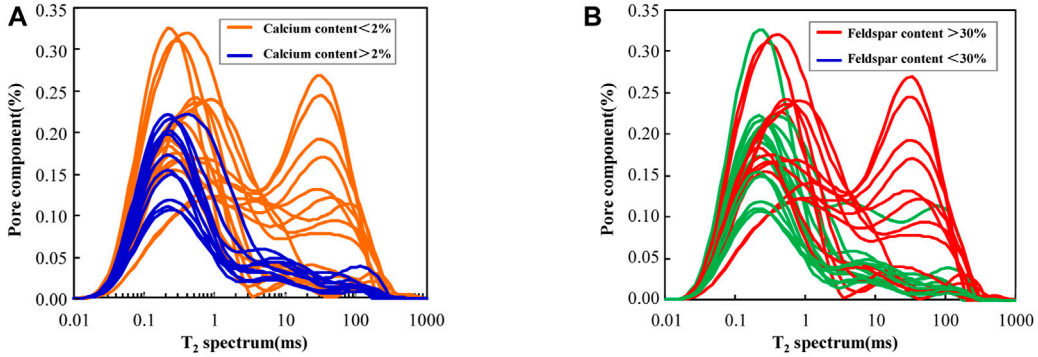

FIGURE 6
NMR T_2 spectrum of core samples with different calcium **(A)** and feldspar **(B)** content.

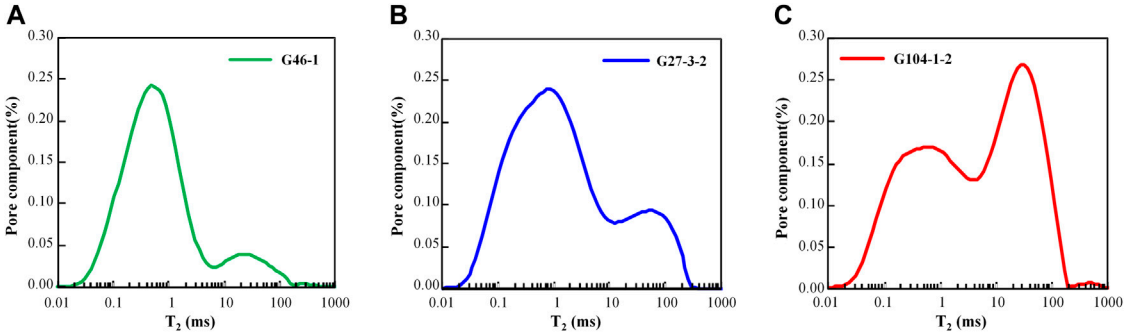

FIGURE 7
NMR T_2 spectrum of core with different development degrees of dissolution pores. **(A)** No.G46-1, low calcium content (0.76%), high feldspar content (46%), undeveloped dissolution pores (secondary surface porosity = 1.5%), poor pore structure. **(B)** No.G27-3-2, low calcium content (1.39%), high feldspar content (42.8%), dissolution pores developed (secondary areal porosity 3.5%), better pore structure. **(C)** No.G104-1-2, low calcium (0.76%), high feldspar content (46%), dissolution pores developed (secondary areal porosity 3.8%), good pore structure.

Compared with common porous minerals, laumontite is much less dense than quartz, plagioclase, and calcite, with an average density of 2.3 g/cm^3. At the same time, due to its high specific surface area (SSA), laumontite can adsorb large amounts of water and has large neutron porosity (CNL>31.3–35.3%). In terms of electrochemistry, the hydrous cation in laumontite cannot migrate through the zeolite skeleton cavity, resulting in poor conductivity. Therefore, laumontite strata generally have high resistivity (Yang and Qiu, 2002).

4.2 Physical properties

The analysis of physical properties showed that Shaximiao Formation was a tight sandstone reservoir with low porosity and permeability. The porosity and permeability of the reservoir ranged from 2% to 10% and 0.01 mD to 0.5 mD, respectively. The means of porosity and permeability were 5.5% and 0.12 mD, respectively. Porosity less than 6% and permeability less than 0.1 mD contributed up to 77.8% and 79.3% to the core physical properties, respectively. In general, core porosity had a good correlation with permeability.

4.3 Pore structure characteristics

The analysis of rock thin section indicated that the pore types of the Shaximiao tight sandstone reservoir were dominated by residual intergranular pore (43.18%) (Figure 4A), feldspar dissolution pore (23.35%) (Figure 4B), and debris dissolution pore (21.28%) (Figure 4C), followed by intergranular dissolution pore (Figures 4D, E) and moldic pore (Figure 4F). No microfractures appeared. According to statistical analysis, the more developed the residual

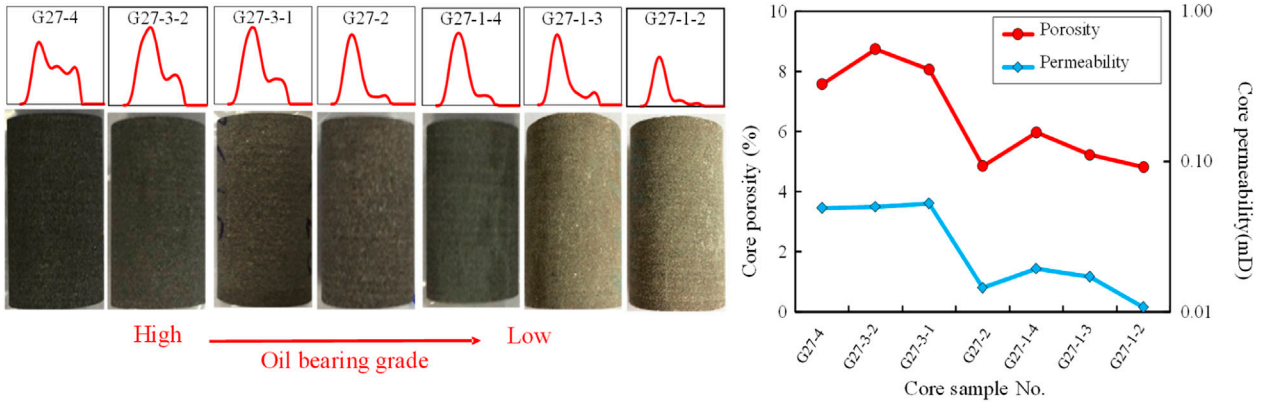

FIGURE 8
Variation of oil-bearing grade with physical properties and pore structure (Well G27)

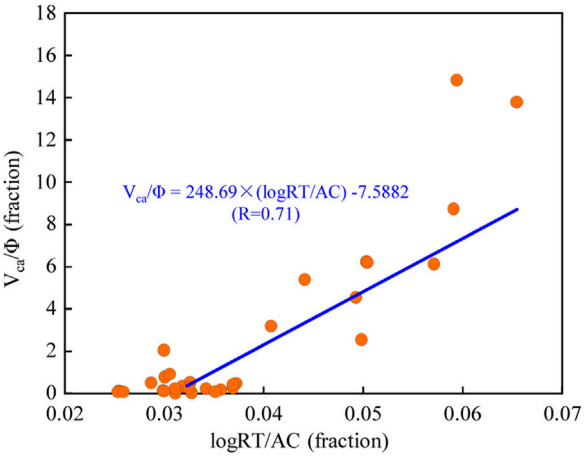

FIGURE 9
Crossplot between logRt/AC and V_{ca}/POR.

intergranular pores and secondary dissolution pores, the better the reservoir pores, and the higher the areal porosity and core porosity.

5 Analysis and discussions

5.1 Influencing factors of oil-bearing grade

Oil bearing grade was synthetically influenced by generating, reservoiring and capping conditions, hydrocarbon charging degree, and reservoir characteristics (Zhang et al., 2017). To study the controlling factors of the oil-bearing grade of calcareous tight sandstone, this paper analyzed the interrelationships between oil bearing grade, lithology, physical properties, and pore types from the perspective of reservoir characteristics.

5.1.1 Influence of lithology on physical properties

The analysis results on the correlation between physical properties and XRD experimental results demonstrated that calcium and feldspar had a greater influence on the physical properties of the reservoir in the Shaximiao Formation. Overall, as the calcium content decreased and the feldspar content increased, the porosity and permeability continued to rise, while the correlation between the content of quartz, clay, and physical properties was not significant (Figure 5). However, a few samples with a high feldspar content but a low calcium content (g21-3-2, g46-1, g46-2) still had poor physical properties. The rock thin section analysis revealed that their residual intergranular pores and secondary dissolution pores were underdeveloped, and part of the pore space was filled by asphalt.

5.1.2 Influence of lithology and dissolution on pore structure

Many studies have confirmed that there is a connection between T_2 spectrum distribution and pore radius (Mao and He, 2005). In this paper, the pore structure of the core was investigated by NMR T_2 spectra (Yan et al., 2017; Yan et al., 2020), and the relationship between the T_2 spectrum and calcium and feldspar content in the core was further analyzed.

From the test results, for the core samples with calcium content greater than 2%, the transverse relaxation time (T_2) ranged from 0.01–3 ms, and the curve exhibited a unimodal distribution of the T_2 spectrum. For core samples with calcium content less than 2%, one part of the curve still showed a unimodal distribution and T_2 between 0.05–6 ms, while the

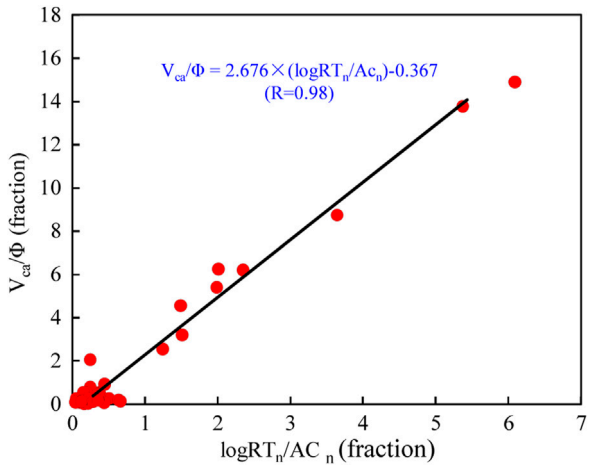

FIGURE 10
Crossplot between $\log Rt_n/AC_n$ and V_{ca}/POR.

other part exhibited bimodal characteristics and T_2 between 4–200 m after the peak (Figure 6A). When the feldspar content of core samples was less than 30%, the curve exhibited a unimodal distribution, and T_2 ranged from 0.02 to 3 m. When the content was greater than 30%, most of the distribution curve exhibited bimodal characteristics, and T_2 was in the range of 7–200 m after the first peak (Figure 6B). In other words, low calcium content, high feldspar content, and good physical properties were the basis for high-quality reservoir space. However, the pore structure of some core samples which can meet the above conditions was still not ideal (Figure 7A), and the reconstructive effect of corrosion of the pore space of such cores was weak. However, the pore structure gradually becomes better with the development of dissolution pores and the increase in secondary areal porosity (Figures 7B, C).

5.1.3 Influence of physical properties and pore structure on oil-bearing grade

The porosity, permeability, and NMR T_2 spectral characteristics of core samples in different oil-bearing grades indicated that the porosity of oily cores mainly ranged from 6% to 12% and the permeability was generally greater than 0.05 mD. Therefore, the physical properties of oily cores were better than those of oil-free cores (Figure 8). Regarding the pore structure characteristics, the T_2 spectrum of oily cores showed a bimodal distribution (Daigle and Johnson, 2015; Gong and Liu, 2020), T_2 ranged from 0.4 to 3 m and 7–200 m. In addition to micropores, meso- and macropores were also developed in oily cores to some extent. The T_2 distribution curves of oil-free cores were almost unimodal and T_2 ranged from 0.3 to 1.5 m. The samples were dominated by small- and micropores, with poor pore structure and weak permeability (Shao et al., 2017).

5.2 Resistivity correction for the effect of calcium content

In conventional sandstone reservoirs, resistivity logging curves were used to analyze the fluid properties and distribution features. Under similar reservoir conditions, the resistivity of the oil-bearing interval was greater than that of the oil-free interval. Based on classic Archie (1942)'s formula, water saturation can be calculated by resistivity curves. However, due to the high calcium content in the tight reservoir in the study area, in the oil-free interval, the resistivity increased significantly and the calculated water saturation was low, resulting in an inaccurate reflection of the oil content of the reservoir. Therefore, in order to eliminate the influence of calcium on resistivity, the calcium of resistivity must be corrected before evaluating the saturation of calcareous tight sandstone reservoir with resistivity logging.

5.2.1 Calculation of calcium content

XRD results were used to calibrate logging curves. The logging response of intervals with high calcium content (V_{ca}) was characterized by short acoustic travel time (AC) and increased resistivity (Rt), and there was no significant correlation between other logging curves. By analyzing the crossplot of AC and logRt with V_{ca} of corresponding reservoir intervals, it was found that their correlation was low, which indicated that apart from lithology (calcium content), AC was

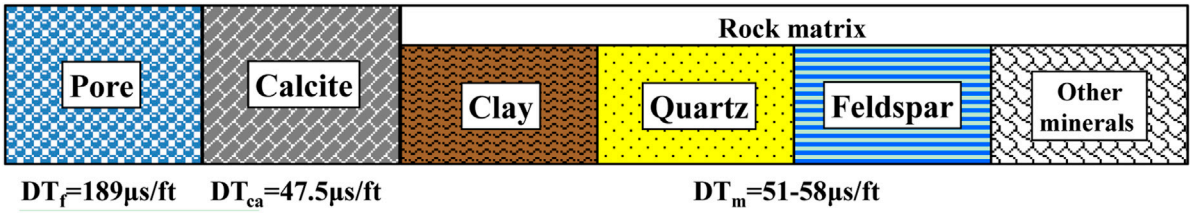

FIGURE 11
Petrophysical volume model of calcareous sandstone.

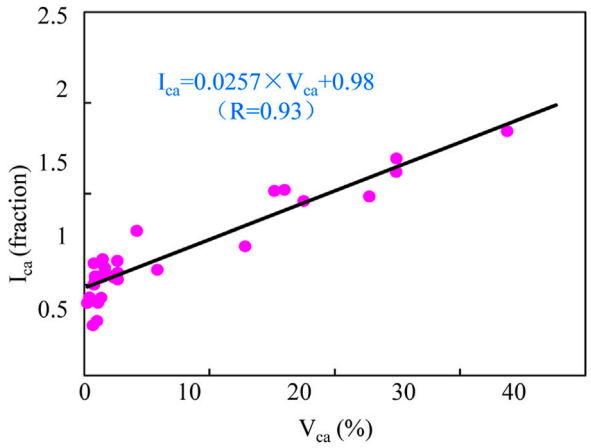

FIGURE 12
Crossplot between I_{ca} and V_{ca}.

also influenced by porosity, and resistivity was influenced by porosity and the formation water salinity (R_W).

Given that the study intervals belong to the same sedimentary type and their R_W is close, the influence of R_W on Rt could be ignored. As the calcium content increased, AC and POR decreased, logRt increased, and the variation trends of V_{ca}/POR and logRt/AC were the same. Although the correlation between logRt/AC and V_{ca}/POR (Figure 9) was higher than that of AC, logRt, and V_{ca} of corresponding intervals, it still did not satisfy the accuracy requirements for log evaluation. According to the analysis, the dimensional differences of data between logRt and AC might lead to a low correlation, and the difference of R_W between Wells might also lead to the deviation of Rt.

The crossplot of logRtn/ACn and Vca/POR (Figure 10) was plotted to weaken the influence of the above factors, that is, the relationship between logging response characteristics and calcium content (Vca) was analyzed with relative variation trends of logRt and AC, instead of their concrete values (Li et al., 2022). After normalization, the values of logRt and AC ranged from 0 to 1. When Vca increased, Rt increased, and AC decreased. The variation trends of Rt and AC were opposite. The normalized ratios could effectively reflect the variation features of logging-sensitive curves caused by Vca change. In addition, the normalized logRt attenuated the influence of the different resistivity of formation water among

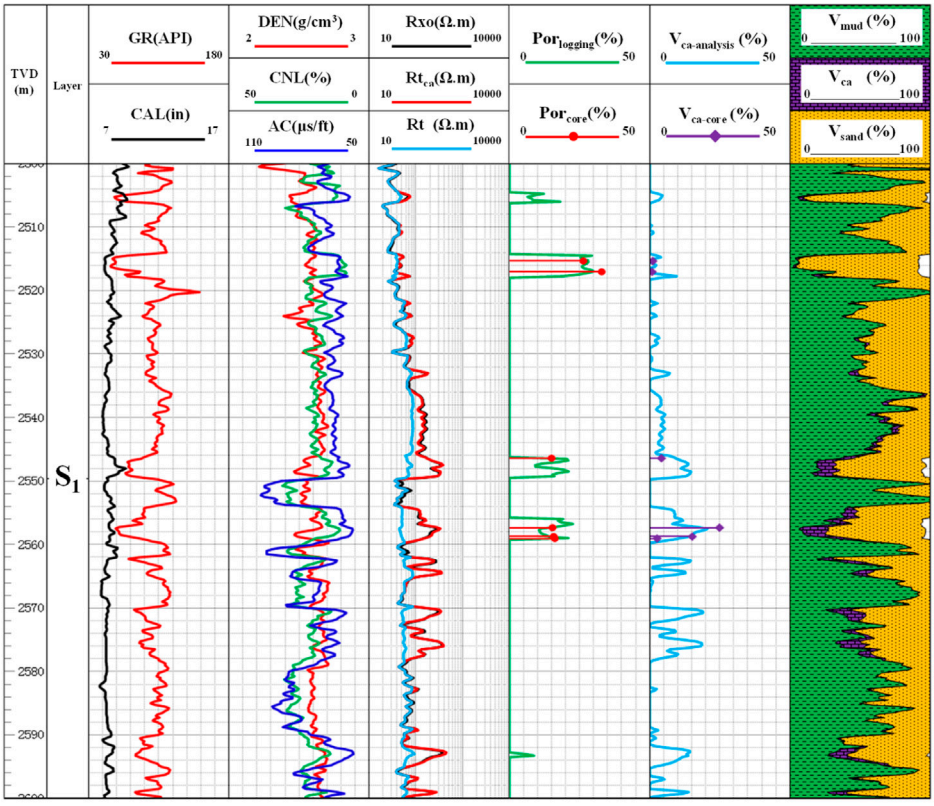

FIGURE 13
Resistivity correction of Well G30.

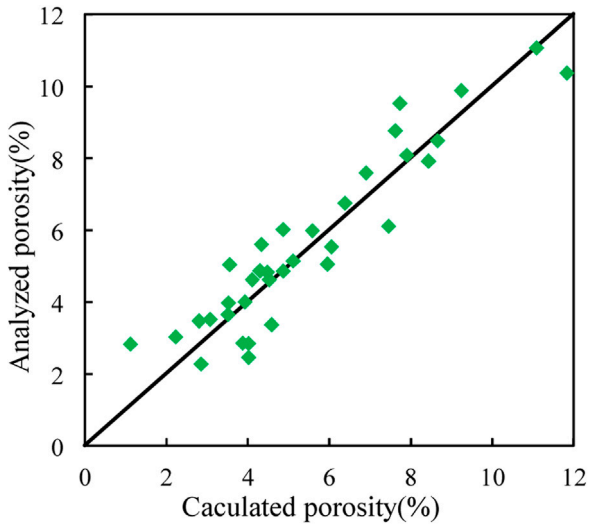

FIGURE 14
Crossplot between core analysis and calculated porosity.

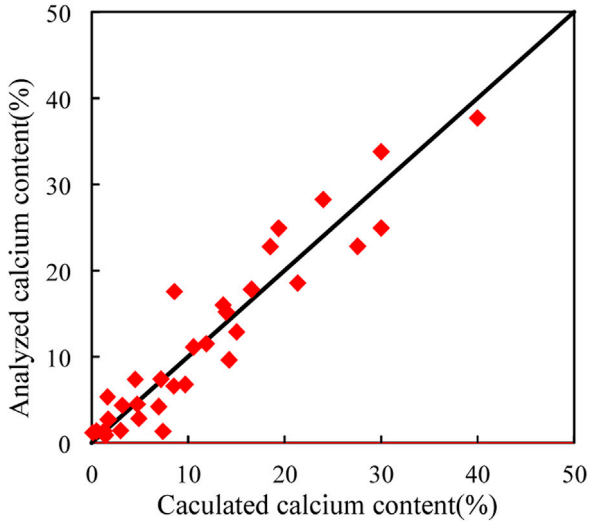

FIGURE 15
Crossplot between core analysis and calculated calcium content.

Wells. The results indicated that logRtn/ACn was highly correlated with Vca/POR, and the model to calculate Vca was derived (Eq. 1):

$$V_{ca} = \left(2.676 \times \frac{\log Rt_n}{AC_n} - 0.367\right) \times \Phi \quad (1)$$

where V_{ca} is the calcium content, %; $\log Rt_n$ is the normalized logRt, fraction; AC_n is the normalized AC, f; and Φ is the porosity, %.

The above model of V_{ca} indicates that obtaining reliable porosity is the prerequisite for the accurate calculation of V_{ca}. To this end, we proposed the petrophysical volume model that considers calcareous content (Figure 11) and established logging response equations (Eqs. 2, 3).

$$1 = \Phi + V_{ca} + V_m \quad (2)$$

$$AC = DT_f \times \Phi + DT_{ca} \times V_{ca} + DT_m \times V_m \quad (3)$$

where Φ is the porosity, %; DT_f is the travel time of fluid, 189 μs/ft; and DT_{ca} is the travel time of calcium, 47.5 μs/ft. DT_m is the travel time of the matrix, DT_m is in the range of 51–58 μs/ft, V_{ca} is the calcium content, %; and V_m is the matrix volume, %.

By combining Eqs. 1–3, the calculation model of porosity was obtained (Eq. 4):

$$\Phi = \frac{AC - DT_m}{(DT_f - DT_m) + (DT_{ca} - DT_m) \times \left(2.676 \times \frac{\log Rt_n}{AC_n} - 0.367\right)} \quad (4)$$

5.2.2 Resistivity correction for the effect of calcium content

In reservoir intervals with high calcium content, calcium will significantly increase the deep lateral resistivity, up to 1000 Ω m. The influence of calcium on resistivity is greater than the effect of fluid properties on resistivity. In accordance with the principle of resistivity logging, the existence of calcium is equivalent to the addition of a heterogeneous and stochastically varying resistivity to the homogeneous sandstone reservoir. In addition, its influence on formation resistivity is closely related to the degree of homogeneity. When the calcium is homogeneously distributed, it is equivalent to high resistance in parallel in the formation, and the influence is limited. When the distribution of calcium is heterogeneous, the formation is equivalent to a high resistance sometimes in series and sometimes in parallel, which will have a significant impact on the formation resistivity. In this case, the water saturation calculation by Archie's formula based on resistivity logging will be greatly affected. The followings are two common scenarios: (1) The water or dry layers with high calcium content are mistaken for oil-water or oil layers. (2) Low-resistivity oil zones with low calcium content are mistaken for water layers.

In order to eliminate the influence of calcium content on water saturation calculation, it is necessary to correct the calcium content of resistivity. In the classic Archie (1942)'s formula, the contribution of oil and gas to resistivity is manifested by the resistivity index, I (I=Rt/Rw). Based on the above principle, in this study, the resistivity index caused by calcium content was defined as Ica, which is the ratio of the resistivity of calcareous formation (logRtca) to that of sandstone formation (logRt). The regression analysis on

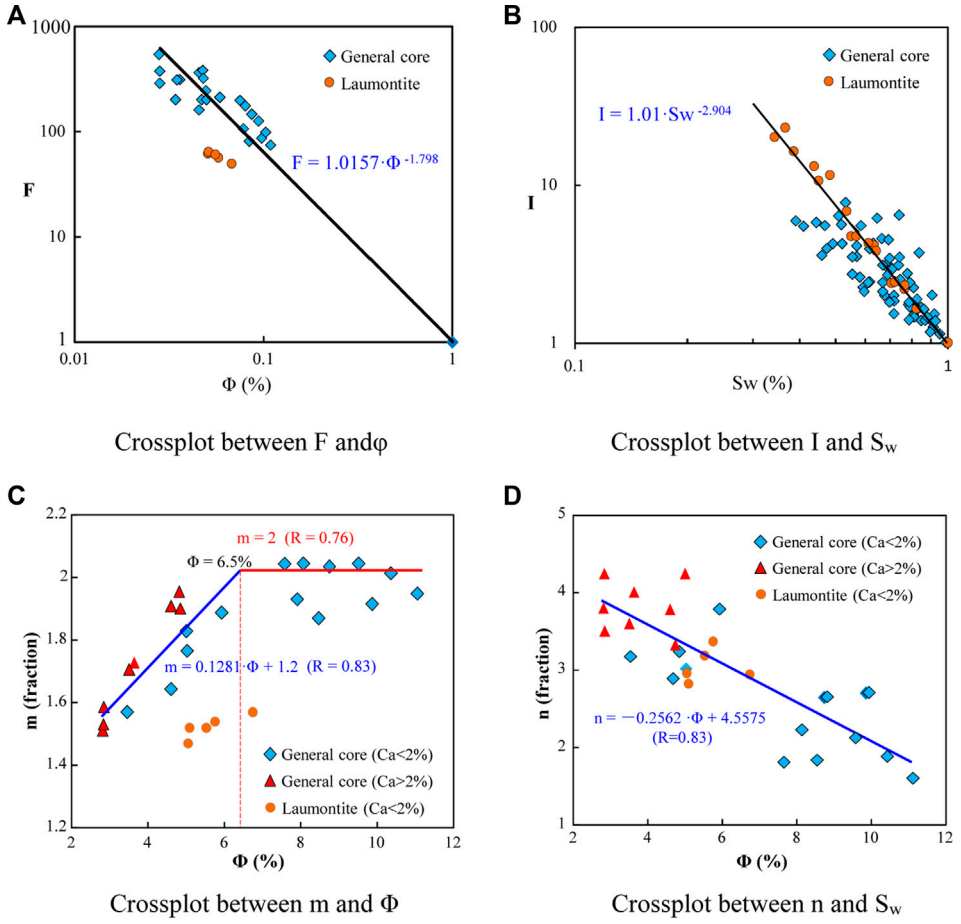

FIGURE 16
Rock-electro parameters. **(A)** Crossplot between F andφ. **(B)** Crossplot between I and S_w. **(C)** Crossplot between m and Φ. **(D)** Crossplot between n and S_w.

calcium content (Vca) and Ica showed that they had a good linear relationship, and the correlation coefficient was 0.93 (Figure 12).

$$I_{ca} = \frac{\log Rt_{ca}}{\log Rt} = 0.0257 \times V_{ca} + 0.98 \quad (5)$$

Then, the correction model for calcium content of resistivity was obtained as follows:

$$Rt = Rt_{ca} \times I_{ca}^{-1} = \frac{Rt_{ca}}{0.0257 \times V_{ca} + 0.98} \quad (6)$$

The above method was used to correct the calcium content of resistivity in Well G30. The resistivity of the calcium-free interval (2510–2530 m) did not change before and after correction, while that of intervals with a high calcium content (2546–2550m, 2554–2560m) decreased significantly after correction (Figure 13). The calculated calcium content and porosity were in good accordance with those from the core analysis. The calcium content and porosity of Wells G21, G27, G30, G36, and G104 were calculated and compared with analyzed calcium content and porosity. Both calculation and analyzed results were in high agreement. The average absolute errors of porosity and calcium content were 3.8% (Figure 14) and 4.2% (Figure 15), respectively.

5.3 Water-saturation calculation of calcareous tight sandstone

Based on resistivity correction, the water saturation of the calcareous sandstone reservoir could be calculated by Archie's formula. As the key parameters in Archie's formula, rock-electro parameters have a direct impact on the calculation accuracy of water saturation and are usually obtained by rock electricity experiments at high pressure and temperature.

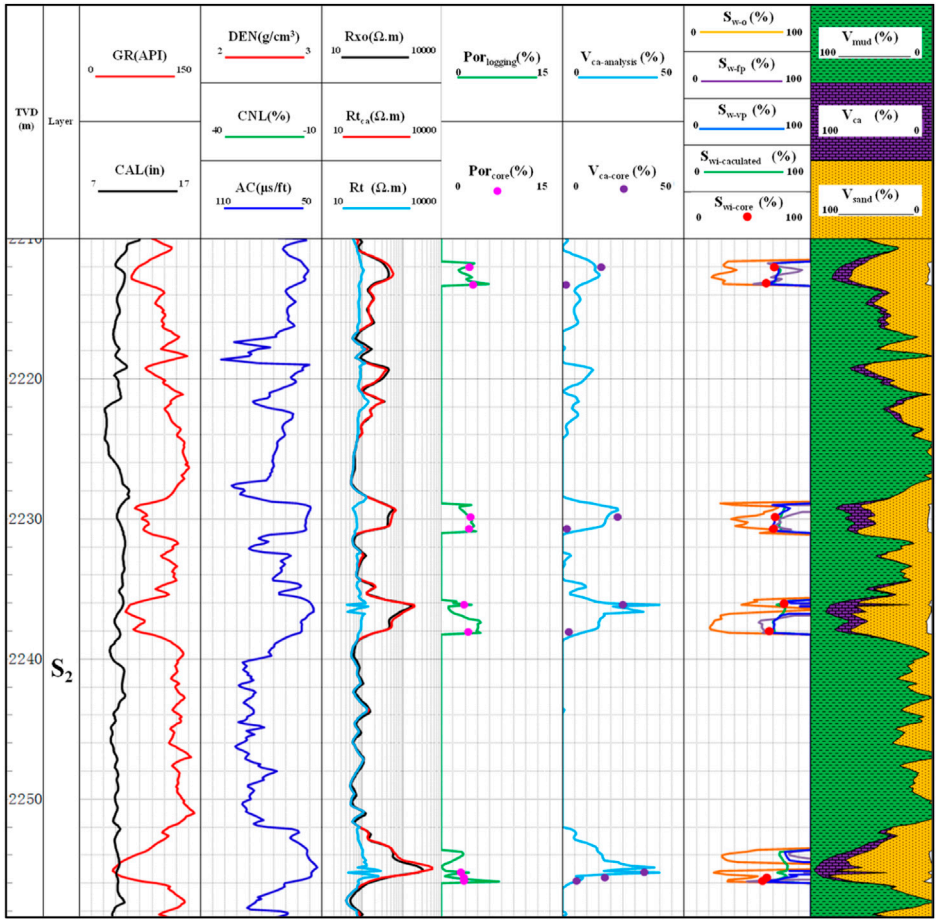

FIGURE 17
Comprehensive interpretation of Well G21.

5.3.1 Archie parameters

5.3.1.1 Fixed Archie parameters

In the rock electricity experiment, it was found that some cores were oversaturated, that is, the actual water inflow exceeded the theoretical water inflow of pores by 22%. By comparing XRD and CTS results for this type of core, it was found that the oversaturation was caused by laumontite cementation in cores. The crystal structure of laumontite contains a lot of cavities and canals and is in the shape of a porous sponge (Koporulin, 2013). After a long time of pressure saturation, water flows into laumontite to form zeolitic water, which can conduct electricity, similar to bound water. In addition, due to the unbalanced electrovalence generated by the displacement of silicon by aluminum, alkali metal ions and water molecules can move between the crystal lattice of laumontite, making the laumontite itself conductive and affecting the accurate calculation of rock-electro parameters.

Due to the above factors, the resistivity of the oversaturated rock decreased significantly, resulting in small F values of samples. By comparison, the n parameter was unrelated to saturation, therefore, oversaturation did not affect n values. After excluding the oversaturated core samples, the parameters of Archie's formula were determined as a = 1, b = 1, m = 1.798, and $n = 2.904$ (Figure 16). However, the influence of the reservoir heterogeneity (lithology, physical property) was not considered in the saturation calculation using fixed rock-electro parameters.

5.3.1.2 Variable Archie parameters

The analysis of the relationship between m, n, and porosity revealed that there was a piecewise functional relationship between m and porosity, and a linear functional relationship between n and porosity. In addition, m and n of calcic samples were greater than those of calcium-free samples. When m and n were fixed, the calculation of S_w must have errors. Therefore, considering the relationship between porosity, m, and n, a statistical regression model was proposed to calculate m

TABLE 1 Water saturation calculation results with different methods.

Core no.	Core analysis water saturation (%)	Previous calculation resultsact (%)		Correcting resistivity			
				Fixed rock-electro parameters (%)		Variable rock-electro parameters (%)	
		Calculated value	Absolute error	Calculated value	Absolute error	Calculated value	Absolute error
1	39.5	14.5	25.0	25.0	14.5	35.5	4.0
2	38.0	20.0	18.0	27.0	11.0	35.0	3.0
3	37.5	25.0	12.5	26.0	11.5	34.5	3.0
4	52.0	16.5	35.5	34.5	17.5	48.5	3.5
5	51.5	25.0	26.5	43.0	8.5	49.0	2.5
6	48.5	35.0	13.5	40.0	8.5	41.0	7.5
7	62.5	28.0	34.5	42.0	20.5	50.5	12.0
8	53.5	44.0	9.5	63.0	9.5	60.0	6.5
9	67.0	37.5	29.5	60.0	7.0	61.6	5.4
10	65.0	31.0	34.0	54.0	11.0	58.0	7.0
11	70.0	34.0	36.0	78.5	8.5	72.5	2.5
12	71.0	45.5	25.5	78.0	7.0	76.0	5.0
13	64.5	47.0	17.5	55.0	9.5	60.5	4.0
14	62.0	51.0	11.0	57.0	5.0	53.0	9.0
15	64.0	56.5	7.5	56.0	8.0	60.5	3.5
16	64.0	61.0	3.0	69.5	5.5	67.0	3.0
17	62.0	60.0	2.0	55.0	7.0	56.0	6.0
18	70.0	75.0	5.0	90.0	20.0	71.5	1.5
19	65.5	82.0	16.5	56.0	9.5	65.0	0.5
20	69.0	85.0	16.0	80.0	11.0	70.5	1.5
21	77.0	87.0	10.0	83.0	6.0	80.0	3.0
Mean absolute error (%)			18.5		10.3	4.5	

and n by porosity. The calculation model for n is as follows (Eq. 7):

$$n = -0.2562 \times \Phi + 4.5575 \quad (7)$$

Taking porosity of 6.5% as the boundary value, the piecewise calculation model of m was obtained (Eqs. 8, 9):

$$\Phi > 6.5\%, \quad m = 2 \quad (8)$$

$$\Phi < 6.5\%, \quad m = 0.1281 \times \Phi + 1.2 \quad (9)$$

5.3.2 *In-situ* application

Archie's formula with fixed and variable parameters was used to calculate S_w of Well G21 (Figure 17).

The core analysis showed that V_{ca} and S_w of intervals between 2211.8–2213.3 m, 2228.9–2230.8 m, 2236.2–2238.3 m, and 2252.7–2255.3 m ranged in 2.7–34.7% and 62–84.5%, respectively. The logging curves were characterized by abnormally low GR and high resistivity responses due to the influence of calcium on the above intervals. In previous studies, S_w measured by the classic Archie's formula without calcium correction for resistivity ranged from 20.5% to 54%, obviously lower than the results from the core analysis. Logging interpretation misidentified intervals as productive strata. After calcium correction, S_w calculated by the model with fixed and variable parameters ranged from 56.5–79% and 60–83%, respectively, close to the results from the core analysis. Logging interpretation

corrected intervals as unproductive strata, and hydraulic fracturing tests confirmed that no industrial oil flowed in the above intervals.

The above methods were adopted to measure the S_w of Wells in the study area, and the results were compared with calculations and core irreducible water saturation (S_{wir}) in previous studies (Table 1). The mean absolute error of S_w in previous research was 18.5%. After calcium correction of resistivity, the mean absolute error of S_w measured by Archie's model with fixed and variable parameters was 10.3% and 4.5%, respectively. The errors were significantly reduced and met the accuracy requirements of reservoir evaluation and oil reserves calculation.

6 Conclusion

(1) Calcium and feldspar are the main minerals controlling the physical properties of the calcareous tight sandstone reservoir in the Shaximiao Formation. Corrosion further improves the porosity and pore structure of the reservoir. In addition, lithology and pore structure jointly control the oil bearing grade of the reservoir.

(2) By using the improved crossplot of $logRt_n/AC_n$ and V_{ca}/POR, the influence of different R_w among Wells and dimensional differences of logging curves was weakened, and the difference in logging response of calcium content was effectively reflected. Based on the calcareous petrophysical volume model, a calculation model of calcium content and porosity of the calcareous sandstone reservoir with high accuracy was proposed.

(3) By introducing the I_{ca} index, the regression relation between V_{ca} and I_{ca} was established, and the resistivity in reservoir intervals with high calcium content was effectively corrected.

(4) The calculation accuracy of S_w in calcareous tight sandstone obtained by putting the resistivity after calcium correction into Archie's formula with variable parameters was significantly better than that of the formula with fixed parameters and previous results. The absolute error was less than 5% compared with water saturation through sealed coring, which met the accuracy requirements of reservoir evaluation and oil and gas reserves calculation.

Data availability statement

The original contributions presented in the study are included in the article/Supplementary Material; further inquiries can be directed to the corresponding author.

Author contributions

ZY: Writing—Original Draft, FS: Data Curation, Investigation. JJ: Conceptualization, Writing—Review and Editing, Investigation. HH: Resources and Editing. DY: Visualization. AH: Editing.

Funding

This research was jointly supported by the National Natural Science Foundation of China (Grant No. U2003102) and Natural Science Foundation of Science and Technology Department in Sichuan Province (Declaration No. 23NSFSC1626).

Conflict of interest

Authors ZY, HH, and AH were employed by the company of Exploration Business Department of PetroChina Southwest Oil and Gas Field Company.

The remaining authors declare that the research was conducted in the absence of any commercial or financial relationships that could be construed as a potential conflict of interest.

Publisher's note

All claims expressed in this article are solely those of the authors and do not necessarily represent those of their affiliated organizations, or those of the publisher, the editors and the reviewers. Any product that may be evaluated in this article, or claim that may be made by its manufacturer, is not guaranteed or endorsed by the publisher.

References

Agbasi, O. E., Igboekwe, M. U., Chukwu, G. U., and Sunday, E. E. (2018). Discrimination of pore fluid and lithology of a well in X Field, Niger Delta, Nigeria. *Arab. J. Geosci.* 11, 274. doi:10.1007/s12517-018-3610-7

Ahmed, A., Elkatatny, S., Gamal, H., and Abdulraheem, A. (2021). Artificial intelligence models for real-time bulk density prediction of vertical complex lithology using the drilling parameters. *Arab. J. Sci. Eng.* 47, 10993–11006. doi:10.1007/s13369-021-05537-3

Archie, G. E. (1942). The electrical resistivity log as an aid in determining some reservoir characteristics. *Trans. AIME* 146, 54–62. doi:10.2118/942054-g

Bai, X., Li, Z., and Lai, F. (2021). Optimal selection method for sweet spots in low-permeability multilayered reservoirs. *Geofluids* 2021, 1–10. doi:10.1155/2021/6698010

Benoit, W. R., Sethi, D. K., and Fertl, W. H. (1980). "Geothermal well log analysis at desert peak, neaada," in Proceeding of the SPWLA, 21thAnnual Logging Symposium, Lafayette, Indiana, July 1980.

Borazjani, O., Ghiasi-Freez, J., and Hatampour, A. (2016). Two intelligent pattern recognition models for automatic identification of textural and pore space characteristics of the carbonate reservoir rocks using thin section images. *J. Nat. Gas. Sci. Eng.* 35, 944–955. doi:10.1016/j.jngse.2016.09.048

Butt, F. M., and Naseem, S. (2022). Lithology identification and gross rock volume estimation of B-Sand in NIM Block, Lower Indus Basin, Pakistan. *Arab. J. Geosci.* 15, 321. doi:10.1007/s12517-021-09381-5

Chipera, S. J., Goff, F., Goff, C. J., and Fittipaldo, M. (2008). Zeolitization of intracaldera sediments and rhyolitic rocks in the 1.25 Ma lake of Valles caldera, New Mexico, USA. *J. Volcanol. Geotherm. Res.* 178 (2), 317–330. doi:10.1016/j.jvolgeores.2008.06.032

Clarkson, C. R., Freeman, M., He, L., Agamalian, M., Melnichenko, Y., Mastalerz, M., et al. (2012). Characterization of tight gas reservoir pore structure using USANS/SANS and gas adsorption analysis. *Fuel* 95, 371–385. doi:10.1016/j.fuel.2011.12.010

Dai, J. X., Ni, Y. Y., and Wu, X. Q. (2012). Tight gas in China and its significance in exploration and exploitation. *Petroleum Explor. Dev.* 39 (3), 277–284. (inChinese). doi:10.1016/s1876-3804(12)60043-3

Daigle, H., and Johnson, A. (2015). Combining mercury intrusion and nuclear magnetic resonance measurements using percolation theory. *Transp. Porous Media* 111, 669–679. doi:10.1007/s11242-015-0619-1

Dev, V. A., and Eden, M. R. (2019). Formation lithology classification using scalable gradient boosted decision trees. *Comput. Chem. Eng.* 128, 392–404. doi:10.1016/j.compchemeng.2019.06.001

Djebbar, T., and Erle, C. D. (2012). *Petrophysics: Theory and practice of measuring reservoir rock and fluid transport properities, 3rd edition*. Elsevier(Singapore) Pte Ltd.

Dong, S., Zeng, L., Xu, C., Dowd, P., Gao, Z., Mao, Z., et al. (2019). A novel method for extracting information on pores from cast thin-section images. *Comput. Geosci.* 130, 69–83. doi:10.1016/j.cageo.2019.05.003

Enkin, R. J., Hamilton, T. S., and Morris, W. A. (2020). The henkel petrophysical plot: Mineralogy and lithology from physical properties. *Geochem. Geophys. Geosyst.* 21 (1), 818. doi:10.1029/2019gc008818

Esfahani, M. R., and Haghighi, M. (2004). Wettability evaluation of Iranian carbonate formations. *J. Pet. Sci. Eng.* 42 (2-4), 257–265. doi:10.1016/j.petrol.2003.12.016

Gong, Y. J., and Liu, K. Y. (2020). Pore throat size distribution and oiliness of tight sands-A case study of the Southern Songliao Basin, China. *J. petroleum Sci. Eng.* 184, 106508. doi:10.1016/j.petrol.2019.106508

Gu, Y. F., Bao, Z. D., and Rui, Z. H. (2018). Complex lithofacies identification using improved probabilistic neural networks. *Petro. S. Journ.* 59 (2), 245–267. doi:10.30632/pjv59n2-2018a9

Huang, D., Li, Y., Liu, M., Yang, J., Bai, R., and Yang, Z. (2017). Reservoir features and exploration potential of the 1st member of Shaximiao Formation of Middle jurassic in central Sichuan Basin. *China Pet. Explor.* 22 (2), 44–49. (In Chinese). doi:10.3969/j.issn.1672-7703.2017.02.005

Jadoon, Q. K., Roberts, E., Thomas, B., Wust, R. J. A., and Shah, S. A. (2016). Petrophysical evaluation and uncertainty analysis of Roseneath and Murteree shales reservoirs in Cooper Basin, Australia (a case study). *J. Petroleum Sci. Eng.* 147, 330–345. doi:10.1016/j.petrol.2016.06.010

Kahle, M., Kleber, M., and Jahn, R. (2002). Review of XRD-based quantitative analyses of clay minerals in soils: The suitability of mineral intensity factors. *Geoderma* 109, 191–205. doi:10.1016/s0016-7061(02)00175-1

Koporulin, V. I. (2013). Formation of laumontite in sedimentary rocks: A case study of sedimentary sequences in Russia. *Lithol. Min. Resour.* 48 (2), 122–137. doi:10.1134/s002449021302003x

Kyle, J. R., and Ketcham, R. A. (2015). Application of high resolution X-ray computed tomography to mineral deposit origin, evaluation, and processing. *Ore Geol. Rev.* 65, 821–839. doi:10.1016/j.oregeorev.2014.09.034

Lai, J., Pang, X., Xiao, Q., Shi, Y., Zhang, H., Zhao, T., et al. (2019). Prediction of reservoir quality in carbonates via porosity spectrum from image logs. *J. Petroleum Sci. Eng.* 173, 197–208. doi:10.1016/j.petrol.2018.10.022

Li, G. X., and Zhu, R. K. (2020). Progress, challenges and key issues of unconventional oil and gas development of CNPC. *China Pet. Explor.* 25 (2), 1–13.

Li, J., Jiang, H., Wang, C., Zhao, Y., Gao, Y., Pei, Y., et al. (2017). Pore-scale investigation of microscopic remaining oil variation characteristics in water-wet sandstone using CT scanning. *J. Nat. Gas. Sci. Eng.* 48, 36–45. doi:10.1016/j.jngse.2017.04.003

Li, S., Zhou, K., Zhao, L., Xu, Q., and Liu, J. (2022). An improved lithology identification approach based on representation enhancement by logging feature decomposition, selection and transformation. *J. Petroleum Sci. Eng.* 209, 109842. doi:10.1016/j.petrol.2021.109842

Liu, G. (2021). Challenges and countermeasures of log evaluation in unconventional petroleum exploration. *Petroleum Explor. Dev.* 48 (5), 891–902. doi:10.11698/PED.2021.05.02

Liu, J., Chang, Q., Lin, C., Zhang, J., and Xia, S. (2016). A new method of deep carbonate lithology identification at the Tadong uplift in the eastern section of the Tarim Basin. *Arab. J. Geosci.* 9, 118. doi:10.1007/s12517-015-2050-x

Lu, W., Zhu, G., and Li, D. (2004). Discovery of sloanite sandstone reservoir of jurassic xiashaximiao Formation in central sichuan region and its significance. *China Pet. Explor.* 5, 53–58.

Ma, M., Li, C., Lv, C., Chen, G., Yang, F., Yan, Y., et al. (2017). Geochemistry and provenance of a multiple-stage fan in the upper miocene to the pliocene in the yinggehai and qiongdongnan basins, offshore south China sea. *Mar. Pet. Geol.* 79, 64–80. doi:10.1016/j.marpetgeo.2016.11.001

Mao, Z. Q., He, Y. D., and Ren, X. J. (2005). An improved method of using NMR T2 distribution to evaluate pore size distribution. *Chin. J. Geophys.* 48 (2), 412–418. doi:10.1002/cjg2.668

Mateen, H., Naveen, H., Ghulam, B., Kanungo, S., Thusu, B., Craig, J., et al. (2022). An assessment of the source potential and reservoir characterization for tight gas exploration in the Subathu Formation shale, Himalayan Foreland Basin, Northwestern India. *J. Asian Earth Sci.* 230, 105205. doi:10.1016/j.jseaes.2022.105205

Roberto, A. (2013). *Flow units: From conventional to tight gas to shale gas to tight oil to shale oil reservoirs[C]*. Monterey, California: Society of Petroleum Engineers. (SPE-165360).

Sauerer, B., Al-Hamad, M., Ma, S. M., and Abdallah, W. (2020). Effect of oil-based-mud filtrate on the wettability of rock surfaces with different mineralogy and topology. *Energy fuels.* 34 (7), 8250–8259. doi:10.1021/acs.energyfuels.0c01335

Shao, X., Pang, X., Jiang, F., Li, L., Huyan, Y., and Zheng, D. (2017). Reservoir characterization of tight sandstones using nuclear magnetic resonance and incremental pressure mercury injection experiments: Implication for tight sand gas reservoir quality. *Energy fuels.* 31, 10420–10431. doi:10.1021/acs.energyfuels.7b01184

Slatt, E. M., and O'Neal, N. R. (2011). Pore types in the Barnett and Woodford gas shales: Contribution to understanding gas storage and migration pathways in fine-grained rocks. *Am. Assoc. Pet. Geol. Bull.* 95 (12), 2017–2030. doi:10.1306/03301110145

Thinesh, K., Seelam, N. K., and Rao., G. S. (2022). Lithology prediction from well log data using machine learning techniques: A case study from talcher coalfield, eastern India. *J. Appl. Geophys.* 199, 104605. doi:10.1016/j.jappgeo.2022.104605

US Energy Information Administration (2018). *International energy outlook 2018*. Washington: US Energy Information.

US Energy Information Administration (2019). *Annual energy outlook 2019 with projections to 2050*. Washington: US Energy Information Administration.

Wu, H., Li, N., Lan, C., Kong, X. Z., and Chai, H. (2013). Standard spectrum measurement and simulation of elemental capture spectroscopy log. *Appl. Geophys.* 10 (1), 109–116. doi:10.1007/s11770-013-0369-1

Wu, S. T., Zou, C. N., Zhu, R. K., Yao, J., Tao, S., Yang, Z., et al. (2016). Characteristics and origin of tight oil accumulations in the upper triassic yanchang formation of the ordos basin, north-Central China. *Acta Geol. Sin. - Engl. Ed.* 90 (5), 1821–1837. doi:10.1111/1755-6724.12819

Yan, J., He, X., Geng, B., Hu, Q. H., Feng, C. Z., Kou, X. P., et al. (2017). Nuclear magnetic resonance T2 spectrum multifractal characteristics and pore structure evaluation. *Appl. Geophys.* 14 (2), 205–215. doi:10.1007/s11770-017-0614-0

Yan, J., He, X., Zhang, S., Feng, C., Wang, J., Hu, Q., et al. (2020). Sensitive parameters of NMR T2 spectrum and their application to pore structure characterization and evaluation in logging profile: A case study from chang 7 in the yanchang formation, heshui area, ordos basin, NW China. *Mar. Petroleum Geol.* 111 (1), 230–239. doi:10.1016/j.marpetgeo.2019.08.025

Yang, X., and Qiu, Y. (2002). Formation process and distribution of laumontite in yanchang formation (upper triassic) of ordos basin. *Acta Sedimentol. Sin.* 20 (4), 628–632. doi:10.1007/s11769-002-0037-5

Yang, Y., Yang, J., and Yang, G. (2016). New research progress of Jurassic tight oil in central Sichuan Basin. *Petroleum Explor. Dev.* 43 (6), 873–882. (In Chinese). doi:10.11698/PED.2016.06.04

Yang, Y., Wang, X., Chen, S., Wen, L., Wu, C., Guan, X., et al. (2022). Sedimentary system evolution and sandbody development characteristics of Jurassic Shaximiao Formation in the central Sichuan Basin. *Nat. Gas. Ind.* 42 (1), 12–24. (in Chinese). doi:10.3787/j.issn.1000-0976.2022.01.002

Zhang, C., Zhu, D., Luo, Q., Liu, L., Liu, D., Yan, L., et al. (2017). Major factors controlling fracture development in the Middle Permian Lucaogou Formation tight oil reservoir, Junggar Basin, NW China. *J. Asian Earth Sci.* 146, 279–295. doi:10.1016/j.jseaes.2017.04.032

Zhang, C. S., Zhang, Y., Shi, X. J., Almpanidis, G., Fan, G., and Shen, X. (2019a). On incremental learning for gradient boosting decision trees. *Neural process. Lett.* 50 (1), 957–987. doi:10.1007/s11063-019-09999-3

Zhang, G., Wang, Z., Gu, X., Sun, Y., Sun, L., and Pan, L. (2019b). Characteristics of lacustrine dolomitic rock reservoir and accumulation of tight oil in the Permian Fengcheng Formation, the Western slope of the Mahu Sag, Junggar Basin, NW China. *J. Asian earth Sci.* 178, 64–80. doi:10.1016/j.jseaes.2019.01.002

Zou, C., Tao, S., and Hou, L. (2014). *Unconventional petroleum geology*. Beijing: Geological Publishing House.

frontiers | Frontiers in Earth Science

TYPE Original Research
PUBLISHED 04 January 2023
DOI 10.3389/feart.2022.1097550

OPEN ACCESS

EDITED BY
Lidong Dai,
Institute of geochemistry (CAS), China

REVIEWED BY
Zhen Li,
Chengdu University of Technology, China
Boye Fu,
Beijing University of Technology, China

*CORRESPONDENCE
Jing Ba,
jba@hhu.edu.cn

SPECIALTY SECTION
This article was submitted to Solid Earth Geophysics, a section of the journal Frontiers in Earth Science

RECEIVED 14 November 2022
ACCEPTED 01 December 2022
PUBLISHED 04 January 2023

CITATION
Ba J, Guo F, Carcione JM and Gei D (2023), P-wave anelasticity in hydrate-bearing sediments based on a triple-porosity model.
Front. Earth Sci. 10:1097550.
doi: 10.3389/feart.2022.1097550

P-wave anelasticity in hydrate-bearing sediments based on a triple-porosity model

Jing Ba[1]*, Fulin Guo[1], José M. Carcione[1,2] and Davide Gei[1,2]

[1]School of Earth Sciences and Engineering, Hohai University, Nanjing, China, [2]National Institute of Oceanography and Applied Geophysics—OGS, Trieste, Italy

P-wave anelasticity (attenuation and dispersion) of hydrate-bearing sediments depends on several factors, namely the properties of the mineral components, hydrate content and morphology, and fluid saturation. Anelasticity is analyzed with a triple-porosity model (stiff pores, clay micropores and hydrate micropores), by considering hydrate as an additional solid skeleton. We relate the hydrate volume ratio, porosity and radii of the hydrate inclusion and clay mineral to the P-wave velocity and attenuation. The model takes wave-induced local fluid flow (mesoscopic loss) at the grain contacts into account. The results are compared with those of a double-porosity and load-bearing models, and verified with well-log data from Offshore Drilling Program sites 1247B and 1250F, and data reported in Nankai Trough, Japan. Model results and data show a good agreement.

KEYWORDS

triple-porosity theory, attenuation, rock physics model, hydrate, dispersion

Introduction

Gas hydrate is an ice-like crystalline medium with a microporous structure composed of gas and water molecules that are formed at low temperature, high pressure and certain gas saturation (Sloan, 1990). Identification of hydrate reservoirs in engineering applications worldwide mainly relies on seismic exploration techniques. The existence of hydrates highly affects the acoustic wave velocity and attenuation. Generally, hydrate-bearing sediments show high compressional (P-) and shear (S-) wave velocities. These velocities and attenuation are usually adopted to estimate the presence of hydrates (Waite et al., 2009). With the increasing hydrate content, the wave velocity increases. Moreover, the morphology and distribution of hydrate also have an effect on the velocities (Ecker et al., 1998; Ecker et al., 2000). However, the relation between attenuation and hydrate content is more complex, as it is associated with mechanisms due to different microporous hydrate forms (Best et al., 2013).

Rock physics is an effective approach to describe the quantitative relation between the rock microstructure and the wave properties. A suitable model associated with the hydrate morphology could be helpful to improve the accuracy in the estimation of hydrate content (Pan et al., 2019). In fact, the hydrate-bearing sediment is a three-phase porous medium, composed of a rock frame saturated with a fluid (usually water) and hydrates (Liu et al.,

2021). Biot (1962) considered wave propagation in fully saturated porous media including anisotropy and viscoelasticity, and a loss mechanism related to the differential motion between the frame and the fluid. Stoll and Bryan. (2009) was the first to systematically apply Biot's theory to marine sediments. Carcione and Gei (2004) proposed a Biot-type theory of two solids and one fluid, in which hydrate is considered as a second skeleton (frame) and water is the pore fluid—grain cementation and friction between the two frames have been considered (see also, Carcione et al. (2005); Gei and Carcione (2003); Gei et al. (2022)). This model has also been used by Guerin and Goldberg (2005).

On the other hand, Ba et al. (2011); Ba et al. (2016) proposed a double-porosity model to describe attenuation due to local fluid flow between soft and stiff pores (mesoscopic or microscopic loss). For the same purpose, Zhang et al. (2017) presented an alternative model based on the triple-porosity structure of sand, gravel and mudstone while, Zhang et al. (2016) applied the BISQ (Biot/squirt) model specifically to marine unconsolidated hydrate-bearing sediments. They found that wave velocity and attenuation increase with increasing hydrate content, in agreement with some measurement data (Chand and Minshull, 2004; Guerin and Goldberg, 2005; Matsushima, 2006), and that porosity has a weak effect on attenuation. Zhan et al. (2022) discussed and compared the feasibility and limitations of existing rock physics models. The combination of different models may be more conducive to explaining the mechanism of attenuation.

Attenuation also depends on the hydrate morphology and microstructure (Priest et al., 2009), as shown by laboratory measurements, including local viscous fluid flow related to the microporous structure of hydrate containing gas and water (Best et al., 2013). Leurer and Brown (2008) proposed a model to explain the viscoelasticity generated by local fluid flow in the presence of clay at grain contacts. Marín-Moreno et al. (2017) developed the hydrate-bearing effective sediment model (HBES) to analyze various loss mechanisms, including those caused by squirt flow in microporous hydrate, viscoelasticity of the hydrate frame and Biot global flow. They analyzed the effect of hydrate morphology on attenuation by comparing results between sediments with and without hydrates. Sahoo et al. (2019) performed high-precision ultrasonic pulse-echo measurements of wave velocity and attenuation in hydrate-bearing sediments. Li et al. (2015) studied the effect of clay content on the mechanical properties of these sediments by applying the tests of multi-stage loading triaxial compression and hydrate decomposition. On the basis of six microscopic hydrate morphologies, Pan et al. (2019) obtained rock-physics templates (RPTs), based on an amplitude-variation with offset (AVO) analysis, and predicted hydrate content, porosity and clay content of permafrost-associated hydrate-bearing sediments at Mount Elbert, North Slope of Alaska.

The hydrate distribution in the pore space is important. In the formation process, gas hydrate is present in different forms due to the influence of the geological setting, formation pressure and geothermal gradient. Ecker et al. (1998) proposed three types of hydrate distributions, namely, grain-contact cementing, grain coating and absent in the grain contacts. Dai et al. (2004) proposed six distributions: grain-contact cementing, grain coating, supporting matrix/grains, pore-filling, matrix and inclusions, and nodules/fracture fillings. Zhan and Matsushima. (2018) considered four distributions: grain-contact cementing, grain coating, load-bearing and pore-filling (Schicks et al., 2006). Three microscopic distribution patterns of hydrates, namely pore filling, contact or encapsulated cementation and load-bearing hydrates, are discussed by Waite et al. (2009).

Understanding the effect of anelasticity on the acoustic properties is not clear, mainly because attenuation behaves differently at different frequency bands. Here, we consider the local fluid flow between stiff pores, hydrates, and clay, based on a triple-porosity model (Zhang et al., 2017). In addition to the double-porosity model, the new model considers the effects of clay micropores. The results agree with log data, providing an effective approach to model the P-wave anelasticity mechanisms of hydrate-bearing sediments.

The model

We consider the main frame or skeleton containing intergranular pores as the host phase, hydrate and clay as two different types of multi-pore inclusions, and describe the hydrate-bearing sediments with a triple-porosity model. It has been observed that hydrate can cement the mineral grain and contributes to the solid skeleton or being part of pore-filling material. Cementation decreases the porosity and increases the bulk modulus of the skeleton. Figure 1 shows three cases where hydrate is 1) part of the pore infill; 2) part of the frame; 3) cementing the grains. We consider the case in panel 2).

In this case, the hydrate-bearing sediment can be regarded as a composite of three skeletons: rock (minerals), hydrate and clay. Basically, hydrate and clay reduce the bulk porosity and combine with the minerals as shown in Figure 2, and then the resulting frame is saturated.

As stated above, the understanding on wave-loss mechanisms of hydrate-bearing sediments is still limited (Best et al., 2013). Figure 3 shows the mechanisms considered in our triple-porosity model, i.e., local fluid flow between the rock skeleton and hydrate and clay frames, and the classical Biot global flow (Zhang et al., 2022).

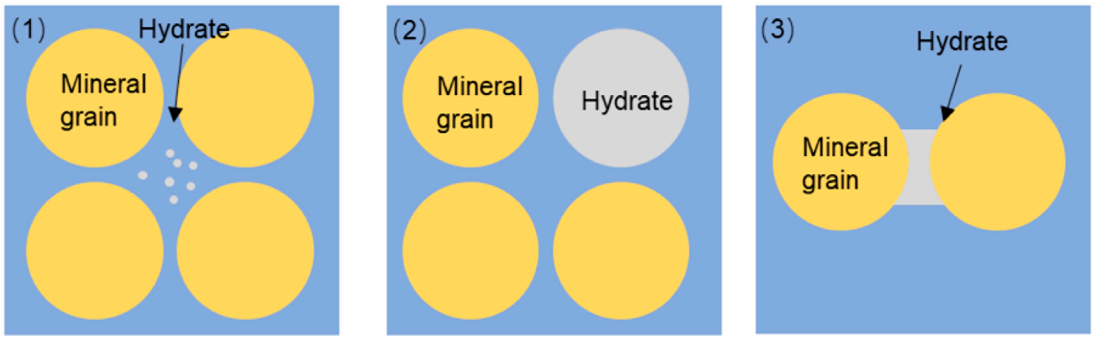

FIGURE 1
Scheme showing the three hydrate morphologies.

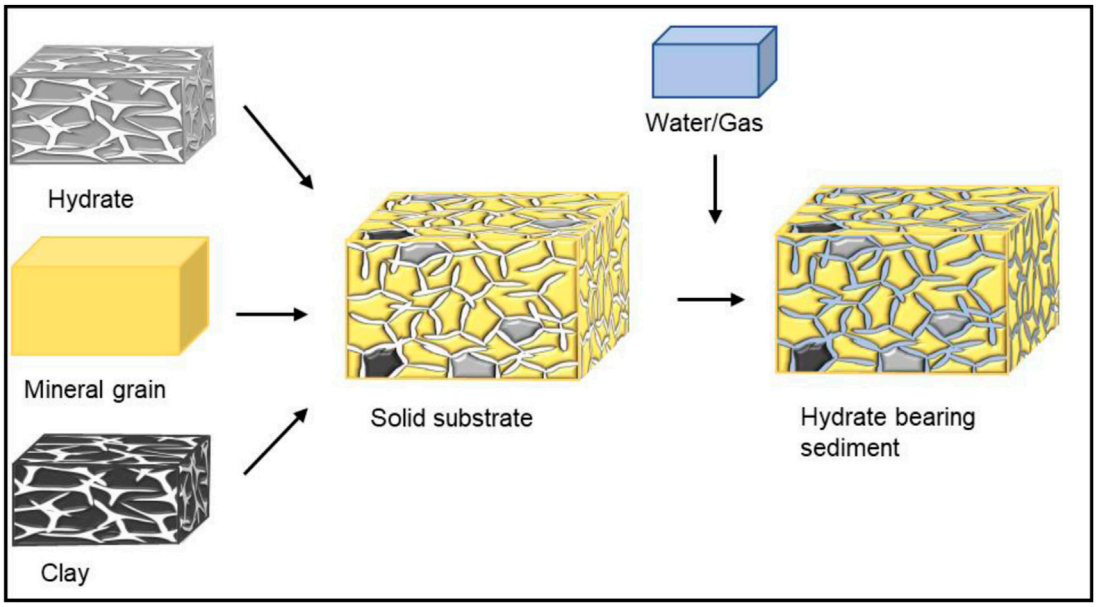

FIGURE 2
Diagram showing hydrate as part of the solid frame (skeleton).

Properties of fluid

If hydrate is part of the frame, the pore fluid is a mixture of water and free gas, such that its effective bulk modulus is (Wood, 1955; Wood et al., 2000; Liu et al., 2017)

$$K_f = \left(\frac{S_w}{K_w} + \frac{S_g}{K_g}\right)^{-1} \tag{1}$$

where S_w and S_g are the water and free gas saturations, K_g and K_w are the respective bulk moduli with $S_w + S_g = 1$.

The effective density of the fluid is

$$\rho_f = \rho_w S_w + \rho_g S_g \tag{2}$$

where ρ_f, ρ_w and ρ_g are the densities of fluid, water and gas, respectively.

Properties of solid phase (composite mineral)

According to the Hill average (Hill, 1952), the moduli of the solid phase considering the presence of hydrate are (Helgerud et al., 1999; Ecker et al., 2000)

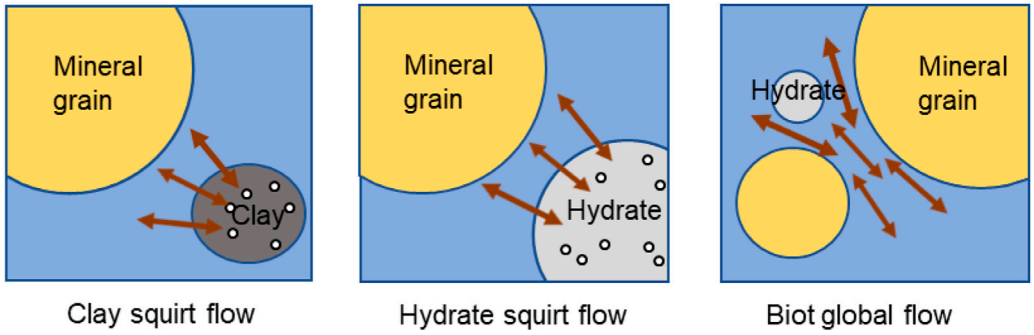

FIGURE 3
Attenuation mechanisms of the triple-porosity model.

$$K_s = \frac{1}{2}\left\{\sum_{i=1}^{4} f_i K_i + \left(\sum_{i=1}^{4} \frac{f_i}{K_i}\right)^{-1}\right\} \tag{3a}$$

$$G_s = \frac{1}{2}\left\{\sum_{i=1}^{4} f_i G_i + \left(\sum_{i=1}^{4} \frac{f_i}{G_i}\right)^{-1}\right\} \tag{3b}$$

where $i = 1, 2, 3$ and 4 indicate calcite, quartz, hydrate and clay, respectively, K_i and G_i are the respective bulk and shear moduli of the $i-th$ constituent, and f_i is the volume fraction of the $i-th$ constituent, with $\sum_1^4 f_i = 1$.

Properties of the frame

Let us define the volume ratios, local porosities and absolute porosities of the host phase made of quartz and calcite, hydrate skeleton and clay skeleton as ν_2, ν_1 and ν_3, ϕ_{20}, ϕ_{10} and ϕ_{30}, and ϕ_2, ϕ_1 and ϕ, respectively, with $\phi_1 = \phi_{10}\nu_1$, $\phi_2 = \phi\nu_2$ and $\phi_3 = \phi_{30}\nu_3$ (Zhang et al., 2017; Wang et al., 2021; Zhang et al., 2021), and

$$\nu_2 = 1 - \nu_1 - \nu_3 \tag{4a}$$

$$\frac{f_3}{\nu_1(1-\phi_{10})} = \frac{f_4}{\nu_3(1-\phi_{30})} = \frac{f_1 + f_2}{\nu_2(1-\phi_{20})} \tag{4b}$$

The porosity of the host phase is

$$\phi_2 = \phi - \phi_1 - \phi_3 \tag{5}$$

where ϕ is the porosity of the rock with hydrate formation.

Compared to the Hashin-Shtrikman upper bound, the Hashin-Shtrikman lower bound is appropriate for estimating the elastic moduli of submarine sediments, where the soft components (clay or soft minerals) are majorly distributed surrounding the stiff grains. The dry-rock elastic moduli are obtained by the modified Hashin-Shtrikman lower bound (Ecker et al., 1998; Dvorkin et al., 1999; Helgerud et al., 1999)

$$K_b = \left(\frac{\phi/\phi_c}{K_{HM} + \frac{4}{3}G_{HM}} + \frac{1-\phi/\phi_c}{K_s + \frac{4}{3}G_{HM}}\right)^{-1} - \frac{4}{3}G_{HM} \quad \phi < \phi_c \tag{6a}$$

$$K_b = \left(\frac{(1-\phi)/(1-\phi_c)}{K_{HM} + \frac{4}{3}G_{HM}} + \frac{(\phi-\phi_c)/(1-\phi_c)}{\frac{4}{3}G_{HM}}\right)^{-1} - \frac{4}{3}G_{HM} \quad \phi > \phi_c \tag{6b}$$

$$G_b = \left(\frac{\phi/\phi_c}{G_{HM} + Z} + \frac{1-\phi/\phi_c}{G_s + Z}\right)^{-1} - Z \quad \phi < \phi_c \tag{7a}$$

$$G_b = \left(\frac{(1-\phi)/(1-\phi_c)}{G_{HM} + Z} + \frac{(\phi-\phi_c)/(1-\phi_c)}{Z}\right)^{-1} - Z \quad \phi > \phi_c \tag{7b}$$

where K_{HM} and G_{HM} are the bulk and shear moduli of the rock under the critical porosity, respectively, and

$$Z = \frac{G_{HM}}{6}\left[\frac{9K_{HM} + 8G_{HM}}{K_{HM} + 2G_{HM}}\right] \tag{8a}$$

$$K_{HM} = \left[\frac{G_s^2 n^2 (1-\phi_c)^2}{18\pi^2(1-\sigma)^2} P\right]^{\frac{1}{3}} \tag{8b}$$

$$G_{HM} = \frac{5-4\sigma}{5(2-\sigma)}\left[\frac{3G_s^2 n^2 (1-\phi_c)^2}{2\pi^2(1-\sigma)^2} P\right]^{\frac{1}{3}} \tag{8c}$$

where ϕ_c is the critical porosity, ranging from 0.36 to 0.4, n is the coordination number (the average number of contacts per grain, ranging from 8 to 9.5), P is the effective stress, $P = (1-\phi)(\rho_s - \rho_f)gh$, ρ_s is the average density of the skeleton, $\rho_s = \sum_1^m f_i\rho_i$, where ρ_i is the density of the $i-th$ constituent, h is the depth below sea floor, g is the acceleration of gravity, and σ is the Poisson ratio of the solid phase.

Properties of the saturated sediment

There are two approaches to relate the hydrate content to the P-wave velocity. One method is the use of empirical relations, such as the time-average equation (Wyllie et al., 1958) and Lee

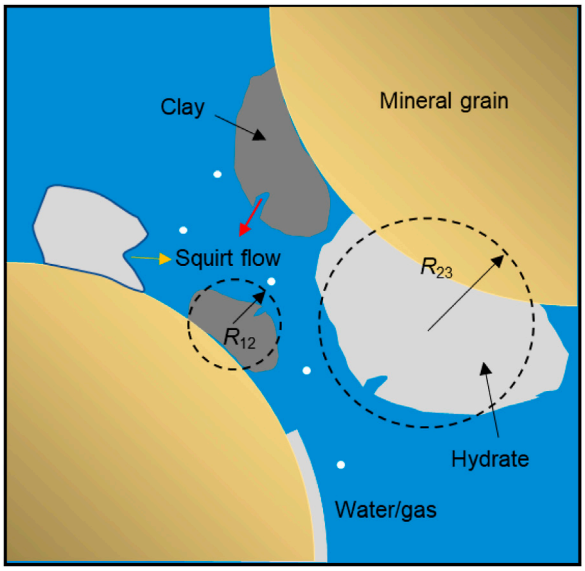

FIGURE 4
Schematic diagram of the proposed triple-porosity model.

weighted equation (Lee et al., 1996; Lee and Collett, 2009), by combining the Wood and time-average equations (Helgerud et al., 1999). Other approaches are poroelasticity and effective medium theories (Helgerud et al., 1999). These methods involve input parameters which are difficult to be obtained in actual applications (Hu et al., 2010).

The double-porosity theory considers that in the process of seismic wave propagation, the micropore structure of the hydrate phase induces a local flow between these micropores and the stiff pores and causes energy loss and velocity dispersion (see Figure 4). This theory, however, ignores the presence of clay, which may also cause flow (Wang et al., 2021). The inclusion of clay leads to the triple-porosity model (see red arrow in Figure 4).

Zhang et al. (2017) developed a theory to model the properties of a saturated medium, where the local fluid-flow mechanisms, responsible for wave attenuation and dispersion, are considered. Based on Hamilton's principle, the dynamical equations can be obtained from the strain energy, kinetic energy and dissipation potential of a triple-porosity medium. The differential equations of motion, extended to the case of hydrate-bearing sediments, are

$$\begin{aligned} &G_b\nabla^2\mathbf{u} + (A+G_b)\nabla e + Q_1\nabla(\xi_1+\phi_2\zeta_{12}) \\ &\quad + Q_2\nabla(\xi_2-\phi_1\zeta_{12}+\phi_3\zeta_{23}) + Q_3(\xi_3-\phi_2\zeta_{23}) \\ &\quad = \rho_{00}\ddot{\mathbf{u}} + \rho_{01}\ddot{\mathbf{U}}^{(1)} + \rho_{02}\ddot{\mathbf{U}}^{(2)} + \rho_{03}\ddot{\mathbf{U}}^{(3)} + b_1\left(\dot{\mathbf{u}}-\dot{\mathbf{U}}^{(1)}\right) \\ &\qquad + b_2\left(\dot{\mathbf{u}}-\dot{\mathbf{U}}^{(2)}\right) + b_3\left(\dot{\mathbf{u}}-\dot{\mathbf{U}}^{(3)}\right) \end{aligned} \tag{9a}$$

$$Q_1\nabla e + R_1\nabla(\xi_1+\phi_2\zeta_{12}) = \rho_{01}\ddot{\mathbf{u}} + \rho_{11}\ddot{\mathbf{U}}^{(1)} - b_1\left(\dot{\mathbf{u}}-\dot{\mathbf{U}}^{(1)}\right) \tag{9b}$$

$$Q_2\nabla e + R_2\nabla(\xi_2-\phi_1\zeta_{12}+\phi_3\zeta_{23}) = \rho_{02}\ddot{\mathbf{u}} + \rho_{22}\ddot{\mathbf{U}}^{(2)} - b_2\left(\dot{\mathbf{u}}-\dot{\mathbf{U}}^{(2)}\right) \tag{9c}$$

$$Q_3\nabla e + R_3\nabla(\xi_3-\phi_2\zeta_{23}) = \rho_{03}\ddot{\mathbf{u}} + \rho_{33}\ddot{\mathbf{U}}^{(3)} - b_3\left(\dot{\mathbf{u}}-\dot{\mathbf{U}}^{(3)}\right) \tag{9d}$$

$$\begin{aligned} &\frac{1}{3}\rho_f R_{12}^2\ddot{\zeta}_{12}\phi_2^2\phi_1\left(\frac{1}{5}+\frac{\phi_{10}}{\phi_{20}}\right) + \frac{1}{3}\left(\frac{\eta}{5\kappa_1}+\frac{\eta}{\kappa_2}\right)R_{12}^2\dot{\zeta}_{12}\phi_2^2\phi_1\phi_{10} \\ &\quad = \phi_2\left(Q_1 e + R_1(\xi_1+\phi_2\zeta_{12})\right) \\ &\qquad - \phi_1\left(Q_2 e + R_2(\xi_2-\phi_1\zeta_{12}+\phi_3\zeta_{23})\right) \end{aligned} \tag{9e}$$

$$\begin{aligned} &\frac{\phi_3}{3}\rho_f R_{23}^2\ddot{\zeta}_{23}{\phi_2}^2\left(\frac{1}{5}+\frac{\phi_{30}}{\phi_{20}}\right) + \frac{1}{3}\left(\frac{\eta}{\kappa_2}+\frac{\eta}{5\kappa_3}\right)R_{23}^2\dot{\zeta}_{23}{\phi_2}^2\phi_3\phi_{30} \\ &\quad = \phi_3\left(Q_2 e + R_2(\xi_2-\phi_1\zeta_{12}+\phi_3\zeta_{23})\right) \\ &\qquad - \phi_2\left(Q_3 e + R_3(\xi_3-\phi_2\zeta_{23})\right) \end{aligned} \tag{9f}$$

where $\dot{\boldsymbol{u}}$, $\dot{\boldsymbol{U}}^{(1)}$, $\dot{\boldsymbol{U}}^{(2)}$, and $\dot{\boldsymbol{U}}^{(3)}$ are the displacement vector of the frame and the average fluid displacement vectors in the hydrate internal pores, intergranular pores and clay micropores, respectively; e, ξ_1, ξ_2, ξ_3 are the displacement divergence fields of the solid and fluids in the three types of pore systems, respectively; ζ_{12}, ζ_{23} are the bulk strain increments caused by the local flow between the hydrate micropores and intergranular pores, and the local flow between the clay micropores and intergranular pores, respectively; ρ_{00}, ρ_{01}, ρ_{02}, ρ_{03}, ρ_{11}, ρ_{22}, and ρ_{33} are the Biot density coefficients; b_1, b_2, and b_3 are dissipation coefficients (Biot, 1962; Zhang et al., 2017; see Appendix A); Q_1, Q_2 and Q_3, are the elastic parameters of coupled solid and fluid, A is the elastic parameter of solid phase, and R_1, R_2, and R_3 are the elastic parameters of flow phase (see Appendix A); κ_1, κ_2 and κ_3 denote the permeabilities of the hydrate skeleton, host phase and clay skeleton, respectively; η is fluid viscosity, R_{12} and R_{23} denote the hydrate inclusion radius and clay inclusion radius, respectively. The above equations are solved with a plane-wave analysis to obtain the phase velocity and attenuation (see Appendix B) (Ba et al., 2011; Ba et al., 2012; Carcione, 2022).

Example

The minerals are calcite, quartz, clay and hydrate, with volume fractions of f_1 = 4%, f_2 = 70%, f_4 = 20% and f_3 = 6%, respectively. The rock porosity with hydrate formation is ϕ = 35%, and the free gas saturation is S_g = 2%. The volume ratios of the hydrate and clay frames are ν_1 = 4% and ν_3 = 13.1%, respectively, and the corresponding local porosities are ϕ_{10} = 2% and ϕ_{30} = 0.5%, respectively. The bulk modulus of hydrate, rock and clay frames are K_{b1} = 0.76 GPa, K_{b2} = 1.27 GPa, and K_{b3} = 1.02 GPa, respectively, the permeability of the host phase is $\kappa_2 = 1\times10^{-11}$ m^2, the permeability of the hydrate or clay frames is $\kappa_1 = \kappa_3 = 1\times10^{-13}$ m^2, and the fluid viscosity is η = 0.001 kg/(m · s). Table 1 shows the properties of the different phases.

The energy loss caused by the fluid flow depends on the radius of the hydrate inclusions with micropores. Figure 5 shows

TABLE 1 Properties of the phases (Helgerud et al., 1999).

Mineral	Bulk modulus (GPa)	Shear modulus (GPa)	Density (g/cm^3)
Quartz	36.00	45.00	2.65
Calcite	76.80	32.00	2.71
Clay	20.90	6.85	2.58
Water	2.25	0.00	1.00
Gas	0.10	0.00	0.23
Hydrate	7.90	3.30	0.90

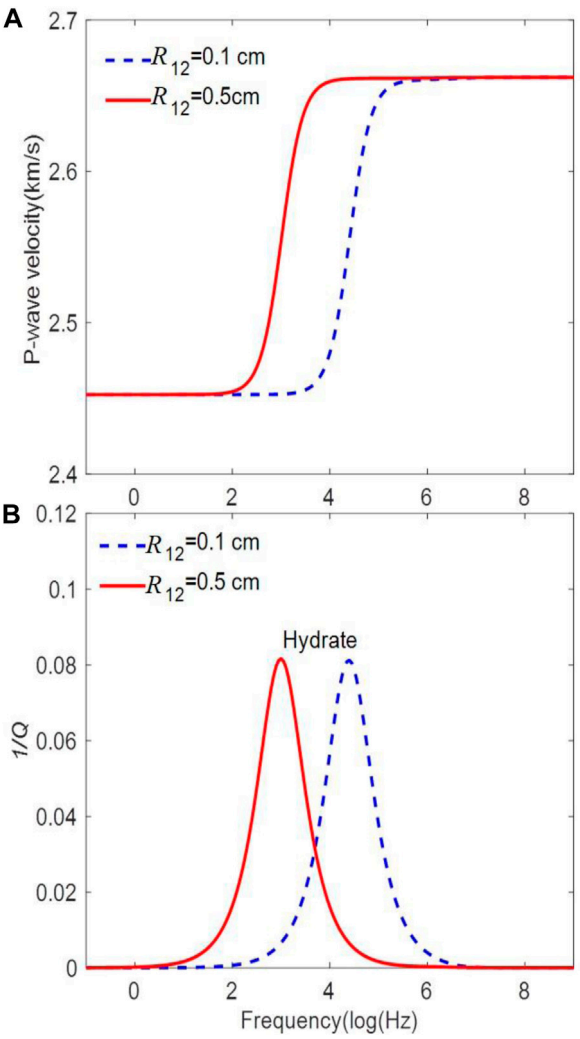

FIGURE 5
Frequency dependence of the P-wave velocity **(A)** and attenuation **(B)** corresponding to the double-porosity model with two radii of the hydrate inclusions.

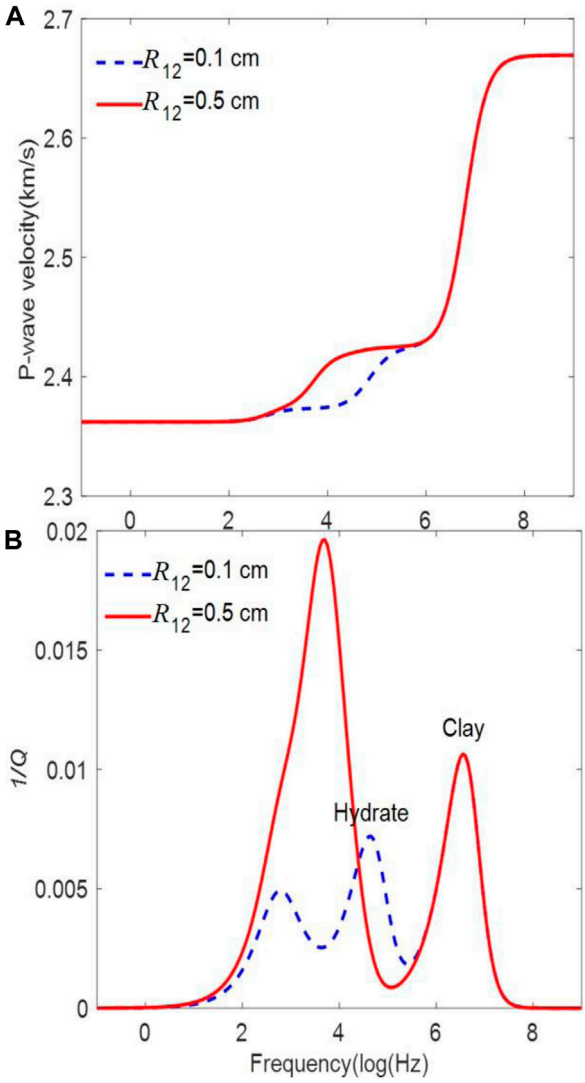

FIGURE 6
Frequency dependence of the P-wave velocity **(A)** and attenuation **(B)** corresponding to the triple-porosity model with two radii of the hydrate inclusions.

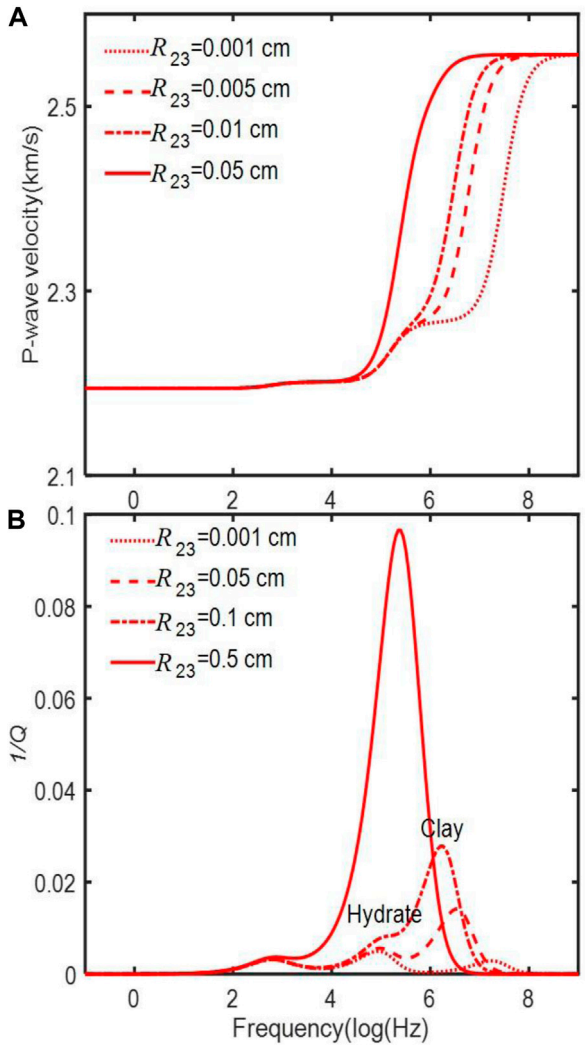

FIGURE 7
Effect of the clay inclusion radius on the P-wave velocity dispersion **(A)** and attenuation **(B)**. The radius of the hydrate inclusion is R_{12} = 0.05 cm, and the rock porosity is ϕ = 20%.

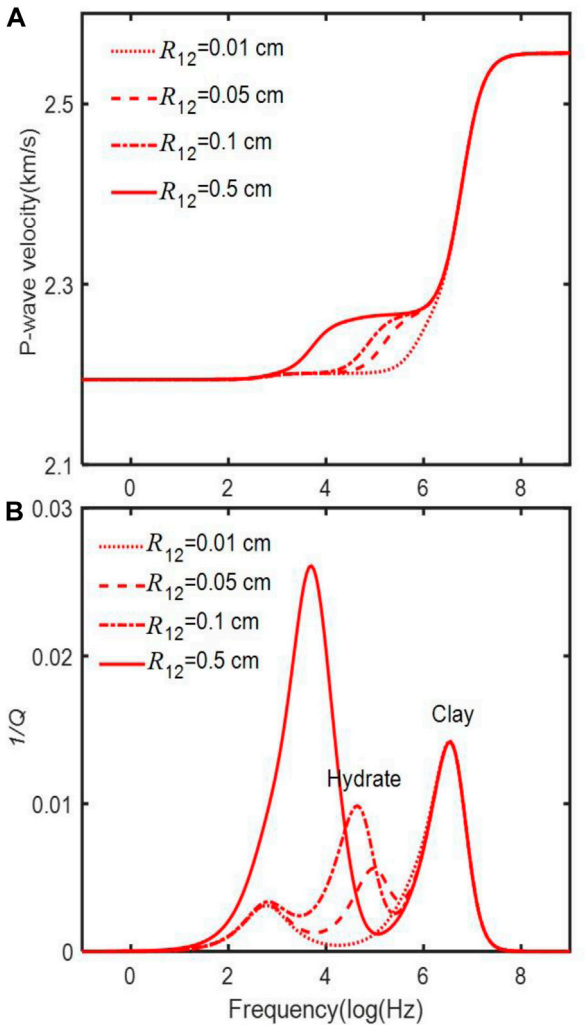

FIGURE 8
Effect of the hydrate inclusion radius on the P-wave velocity dispersion **(A)** and attenuation **(B)**. The radius of the clay inclusion is R_{23} = 0.005 cm, and the rock porosity is ϕ = 20%.

the results of the double-porosity theory (clay is considered part of the host phase and hydrate is an inclusion), where we can observe a single inflection point and attenuation peak. With increasing radius of these inclusions, the local fluid-flow attenuation peak moves to the low frequencies. The global fluid-flow peak, occurring at high frequencies, is much weaker, almost negligible.

On the other hand, Figure 6 shows the results of the triple-porosity theory, which exhibits the two local fluid-flow mechanisms, between the stiff pores and the soft pores of clay and hydrate phases. The global Biot peak is also present. The clay inclusion radius is R_{23} = 0.005 cm. The peak due to hydrate merges with the global flow peak when the radius of the hydrate inclusions increase, while the peaks due to clay is not affected.

Figures 7A, B show the P-wave velocity and dissipation factor as a function of frequency for different clay inclusion radii, respectively. Changes can be observed at high frequencies. When the peaks are close, higher attenuation is observed.

Figures 8A, B show the P-wave velocity and dissipation factor as a function of frequency for different hydrate inclusion radii, respectively, where we can see differences at middle frequencies.

Figures 9A, B show the P-wave velocity and dissipation factor as a function of frequency for different porosities, respectively, where we can see that increasing porosity enhances the loss due to the local flow related to clay and the global flow.

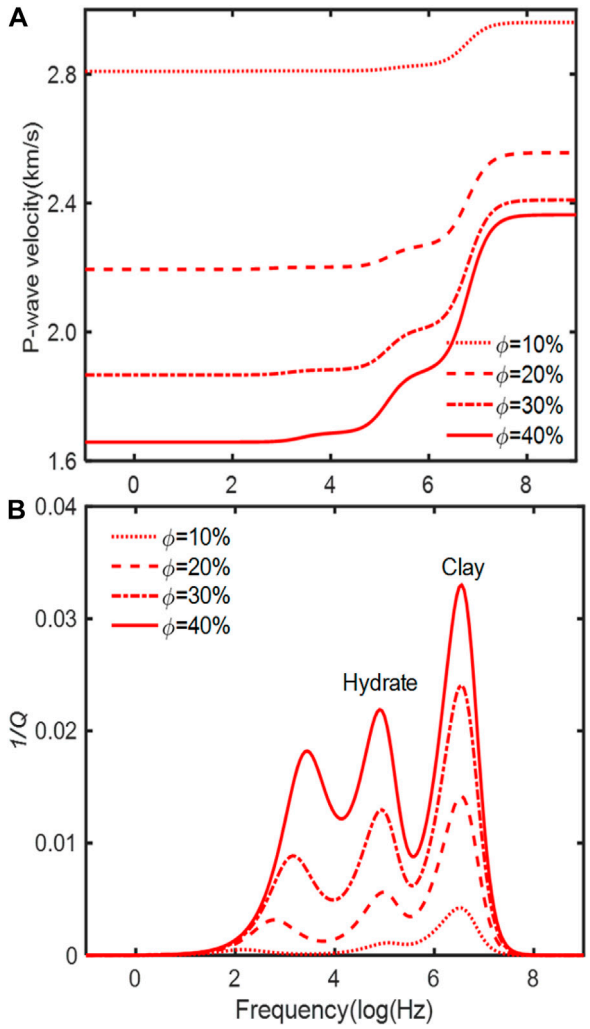

FIGURE 9
Effect of porosity on the P-wave velocity dispersion **(A)** and attenuation **(B)**. The radius of the hydrate inclusion is R_{12} = 0.005 cm, and the radius of the clay inclusion is R_{23} = 0.05 cm.

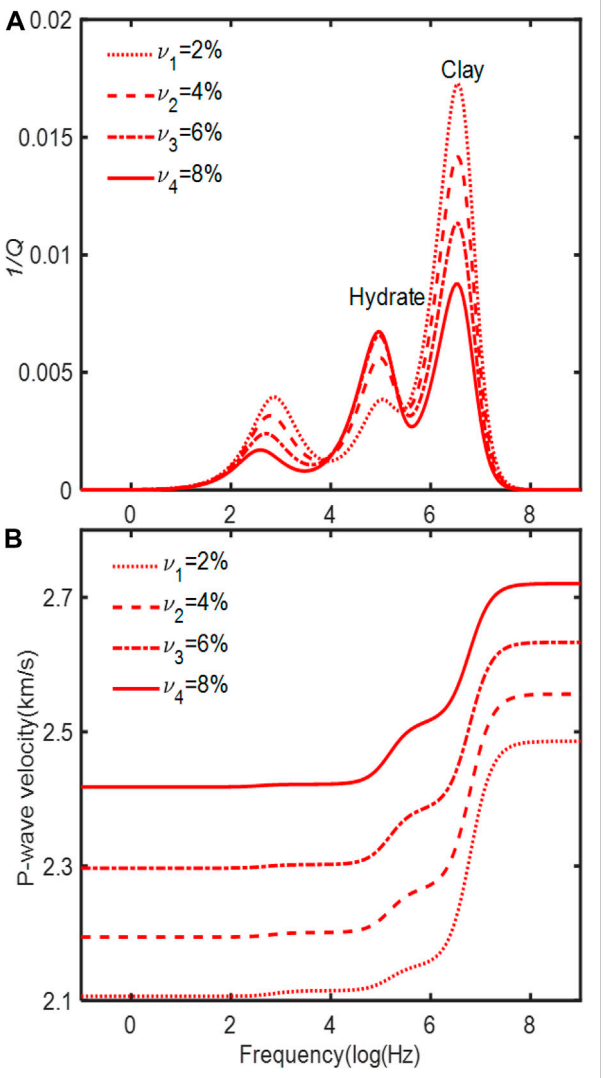

FIGURE 10
Effect of the hydrate volume ratios on the P-wave velocity dispersion **(A)** and attenuation **(B)**. The radius of the hydrate inclusions is R_{12} = 0.005 cm, and the radius of the clay inclusions is R_{23} = 0.05 cm.

Finally, Figures 10A, B show the P-wave phase velocity and dissipation factor as a function of frequency for different hydrate volume ratios, respectively. With the increase of hydrate volume ratio, the P-wave anelasticity due to the hydrate inclusions increase, while those of the clay local flow and global flow decrease. The hydrate volume ratio has no apparent effect on the characteristic frequencies of the peaks.

Comparison with well-log data

The Offshore Drilling Program (ODP) drilled through a gas hydrate stabilization zone on the Cascadia edge off Oregon, providing information on the physical properties of hydrate-bearing sediments. The present model is applied to log data of wells 1247B and 1250F of the ODP204 cruise by Pan et al. (2019) and to data obtained by Zhan and Matsushima. (2018) in the Nankai Trough, in Japan.

ODP data

Figures 11A, B show the theoretical and measured (symbols) P-wave velocities as a function of porosity and hydrate saturation, where S_h denotes hydrate saturation (with the relation of $\nu_1 = \phi S_h$), between 0 and 19%, corresponding to

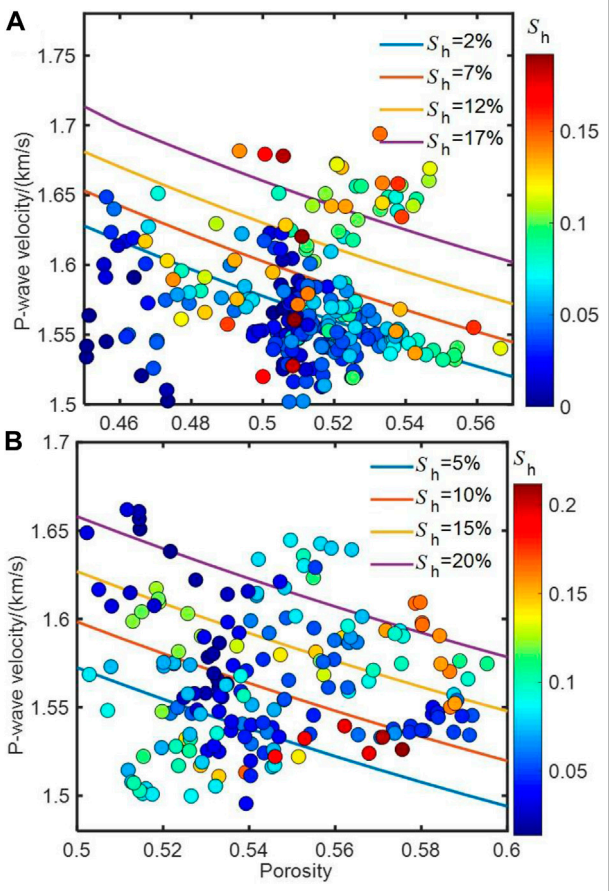

FIGURE 11
Measured P-wave velocity (symbols) as a function of porosity for different hydrate saturations in wells 1247B **(A)** and 1250F **(B)** compared to the model results (solid lines).

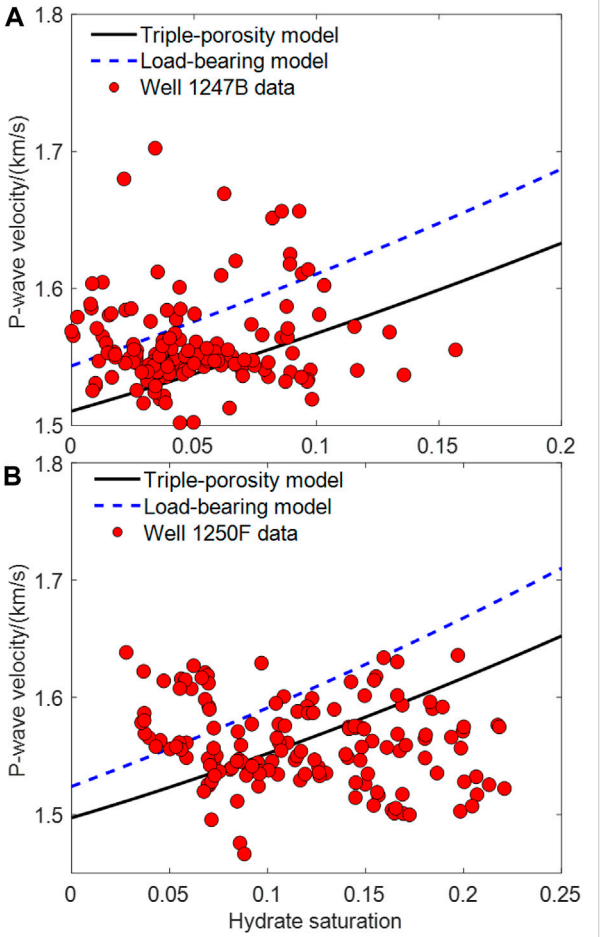

FIGURE 12
Measured P-wave velocity data (symbols) compared to the results of the triple-porosity and load-bearing models varying with hydrate saturation in Wells 1247B **(A)** and 1250F **(B)**.

wells 1247B and 1250F, respectively. The variations of scatters with respect to the colorbar reflect the trend that the P-wave velocity of hydrate reservoir rocks decreases with increasing porosity and increases with hydrate saturation. The agreement is good, with the velocity decreasing with increasing porosity and decreasing hydrate saturation.

Figures 12A, B shows the P-wave velocity as a function of the hydrate saturation in the two wells. In well 1247B the porosity range is ϕ = 0.525–0.535, with an average of 0.53, while that of well 1250F is ϕ = 0.545–0.555 with an average of 0.55. The clay volume ratio in both wells is 0.2 (Pan et al., 2019). Again, the agreement is satisfactory. There is a positive correlation between the P-wave velocity and hydrate saturation. Also shown are the results of the load-bearing model (Best et al., 2013), whose values are generally higher than the measured ones. For well 1250F, at the hydrate saturation range of 0.1–0.15, the average deviation of the triple-porosity model predictions with respect to the logging data is 22.84 m/s and that of the load-bearing model is 48.93 m/s.

Nankai-trough data

We consider the sonic-log and VSP data obtained by Zhan and Matsushima. (2018) in the Nankai Trough, Japan. The frequency is 14 kHz, the strata rock porosity is approximately in the range of ϕ = 35%–43%, the grain coordination number is n = 8.5, and the seawater viscosity is η = 0.0018 kg/(m•s). Figures 13A, B compare the measured and theoretical P-wave velocities and dissipation factor as a function of hydrate saturation, for the double- and triple-porosity models. The theoretical porosity is ϕ = 35%, the clay radius is R_{23} = 0.2 cm, and the hydrate inclusion radius is R_{12} = 0.075 cm. The velocity gradually increases with hydrate saturation, and the variation of the measured P-wave attenuation is relatively large, possibly related to different hydrate morphologies not considered here (see Figure 1). The first model predicts a higher velocity when the hydrate saturation exceeds 20%. The triple-porosity model shows a better agreement.

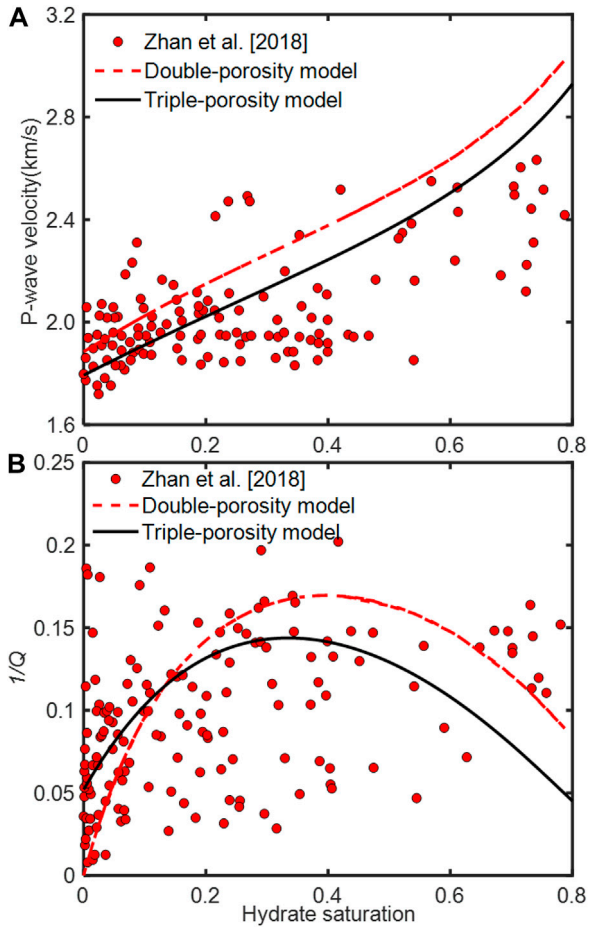

FIGURE 13
Measured P-wave velocity **(A)** and dissipation factor **(B)** (symbols) compared to the results of the double- and triple-porosity models.

Conclusion

The mechanisms of wave propagation in hydrate-bearing sediments are analyzed by using a triple-porosity model. Specifically, we obtain the P-wave velocity and attenuation as a function of frequency, inclusion radius of the clay and hydrate phases, porosity, and hydrate volume ratio. The model considers three attenuation mechanisms, namely, two due to local fluid flow between the rock frame and clay and hydrate inclusions (mesoscopic loss) and the classical global Biot loss. Local flow effects dominate at low (seismic) frequencies. Well-log data from ODP204 site and offshore Japan are compared to the model predictions, which show a good agreement.

Data availability statement

The original contributions presented in the study are included in the article/supplementary material, further inquiries can be directed to the corresponding author.

Author contributions

JB: modeling, writing and verification. FG: modeling and writing. JC: writing and verification. DG: writing and verification.

Funding

The authors were grateful to the support of the Jiangsu Innovation and Entrepreneurship Plan, research funds from SINOPEC Key Laboratory of Geophysics, Jiangsu Province Science Fund for Distinguished Young Scholars (BK20200021), and National Natural Science Foundation of China (41974123).

Conflict of interest

The authors declare that the research was conducted in the absence of any commercial or financial relationships that could be construed as a potential conflict of interest.

Publisher's note

References

Ba, J., Carcione, J. M., Cao, H., Du, Q. Z., Yuan, Z. Y., and Lu, M. H. (2012). Velocity dispersion and attenuation of P waves in partially-saturated rocks: Wave propagation equations in double-porosity medium. Chinese J. *Geophys.* 55, 219–231. doi:10.6038/j.issn.0001-5733.2012.01.021

Ba, J., Carcione, J. M., and Nie, J. X. (2011). Biot-Rayleigh theory of wave propagation in double-porosity media. *J. Geophys. Res.* 116, B06202. doi:10.1029/2010jb008185

Ba, J., Zhao, J., Carcione, J. M., and Huang, X. X. (2016). Compressional wave dispersion due to rock matrix stiffening by clay squirt flow. *Geophys. Res. Lett.* 43, 6186–6195. doi:10.1002/2016gl069312

Best, A. I., Priest, J. A., Clayton, C. R. I., and Rees, E. V. L. (2013). The effect of methane hydrate morphology and water saturation on seismic wave attenuation in sand under shallow sub-seafloor conditions. *Earth Planet. Sci. Lett.* 368, 78–87. doi:10.1016/j.epsl.2013.02.033

Biot, M. (1962). Generalized theory of acoustic propagation in porous dissipative media. *J. Acoust. Soc. Am.* 34, 1254–1264. doi:10.1121/1.1918315

Carcione, J. M., and Gei, D. (2004). Gas-hydrate concentration estimated from P- and S-wave velocities at the Mallik 2L-38 research well, Mackenzie Delta, Canada. *J. Appl. Geophy.* 56, 73–78. doi:10.1016/j.jappgeo.2004.04.001

Carcione, J. M., Gei, D., Rossi, G., and Madrussani, G. (2005). Estimation of gas-hydrate concentration and free-gas saturation at the Norwegian-Svalbard continental margin. *Geophys. Prospect.* 53, 803–810. doi:10.1111/j.1365-2478.2005.00502.x

Carcione, J. M. (2022). *Wave fields in real media. Theory and numerical simulation of wave propagation in anisotropic, anelastic, porous and electromagnetic media*. 4th Edn. Amsterdam: Elsevier.

Chand, S., and Minshull, T. A. (2004). The effect of hydrate content on seismic attenuation: A case study for mallik 2L-38 well data, mackenzie delta, Canada. *Geophys. Res. Lett.* 31, L14609. doi:10.1029/2004gl020292

Dai, J., Xu, H., Snyder, F., and Dutta, N. (2004). Detection and estimation of gas hydrates using rock physics and seismic inversion: Examples from the northern deepwater Gulf of Mexico. *Lead. Edge* 23, 60–66. doi:10.1190/1.1645456

Dvorkin, J., Prasad, M., Sakai, A., and Lavoie, D. (1999). Elasticity of marine sediments: Rock physics modeling. *Geophys. Res. Lett.* 26, 1781–1784. doi:10.1029/1999gl900332

Ecker, C., Dvorkin, J., and Nur, A. M. (2000). Estimating the amount of gas hydrate and free gas from marine seismic data. *Geophysics* 65, 565–573. doi:10.1190/1.1444752

Ecker, C., Dvorkin, J., and Nur, A. M. (1998). Sediments with gas hydrates: Internal structure from seismic AVO. *Geophysics* 63, 1659–1669. doi:10.1190/1.1444462

Gei, D., and Carcione, J. M. (2003). Acoustic properties of sediments saturated with gas hydrate, free gas and water. *Geophys. Prospect.* 51, 141–158. doi:10.1046/j.1365-2478.2003.00359.x

Gei, D., Carcione, J. M., and Picotti, S. (2022). "Seismic rock physics of gas-hydrate bearing sediments," in *World atlas of submarine gas hydrates in continental margins*. Editor J. Mienert (Springer), 55–63.

Guerin, G., and Goldberg, D. (2005). Modeling of acoustic wave dissipation in gas hydrate-bearing sediments. *Geochem. Geophys. Geosyst.* 6, Q07010. doi:10.1029/2005gc000918

Helgerud, M. B., Dvorkin, J., Nur, A., Sakai, A., and Collett, T. (1999). Elastic-wave velocity in marine sediments with gas hydrates: Effective medium modeling. *Geophys. Res. Lett.* 26, 2021–2024. doi:10.1029/1999gl900421

Hill, R. (1952). The elastic behaviour of a crystalline aggregate. *Proc. Phys. Soc. A* 65, 349–354. doi:10.1088/0370-1298/65/5/307

Hu, G. W., Ye, Y. G., Zhang, J., Liu, C. L., Diao, S. B., and Wang, J. S. (2010). Acoustic properties of gas hydrate–bearing consolidated sediments and experimental testing of elastic velocity models. *J. Geophys. Res.* 115, B02102. doi:10.1029/2008JB006160

Lee, M., Hutchinson, D., Collett, I., and Dillon, W. P. (1996). Seismic velocities for hydrate-bearing sediments using weighted equation. *J. Geophys Res.* 101, 20347–20358. doi:10.1029/96jb01886

Lee, M. W., and Collett, T. S. (2009). Gas hydrate saturations estimated from fractured reservoir at Site NGHP-01-10, Krishna-Godavari Basin, India. *J. Geophys. Res.* 114, B07102. doi:10.1029/2008JB006237

Leurer, K. C., and Brown, C. (2008). Acoustics of marine sediment under compaction: Binary grain-size model and viscoelastic extension of Biot's theory. *J. Acoust. Soc. Am.* 123, 1941–1951. doi:10.1121/1.2871839

Li, C., Feng, K., and Liu, X. (2015). Retracted article: Analysis of P-wave attenuation in hydrate-bearing sediments in the shenhu area, south China sea. *Mar. Geophys. Res.* 36, 357. doi:10.1007/s11001-014-9241-9

Liu, J., Liu, J, P., Cheng, F., Wang, J., and Liu, X, X. (2017). Rock-physics models of hydrate-bearing sediments in permafrost, Qilian Mountains, China. *Appl. Geophys.* 4 (1), 31–39. doi:10.1007/s11770-017-0608-y

Liu, L., Zhang, X., and Wang, X. (2021). Wave propagation characteristics in gas hydrate-bearing sediments and estimation of hydrate saturation. *Energies* 14 (4), 804. doi:10.3390/en14040804

Marín-Moreno, H., Sahoo, S. K., and Best, A. I. (2017). Theoretical modeling insights into elastic wave attenuation mechanisms in marine sediments with pore-filling methane hydrate. *J. Geophys. Res. Solid Earth* 122, 1835–1847. doi:10.1002/2016jb013577

Matsushima, J. (2006). Seismic wave attenuation in methane hydrate-bearing sediments: Vertical seismic profiling data from the Nankai Trough exploratory well, offshore tokai, central Japan. *J. Geophys. Res.* 111, B10101. doi:10.1029/2005jb004031

Pan, H. J., Li, H. B., Grana, D., Zhang, Y., Liu, T., Geng, C., et al. (2019). Quantitative characterization of gas hydrate bearing sediment using elastic-electrical rock physics models. *Mar. Petroleum Geol.* 105, 273–283. doi:10.1016/j.marpetgeo.2019.04.034

Priest, J. A., Rees, E. V. L., and Clayton, C. R. I. (2009). Influence of gas hydrate morphology on the seismic velocities of sands. *J. Geophys. Res.* 114, B11205. doi:10.1029/2009jb006284

Sahoo, S. K., North, L. J., Marín-Moreno, H., Minshull, T. A., and Best, A. I. (2019). Laboratory observations of frequency-dependent ultrasonic P-wave velocity and attenuation during methane hydrate formation in Berea sandstone. *Geophys. J. Int.* 219, 713–723. doi:10.1093/gji/ggz311

Schicks, J. M., Naumann, R., Erzinger, J., Hester, K. C., Koh, C. A., and Dendy Sloan, E. (2006). Phase transitions in mixed gas hydrates: Experimental observations versus calculated data. *J. Phys. Chem. B* 110 (23), 11468–11474. doi:10.1021/jp0612580

Sloan, D. (1990). *Clathrate hydrates of natural gases*. Boca Raton, Fla: CRC Press.

Stoll, D., and Bryan, G. (2009). Wave attenuation in saturated sediments. *J. Acoust. Soc. Am.* 47, 1440–1447. doi:10.1121/1.1912054

Waite, W. F., Santamarina, J. C., Cortes, D. D., Dugan, B., Espinoza, D. N., Germaine, J., et al. (2009). Physical properties of hydrate-bearing sediments. *Rev. Geophys.* 47, RG4003. doi:10.1029/2008rg000279

Wang, W., Ba, J., Carcione, J. M., Liu, X., and Zhang, L. (2021). Wave properties of gas-hydrate bearing sediments based on poroelasticity. *Front. Earth Sci. (Lausanne)* 9, 640424. doi:10.3389/feart.2021.640424

Wood, A. W. (1955). *A textbook of sound*. New York: McMillan Co.

Wood, A. W., Holbrook, W., and Hoskins, H. (2000). *In situ* measurements of P-wave attenuation in the methane hydrate-and agas-bearing sediments of the Blake Ridge. *Proc. Odp. Sci. Results* 164, 265–272. doi:10.2973/odp.proc.sr.164.246.2000

Wyllie, M. J., Gregory, A. R., and Gardner, G. H. F. (1958). An experimental investigation of factors affecting elastic wave velocities in porous media. *Geophysics* 23, 459–493. doi:10.1190/1.1438493

Zhan, L., Liu, B., Zhang, Y., and Lu, H. (2022). Rock physics modeling of acoustic properties in gas hydrate-bearing sediment. *J. Mar. Sci. Eng.* 10, 1076. doi:10.3390/jmse10081076

Zhan, L. S., and Matsushima, J. (2018). Frequency-dependent*P*-wave attenuation in hydrate-bearing sediments: A rock physics study at Nankai Trough, Japan. *Geophys. J. Int.* 214, 1961–1985. doi:10.1093/gji/ggy229

Zhang, R. W., Li, H. Q., and Wen, P. F. (2016). The velocity dispersion and attenuation of marine hydrate-bearing sediments. *Chin. J. Geophys.* 59 (9), 3417–3427. doi:10.6038/jcg20160924

Zhang, L., Ba, J., and Yin, W. (2017). Seismic wave propagation equations of conglomerate reservoirs: A triple-porosity structure model. *Chin. J. Geophys.* 60 (3), 1073–1087. doi:10.6038/cjg20170320

Zhang, L., Ba, J., and Carcione, J. M (2021). Wave propagation in infinituple-porosity media. *Geophysical Research: Solid Earth* 126, e2020JB021266. doi:10.1029/2020JB021266

Zhang, L., Ba, J., Carcione, J. M, and Wu, C. (2022). Seismic wave propagation in partially saturated rocks with a fractal distribution of fluid-patch size. *Journal of Geophysical Research: Solid Earth* 127, e2021JB023809. doi:10.1029/2021JB023809

Appendix A: The explicit expressions of the elastic parameters are (Zhang et al., 2017)

$$A = (1-\phi)K_s - \frac{2}{3}G_b - \frac{K_s}{K_f}(Q_1 + Q_2 + Q_3)$$
$$Q_1 = \frac{\phi_1\beta_1 K_s}{\beta_1+\gamma}\ Q_2 = \frac{\phi_2 K_s}{1+\gamma}\ Q_3 = \frac{\phi_3 K_s}{\beta_2\gamma+1} \tag{A1}$$
$$R_1 = \frac{\phi_1 K_f}{\beta_1/\gamma+1}\ R_2 = \frac{\phi_2 K_f}{1/\gamma+1}\ R_3 = \frac{\phi_3 K_f}{1/(\beta_2\gamma)+1}$$

where

$$\gamma = \frac{K_s}{K_f}\frac{\phi_1\beta_1 + \phi_2 + \frac{\phi_3}{\beta_2}}{(1-\phi) - \frac{K_b}{K_s}} \tag{A2}$$

and

$$\beta_1 = \frac{\phi_{20}}{\phi_{10}}\left[\frac{1/K_h - (1-\phi_{10})/K_{b1}}{1/K_m - (1-\phi_{20})/K_{b2}}\right] \tag{A3}$$

$$\beta_2 = \frac{\phi_{30}}{\phi_{20}}\left[\frac{1/K_m - (1-\phi_{20})/K_{b2}}{1/K_c - (1-\phi_{30})/K_{b3}}\right] \tag{A4}$$

where K_{b1}, K_{b2} and K_{b3} are the bulk moduli of hydrate, rock, and clay frames, respectively, and K_h, K_m and K_c are the bulk moduli of hydrate, minerals and clay, respectively.

The tortuosities of the three phases are

$$\chi_1 = \frac{1}{2}\left(1+\frac{1}{\phi_{10}}\right)\chi_2 = \frac{1}{2}\left(1+\frac{1}{\phi_{20}}\right)\chi_3 = \frac{1}{2}\left(1+\frac{1}{\phi_{30}}\right) \tag{A5}$$

Then, the density parameters are

$$\begin{aligned}&\rho_{11} = \chi_1\phi_1\rho_f\ \rho_{22} = \chi_2\phi_2\rho_f\ \rho_{33} = \chi_3\phi_3\rho_f\\ &\rho_{01} = \phi_1\rho_f - \rho_{11}\ \rho_{02} = \phi_2\rho_f - \rho_{22}\ \rho_{03} = \phi_3\rho_f - \rho_{33}\\ &\rho_{00} = \nu_1(1-\phi_{10})\rho_h + \nu_2(1-\phi_{20})\rho_m + \nu_3(1-\phi_{30})\rho_c - \rho_{01} - \rho_{02} - \rho_{03}\end{aligned} \tag{A6}$$

where ρ_m, ρ_h and ρ_c are the densities of minerals, hydrate and clay, respectively. Moreover,

$$b_1 = \frac{\phi_1\phi_{10}\eta}{\kappa_1} \tag{A7}$$
$$b_2 = \frac{\phi_2\phi_{20}\eta}{\kappa_2} \tag{A8}$$
$$b_3 = \frac{\phi_3\phi_{30}\eta}{\kappa_3} \tag{A9}$$

A plane-wave analysis is performed by substituting a time harmonic kernel $e^{j(\omega t - \mathbf{k}\cdot\mathbf{x})}$ (where ω is the angular frequency, $\mathbf{k}$ is the wave number vector, and $\mathbf{x}$ is the spatial variable vector) into Eqs 9a–9fa–f9a–9f (Zhang et al., 2017). The resulting dispersion equation is

$$\begin{vmatrix} a_{11}k^2+b_{11} & a_{12}k^2+b_{12} & a_{13}k^2+b_{13} & a_{14}k^2+b_{14}\\ a_{21}k^2+b_{21} & a_{22}k^2+b_{22} & a_{23}k^2+b_{23} & a_{24}k^2+b_{24}\\ a_{31}k^2+b_{31} & a_{32}k^2+b_{32} & a_{33}k^2+b_{33} & a_{34}k^2+b_{34}\\ a_{41}k^2+b_{41} & a_{42}k^2+b_{42} & a_{43}k^2+b_{43} & a_{44}k^2+b_{44}\end{vmatrix} = 0 \tag{B1}$$

where

$$\begin{aligned}
&a_{11} = A + 2G_b + (Q_1\phi_2 - Q_2\phi_1)M_0^{(12)} + (Q_2\phi_3 - Q_3\phi_2)M_0^{(23)}\\
&a_{12} = Q_1 + (Q_1\phi_2 - Q_2\phi_1)M_1^{(12)} + (Q_2\phi_3 - Q_3\phi_2)M_1^{(23)}\\
&a_{13} = Q_2 + (Q_1\phi_2 - Q_2\phi_1)M_2^{(12)} + (Q_2\phi_3 - Q_3\phi_2)M_2^{(23)}\\
&a_{14} = Q_3 + (Q_1\phi_2 - Q_2\phi_1)M_3^{(12)} + (Q_2\phi_3 - Q_3\phi_2)M_3^{(23)}\\
&a_{21} = Q_1 + \phi_2R_1M_0^{(12)}\ a_{22} = R_1 + \phi_2R_1M_1^{(12)}\\
&a_{23} = \phi_2R_1M_2^{(12)}\ a_{24} = \phi_2R_1M_3^{(12)}\\
&a_{31} = Q_2 - R_2(\phi_1M_0^{(12)} - \phi_3M_0^{(23)})\ a_{32} = -R_2(\phi_1M_1^{(12)} - \phi_3M_1^{(23)})\\
&a_{33} = R_2(1 - \phi_1M_2^{(12)} + \phi_3M_2^{(23)})\ a_{34} = R_2(-\phi_1M_3^{(12)} + \phi_3M_3^{(23)})\\
&a_{41} = Q_3 - \phi_2R_3M_0^{(23)}\ a_{42} = -\phi_2R_3M_1^{(23)}\\
&a_{43} = -\phi_2R_3M_2^{(23)}\ a_{44} = R_3(1 - \phi_2M_3^{(23)})\\
&b_{11} = -\rho_{00}\omega^2 + j\omega(b_1+b_2+b_3)\ b_{12} = -\rho_{01}\omega^2 - j\omega b_1\\
&b_{13} = -\rho_{02}\omega^2 - j\omega b_2\ b_{14} = -\rho_{03}\omega^2 - j\omega b_3\\
&b_{21} = -\rho_{01}\omega^2 - j\omega b_1\ b_{22} = -\rho_{11}\omega^2 + j\omega b_1\ b_{23} = b_{24} = 0\\
&b_{31} = -\rho_{02}\omega^2 - j\omega b_2\ b_{33} = -\rho_{22}\omega^2 + j\omega b_2\ b_{32} = b_{34} = 0\\
&b_{41} = -\rho_{03}\omega^2 - j\omega b_3\ b_{44} = -\rho_{33}\omega^2 + j\omega b_3\ b_{42} = b_{43} = 0
\end{aligned} \tag{B2}$$

$$S_{12} = \frac{-\phi_1\phi_2^2R_{12}^2\omega\left(\rho_f\omega(1/5 + \phi_{10}/\phi_{20}) + j(\eta/(5\kappa_1) + \eta/\kappa_2)\phi_{10}\right)}{3}$$
$$- \phi_2^2R_1 - \phi_1^2R_2$$
$$S_{23} = \frac{-\phi_3\phi_2^2R_{23}^2\omega\left(\rho_f\omega(1/5 + \phi_{30}/\phi_{20}) + j(\eta/(5\kappa_3) + \eta/\kappa_2)\phi_{30}\right)}{3}$$
$$- \phi_3^2R_2 - \phi_2^2R_3$$
$$M_0^{(12)} = \frac{(Q_1\phi_2 - Q_2\phi_1)/S_{12} + \phi_1\phi_3R_2(Q_2\phi_3 - Q_3\phi_2)/(S_{12}S_{23})}{1 + (\phi_1\phi_3R_2)^2/(S_{12}S_{23})}$$
$$M_1^{(12)} = \frac{\phi_2R_1/S_{12}}{1 + (\phi_1\phi_3R_2)^2/(S_{12}S_{23})}$$
$$M_2^{(12)} = \frac{-\phi_1R_2/S_{12} + \phi_1\phi_3^2R_2^2/(S_{12}S_{23})}{1 + (\phi_1\phi_3R_2)^2/(S_{12}S_{23})}$$
$$M_3^{(12)} = \frac{-\phi_1\phi_2\phi_3R_2R_3/(S_{12}S_{23})}{1 + (\phi_1\phi_3R_2)^2/(S_{12}S_{23})}$$
$$M_0^{(23)} = \frac{(-M_0^{(12)}\phi_1\phi_3R_2 + Q_2\phi_3 - Q_3\phi_2)}{S_{23}}$$
$$M_1^{(23)} = -M_1^{(12)}\phi_1\phi_3R_2/S_{23}$$
$$M_2^{(23)} = \frac{(-M_2^{(12)}\phi_1\phi_3R_2 + \phi_3R_2)}{S_{23}}$$
$$M_3^{(23)} = (-M_3^{(12)}\phi_1\phi_3R_2 - \phi_2R_3)/S_{23} \tag{B3}$$

where η is fluid viscosity. $j = \sqrt{-1}$.

$$V_P = \frac{\omega}{\mathrm{Re}(k)} \tag{B4}$$
$$Q^{-1} = \frac{-\mathrm{Im}(k^2)}{\mathrm{Re}(k^2)} \tag{B5}$$

frontiers | Frontiers in Earth Science

TYPE Original Research
PUBLISHED 06 January 2023
DOI 10.3389/feart.2022.1103321

OPEN ACCESS

EDITED BY
Qiaomu Qi,
Chengdu University of Technology, China

REVIEWED BY
Shuxian Jiang,
Southwest Petroleum University, China
Jing Ba,
Hohai University, China

*CORRESPONDENCE
Hemin Yuan,
yhm3414@gmail.com

SPECIALTY SECTION
This article was submitted to Solid Earth Geophysics,
a section of the journal
Frontiers in Earth Science

RECEIVED 20 November 2022
ACCEPTED 21 December 2022
PUBLISHED 06 January 2023

CITATION
Yuan H, Han X, Zhang X and Wang Y (2023), Evaluation of the consolidation status of heavy oil sands through rock physics analysis: A case study from Fengcheng oilfield.
Front. Earth Sci. 10:1103321.
doi: 10.3389/feart.2022.1103321

Evaluation of the consolidation status of heavy oil sands through rock physics analysis: A case study from Fengcheng oilfield

Hemin Yuan[1]*, Xuehui Han[2], Xin Zhang[3] and Yang Wang[4]

[1]School of Geophysics and Information Technology, China University of Geosciences (Beijing), Beijing, China, [2]School of Geosciences, China University of Petroleum (East China), Qingdao, China, [3]Research Institute of Petroleum Exploration and Development, Beijing, China, [4]SINOPEC Geophysical Research Institute, Nanjing, China

Heavy oil is an important unconventional oil resource with huge availability worldwide, which also forms the primary oil source in Fengcheng oilfield, XinJiang, China. The elastic properties and consolidation status of heavy oil sands are of significant values as they can provide guidance for reservoir exploration and production. However, due to the lack of detailed rock physics investigation of the heavy oil sands in Fengcheng oilfield, the knowledge about their micro-scale elastic properties and consolidation status is still limited. Based on the well log data and laboratory measurements, we performed rock physics analysis of the heavy oil sands' elastic properties. We first analyzed the well logs to determine the oil sands formations and then quantitatively delineated the relations between density, porosity, and velocity. Combining with laboratory measured data, we applied theoretical rock physics models to characterize the consolidation status of the heavy oil sands. Our results show that the oil sands in this area are poorly consolidated with a loose rock frame. Overall, this study highlights the micro-scale elastic properties of the heavy oil sands in Fengcheng oilfield and also reveals the consolidation status. It presents a method of integrating well log, laboratory data, and rock physics analysis to evaluate the consolidation status of heavy oil sands, which can facilitate the future detailed petrophysical analysis and provide important information for seismic characterization and drilling risk evaluation.

KEYWORDS

heavy oil sands, consolidation status, rock physics modeling, acoustic velocity, unconventional reservoir

1 Introduction

Heavy oil is an important alternative oil resource to conventional oil and gas reservoirs because of its huge availability all over the world, which is twice the conventional oil reservoirs (Meyer and Attanasi, 2003). It also constitutes over 20% of China's oil reservoirs, making it an important reservoir type in China (Zhang et al., 2005). Fengcheng oilfield is located at the northwest of the Junggar Basin, about 130 km northeast of Karamay city. This oilfield was initially discovered in the late 1950s and covers an area of 200 km^2 with 3.6×10^8 t heavy oil in store (Zhou, 2016), making it the third largest sub-oilfield in the Xinjiang oilfield system. The map in Figure 1 shows the geographical location, the oil-bearing zone, and the exploratory wells of Fengcheng oilfield, providing a brief view of the geographical background.

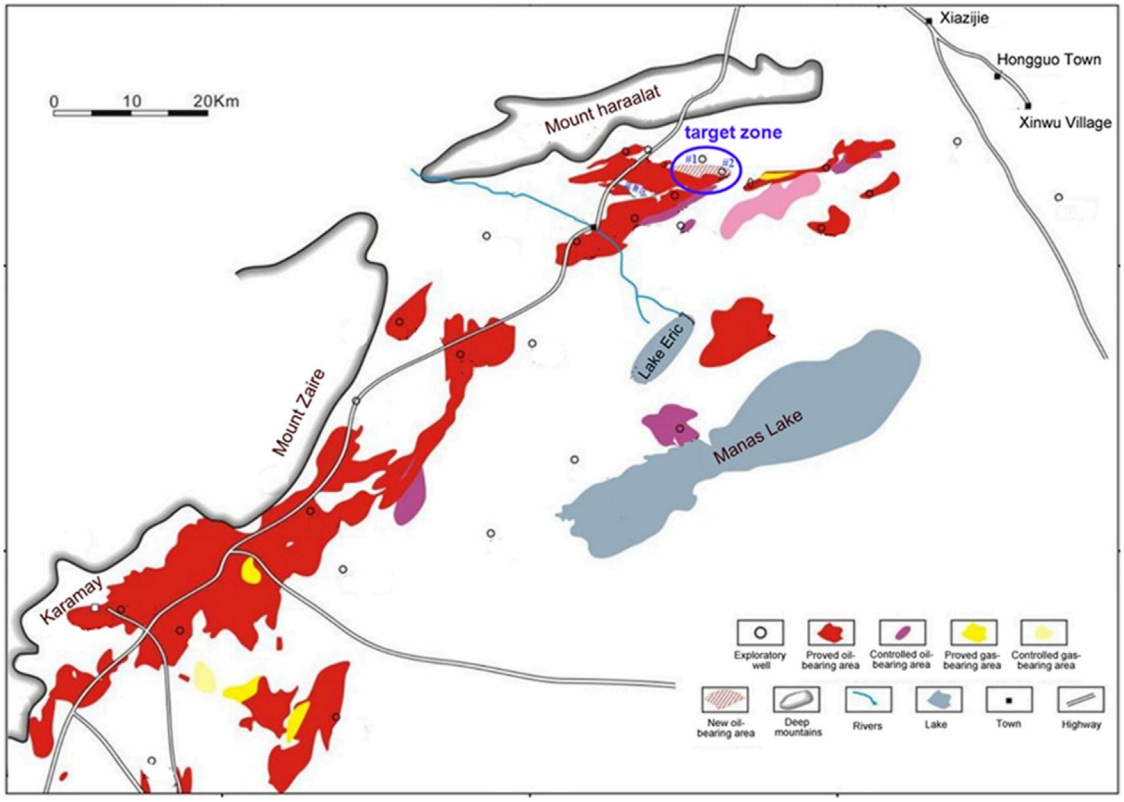

FIGURE 1
Geographical location map of Fengcheng oilfield (adapted from Zhou, 2016).

Geologically, the regional structure of Fengcheng oilfield is located in the Mesozoic overlap pinch out zone on the hanging wall of the Xiahongbei fault in the Wuxia fault fold belt, northwest margin of the Junggar basin. From top to bottom, the formations can be divided into the Cretaceous Tugulu group, Jurassic Qigu formation, Sangonghe formation, Badaowan Formation, Triassic, Permian, and Carboniferous. The Jurassic system is in angular unconformity contact with the overlying and underlying strata, and the upper and lower Jurassic systems are also in angular unconformity contact (Huang et al., 2020). Oil sands in this area mainly develop in shallow strata of Cretaceous Qingshuihe Formation K_{1q} and Jurassic Qigu formation J_{3q} (Huang et al., 2020), and our target strata is located in J_{3q}.

Compared to conventional oil reservoirs, the heavy oil reservoir in Fengcheng oilfield generally locates at shallow depth (several hundred meters). Oil has a density of .96 g/cm^3 (API = 16), close to water density, making it difficult to distinguish the oil formations from water formations. Moreover, it has a viscosity over 5×10^5 mPa s (at 20°C) (Huang et al., 2020), increasing the difficulty of production. The high density plus high viscosity also cause troubles for reservoir exploration and production assessment. To better characterize the heavy oil reservoir through seismic methods and to improve the evaluation of drilling risks in production, it requires inspecting the heavy oil sands elastic properties and consolidation status under *in situ* conditions. However, current methods for characterizing the elastic properties of Fengcheng heavy oil reservoirs mainly involve well logs inspection without rock physics analysis and modeling (Huang et al., 2020); thus, they cannot be integrated with seismic methods effectively, resulting in limited knowledge of the reservoirs in large scales.

This rock physics study is performed to systematically investigate the elastic properties and consolidation status of heavy oil sands in Fengcheng oilfield. Petrophysical analysis of the well logs was firstly conducted to determine the oil sands formations and the corresponding elastic properties. Then, the porosity log was predicted by combining the neutron and density logs, and the velocity differences in different sections were also analyzed. Based on the identified heavy oil formations and laboratory measurement, the heavy oil sands' velocities were theoretically modeled, and the rocks' consolidation status was evaluated. Finally, the modeling results of the two nearby wells were compared, and the reasons of the differences were explained.

2 Methodology

The available data include two sets of well logs (from well #1 and well #2 as indicated in the blue circle in Figure 1), laboratory measured

TABLE 1 Measured porosity and oil saturation of the core samples from well #1.

Sample	1	2	3	4	5	6	Average
Depth (m)	403.8	404.26	411.13	414.48	415.10	423.4	—
Porosity (%)	31.3	31.4	33.4	33.0	33.3	26.1	—
Saturation (%)	57.2	51.5	62.3	61.8	58.5	55.2	57.8

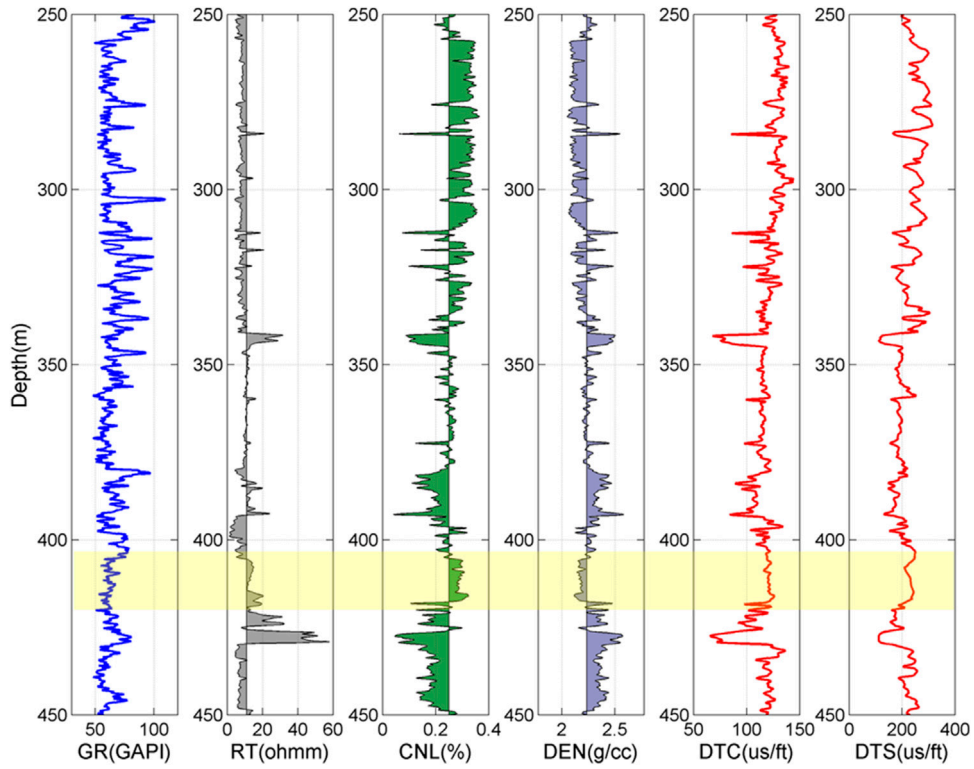

FIGURE 2
Well logs of well #1 from Fengcheng oilfield. GR means gamma ray log; RT means resistivity log; CNL means compensated neutron log; DEN means density log; DTC means compressional wave slowness log; DTS means shear wave slowness log; and the yellow section marks the target zone.

porosity and oil saturation of 6 samples (Table 1), and statistical grain sizes of the formations in well #1. The laboratory data are from the measurements in the Applied Petrophysics Lab (APL) in China University of Petroleum (East China).

2.1 Well log analysis

The well logs of well #1 include GR, RT, CNL, DTC, DTS, and DEN logs, which are shown in Figure 2.

In Figure 2, it can be seen that 342–346 m depth section has relatively low GR, high RT, low CNL, low DTC, low DTS, and high DEN, which means it has low clay content, low porosity, high P-wave velocity (Vp), high S-wave velocity (Vs), and high density. These characteristics suggest that it is impossible to be oil sands; rather, it is more likely to be tight sand or limestone. The 379–383 m section has similar characteristics as the 342–346 m section, except that the GR is higher, suggesting the higher clay content, thus it is probably shale. The 386–392 m depth section has low GR and high RT, and CNL is around 30%. The Vp, Vs, and density are smaller than those of the above and beneath layers. It might be oil sands. The 403–425 m section is featured with low GR, high RT, high CNL, high DTC, high DTS, and low DEN, which are the typical characteristics of oil sands. We conclude it as the oil sands layer, which is also confirmed by the core samples (Table 1). The 426–430 m section is featured with high GR, high RT, low CNL, low DTC, low DTS, and high DEN, suggesting it has high clay content, low porosity, high Vp, high Vs, and high density. It is highly possible that this section is corresponding to a shale layer. Considering that the laboratory measured samples are from the depth of 403–425 m, to better integrate the log data and laboratory measurements, we take this depth section as the target zone (the yellow marked zone in Figure 2). All the following processing and analysis of well #1 are based on this section.

2.2 Porosity estimation

It is essential to first obtain the porosity to characterize the oil sands properties. The porosities of six core samples were measured using mercury intrusion porosimetry, which was conducted in APL, as shown in Table 1. However, to quantitatively analyze the rock properties of the whole depth section, it is necessary to estimate the porosity log. Here, we combine the density log and neutron log to predict the porosity. First, we assume the oil sands are fully saturated (by oil and water). Then, the rock bulk density can be represented as follows:

$$\rho_b = \rho_g\left(1 - \phi_\rho\right) + \rho_o\phi_\rho S_o + \rho_w\phi_\rho S_w, \quad (1)$$

where ρ_b is the rock bulk density; ρ_g, ρ_o, and ρ_w are the densities of the grains, oil, and water, respectively. The strata are sand, and so, the grain density is assumed to be 2.65 g/cm^3. ϕ_ρ is porosity; S_o and S_w are the oil and water saturation, respectively; and $S_o + S_w = 1$ (full saturation).

In Eq. 1, since the porosity and oil saturation are unknown, it is impossible to invert the porosity with these available data.

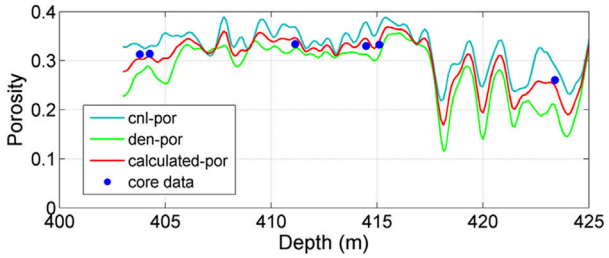

FIGURE 3
Calculated porosity log. The cyan line indicates the CNL-log predicted porosity, the green line indicates the density-log predicted porosity, and the red line indicates the estimated porosity using the current method. It is clear that the estimation matches the laboratory measured data, demonstrating the reliability of the estimation results.

Considering that the oil density (.96 g/cm^3) is close to water density (1.0 g/cm^3), we further assume the oil has the same density as water (the uncertainty will be analyzed in the *Discussion* section), then Eq. 1 can be simplified.

$$\rho_b = \rho_g\left(1-\phi_\rho\right)+\rho_w\phi_\rho, \tag{2}$$

and the porosity can be calculated with the following equation:

$$\phi_\rho = \frac{\rho_g-\rho_b}{\rho_g-\rho_w} = \frac{2.65-\rho_b}{1.65}. \tag{3}$$

Then, following the method of Aliyeva et al. (2012), true porosity ϕ can be estimated by averaging this density-porosity ϕ_ρ and neutron—porosity ϕ_N (CNL log in Figure 2) in the following equation :

$$\phi = \left(\phi_\rho+\phi_N\right)/2. \tag{4}$$

The estimated porosity is compared with the laboratory measured porosity in Figure 3. It can be seen that the CNL-log predicted result evidently overestimates the porosity, while the density-log predicted result underestimates the porosity. Comparatively, the calculated porosity log matches well with the measured core data, demonstrating that the prediction is reliable.

2.3 Velocity analysis

To better understand the relations between the velocities, Vp/Vs ratios, depth, density, and porosity, we plot the scattered data in Figures 4, 5.

In Figure 4, one most evident observation is that the oil sands formation is very shallow, only around 400 m. This depth is much shallower than the conventional oil reservoirs, which are generally buried over one thousand meters. The density is between 2.1 and 2.5 g/cm^3, Vp is between 2.4 and 3.1 km/s, and Vs is between 1.2 and 1.9 km/s, relatively smaller than conventional oil-bearing sandstones. In addition, it can be found that the data distribute in two distinct zones: the data of 403–418 m depth section mainly cluster around

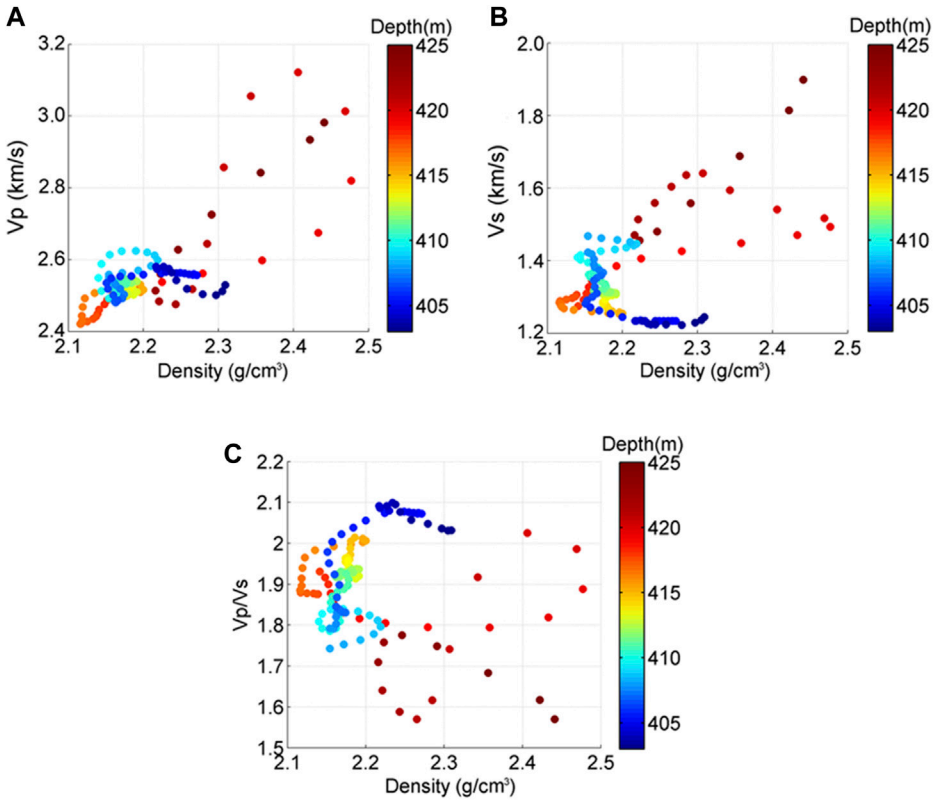

FIGURE 4
Cross-plot of density, depth, and **(A)** Vp, **(B)** Vs, and **(C)** Vp/Vs ratio.

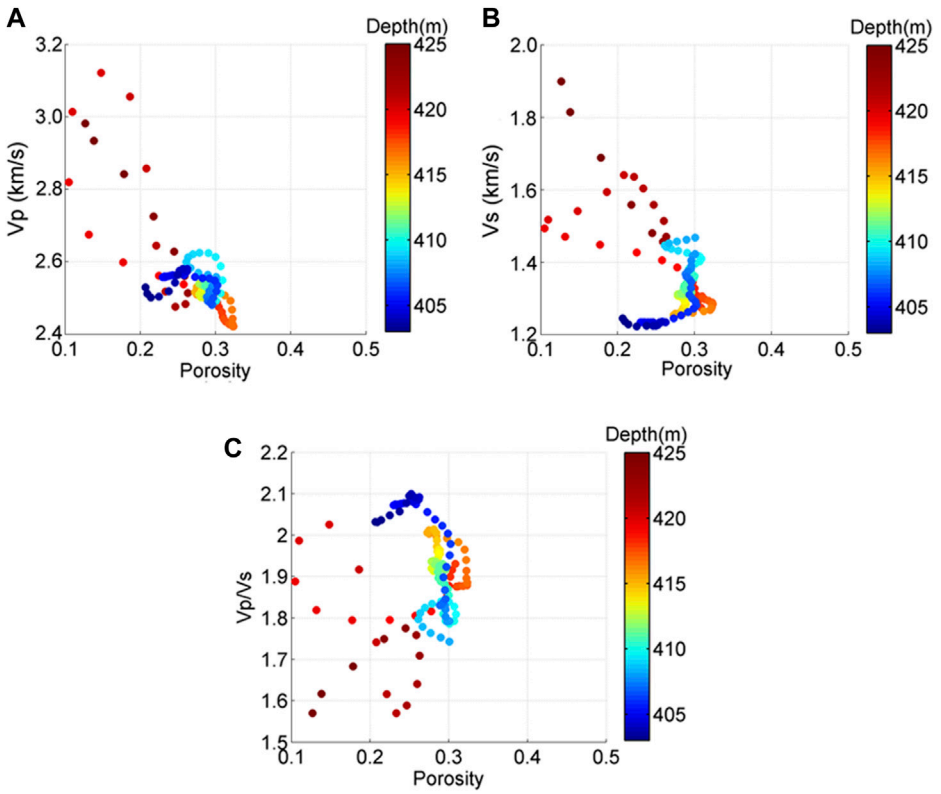

FIGURE 5
Cross-plot of porosity, depth, and **(A)** Vp, **(B)** Vs, and **(C)** Vp/Vs ratio.

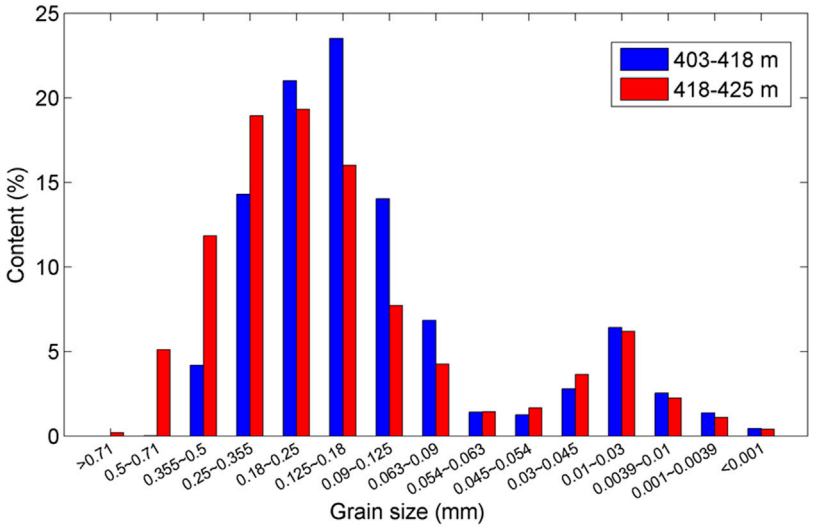

FIGURE 6
Statistical distribution of the grain size.

2.1–2.3 g/cm^3 with Vp of 2.4–2.62 km/s and Vs of 1.2–1.48 km/s; while the data of 418–425 m depth section have relative larger density between 2.3 and 2.5 g/cm^3, larger Vp of 2.6–3.1 km/s, and larger Vs of 1.4–1.9 km/s. Considering that the two sections do not have much depth gap, the differences are impossible to be caused by the compaction and pressure; rather, it should be owing to other factors, e.g., matrix heterogeneity. Figure 6 shows the statistical distribution of grain sizes of the sections. It can be observed that the 418–425 m section has more large-size grains (size above .25 mm) and less middle-size grains (.063–.25 mm) than the 403–418 m section. On the other hand, the 403–418 m section has relatively better sorting as its grain sizes focus in a narrower range. These different grain size

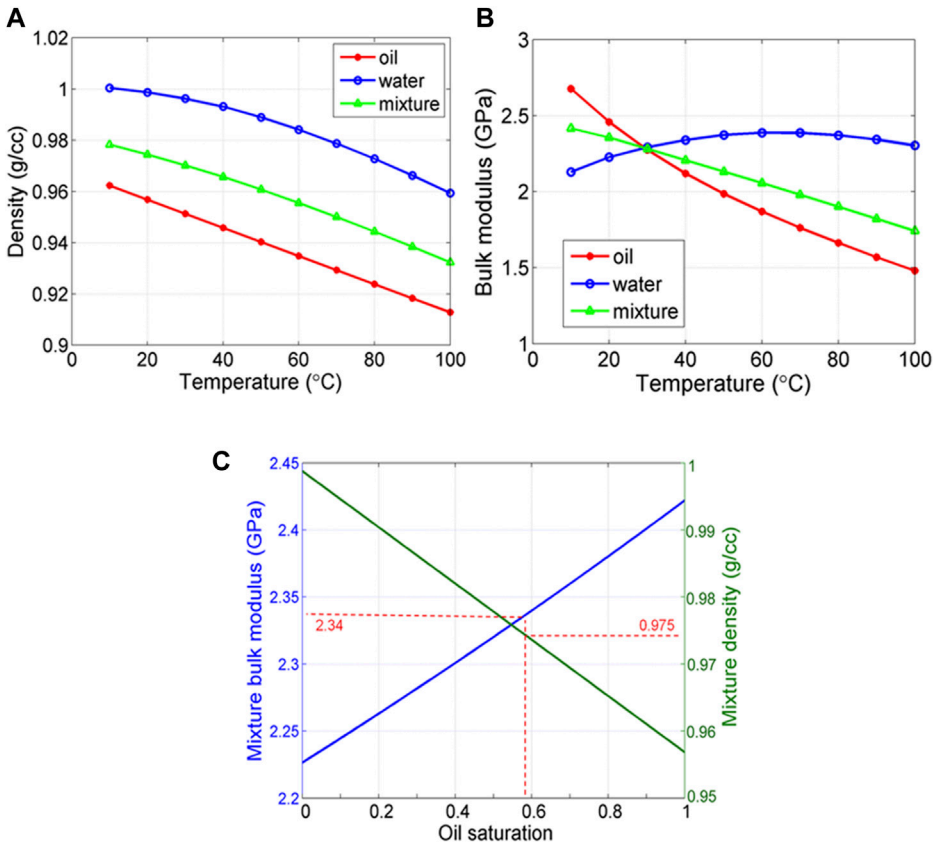

FIGURE 7
Variation of **(A)** bulk modulus and **(B)** density of the heavy oil, water, and fluid mixture with temperature. **(C)** Variation of bulk modulus and density of the fluid mixture with oil saturation. The bulk modulus of the fluid mixture is predicted using Wood's equation.

distributions and sorting can cause heterogeneity of the sand matrix. This is also verified by the porosity log in Figure 3, which shows that the 403–418 m section has relatively larger and stable porosities than the 418–425 m section. Hence, the matrix heterogeneity is a possible reason for the different velocities (more discussion is shown in the *Discussion* section).

The oil sands have large porosities (Figure 5), which could go up to .33. In addition, porosity distributes in a wide range between .11 and .33, further justifying the heterogeneity. The Vp/Vs ratios are mostly above 1.75, which are relatively larger than conventional sandstones. In addition, the deep-section sands (418–425 m) have relatively lower porosity, consistent with the porosity log in Figure 3; and their Vp/Vs ratios are smaller compared to the shallow section sands (403–418 m), which can also be attributed to the matrix heterogeneity as explained previously. Overall, most of the data are clustered at Vp of 2.4–2.65 km/s and Vs of 1.2–1.48 km/s, evidently smaller than conventional sandstones.

3 Rock physics modeling

3.1 Fluid mixture modeling

To simulate the oil sands elastic properties, it is essential to know the frame and fluid properties. According to the previous studies in this area (Guo and Han, 2016; Huang et al., 2020), the rock frame is primarily composed of quartz sand grains. Hence, the moduli of the rock matrix can be referred to the moduli of quartz with a bulk modulus of 37 GPa and shear modulus of 45 GPa.

Because heavy oil properties are highly temperature-dependent, it is necessary to figure out the heavy oil properties under *in situ* conditions. The *in situ* pressure is around 5 MPa (Guo and Han, 2016). Considering that the surface temperature is around 10°C, the depth is around 400 m, the geothermal gradient is around 25°C/km, and the *in situ* temperature is approximately 20°C. The density of the fluid mixture can be calculated by the following equation:

$$\rho_R = \sum_{i=1}^{N} f_i \rho_i, \tag{5}$$

where ρ_R is the effective density of the mixture and f_i and ρ_i are the fraction and density of the *i*th component, respectively. The calculated mixture density is shown in Figure 7A.

According to the prediction of the FLAG program (developed by FLUIDS/DHI consortium of University of Houston and Colorado School of Mines), the bulk modulus of heavy oil and water under different temperatures are presented in Figure 7B (the oil shear modulus is around .038 GPa under the *in situ* condition, which has negligible influence on the elastic properties of oil sands and, thus, is not presented). It is clear

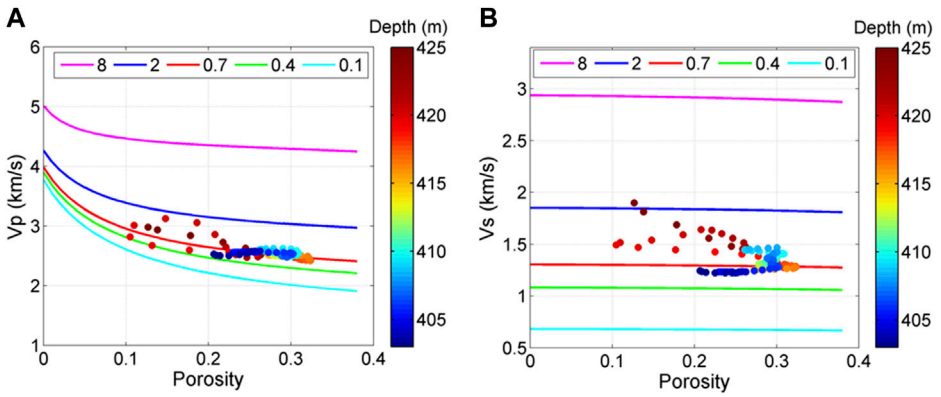

FIGURE 8
Hertz–Mindlin model simulation results of **(A)** P-wave velocity and **(B)** S-wave velocity. Different lines indicate simulation results with different coordination numbers. It is clear that most of the data locate around the line with a coordination number of .7.

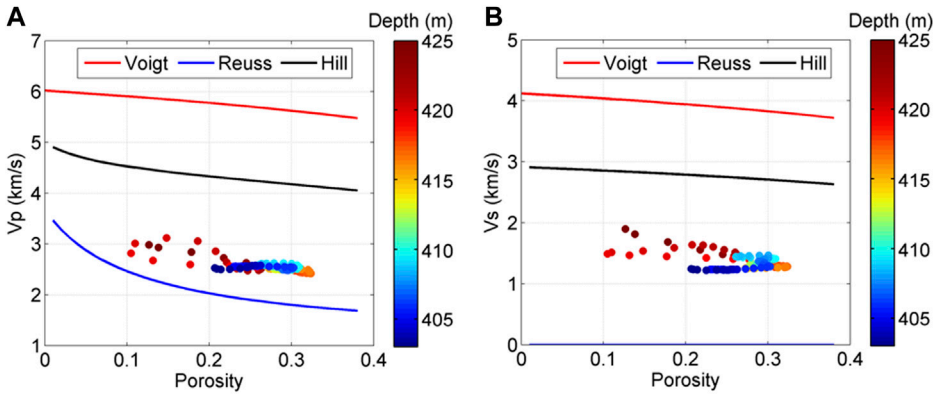

FIGURE 9
VRH simulation results of **(A)** P-wave velocity and **(B)** S-wave velocity.

that the bulk modulus of heavy oil decreases quickly with increasing temperature, revealing the high temperature-sensitivity of the oil, which also justifies the popularity of the thermal production method of heavy oil reservoirs (Yuan et al., 2017). Moreover, it can be seen that the bulk modulus of heavy oil and water are 2.46 and 2.25 GPa, respectively, at 20°C. Since the pores are filled with oil and water, it is necessary to figure out the moduli of the fluid mixture, which is assumed under iso-stress condition and can be estimated through the Wood equation (Wood, 1955) given as follows:

$$1/K_R = \sum_{i=1}^{N} f_i/K_i, \quad (6)$$

where K_R is the effective bulk modulus of the mixture and f_i and K_i are the fraction and bulk modulus of the *i*th component, respectively. As shown in Figure 7B, the bulk modulus of the fluid mixture also decreases with increasing temperature, demonstrating the effect of heavy oil in pore fluids; moreover, it is approximately 2.34 GPa at 20°C. Notably, since the water shear modulus is zero, the mixture shear modulus should also be zero according to the Wood equation.

Given that the average saturation is around 58% (Table 1), the predicted mixture density and bulk moduli are .975 g/cm^3 and 2.34 GPa, respectively, as shown in Figure 7C. After the effective bulk modulus of the pore fluid mixture is obtained, the moduli of the oil sands can be estimated with theoretical models. In the subsequent section, we choose the Hertz–Mindlin model, Voigt–Reuss-Hill average, and iso-frame model to conduct the simulation, which are effective and commonly used in characterizing rocks' consolidation status.

3.2 Hertz–Mindlin modeling

The first model we use is the Hertz–Mindlin model, which establishes the relations between rock moduli, porosity, grain contact, and pressure and can be used to predict the elastic properties of precompacted granular rocks (Mindlin, 1949). It has also been used to estimate the frame modulus of heavy oil sands (Lerat et al., 2010). We use this model to calculate the effective moduli of the dry rock frame and then use the Gassmann equation (Gassmann, 1951) to predict the velocities of the fully saturated oil sands. Figure 8 shows the modeling results.

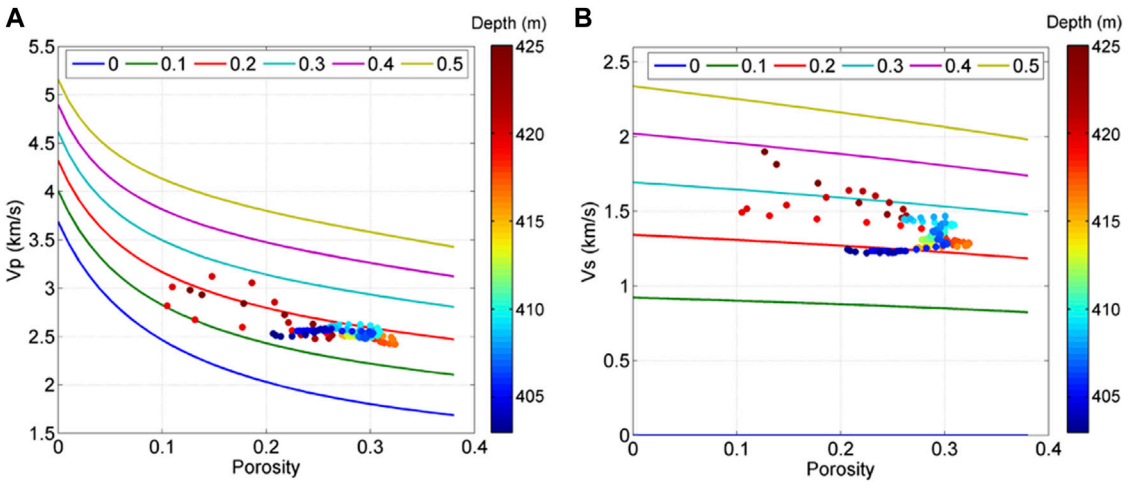

FIGURE 10
Iso-frame model simulation results of **(A)** P-wave velocity and **(B)** S-wave velocity. Different lines represent the modeling results with different IF values.

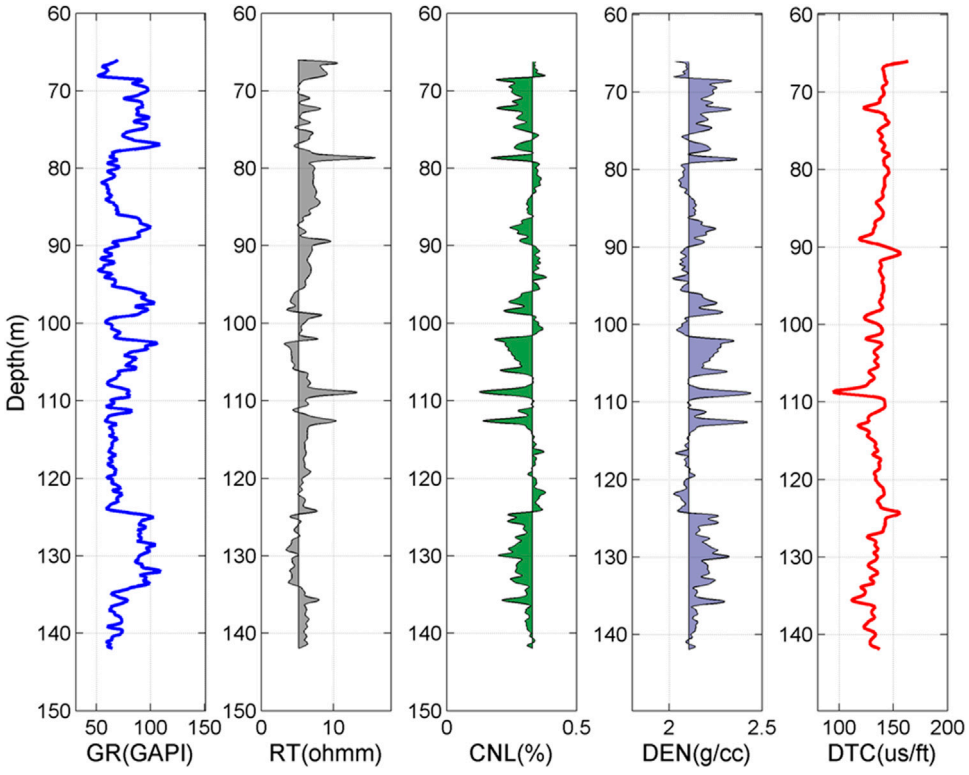

FIGURE 11
Well logs of well #2. Note that this well does not include the S-wave velocity log.

In Figure 8, the simulation results vary significantly with the coordination number, which describes the number of grain contacts and is an important parameter in the Hertz–Mindlin model. A coordination number of 8, which is a commonly used value for unconsolidated rocks (Hossain et al., 2011), evidently overestimates both Vp and Vs. A coordination number of 1 still overestimates the velocities, while the .4 and .1 coordination numbers underestimate the velocities. The simulation results of .7 coordination number match both Vp and Vs of the data, which indicates that the contacts between the sand grains are quite scarce. This suggests that most of the sand grains are isolated by the pore fluids without much contact and the rock frame is poorly compacted, which is reasonable in light of the shallow depth.

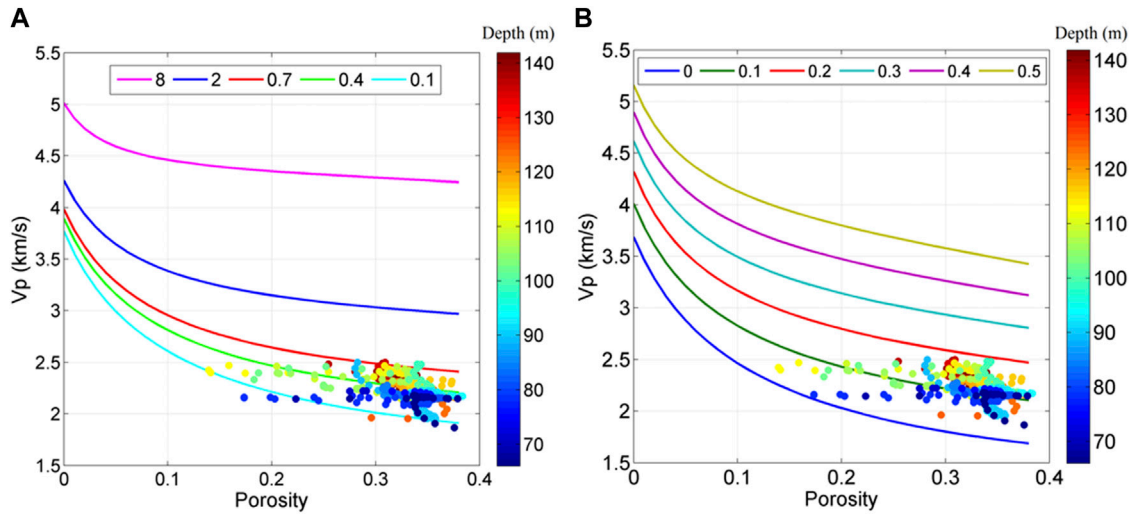

FIGURE 12
Simulated P-wave velocities with **(A)**the Hertz–Mindlin model and **(B)** iso-frame model.

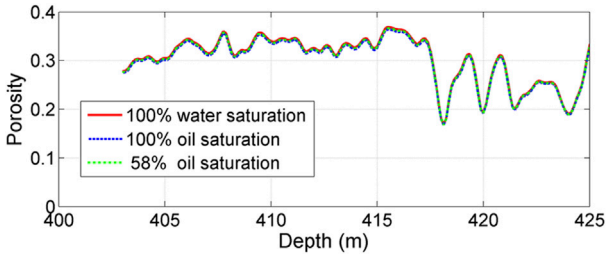

FIGURE 13
Predicted porosity logs under the cases of different oil saturations.

3.3 Voigt–Reuss–Hill (VRH) modeling

To further analyze the rock properties, we also apply the Voigt–Reuss modeling, which describes the iso-strain and iso-stress conditions of the rock components (Hill, 1952), and they are also recognized as the physical upper and lower bounds of the rocks' moduli. Hill modeling is also applied, which is the average of the Voigt and Reuss bounds and is commonly used to estimate the effective properties of rocks with multiple components (Domenico, 1976; Mavko et al., 2009). This VRH model has also been adopted to analyze oil sands velocities in previous works (Javanbakhti, 2018; Yuan et al., 2020). The modeling results are shown in Figure 9.

In Figure 9, the data are far below the upper Voigt bound and even below the Hill average. On the other hand, it is close to the Reuss bound, suggesting that most of the components of the oil sands are under iso-stress condition. This further indicates that the sand grains are mostly in the suspension status, which is also consistent with the aforementioned analysis that the grains have few contacts and the frame is poorly consolidated.

3.4 Iso-frame (IF) modeling

The iso-frame model is another effective tool to analyze the rock elastic properties, which is developed by Fabricius (2003). It describes the rock's elastic properties between the modified upper and lower Hashin–Shtrikman bounds (Hashin and Shtrikman, 1963) and assumes that part of the sand grains are supporting the frame, while the remaining part are in the suspension status (Fabricius, 2003). It can also be used to analyze the rock consolidation status. This model uses an IF parameter to represent the percentage of grains in a load-bearing frame, and thus 1-IF is the percentage of grains in suspension. The modeling results are shown in Figure 10.

In Figure 10, for Vp, all the data distribute between IF = .1 and IF = .3 with the most gathering around IF = .2. For Vs, most of the data locate between IF = .2 and IF = .4, and the largest cluster is also around IF = .2. Hence, it suggests that approximately 80% of the sand grains are in the suspension status, while only 20% grains are supporting the frame. This further demonstrates that the rock frame is quite loose and poorly consolidated, which is consistent with the aforementioned analysis.

3.5 Modeling results of well #2

Among the abovementioned three models, it seems that compared to the VRH model, the Hertz–Mindlin model and IF model can provide more quantitative assessment of the rock consolidation status (Hertz–Mindlin model with .7 coordination number and IF model with .2 IF value), and they generally match the data better. Hence, we also apply them on the logs of well #2 (Figure 11) to evaluate the consolidation status, which is located near well #1. The simulated sections are the sections of 77.6–86.1, 89.2–95.5, 99.1–102.1, and 104.0–124.4 m. These sections show low GR, high RT, high CNL, low DEN, and high DTC logs, and thus are assumed oil sands formations. Since well #2 does not include the

TABLE 2 Uncertainties of the fluid mixture bulk modulus and density. The uncertainties are calculated by comparing the modulus and density values with the values at 58% saturation.

Oil saturation (%)	Bulk modulus (GPa)	Uncertainty of bulk modulus (%)	Density (g/cm^3)	Uncertainty of density (%)
58	2.340	—	.975	—
51.5	2.325	.64	.973	.21
62.3	2.345	.21	.978	.31

S-wave velocity log, we only show the modeling results of the P-wave velocity. The modeling results are shown in Figure 12.

In the Hertz–Mindlin modeling in Figure 12A, most of the data distribute around the curve of .4 coordination number, indicating that the average grain contact is around .4. In the IF modeling in Figure 12B, the data mainly cluster around the curve of .1 IF value, suggesting that only about 10% sand grains are supporting the load-bearing frame, while the remaining 90% are in the suspension status. These simulation results both demonstrate that the sand grains are barely, connected and the oil sands are poorly consolidated.

4 Discussion

The oil sands layers are generally featured with large porosity, low Vp, and low Vs, and since the rock matrix is mainly composed of quartz sands, the GR log is of low value. In well #1, we use 403–425 m as the target oil sands section, which does not rule out the possibility of the other sections. For instance, the sections of 350–370 and 386–392 m also show some characteristics of oil sands formation. We use the 403–425 m section because in this section we have laboratory-measured core samples that can confirm the oil presence and also can combine with the section of logs to jointly characterize the oil sands properties. In well #2, we did not perform detailed analysis of the section and assumed the 77.6–86.1, 89.2–95.5, 99.1–102.1, and 104.0–124.4 m sections as the oil sands formations since they have similar characteristics with the oil sands formation in well #1. Moreover, all the data are concentrated in narrow ranges in Figure 12, suggesting that even only a few sections are oil sands layers; they still cluster around the simulation results.

In porosity estimation, the oil density is assumed the same as water density (1.0 g/cm^3), which can introduce uncertainty. To analyze the uncertainty, we replace the water with oil completely and then calculate the changes. Then, Eq. 3 changes to the following equation:

$$\phi_\rho = \frac{\rho_g - \rho_b}{\rho_g - \rho_o} = \frac{2.65 - \rho_b}{1.69}. \tag{7}$$

Also, the relative error can be obtained through the following equation:

$$error1 = \left(\frac{2.65 - \rho_b}{1.65} - \frac{2.65 - \rho_b}{1.69}\right) \Big/ \left(\frac{2.65 - \rho_b}{1.65}\right) = 2.4\%. \tag{8}$$

In addition, if according to Table 1, the oil saturation is 58%, then the density of fluid mixture ρ_m is

$$\rho_m = \rho_o S_o + \rho_w (1 - S_o) = 0.98\ \mathrm{g/cm^3}, \tag{9}$$

and the corresponding uncertainty is

$$error2 = \left(\frac{2.65 - \rho_b}{1.65} - \frac{2.65 - \rho_b}{1.67}\right) \Big/ \left(\frac{2.65 - \rho_b}{1.65}\right) = 1.2\%. \tag{10}$$

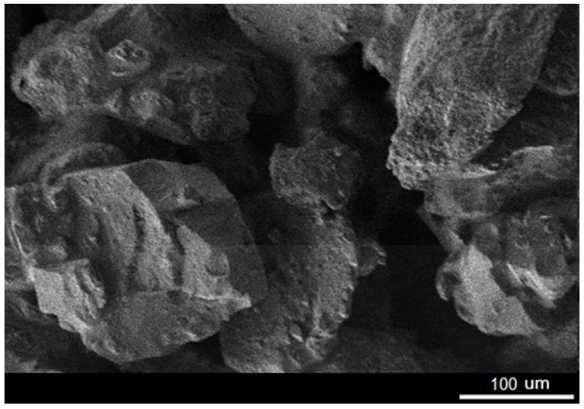

FIGURE 14
The SEM image of oil sands from Fengcheng oilfield.

Both the two cases have very small uncertainties. To visually inspect the uncertainties, we plot them in Figure 13. It is clear that the uncertainties are so small that the predicted porosity logs almost overlap each other, which justifies that the assumption of the same density of oil and water leads to trivial uncertainty and has ignorable influence on the estimated porosity.

The section of 418–425 m has relatively higher velocities than the section of 403–418 m. Considering that these two sections only have around a 20 m depth gap with up to 5% pressure difference, the pressure and compaction effect cannot be the reason. Instead, it is more possibly to be caused by the matrix heterogeneity induced by the grain size distribution pattern. As illustrated in Figure 6, the deep section (418–425 m) has more large-size grains, while the shallow section (403–418 m) has better sorting with relatively narrower-ranged grain sizes. According to the measurements and analysis of Han et al. (2007), the heavy oil sands with larger grain sizes tend to have larger velocities, and the oil sands with better sorting tend to have smaller velocities. Hence, the grain size distribution and sorting caused matrix heterogeneity, which is also confirmed by the porosity log in Figure 3, appears as a possible reason for the velocity difference of the two sections.

Due to the lack of XRD/thin section analysis of the core samples, detailed mineral components of the matrix are unknown. However, based on the previous studies conducted in the same area (Guo and Han, 2016; Huang et al., 2020), the matrix is mainly composed of quartz sand grains. Hence, we also assume the pure quartz sand matrix. On the other hand, however, if the matrix contains clay which has smaller bulk modulus, shear modulus, and density than quartz, then the matrix density and moduli would both be smaller. In such

case, the predicted porosity would be larger, and the predicted velocities would be smaller than the current values.

A lot of rock physics models are available for simulating oil sands elastic properties (Guo and Han, 2016; Yuan et al., 2020; Qi et al., 2021; Zhang et al., 2021; Zhang et al., 2022). However, only three models (Hertz–Mindlin model, Voigt–Reuss–Hill average, and iso-frame model) are used here, mainly due to two reasons. First of all, the target of the study is to evaluate the consolidation status of the oil sands, and these three models can best serve the purpose through the associated parameters (coordination number in the Hertz–Mindlin model, closeness to Reuss bound in the VRH model, and IF value in the iso-frame model). In particular, the Hertz–Mindlin model and iso-frame model can provide the quantitative assessment of the consolidation status (e.g., coordination number = .7 in the Hertz–Mindlin model and IF = .2 in the iso-frame model). Moreover, these models have also been adopted to simulate the elastic properties of oil sands before (Lerat et al., 2010; Wolf, 2010; Yuan et al., 2020), suggesting that they are suitable for oil sands modeling. Hence, considering the aforementioned two factors, we choose these models to simulate the oil sands.

In the modeling process, a constant oil saturation of 58% is used, which is derived from the average value in Table 1. However, the true oil saturation based on the core measurement varies from 51.5% to 62.3%. To further inspect the influence of saturation variation, the associated bulk modulus and density are picked in Figure 7C, which can be used to calculate uncertainties, as shown in Table 2. It is clear that the uncertainties of the bulk modulus and density of the fluid mixture caused by saturation variation are quite small (bulk modulus uncertainty is below .7%, and density uncertainty is below .3%).

Given that the pore fluids consist of heavy oil and water (oil saturation is around 58%, and water saturation is around 42%), they are assumed under iso-stress condition, and the Wood equation is adopted for pore fluids mixing. Hence, the shear modulus of the fluids mixture is zero. However, the heavy oil under *in situ* condition is at a semisolid state with a shear modulus (Trippetta and Geremia, 2019), which is around .038 GPa as predicted by the FLAG program. This viscous oil might choke the pore throats and reduce pore connectivity, resulting in patchy distribution of the pore fluids. In such case, the pore fluids are under iso-strain condition, which is more appropriate to simulate with Voigt bound (Mavko et al., 2009). Thus, the corresponding shear and bulk moduli of the fluids mixture would be .022 and 2.35 GPa, respectively, which, however, is not much different from the current value using the Wood equation (2.34 GPa). Therefore, it can be inferred that the fluids mixing with Voigt bound could have some influences on the modeling results, but the differences cannot be significant.

The simulation results of the VRH model and IF model both suggest that the oil sands' frame is very loose. The Hertz–Mindlin model results directly demonstrate that the grain contacts are quite scarce and most of the grains are in the suspension status, further justifying the poorly consolidated rock frame. These aforementioned results are consistent with the laboratory SEM observations in Figure 14. It is evident that the grains are separated without much contact between them, which justifies that the oil sands are poorly consolidated.

On the other hand, however, even all the aforementioned models reach the same conclusion of loose frame and rarely-connected grains, the grains are not completely isolated, and the frame does have some consolidation. In the Hertz–Mindin modeling result, the coordination number is around .7, meaning that the average grain contact is .7, which, although small, is still above 0. In the VRH modeling result, the data distributes close to Reuss bound, but there is still some gap between them. This gap is because the grains are not completely separated, and there are still some grain contacts remaining. In the IF modeling, although the results suggest that 80% of the grains are in suspension, there are still 20% remaining in the load-bearing frame.

Comparing Figures 8, 10, 12, it can be found that well #2 has a smaller coordination number and IF value than well #1, which suggests that the rock frame of oil sands in well #2 is weaker than that in well #1. We think there are three possible reasons. The first one is that the formations in #2 are shallower than in #1 (100 m compared to 400 m). The shallower depth means smaller overburden pressure, and thus the rock frame is less compacted than that in well #1. Under this condition, the simulation results have no problem and correctly reveal the consolidation status of these formations in well #2. The second reason is related to the clay content. By comparing Figures 2, 11, it can be found that well #2 has higher values of GR log than well #1, which indicates it has higher clay content. This higher clay content makes the true rock matrix "softer" with smaller moduli, and thus the simulation results using the (default) quartz mineral matrix overestimate the velocities, leading to the conclusion of relatively weaker oil sands in well #2. A third possible reason is about the oil saturation. In well #1, the saturation is around 58% (according to Table 1). However, if the saturation of the oil sands in well #2 is lower than 58%, then according to Eq. 6, the true bulk modulus of the fluids mixture will be smaller than 2.34 GPa, resulting in an overestimation of the simulation results which uses 2.34 GPa as the bulk modulus of fluids mixture. Given that the formations in well #2 are shallower than in well #1, this is also a reasonable and possible explanation.

Overall, even though there are differences between the estimated parameters of the Hertz–Mindlin model and IF model in wells #1 and #2, the differences are small and they both demonstrate that the oil sands in this area are loose and poorly consolidated, which can provide useful information for seismic characterization and production evaluation of the oil sands reservoirs in this oilfield.

5 Conclusion

The heavy oil sands in Fengcheng oilfield are located at shallow depth with Vp between 2.4 and 3.1 km/s and Vs between 1.2 and 1.9 km/s. The porosities are mostly between .2 and .4, and the average oil saturation obtained from the laboratory measurement is around 58%.

The predicted porosity through combining the density log and neutron log matches well with the laboratory measured sample porosities, demonstrating the effectiveness of the method. The grain size distribution and different sorting lead to the matrix heterogeneities, which further cause the different velocities of the shallow section (403–418 m) and deep section (418–425 m) in well #1. The theoretical modeling demonstrates that the rock velocities are generally at low level. The results suggest that the grain contacts are scarce, and the frame is loose and poorly consolidated, which are consistent with the SEM observations. Overall, this study demonstrates that the integration of well log, laboratory data, and rock physics models works effectively in analyzing the consolidation status of the heavy oil sands, which can provide valuable implications for seismic characterization and drilling risk evaluation.

Data availability statement

The original contributions presented in the study are included in the article/Supplementary Material; further inquiries can be directed to the corresponding author.

Author contributions

HY: conceptualization, methodology, funding acquisition, and writing—original draft. XH: conceptualization and data acquisition. XZ: writing—revising draft and project administration. YW: writing—revising draft.

Funding

This research was supported by the National Natural Science Foundation of China (Grant 42104118, U1839208, and 41804132) and New Teacher Research Ability Improvement Project in China University of Geosciences (Beijing).

Acknowledgments

The authors are grateful to the colleagues in China University of Geosciences (Beijing) for support and discussion.

Conflict of interest

The authors declare that the research was conducted in the absence of any commercial or financial relationships that could be construed as a potential conflict of interest.

Publisher's note

References

Aliyeva, S., Dvorkin, J., and Zhang, W. (2012). *Oil sands: Rock physics analysis from well data, alberta, Canada*. Las Vegas, NV: SEG Tech. Program Expanded Abstr, 1–5.

Domenico, S. N. (1976). Effect of brine-gas mixture on velocity in an unconsolidated sand reservoir. *Geophysics* 41, 882–894. doi:10.1190/1.1440670

Fabricius, I. L. (2003). How burial diagenesis of chalk sediments controls sonic velocity and porosity. *AAPG Bull.* 87, 1755–1778. doi:10.1306/06230301113

Gassmann, F. (1951). Elastic waves through a packing of spheres. *Geophysics* 16, 673–685. doi:10.1190/1.1437718

Guo, J., and Han, X. (2016). Rock physics modelling of acoustic velocities for heavy oil sand. *J. Petrol. Sci. Eng.* 145, 436–443. doi:10.1016/j.petrol.2016.05.028

Han, D. H., Yao, Q. L., and Zhao, H. Z. (2007). Complex properties of heavy oil sand. *Seg. Tech. Program Expand. Abstr.*, 1605. doi:10.1190/1.2792803

Hashin, Z., and Shtrikman, S. (1963). A variational approach to the theory of the elastic behaviour of multiphase materials. *J. Mech. Phys. Solids.* 11, 127–140. doi:10.1016/0022-5096(63)90060-7

Hill, R. T. (1952). On discontinuous plastic states, with special reference to localized necking in thin sheets. *J. Mech. Phys. Solid* 1, 19–30. doi:10.1016/0022-5096(52)90003-3

Hossain, Z., Mukerji, T., Dvorkin, J., and Fabricius, I. L. (2011). Rock physics model of glauconitic greensand from the North Sea. *Geophysics* 76 (6), E199–E209. doi:10.1190/geo2010-0366.1

Huang, W., Wang, X., Sun, X., Xie, Z., Zhou, B., Xiong, W., et al. (2020). Exploration and production practice of oil sands in Fengcheng oilfield of Junggar Basin, China. *J. Pet. Explor Prod. Technol.* 10, 1277–1287. doi:10.1007/s13202-019-00828-w

Javanbakhti, A. R. (2018). *Empirical modeling of the saturated shear modulus in heavy oil saturated rocks*. Calgary, AB: Ph.D. Dissertation, University of Calgary.

Lerat, O., Adjemian, F., Baroni, A., Etienne, G., Renard, G., Bathellier, F., et al. (2010). Modelling of 4D seismic Data for the monitoring of steam chamber growth during the SAGD process. *J. Can. Petrol.Technol.* 49, 21–30. doi:10.2118/138401-pa

Mavko, G., Mukerji, T., and Dvorkin, J. (2009). *The rock physics handbook: Tools for seismic analysis in porous cambridge*. London, UK: Cambridge University Press.

Meyer, R., and Attanasi, E. (2003). *Heavy oil and natural bitumen- strategic Petroleum resources*. Reston, VA: U.S. Geological Survey.

Mindlin, R. D. (1949). Compliance of elastic bodies in contact. *J. Appl. Mech.* 16, 259–268. doi:10.1115/1.4009973

Qi, H., Ba, J., Carcione, J. M., and Zhang, L. (2021). Temperature-dependent wave velocities of heavy oil-saturated rocks. *Lithosphere* 3, 3018678. doi:10.2113/2022/3018678

Trippetta, F., and Geremia, D. (2019). The seismic signature of heavy oil on carbonate reservoir through laboratory experiments and AVA modelling. *J. Petrol Sci. Eng.* 177, 849–860. doi:10.1016/j.petrol.2019.03.002

Wolf, K. (2010). *Laboratory measurements and reservoir monitoring of bitumen sand reservoirs*. Stanford, CA: Stanford University.

Wood, A. W. (1955). *A textbook of sound*. New York: McMillan Co.

Yuan, H., Han, D. H., Li, H., and Zhang, W. (2020). The effect of rock frame on elastic properties of bitumen sands. *J. Petrol Sci. Eng.* 194, 107460. doi:10.1016/j.petrol.2020.107460

Yuan, H., Han, D. H., and Zhang, W. (2017). Seismic characterization of heavy oil reservoir during thermal production: A case study. *Geophysics* 82 (1), B13–B27. doi:10.1190/geo2016-0155.1

Zhang, L., Ba, J., and Carcione, J. M. (2021). Wave propagation in infinituple-porosity media. *J. Geophys. Res. Solid Earth.* 126 (4), e2020JB021266. doi:10.1029/2020jb021266

Zhang, L., Ba, J., Carcione, J. M., and Wu, C. (2022). Seismic wave propagation in partially saturated rocks with a fractal distribution of fluid-patch size. *J. Geophys. Res. Solid Earth.* 127 (2), e2021JB023809. doi:10.1029/2021jb023809

Zhang, S., Zhang, Y., Wu, S., Liu, S., Li, X., and Li, S. (2005). "Status of heavy oil development in China," in SPE International Thermal Operations and Heavy Oil Symposium, Calgary, Alberta, Canada, November 1–3, 2005. SPE-97844-MS.

Zhou, W. (2016). *Study on sedimentary reservoirs of J3q3 Jurassic Qigu formation in wellblock Fengzhong 010 of Fengcheng oilfield*. Beijing): China University of Petroleum.

frontiers | Frontiers in Earth Science

TYPE Original Research
PUBLISHED 10 January 2023
DOI 10.3389/feart.2022.1075151

OPEN ACCESS

EDITED BY
Qiaomu Qi,
Chengdu University of Technology, China

REVIEWED BY
Peng Zhu,
Chengdu University of Technology, China
Jingjing Zong,
University of Electronic Science and Technology of China, China

*CORRESPONDENCE
Mehdi Mokhtari,
mxm4487@louisiana.edu

SPECIALTY SECTION
This article was submitted to Solid Earth Geophysics, a section of the journal Frontiers in Earth Science

RECEIVED 20 October 2022
ACCEPTED 11 November 2022
PUBLISHED 10 January 2023

CITATION
Jiang S, Mokhtari M and Song J (2023), Comparative study of elastic properties of marl and limestone layers in the Eagle Ford formation.
Front. Earth Sci. 10:1075151.
doi: 10.3389/feart.2022.1075151

Comparative study of elastic properties of marl and limestone layers in the Eagle Ford formation

Shuxian Jiang[1], Mehdi Mokhtari[2]* and Jinze Song[1]

[1]Petroleum and Natural Gas Engineering School, Southwest Petroleum University, Chengdu, China, [2]Petroleum Engineering Department, University of Louisiana at Lafayette, Lafayette, LA, United States

Eagle Ford Formation has significant heterogeneity due to the existence of marl and interbedded limestone layers. The objective of this paper is to study the elastic properties of different layers in the Eagle Ford Formation. To achieve the goal, the relationships between compressional and shear velocities in marl and limestone layers were investigated in two representative Eagle Ford wells. These empirical equations can be used to estimate the shear velocity in Eagle Ford wells without sufficient well log data. Moreover, correlations between elastic properties and GR were obtained. Among all layers in the Eagle Ford Formation, marl layers of the lower Eagle Ford have the lowest averaged values of compressional velocity, shear velocity and dynamic Young's modulus, while the limestone layers of the upper Eagle Ford have the highest averaged values of these three elastic parameters. In addition, the effect of elastic properties of shale layers on the aspect ratio of unconfined and confined fractures were evaluated. The influence of Young's modulus contrast of shale layers on the aspect ratio of confined fractures was remarkable.

KEYWORDS

elastic properties, marl layer, limestone layer, eagle ford shale, aspect ratio, fracture

Introduction

In the unconventional reservoir stimulation, hydraulic fracturing design is usually performed in layered shales, which are stratified by layers with distinct mechanical properties. Elastic parameters are crucial to seismic imaging, wellbore stability and hydraulic fracturing treatment. The elastic parameters including compressional velocity, shear velocity, Young's modulus, Poisson's ratio, and minimum horizontal stress can be obtained from mechanical well logs. However, the high expense of the mechanical well logging limits the usage of well logs. Therefore, it is time and cost efficient to estimate elastic properties from conventional well logs.

Compressional and shear velocities are widely used in geological and geophysical applications. Pickett, 1963 popularized the use of compressional and shear velocity ratio as a lithology indicator. In addition to lithology, porosity is also related to sonic velocities in shaly sandstone or carbonate rocks (Rafavich et al., 1984; Han et al., 1986). The relationship between compressional velocity and shear velocity were investigated in formations with different lithologies (Hossain et al., 2012). This relationship can be used

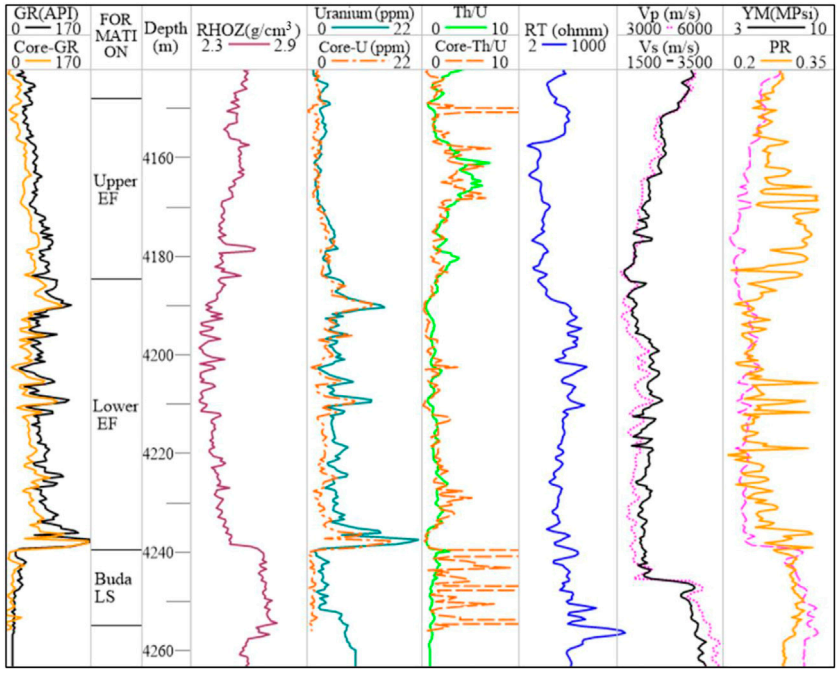

FIGURE 1
Well logs of the studied Eagle Ford well in Dewitt County, Texas.

to predict shear velocity for wells lack of shear velocity data. Castagna et al. 1985) developed a positive linear relationship between compressional velocity and shear velocity according to velocity and field seismic measurement in mudrocks. Greenberg and Castagna (1992) developed coupled equations to estimate shear velocity in porous rocks. Vernik et al., 2002 developed the non-linear relationship between compressional and shear velocity, especially for low velocity sandstone. In shale formations, sonic velocities are influenced by gamma ray intensity, clay content and TOC (Xu and White, 1995 and, Xu and White, 1996, Altowairqi et al., 2015). The compressional and shear velocities of synthetic shale samples were measured. Results showed that sonic velocities were negatively related to TOC and clay content.

Although previous researchers have investigated the elastic properties of the Eagle Ford Formation (Hsu and Nelson, 2002; Yang et al., 2019; Kim, 2021), most of the results focused on the average values of reservoir properties over a certain depth interval or on presentative shale samples. Little research has been done on the characterization and quantification of the elastic properties in marl and interbedded limestone layers. In this study, the correlations of velocities as well as correlations of elastic properties and gamma ray or clay content in marl and limestone layers of the Eagle Ford Formation will be developed respectively. Moreover, the effect of elastic moduli on fracture aperture of layered shale is discussed in this study.

Elastic properties of marl and limestone layers of the Eagle Ford Shale in Dewitt County

Description of the Eagle Ford formation

The well in this study is on the southwest side of the San Marcos arch and is close to the Edwards Reef Margin and the Sligo Reef Margin. It is in the jointed zone of the gas condensate and dry gas zone. Vertically, the Eagle Ford Formation can be divided into the Upper and Lower Eagle Ford based on previous research (Donovan et al., 2015; Breyer et al., 2016; Zumberge et al., 2016) as shown in Figure 1.

There are obvious differences in the well logs of the Eagle Ford Formation and the Buda Limestone. Buda Limestone has much lower gamma ray intensity, higher density, lower Uranium, higher Thorium/Uranium ratio (Th/U), higher compressional and shear velocities than the Eagle Ford Formation. The Th/U ratio is a redox indicator of the depositional environment. In most of the Eagle Ford black shales, the Th/U ratio is less than 2, indicating anoxic environment (Jiang and Mokhtari, 2019).

The Lower Eagle Ford can be differentiated from the Upper Eagle Ford with higher gamma ray intensity, high Uranium concentration, low Th/U ratio and higher resistivity (plotted in logarithmic scale). The gamma ray intensity and spectral gamma intensity from well logs and core measurement are shown in Figure 1.

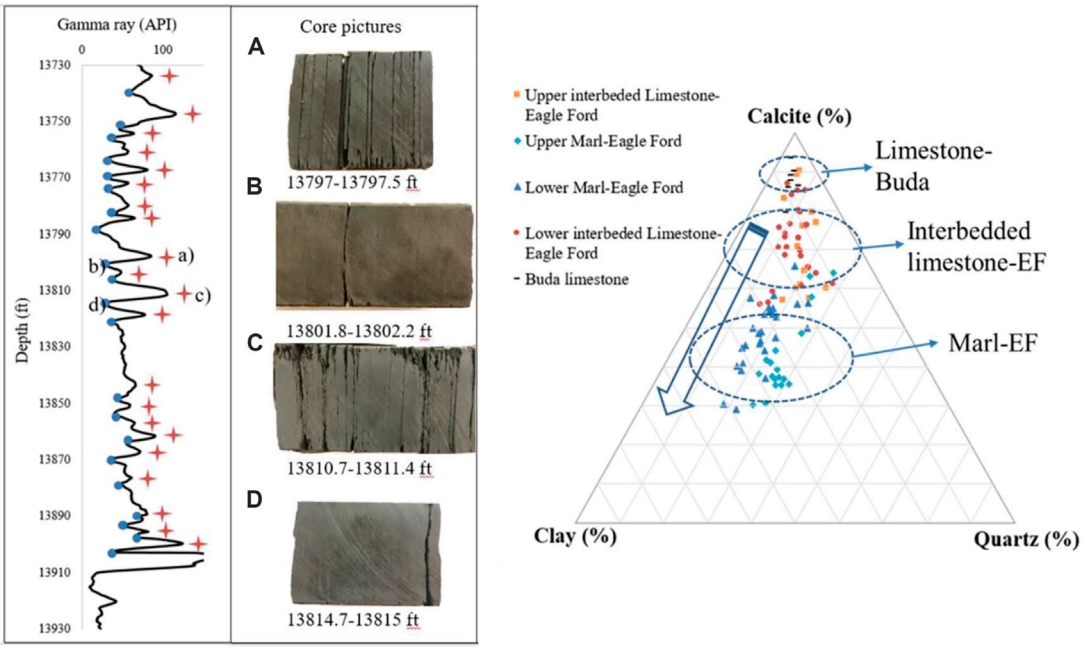

FIGURE 2
Left: Marl and limestone layers of the Eagle Ford Formation in Dewitt County, Texas **(A,C)** Core samples from marl layers; **(B,D)** core samples from limestone layers. Right: Ternary plot of the marl and limestone layers in the Eagle Ford and Buda Formation.

The gamma ray intensity from core measurement is close to data from well logs and can be used in logging depth correction. It can be seen from the spectral gamma ray data that the Th/U ratio in the Lower Eagle Ford is much lower than in the Upper Eagle Ford. As shown in Figure 1, the Th/U ratios measured from cores have more variations than the Th/U ratios from well logging, though the trends of the two curves are quite the same. Since the hand-held spectral core gamma instrument collects Th, U and K data every 0.17 ft (5 cm) along the core samples, it can collect spectral gamma of layers with different characteristics. Additionally, compared with spectral gamma logging, spectral core gamma measurement can avoid well bore environmental distortion.

Based on well log and core sample analysis, there are distinct differences in reservoir properties of the marl and limestone layers. As depicted in Figure 2, samples from the marl layers are darker and flakier than those from limestone layers. XRD results show that the calcite content of marl layers ranges from 30% to 70% and clay content ranges from 20% to 50%. The interbedded limestone layers contain less clay (5%–30%) and more calcite (55%–90%) than marl layers.

Correlations of compressional and shear velocities in marl and limestone layers

Castagna et al. (1985) raised an empirical correlation according to water saturated mudrocks that are mainly composed of quartz and clay minerals. It is commonly referred as mudrock line with Eq.1. In 1993, Castagna et al. raised sonic velocity correlations in carbonate rocks. For water saturated limestone, the compressional velocity can be expressed as Eq.2. These empirical correlations are valid for specific formations and variations in rock properties such as mineralogy and porosity can affect the accuracy of the estimation results. Eq. 1 is widely used in the shear velocity estimation in clastic silicate rocks that are composed primarily of clay and quartz. It can provide us with reasonable results of shear velocity for consolidated rocks with compressional velocity greater than 2.6 km/s. However, the mudrock line underestimated shear velocity for unconsolidated sediments and may not work well in calcite-rich shales. Eq. 2 shows the empirical correlations of compressional and shear velocities in water saturated limestone of a certain area, and it may not applicable in other areas.

$$V_P\,(km/s) = 1.16V_S\,(km/s) + 1.36 \quad (1)$$

$$V_S\,(km/s) = -0.055V_P^2\,(km/s) + 1.017V_P\,(km/s) - 1.031 \quad (2)$$

Here we develop the correlation between compressional and shear velocity in Eagle Ford Formation and adjacent Buda Limestone (Figure 3). Buda Limestone is included in the analysis since it can be treated as the boundary of shale with highest calcite content. The correlations raised by Castagna et al.

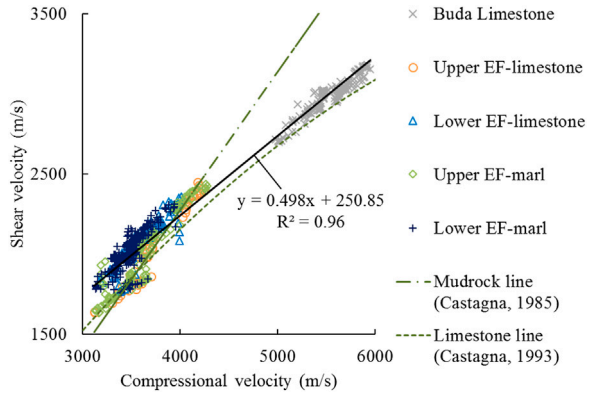

FIGURE 3
Correlations of compressional and shear velocity in Dewitt County.

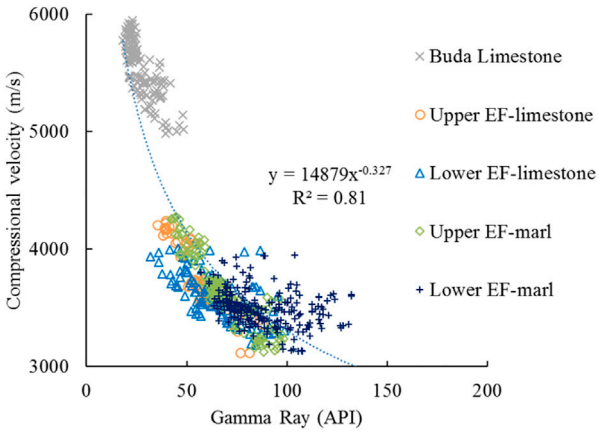

FIGURE 4
Correlations of compressional velocity and gamma ray in different layers.

TABLE 1 Correlations of compressional and shear velocity of Eagle Ford well in Dewitt County (in m/s).

Layer	Correlations in eagle ford well in dewitt county	R^2
All layers	V_s = 0.498 V_p + 250.85	0.96
Upper limestone	V_s = 0.396 V_p + 736.30	0.43
Upper marl	V_s = 0.718 V_p - 598.92	0.88
Lower limestone	V_s = 0.628 V_p - 181.54	0.80
Lower marl	V_s = 0.630 V_p - 174.50	0.63
Buda limestone	V_s = 0.442 V_p + 551.51	0.84

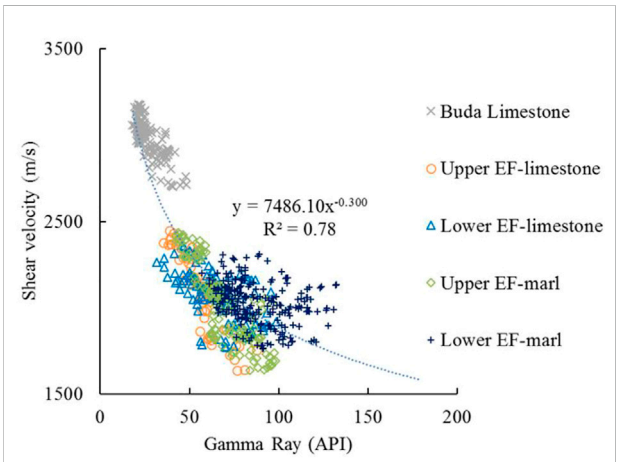

FIGURE 5
Correlations of shear velocity and gamma ray in different layers.

were plotted. The Castagna line 1985) can fit some of the data in the Eagle Ford, but it starts to diverge when the velocity increases and cannot fit the Buda limestone data. The Castagna et al., 1993 has a similar tend but still deviates from the data. As shown in Figure 3, there is a good positive linear relationship between compressional and shear velocity with R^2 value of 0.96. The correlations in different layers of the Eagle Ford well in Dewitt County are summarized in Table 1. For wells without shear velocity data, V_s can be estimated based on the proposed correlations, especially in the marl layers of Upper Eagle Ford, interbedded limestone layers of Lower Eagle Ford and the Buda Limestone layers.

Correlations of elastic properties with gamma ray in marl and limestone layers

The elastic properties of different layers and the correlations between elastic properties and gamma ray intensity are shows in Figures 4, 5, 6, 7 and Tables 2, 3. According to Figures 4, 5, compressional and shear velocities have a power law relationship with gamma ray. The Buda Limestone on the upper left of the figures shows the lowest gamma ray (ranging from 18 API to 48 API) and highest compressional velocity (ranging from 4981 m/s to 5949 m/s) and shear velocity (ranging from 2701 m/s to 3181 m/s). Compared with the Buda Limestone layer, the Eagle Ford layers have much lower sonic velocities.

Among the marl and interbedded limestone layers in the upper and lower Eagle Ford, marl layers of the lower Eagle Ford have the highest average value of gamma ray 97 API and lowest average values of compressional velocity 3496 m/s and shear velocity 2027 m/s. In contrast, interbedded limestone layers of the upper Eagle Ford have the lowest average values of gamma

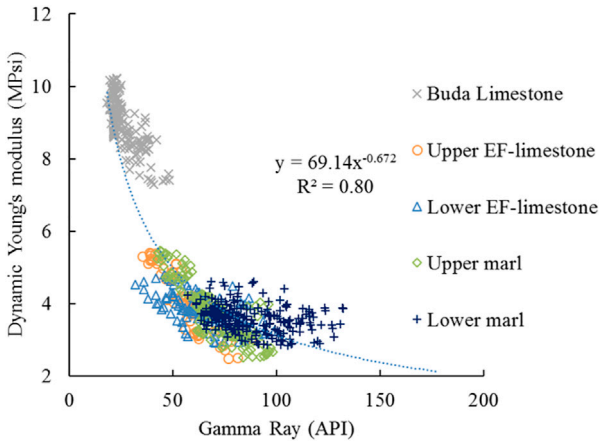

FIGURE 6
Correlations of dynamic Young's Modulus and gamma ray in different layers.

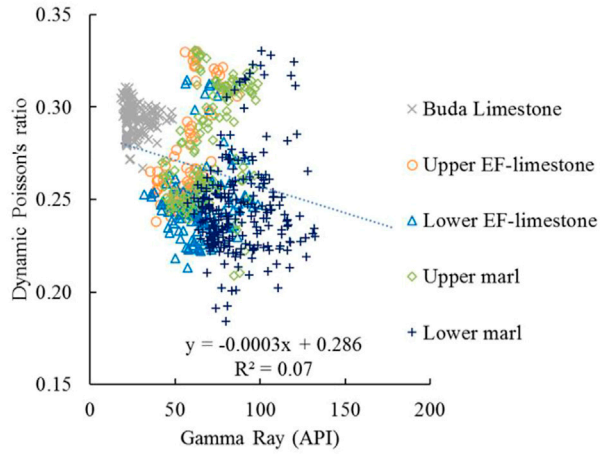

FIGURE 7
Correlations of dynamic Poisson's ratio and gamma ray in different layers.

ray 57 API and highest average value of compressional velocity 3751 m/s and shear velocity 2084 m/s.

Table 2 shows the correlation of compressional velocity, shear velocity and gamma ray in different layers of the Eagle Ford well in Dewitt County (in m/s). In the marl and interbedded limestone layers in the Upper Eagle Ford, there is a good negative linear relationship between the sonic velocities and gamma ray intensity. However, in the Lower Eagle Ford and Buda Limestone, there is a weak or no correlation between compressional velocity, shear velocity and gamma ray. Attention should be paid when R^2 is used to evaluate the fit of nonlinear relationships. Since R^2 is calculated based on the linear regression model assumption, the increase of R^2 does not always relate to better nonlinear models.

Based on compressional and shear velocities, the mechanical properties such as dynamic Young's modulus and dynamic Poisson's ratio can be obtained through Eqs 3, 4.

$$E_d = 0.145 \times 10^{-6} \rho_b V_s^2 \left(\frac{3V_p^2 - 4V_s^2}{V_p^2 - V_s^2} \right) \quad (3)$$

$$\nu_d = \frac{1}{2} \left(\frac{V_p^2 - 2V_s^2}{V_p^2 - V_s^2} \right) \quad (4)$$

where E_d is the dynamic Young's modulus of rock, MPsi; υ_m is the dynamic Poisson's ratio of rock, dimensionless; ρ_b is density of rock, g/cm^3; V_p is the compressional velocity of rock, m/s; V_s is the shear velocity of rock, m/s.

The mechanical properties of different layer and the correlation of mechanical properties with gamma ray intensity are shown in Figures 6, 7 and Table 3. Figure 6 depicts the relationship between dynamic Young's modulus and gamma ray. Young's modulus decreases with gamma ray and the data points fall into two clusters. Buda limestone shows the higher dynamic Young's modulus with an average value of 8.9 Mpsi and the Eagle Ford Formation has much lower dynamic Young's modulus. Among the marl and interbedded limestone layers in the upper and lower Eagle Ford, marl layers of the lower Eagle Ford have the lowest averaged value of dynamic Young's modulus

TABLE 2 Correlations of compressional velocity, shear velocity and gamma ray of Eagle Ford well in Dewitt County (in m/s).

Layer	Correlations of V_p and GR	R^2	Correlations of V_s and GR	R^2
All layers	$V_p = 14{,}879\ GR^{-0.327}$	0.81	$V_s = 7486\ GR^{-0.300}$	0.78
Upper limestone	$V_p = -21.30\ GR + 4962.3$	0.83	$V_s = -16.90\ GR + 3045.9$	0.79
Upper marl	$V_p = -18.38\ GR + 4915.0$	0.84	$V_s = -13.07\ GR + 2922.4$	0.72
Lower limestone	$V_p = -9.12\ GR + 4185.2$	0.44	$V_s = -6.01\ GR + 2464.1$	0.39
Lower marl	—	—	—	—
Buda limestone	$V_p = -21.32\ GR + 6064.6$	0.43	$V_s = -11.98\ GR + 3299.5$	0.58

TABLE 3 Summary of parameters in different layers of the Eagle Ford and adjacent formation in Dewitt County.

Layers		GR (API)	V_p (m/s)	V_s (m/s)	Dynamic YM (Mpsi)	Dynamic υ
Buda	Mean	26	5514	2990	8.9	0.29
Limestone	Min	18	4981	2701	7.3	0.27
	Max	48	5949	3181	10.2	0.31
EF Upper limestone	Mean	57	3751	2084	4.5	0.28
	Min	35	3118	1638	2.5	0.24
	Max	88	4240	2448	5.4	0.33
EF Lower limestone	Mean	64	3598	2077	3.8	0.25
	Min	32	3183	1769	2.9	0.21
	Max	99	4009	2360	4.8	0.31
EF Upper marl	Mean	69	3648	2041	3.8	0.28
	Min	42	3126	1635	2.5	0.21
	Max	98	4075	2436	5.5	0.33
EF Lower marl	Mean	97	3496	2027	3.6	0.25
	Min	57	3134	1761	2.8	0.18
	Max	132	3951	2311	4.6	0.33

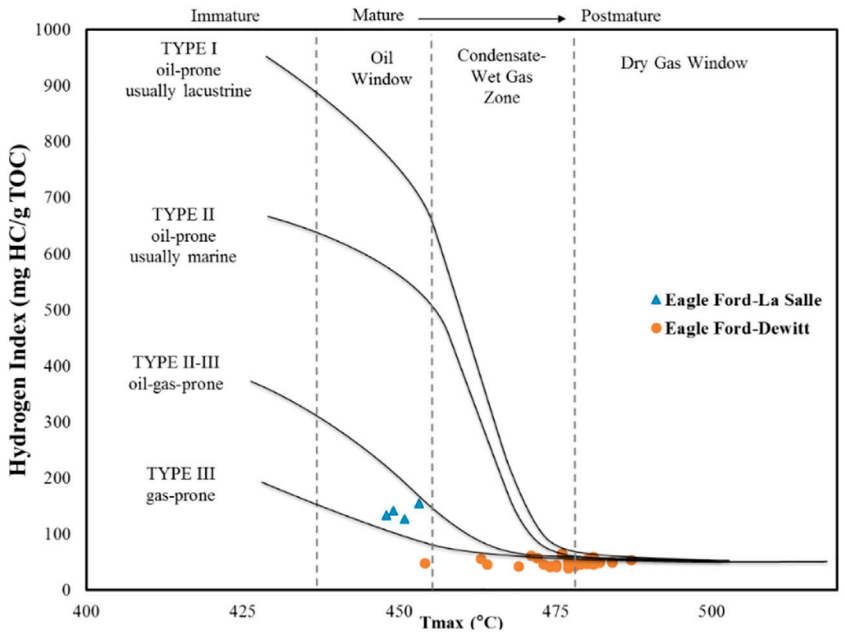

FIGURE 8
Maturity level of two Eagle Ford wells.

(3.6 Mpsi) while the limestone layers of the upper Eagle Ford have the highest averaged value (4.5 Mpsi).

In addition to the cross plots of compressional velocity, shear velocity and dynamic Young's modulus against gamma ray, the relationships between dynamic Poisson's ratio and gamma ray in different layers are also explored. As shown in Figure 7, there is no obvious difference among the three formations and no linear correlation between Poisson's ratio and gamma ray. There is no obvious difference in Poisson's ratio in the Eagle Ford Formation and the Buda Limestone. The average values of Poisson's ratio in the Buda Limestone, Upper Eagle Ford, and Lower Eagle Ford are 0.29, 0.28, and 0.25, respectively.

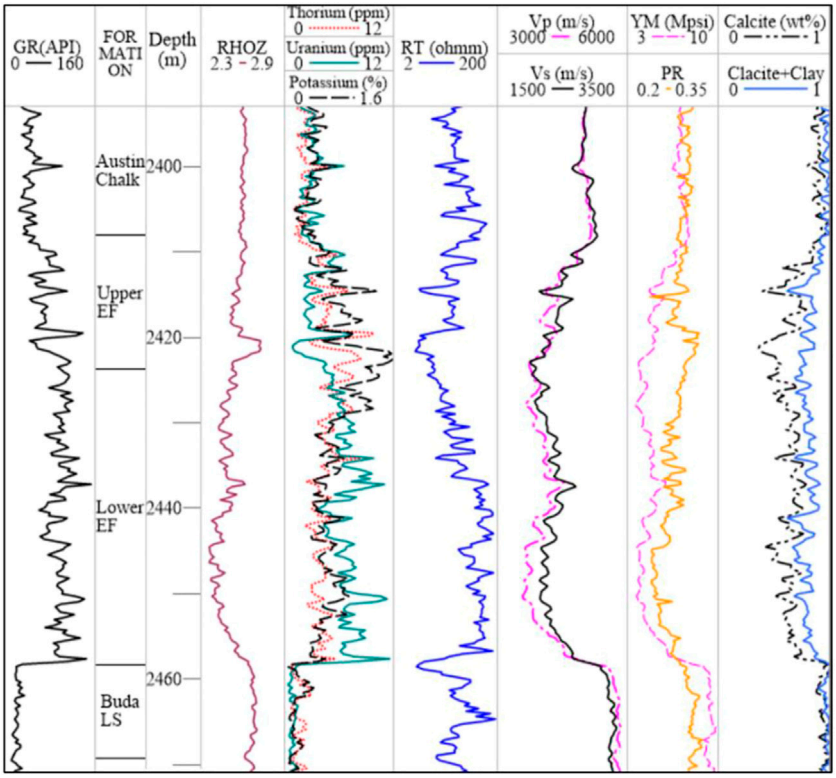

FIGURE 9
Well logs of a well in LaSalle County, showing the Eagle Ford shale and the adjacent formation unit.

Elastic properties of marl and limestone layers of the Eagle Ford Shale in La Salle county

For a better understanding of the elastic properties of the Eagle Ford Formation, another well located in La Salle County, Texas was studied. Figure 8 shows the maturity level of samples from the two wells. Samples from La Salle County are in the oil window and most samples from Dewitt County are in the condensate gas and dry gas window.

The well log information of the well in La Salle County is shown in Figure 9. The Eagle Ford Formation has higher gamma ray intensity, lower compressional and shear velocities, lower calcite content than the overlying Austin Chalk and the underlying Buda Limestone. The contact between the Upper and Lower Eagle Ford is marked by an increase in the gamma ray, especially the Uranium concentration. Additionally, the Lower Eagle Ford, which has higher organic richness, shows lower bulk density and higher resistivity than the Upper Eagle Ford.

At depth interval 2420 m–2423 m, the peak of potassium in the Upper Eagle Ford indicates the existence of ash bed layer (Mokhtari et al., 2016), which has much higher clay content than other parts of the formation. The features of ash bed are consistent with the results of Kiipli et al. (2008). Ash bed layers differ from the host rock by high concentrations of Al, P, Zr, Pb, and K as well as high clay content.

Correlations of compressional and shear velocities in marl and limestone layers in La Salle county

According to the contents of calcite and clay, we set a threshold of 75 API for categorizing limestone and marl layers in the upper Eagle Ford and a threshold of 105 API in the Lower Eagle Ford. The correlations between compressional and shear velocity in the Eagle Ford Formation and adjacent Buda Limestone are shown in Figure 10.

There is a good positive linear relationship between compressional and shear velocity. Among the three correlations, $V_s = 0.518\ V_p + 240.56$ is the best fit line for the data of Eagle Ford, the overlying Austin Chalk and the underlying Buda Limestone. The correlations in different layers of the Eagle Ford well in La Salle County are summarized in Table 4. For wells without shear velocity data,

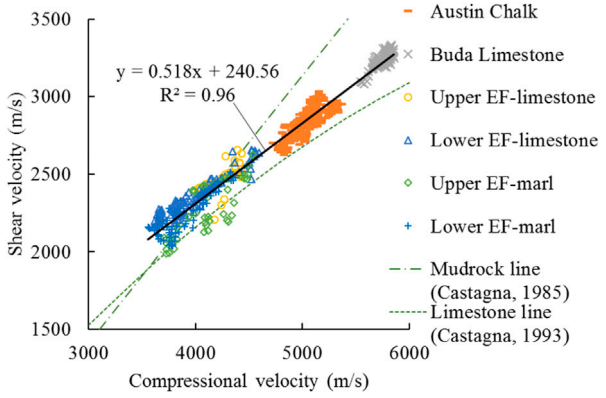

FIGURE 10
Correlations of compressional and shear velocity in La Salle County.

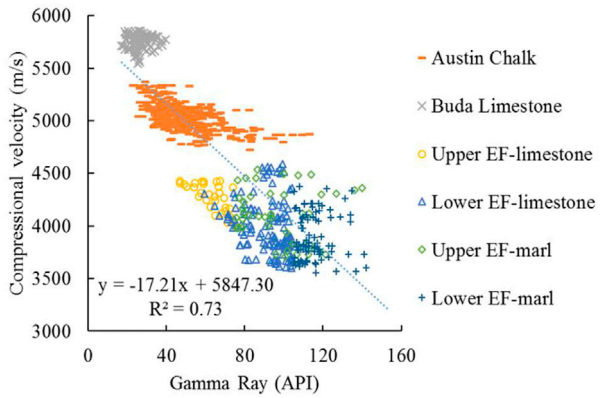

FIGURE 11
Correlations of compressional velocity and gamma ray in different layers.

TABLE 4 Correlations of compressional and shear velocities of Eagle Ford well in La Salle County (in m/s).

Layer	Correlations in eagle ford well in La Salle county	R^2
All layers	V_s = 0.518 V_p + 240.56	0.96
Upper limestone	V_s = 0.440 V_p + 599.43	0.39
Upper marl	V_s = 0.552 V_p + 8.47	0.64
Lower limestone	V_s = 0.455 V_p + 532.95	0.89
Lower marl	V_s = 0.500 V_p + 297.55	0.75
Buda limestone	V_s = 0.596 V_p - 186.51	0.64
Austin chalk	V_s = 0.543 V_p + 107.58	0.64

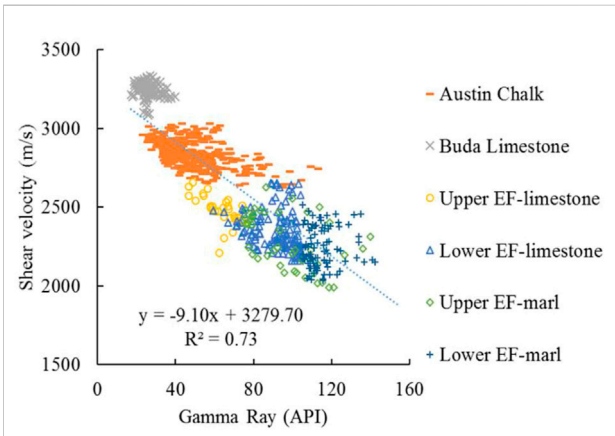

FIGURE 12
Correlations of shear velocity and gamma ray in different layers.

V_s can be estimated based on the proposed correlation, especially in the Lower Eagle Ford Formation.

Correlations of elastic properties with gamma ray in marl and limestone layers in La Salle County

The elastic properties of different layer and the correlation between elastic properties and gamma ray intensity and clay content are shown in Figures 11, 12, 13, 14 and Table 5. According to Figures 11, 12, and Table 5, compressional and shear velocities have good negative linear relationships with gamma ray. The Buda Limestone on the upper left of the figures shows the lowest gamma ray (ranging from 17 API to 40 API) and highest compressional velocity (ranging from 5546 m/s to 5857 m/s) and shear velocity (ranging from 3082 m/s to 3333 m/s). The Austin Chalk has higher gamma ray (ranging from 23 API to 113 API), lower compressional velocity (ranging from 4728 m/s to 5370 m/s) and shear velocity (ranging from 2624 m/s to 3031 m/s) than the Buda Limestone.

Among the marl and limestone layers in the upper and lower Eagle Ford, marl layers of the lower Eagle Ford have the highest average value of gamma ray 115 API, lowest average values of compressional velocity 3892 m/s and shear velocity 2243 m/s. In contrast, limestone layers of the upper Eagle Ford have the lowest average values of gamma ray 63 API and highest average value of compressional velocity 4275 m/s and shear velocity 2480 m/s. The correlations of compressional velocity, shear velocity and gamma ray show that there is a weak or no relationship between sonic velocities and gamma ray in different layers of the Eagle Ford well in La Salle County.

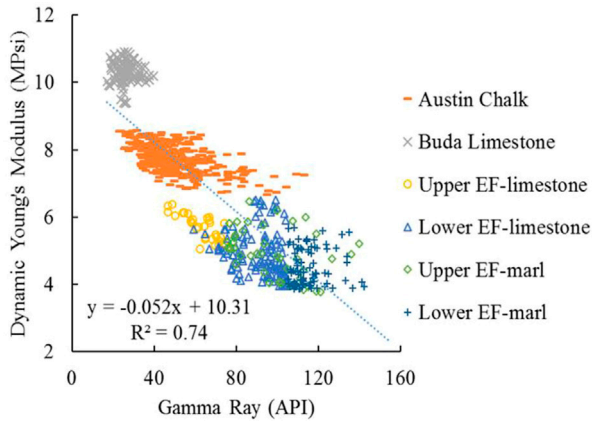

FIGURE 13
Correlations of dynamic Young's Modulus and gamma ray in different layers.

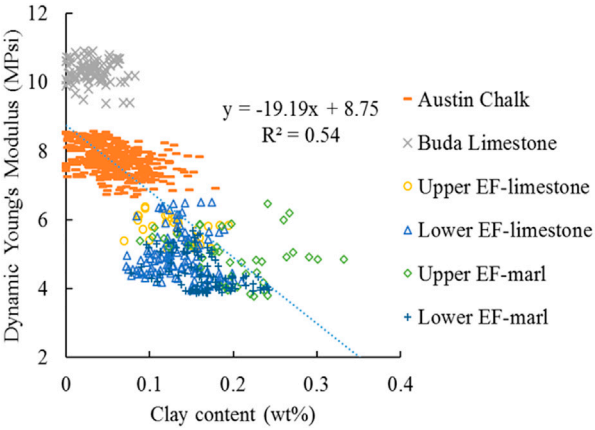

FIGURE 14
Correlations of dynamic Young's Modulus and clay content in different layers.

Figure 13 depicts the relationship between dynamic Young's modulus and gamma ray. Young's moduli decrease with gamma ray and the data points fall into three clusters. Buda limestone shows the highest Young's modulus with an average value of 10.3 Mpsi and the Eagle Ford Formation has the lowest Young's modulus. Among the marl and limestone layers in the upper and lower Eagle Ford, marl layers of the lower Eagle Ford have the lowest averaged value of Young's modulus (4.5 Mpsi) while the limestone layers of the upper Eagle Ford have the highest averaged value (5.7 Mpsi).

Figure 14 depicts the relationship between dynamic Young's modulus and clay content. Similarly, there is a clear difference among the group of Austin Chalk, Buda Limestone and Eagle Ford Formation. But the negative linear relationship between Young's modulus and clay content is relatively weak.

The comparison of elastic parameters in different layers of two Eagle Ford wells is shown in Table 6. Buda Limestone has the least variations in gamma ray intensity, compressional and shear velocities and Young's moduli in these two wells. Compressional and shear velocities of the well in La Salle County are more than 11% higher than the well in Dewitt County in marl and limestone layers of the Eagle Ford Formation. It can be seen from the comparison of mechanical properties of two Eagle Ford wells that dynamic Poisson's ratio of two wells is similar while dynamic Young's modulus in La Salle County is more than 25% higher than in Dewitt County.

The San Marcos Arch traverses the Eagle Ford play and extends towards the Gulf of Mexico southeasterly. The Edwards City shelf margin and the Sligo shelf margin spread toward southwest in parallel and then separate. In this study, the well in La Salle County is on the north side of the Edwards City shelf margin, while the well in Dewitt County is close to the Edwards Reef Margin and the Sligo Reef Margin. Both of these two wells are on the southwest side of the San Marcos arch. Therefore, caution should be paid when these results are generalized to other areas, such as Fayette county and Lavaca county, which are on the northeast side of the San Marcos arch.

Discussion

Characterization of elastic properties of the marl and limestone layers in shale formations is crucial to hydraulic fracture design. The aperture or aspect ratio of fractures can be affected by factors such as layer thickness ratio, overburden stress and so on. The modulus contrast between adjacent layers is an essential factor in the investigation of fracturing behaviours and the effect of elastic properties on fracture aperture should be analyzed.

The FEM models of layered shale with an unconfined fracture and confined fractures are shown in Figure 15. In the numerical modelling, several assumptions are made: 1) there is no slip and opening along the layer boundaries; 2) there is a plane strain condition for the entire model; 3) the marl layers that are adjacent to the middle limestone layer have the same elastic properties. The bottom boundary is fixed in the y direction and the middle point of the bottom boundary is fixed in the x direction, so $u_y(B)=0$ and $u_x(B)=0$ at $x=0$. A constant displacement condition is imposed along the left and right boundaries, so $u_x(L)= -u_x$ and $u_x(R)=u_x$.

In the unconfined fracture model of layered shale (Figure 15A), E_l, υ_l, and T_l are the Young's modulus, Poisson's ratio and thickness of the limestone layer. E_m, υ_m, and T_m are the Young's modulus, Poisson's ratio and thickness of the limestone layer. W and T are the width and overall thickness

TABLE 5 Summary of elastic parameters in different layers of the Eagle Ford and adjacent formation in La Salle County.

Layers		GR (API)	Clay (wt%)	V_p (m/s)	V_s (m/s)	Dynamic YM (Mpsi)	Dynamic υ
Austin	Mean	49	0.06	5033	2839	7.8	0.27
Chalk	Min	23	0.00	4728	2624	6.7	0.24
	Max	113	0.18	5370	3031	8.6	0.30
Buda	Mean	26	0.03	5754	3240	10.3	0.27
Limestone	Min	17	0.00	5546	3082	9.4	0.25
	Max	40	0.08	5857	3333	10.9	0.28
EF Upper limestone	Mean	63	0.15	4275	2480	5.7	0.25
	Min	47	0.07	4022	2210	5.1	0.20
	Max	75	0.49	4429	2657	6.4	0.31
EF Lower limestone	Mean	92	0.14	3999	2354	4.9	0.23
	Min	59	0.07	3604	2160	4.0	0.18
	Max	105	0.21	4592	2655	6.5	0.29
EF Upper marl	Mean	98	0.20	4112	2279	5.0	0.28
	Min	76	0.09	3712	1990	3.8	0.22
	Max	140	0.33	4535	2626	6.5	0.32
EF Lower marl	Mean	115	0.16	3892	2243	4.5	0.25
	Min	105	0.08	3557	2036	3.9	0.20
	Max	142	0.24	4375	2514	5.7	0.30

TABLE 6 Comparison of elastic parameters in different layers of two Eagle Ford wells.

Property	Wells	Buda limestone	Upper EF limestone	Lower EF limestone	Upper EF marl	Lower EF marl
GR (API)	Dewitt	26	57	64	69	97
	La Salle	26	63	92	98	115
	Difference	0%	11%	44%	42%	19%
V_p (m/s)	Dewitt	5514	3751	3598	3648	3496
	La Salle	5754	4275	3999	4112	3892
	Difference	4%	14%	11%	13%	11%
V_s (m/s)	Dewitt	2990	2084	2077	2041	2027
	La Salle	3240	2480	2354	2279	2243
	Difference	8%	19%	13%	12%	11%
Dynamic YM (Mpsi)	Dewitt	8.9	4.5	3.8	3.8	3.6
	La Salle	10.3	5.7	4.9	5.0	4.5
	Difference	16%	27%	29%	32%	25%
Dynamic ϒ	Dewitt	0.29	0.28	0.25	0.28	0.25
	La Salle	0.27	0.25	0.23	0.28	0.25
	Difference	−7%	−11%	−8%	0%	0%

of the layers. H is the fracture height and ε_{xx} (ave) is the average strain in the x direction. In the confined fracture model (Figure 15B), three fractures are equally spaced and the fracture height is equal to the thickness of the limestone layer. S is the distance between fractures.

In order to investigate the effects of elastic properties of the marl and limestone layers on the fracture aspect ratio, one parameter is changed at one time and other parameters are kept constant. Figure 16 shows that the relative change of the unconfined fracture aspect ratio is positively related to the ratio

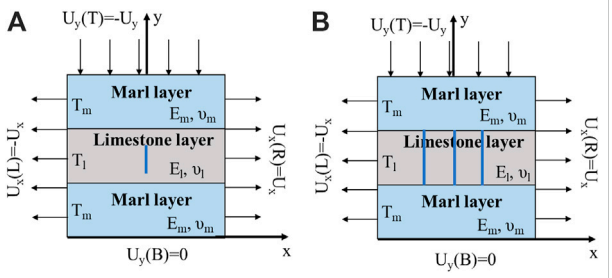

FIGURE 15
FEM model and its boundary conditions of layered shale. **(A)** Unconfined fracture model; **(B)** confined fracture model with three fractures (revised from Bai et al., 2000).

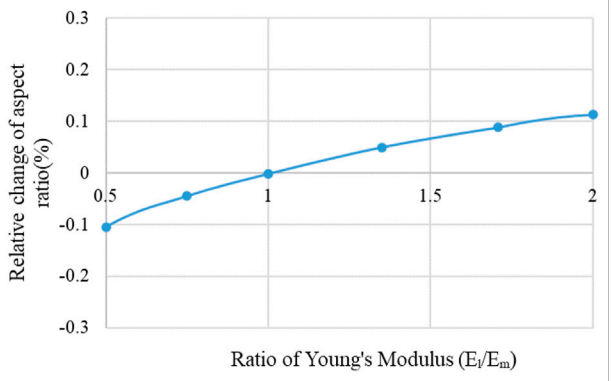

FIGURE 16
Correlations of relative change of aspect ratio and Young's modulus ratio of adjacent layers in unconfined fracture model ($\upsilon_m=\upsilon_l=0.25$, ε_{xx} (ave)=0.002, $H/T_l=0.1$, $T_l=0.2$m, $T_m=0.3$ m).

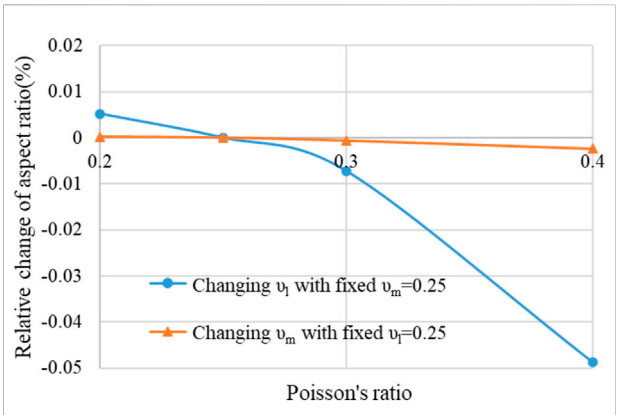

FIGURE 17
Correlations of relative change of aspect ratio and Poisson's ratio in unconfined fracture model ($E_m=E_l=5$ MPsi, ε_{xx} (ave)=0.002, $H/T_l=0.1$, $T_l=0.2$m, $T_m=0.3$ m).

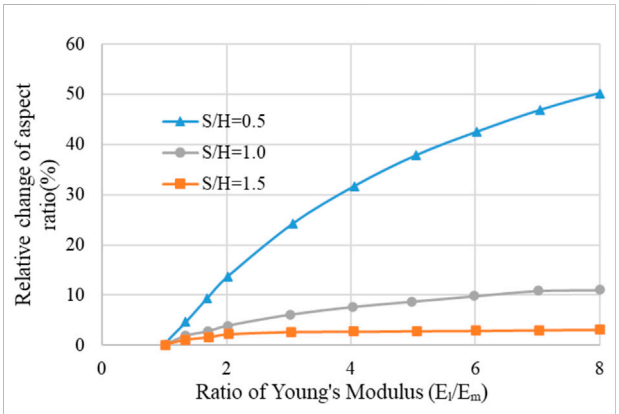

FIGURE 18
Correlations of relative change of aspect ratio and Young's modulus ratio of adjacent layers in confined fracture model ($\upsilon_m=\upsilon_l=0.25$, ε_{xx} (ave)=0.002, $T_l=H=0.2$m, $T_m=0.3$ m).

of the Young's modulus of the limestone layer to that of the marl layer (E_l/E_m).

According to the elastic properties of the Eagle Ford Shale in Dewitt County (shown in Table 3), the Young's modulus ratio of the Upper Eagle Ford Shale ranges from 1.0 to 2.2, while the ratio of the Lower Eagle Ford Shale ranges from 1.0 to 1.7. According to the elastic properties of the Eagle Ford Shale in La Salle County (shown in Table 5), the Young's modulus ratio of the Upper Eagle Ford Shale ranges from 1.3 to 1.7, while the ratio of the Lower Eagle Ford Shale ranges from 1.0 to 1.7. Therefore, the relative change of aspect ratio with respect to the Young's modulus ratio is less than 0.1%.

Figure 17 illustrates the variations of the relative change of aspect ratio with Poisson's ratio. As shown in Table 3, the Poisson's ratio of the Upper and Lower Eagle Ford Shale in Dewitt county ranges from 0.21 to 0.33 and 0.18 to 0.33, respectively. As shown in Table 5, the Poisson's ratio of the Upper and Lower Eagle Ford Shale in La Salle County ranges from 0.20 to 0.32 and 0.18 to 0.30, respectively. Therefore, the absolute value of relative change of aspect ratio with respect to the ratio of Poisson's ratio is less than 0.01%.

It can be concluded from Figures 16, 17 that the influence of elastic properties of the Eagle Ford Shale on the aspect ratio of the unconfined fracture can be negligible in these two areas.

The effect of elastic properties of the layered shale on the aspect ratio of confined fractures is shown in Figures 18, 19. Figure 18 shows the relative change of aspect ratio increases with the ratio of the Young's modulus of limestone layer to that of the marl layer. In addition, the relative change of aspect ratio increases significantly when the ratio of fracture spacing to layer thickness is low.

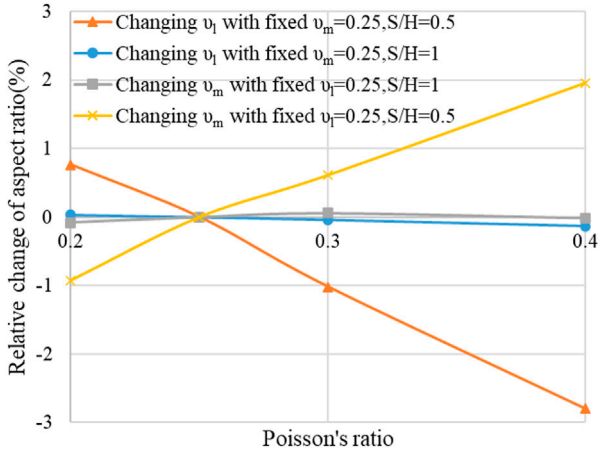

FIGURE 19
Correlations of relative change of aspect ratio and Poisson's ratio in confined fracture model (E_m=E_l=5 MPsi, ε_{xx} (ave)=0.002, T_l=H=0.2m, T_m=0.3 m).

Taking the Eagle Ford Shale in Dewitt County as an example, the ratio of Young's modulus ranges from 1.0 to 2.2 and from 1.0 to 1.7 in the Upper and Lower Eagle Ford, respectively. The corresponding relative change of aspect ratio can reach up to 14% when S/H equals 0.5.

Correlations of the relative change of aspect ratio and Poisson's ratio in the confined fracture model are shown in Figure 19. Taking the Eagle Ford Shale in La Salle County as an example, the Poisson's ratio ranges from 0.20 to 0.32 and from 0.18 to 0.30 in the Upper and Lower Eagle Ford respectively. The corresponding relative change of aspect ratio is less than 1%, indicating the effect of Poisson's ratio on aspect ratio is negligible.

Conclusion

The elastic properties of the marl and limestone layers in the Eagle Ford Shale were analyzed in this study. Additionally, the effect of elastic properties on aspect ratio of unconfined and confined fractures were evaluated. The following conclusions can be drawn:

(1) Shear velocity has a positive linear relationship with compressional velocity in the Eagle Ford and adjacent formations. Two relationships including V_s = 0.498 V_p + 250.85 and V_s = 0.518 V_p + 240.56 were developed for two wells with R^2 value of 0.96. Correlations of shear velocity and compressional velocity in marl and interbedded limestone layers of Eagle Ford Formation were obtained.
(2) There are power law or negative linear relationships between compressional velocity, shear velocity, dynamic Young's modulus and gamma ray intensity in the Eagle Ford well in Dewitt County and La Salle County. No correlation between Poisson's ratio and gamma ray or clay content exists.
(3) Comparison of elastic properties shows that there are more variations in dynamic Young's modulus, less variations in compressional and shear velocities and no obvious difference in dynamic Poisson's ratio.
(4) The effect of Young's modulus ratio on the aspect ratio of confined fractures is remarkable when the ratio of fracture spacing to layer thickness is low, while the influence of elastic properties contrast of shale layers on the aspect ratio of the unconfined fracture can be negligible in the Eagle Ford wells in Dewitt County and La Salle County.

Data availability statement

The original contributions presented in the study are included in the article/supplementary material, further inquiries can be directed to the corresponding author.

Author contributions

SJ: investigation, data analysis, writing—original draft, MM: methodology, supervision, JS: software, validation.

Conflict of interest

The authors declare that the research was conducted in the absence of any commercial or financial relationships that could be construed as a potential conflict of interest.

Publisher's note

References

Altowairqi, Y., Rezaee, R., Evans, B., and Urosevic, M. (2015). Shale elastic property relationships as a function of total organic carbon content using synthetic samples. *J. Petroleum Sci. Eng.* 133, 392–400. doi:10.1016/j.petrol.2015.06.028

Breyer, J. A., Denne, R. A., Kosanke, T., and Spaw, J. M. (2016)., 110. Texas, U.S.A, 369–389.Facies, fractures, pressure, and production in the Eagle Ford shale (cretaceous) between the san Marcos arch and the maverick basin. *AAPG Mem.*

Castagna, J. P., Batzle, M. L., and Eastwood, R. L. (1985). Relationships between compressional-wave and shear-wave velocities in clastic silicate rocks. *Geophysics* 50 (4), 571–581. doi:10.1190/1.1441933

Castagna, J. P., Batzle, M. L., and Kan, T. K. (1993). Rock physics – the link between rock properties and AVO response. *Investigations Geophys.* 8, 135–171.

Donovan, A. D., Gardner, R. D., and Pramudito, A. (2015). Chronostratigraphic relationships of the woodbine and Eagle Ford groups across Texas. *Gulf Coast Assoc. Geol. Soc. Trans.* 4, 67–87.

Greenberg, M. L., and Castagna, J. P. (1992). Shear-wave velocity estimation in porous rocks: Theoretical formulation, preliminary verification and applications. *Geophys. Prospect.* 40 (2), 195–209. doi:10.1111/j.1365-2478.1992.tb00371.x

Han, D., Nur, A., and Morgan, D. (1986). Effects of porosity and clay content on wave velocities in sandstones. *Geophysics* 51 (11), 2093–2107. doi:10.1190/1.1442062

Hossain, Z., Mukerji, T., and Fabricius, I. L. (2012). Vp-Vs relationship and amplitude variation with offset modelling of glauconitic greensand. *Geophys. Prospect.* 60, 117–137. doi:10.1111/j.1365-2478.2011.00968.x

Hsu, S., and Nelson, P. (2002). Characterization of Eagle Ford shale. *Eng. Geol.* 67 (1–2), 169–183. doi:10.1016/s0013-7952(02)00151-5

Jiang, S., and Mokhtari, M. (2019). Characterization of marl and interbedded limestone layers in the Eagle Ford Formation, DeWitt county, Texas. *J. Petroleum Sci. Eng.* 172, 502–510. doi:10.1016/j.petrol.2018.09.094

Kiipli, T., Soesoo, A., Kallaste, T., and Kiipli, E. (2008). Geochemistry of telichian (silurian) K-bentonites in Estonia and Latvia. *J. Volcanol. Geotherm. Res.* 171 (1), 45–58. doi:10.1016/j.jvolgeores.2007.11.005

Kim, J. (2021). New geomechanical application utilizing MWD gamma ray logs: An Eagle Ford case study. *J. Petroleum Sci. Eng.* 196, 108043–108113. doi:10.1016/j.petrol.2020.108043

Mokhtari, M., Honarpour, M. M., Tutuncu, A. N., and Boitnott, G. N. (2016). Characterization of elastic anisotropy in Eagle Ford shale: Impact of heterogeneity and measurement scale. *SPE Reserv. Eval. Eng.* 19 (3), 429–439. doi:10.2118/170707-PA

Pickett, G. R. (1963). Acoustic character logs and their applications in formation evaluation. *J. Petroleum Technol.* 15 (6), 659–667. doi:10.2118/452-PA

Rafavich, E., Kendall, C. H., and Todd, T. P. (1984). The relationship between acoustic properties and the petrographic character of carbonate rocks. *Explor. Geophys.* 15 (3), 193. doi:10.1071/eg984193

Vernik, L., Fisher, D., and Bahret, S. (2002). Estimation of net-to-gross from P and S impedance in deepwater turbidites. *Lead. Edge* 21 (4), 380–387. doi:10.1190/1.1471602

Xu, S., and White, R. E. (1995). A new velocity model for clay-sand mixtures. *Geophys. Prospect.* 43 (1), 91–118. doi:10.1111/j.1365-2478.1995.tb00126.x

Xu, S., and White, R. E. (1996). A physical model for shear-wave velocity prediction. *Geophys. Prospect.* 44 (4), 687–717. doi:10.1111/j.1365-2478.1996.tb00170.x

Yang, S., Wu, K., Xu, J., Li, J., and Chen, Z. (2019). Roles of multicomponent adsorption and geomechanics in the development of an Eagle Ford shale condensate reservoir. *Fuel* 242, 710–718. doi:10.1016/j.fuel.2019.01.016

Zumberge, J., Illich, H., and Waite, L. (2016). Petroleum geochemistry of the cenomanian–turonian Eagle Ford oils of south Texas. *AAPG Mem.* 110, 135–165.

frontiers | Frontiers in Earth Science

TYPE Original Research
PUBLISHED 12 January 2023
DOI 10.3389/feart.2022.1065630

OPEN ACCESS

EDITED BY
Qiaomu Qi,
Chengdu University of Technology, China

REVIEWED BY
Jiajia Gao,
Southwest Petroleum University, China
Sheng-Qing Li,
China University of Petroleum, China

*CORRESPONDENCE
Jing Ba,
jingba@188.com

SPECIALTY SECTION
This article was submitted to Solid Earth Geophysics, a section of the journal Frontiers in Earth Science

RECEIVED 10 October 2022
ACCEPTED 08 November 2022
PUBLISHED 12 January 2023

CITATION
Ba J, Pan X, Carcione JM and Ma R (2023), Effects of pressure and fluid properties on P-wave velocity and attenuation of tight sandstones. *Front. Earth Sci.* 10:1065630. doi: 10.3389/feart.2022.1065630

Effects of pressure and fluid properties on P-wave velocity and attenuation of tight sandstones

Jing Ba[1]*, Xuming Pan[1], José M. Carcione[1,2] and Rupeng Ma[1]

[1]School of Earth Sciences and Engineering, Hohai University, Nanjing, China, [2]National Institute of Oceanography and Applied Geophysics (OGS), Trieste, Italy

Tight reservoirs are distributed in several basins in China, with great exploration prospects and high production potential. These reservoirs have low porosity and permeability and a significant spatial heterogeneity, and this complexity requires new developments on the experimental and theoretical researches of wave propagation. To this purpose, we have conducted ultrasonic experiments on seven tight sandstones collected from the shale-oil strata as a function of the confining pressure. We obtained the P-wave velocity and attenuation by using the spectral-ratio method. The results show that attenuation decreases with pressure, and increases with porosity and permeability and that oil saturation causes more losses compared to water and gas saturations. Moreover, we observe a relaxation peak at 40% water saturation in the gas-water case. Then, we develop a tight-rock model combining three theories [Voigt-Reuss-Hill (VRH), Differential Effective Medium (DEM) and double double-porosity (DDP)], where inclusions are assumed to represent cracks or grain contacts, with different porosity and compressibility as the host. The model reasonably predicts P-wave velocity dispersion and attenuation, which increase with water saturation, and the related relaxation frequency moves to low frequencies.

KEYWORDS

tight sandstones, P-wave velocity and attenuation, confining pressure, fluid saturation, double double-porosity model

1 Introduction

The development of tight reservoirs is of significance to increase crude-oil production and optimize energy supply. These reservoirs have low porosity and permeability and a high heterogeneity (Zou et al., 2013), which make it difficult for exploration and production activities. Previous studies showed that the clay particle arrangement, layering, cracks, and low-aspect-ratio pores cause the heterogeneity of these reservoirs, which together with the stress conditions, highly affect the seismic waves (Zhubayev et al., 2016). In this context, wave-induced local fluid flow associated with the pore fluid is an important cause of dissipation (Ba et al., 2015).

Many experimental studies have analyzed the effects of confining and pressures, fluid properties and saturation on attenuation (Biot, 1962; Born, 1941; Dvorkin et al., 1994, 1995; Toksöz, et al., 1979; Johnston et al., 1979, 1986; Mavko and Mukerji, 1998; Li et al., 2018; Ma et al., 2019; Ma and Ba, 2020; White et al., 1975; Johnston et al., 1979; Winkler, 1985; Sams et al., 1997; Pimienta et al., 2015; Pimienta et al., 2016; Chapman et al., 2016, 2017). In particular, the P-wave velocity of tight sandstones is more affected than that of normal sandstones (Tutuncu et al., 1994). Waves induce wave-induced local fluid flow (WIFF) through a heterogeneity rock, generating a fluid pressure gradient between regions with different compressibilities and consistent P-wave energy dissipation (Pride et al., 2004; Ba et al., 2016). Permeability, porosity, fluid viscosity, saturation and frame heterogeneity play an important role in this process (Zhao et al., 2017). For instance, the shear modulus of a rock saturated with brine is less than that of a dry rock (Sharma et al., 2013), and attenuation of water-saturated rocks is stronger than that of dry rocks at the ultrasonic frequency band (Johnston and Toksoz, 1980). Wei et al. (2021) showed that in high clay-content rocks, water replacing gas enhances the P-wave dissipation.

White et al. (1975) considered fine layers with different fluids to analyze the mesoscopic WIFF process (Carcione, 2022). Dvorkin and Nur. (1993) presented a macro/microscopic Biot/squirt (BISQ) model for wave velocity and attenuation at sonic/ultrasonic frequencies. Ba et al. (2011) combined Biot poroelasticity and the Rayleigh theory for the expansion-contraction oscillation of a spherical fluid pocket to develop a double-porosity WIFF-type model. Zhang et al. (2017) extended this model to triple porosity. Cheng et al. (2020) extended the cracks and pores effective medium (CPEM) model to all frequencies, based on the Zener mechanical model, analyzing the effect of pressure on the P wave. Ren et al. (2020) combined the theories of microscopic squirt flow and mesoscopic patchy-saturation. Ba et al. (2017) presented a double double-porosity (DDP) model, which considers two types of heterogeneities and patchy saturation. This model was applied to tight rocks containing sub-pore heterogeneities and saturated with immiscible fluids, and used by Guo et al. (2018) for tight sandstones. The model predictions for fully- and partially-saturated rocks are in good agreement with the experiments.

In this work, we show P-wave ultrasonic measurements on the tight rock samples at different pressures and fluid saturations and analyze their effect on velocity attenuation. Then, we

TABLE 1 Properties of the seven samples of the Yanchang formations.

Sample	Porosity (%)	Permeability (mD)	Dry-rock density (g/cm^3)	Clay content (%)
1–19	5.065	0.018	2.44	5.59
1–12	7.220	0.020	2.49	5.87
1–23	8.998	0.078	2.41	4.61
2–7	9.000	0.036	2.42	3.46
1–3	9.201	0.038	2.44	7.12
2–9	9.222	0.066	2.41	5.35
2–8	10.165	0.096	2.37	6.07

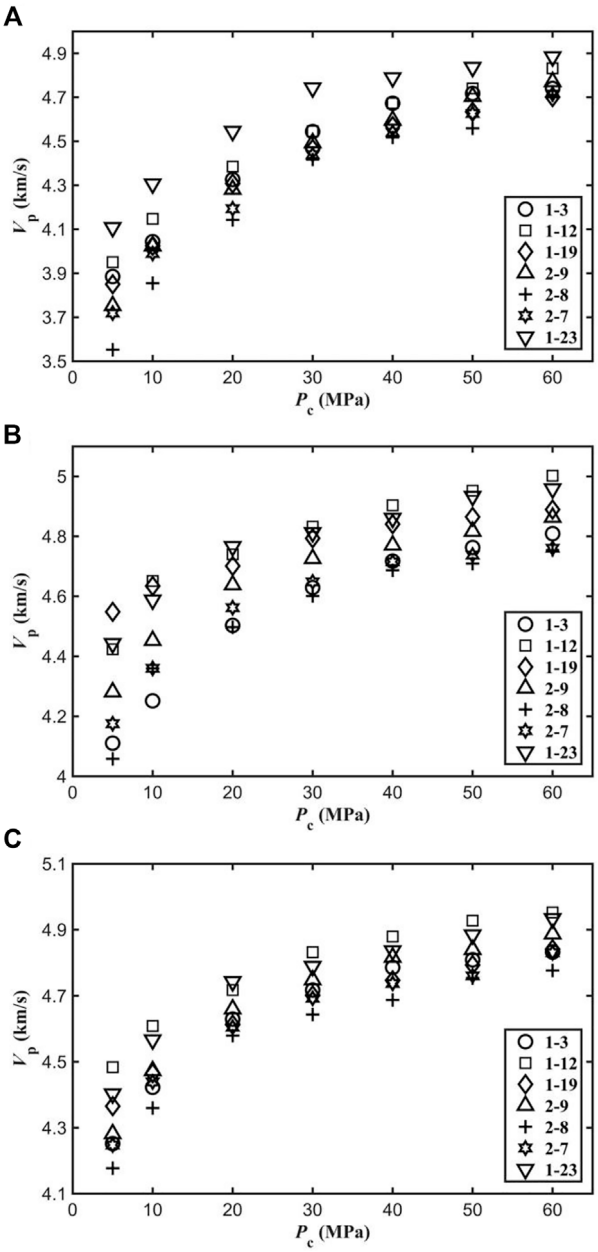

FIGURE 1
P-wave velocity as a function of confining pressure for the seven samples at gas- **(A)**, water- **(B)** and oil- **(C)** saturation conditions.

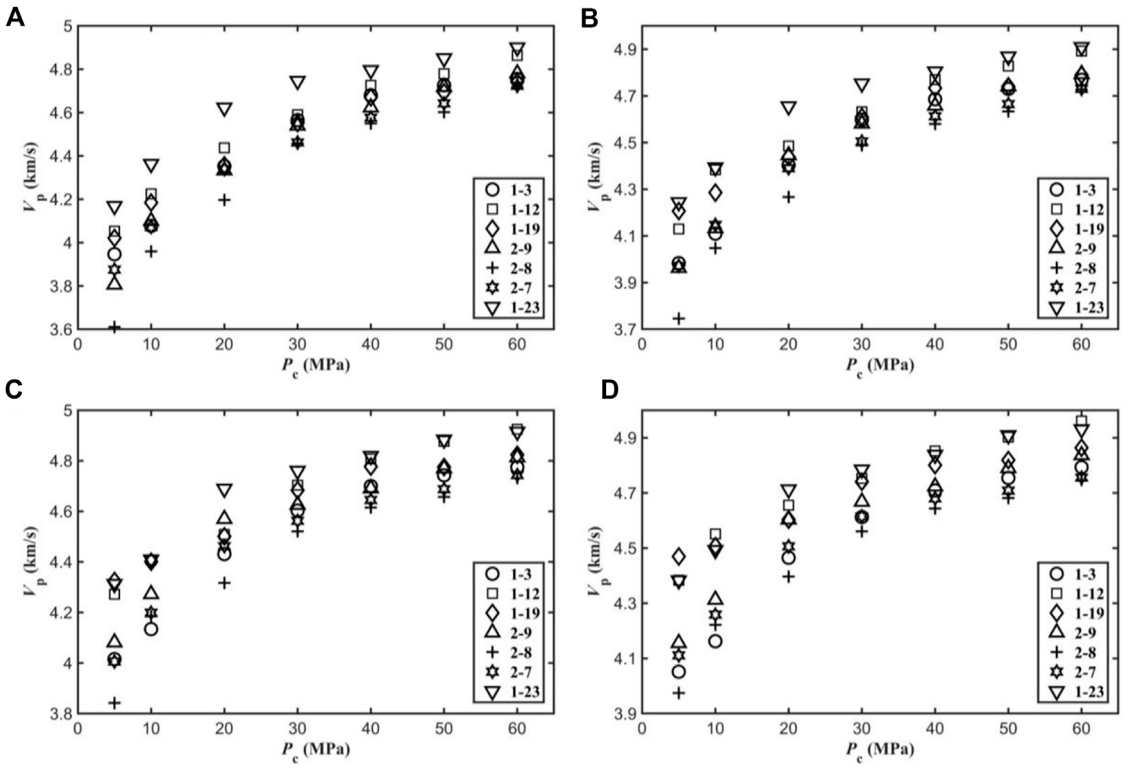

FIGURE 2
P-wave velocity as a function of confining pressure for the seven samples at water saturations of 20 **(A)**, 40 **(B)**, 60 **(C)** and 80% **(D)** (gas-water case).

combined the VRH, DEM and DDP theories to establish a predictive theoretical model that takes into account the effects of pressure, frame properties (porosity and permeability) and fluid properties and distribution on the P-wave behavior. In this work we consider the two types of heterogeneities of fabric structure and patchy saturation, and the prediction results of P-wave responses as a function of porosity, saturation and confining pressure are obtained with respect to the properties of microcrack and gas pocket.

2 Experiments

2.1 Tight-rock samples

Tight reservoirs of Member 7 of the Yanchang formations in the Ordos Basin are dominated by lacustrine deposits. The topography it is high in the east basin and low in the west, with complex tectonic histories and a wide distribution of high-quality source rocks. There are ten members in the Yanchang formations, of which member 7 reached its peak in the depositional period of the lake basin and developed a great amount of high-quality source rocks. Member 7 of Yanchang formations is buried at a depth of about 1,200–2,350 m. The reservoir lithology is mainly tight sandstone intercalated with mudstone/shale, and shale intercalated with thin silt/fine sandstone. Micro-nanoscale pore throats are developed, and the pore structure is conducive to the accumulation of hydrocarbons.

Seven tight-sandstone samples are collected from the target formation at the depth range of 1,800–2,150 m for X-ray diffraction tests. The mineral compositions are mainly quartz, feldspar, carbonate minerals, clay minerals and a small amount of siderite. The quartz content is relatively high, ranging between 48.59% and 56.81%, and the feldspars are mainly potassium feldspar and plagioclase, with the plagioclase content generally higher than that of potassium feldspar. The carbonate minerals are calcite and dolomite, with a small amount of ankerite, and the clay minerals are zeolite and chlorite. The automated permeameter of Core Measurement System is used to measure porosity and permeability. The porosity is measured by the gas-expansion method, and the dry-rock density is obtained from the ratio of rock mass to total volume. The properties of seven samples are given in Table 1.

2.2 Experimental set-up

We cut the rock samples into cylinders with a diameter of 25.08–25.14 mm and a length of 48.89–50.09 mm, and an aluminum standard is prepared with the same shape of

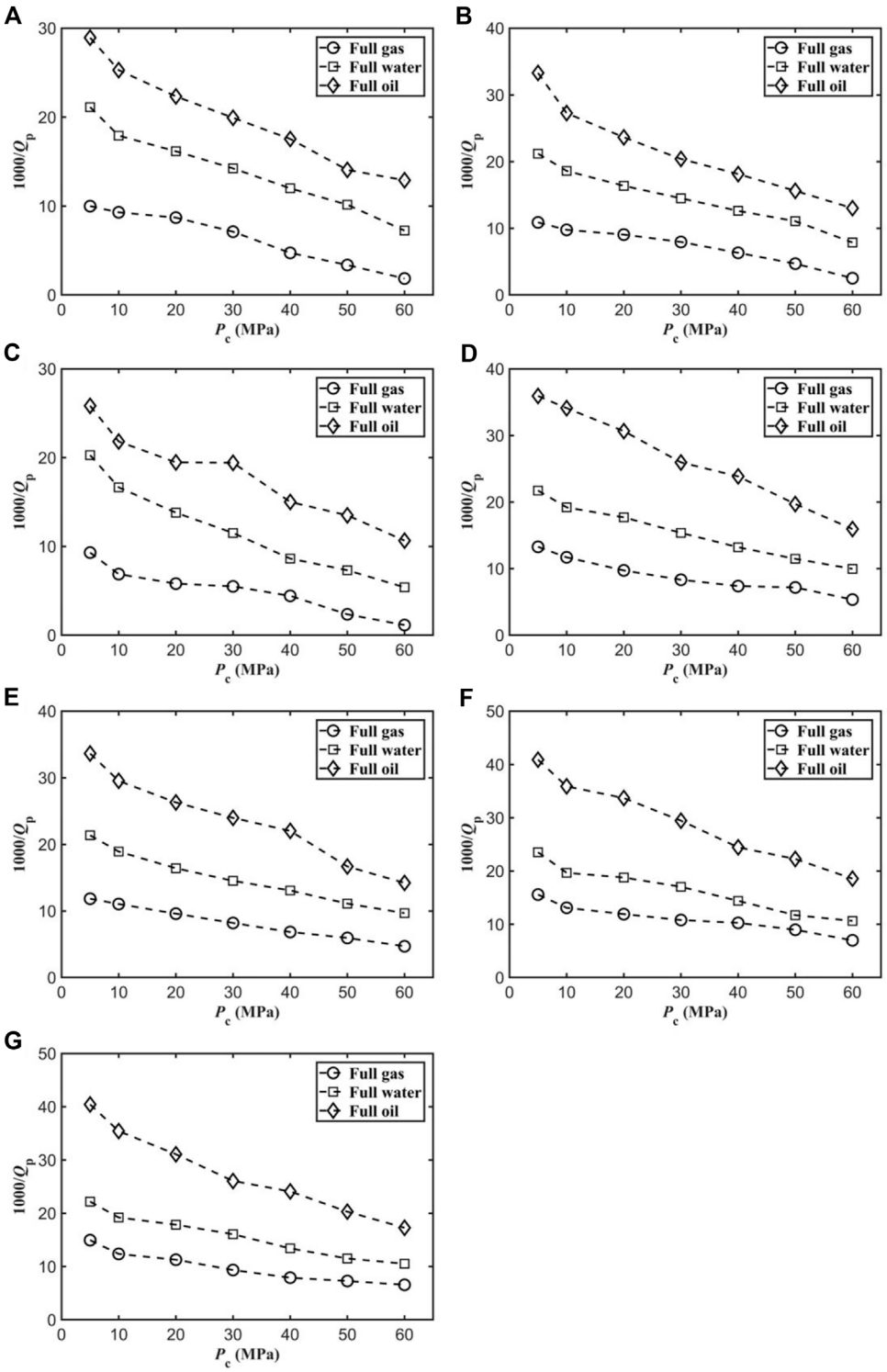

FIGURE 3
P-wave attenuation of samples 1–3 **(A)**, 1–12 **(B)**, 1–19 **(C)**, 1–23 **(D)**, 2–7 **(E)**, 2–8 **(F)** and 2–9 **(G)** as a function of confining pressure.

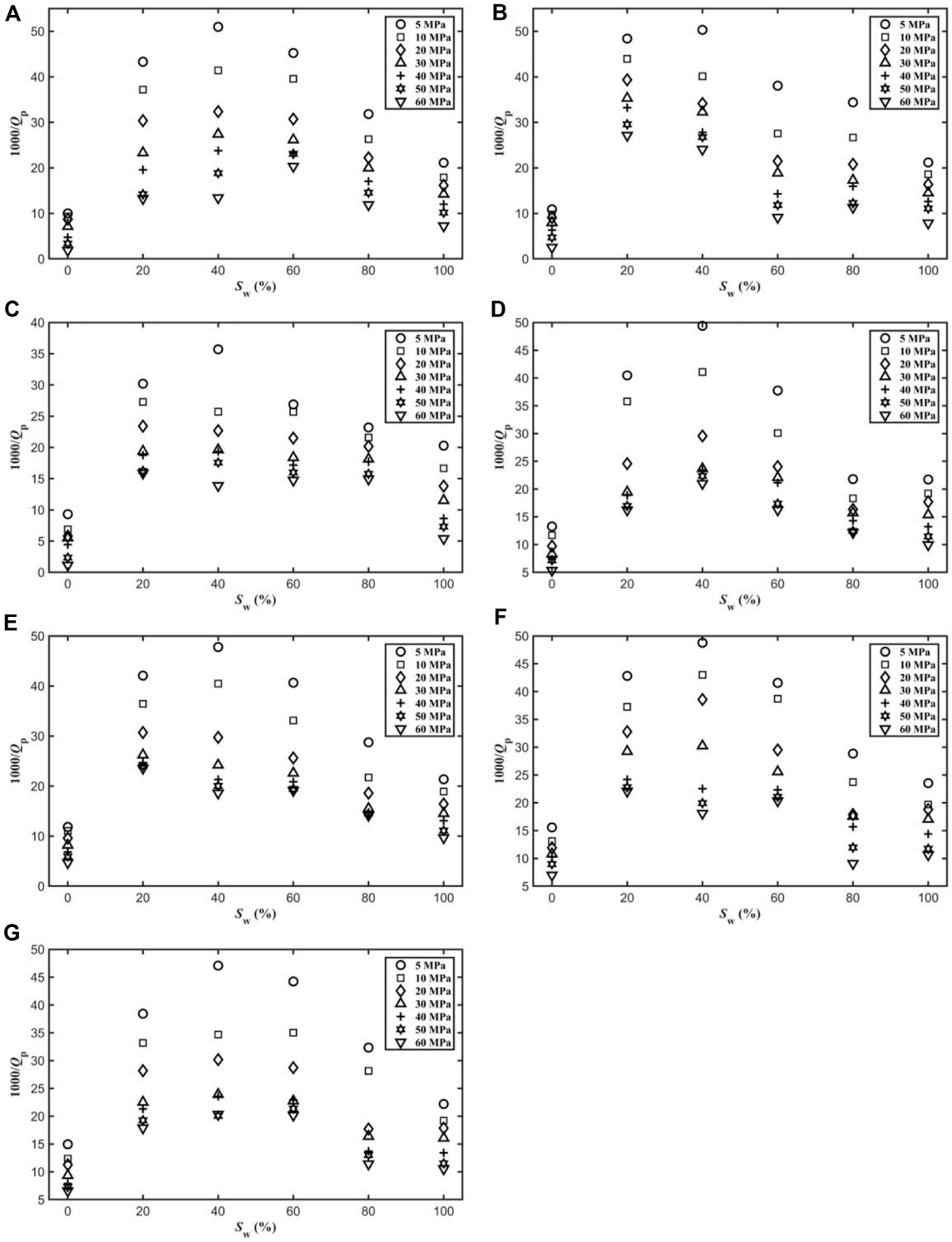

FIGURE 4
P-wave attenuation as a function of water saturation for samples of 1–3 **(A)**, 1–12 **(B)**, 1–19 **(C)**, 1–23 **(D)**, 2–7**(E)**, 2–8 **(F)** and 2–9 **(G)**, and different confining pressures.

each sample for reference. The same experimental setup as in Guo et al. (2009) is used for the ultrasonic measurements. The frequency of the generated pulse is about 0.55 MHz, and the gas (nitrogen)-saturated, water-saturated, oil (kerosene)-saturated and partially-saturated samples are measured under the different confining pressures.

2.2.1 Gas-saturation tests

The samples are first dried, then sealed with rubber sleeves and placed in the device. At the confining pressures of 5 and 10 MPa, the pore pressure is increased by 5 MPa by injecting nitrogen. On the other hand, the confining pressure is set to 20, 30, 40, 50, and 60 MPa, and the pore pressure kept to 15 MPa. The temperature in all the tests is 30°C. Then, we record the P-wave waveforms for each case.

2.2.2 Water- and oil-saturation tests

The samples are saturated by the vacuuming and pressurization method, and the procedure is the same as that of the previous test.

2.2.3 Partially-saturation test with gas and water

The samples are heated in an oven to change the water saturation, which is controlled by weighing. The sample is then sealed, and placed in a container. Nitrogen gas is injected to control the pore pressure.

2.3 P-wave attenuation estimation

The spectral ratio method (Guo et al., 2009; Ba et al., 2018; Gao et al., 2019) is applied to estimate the P-wave attenuation (inverse quality factor $1/Q$). If the sub-indices 1 and 2 denote the rock and aluminum, the plane wave amplitudes can be expressed as

$$A_1(f) = G_1(x)\mathrm{e}^{-\alpha_1(f)x}\mathrm{e}^{-i(2\pi ft-k_1x)} \tag{1a}$$

$$A_2(f) = G_2(x)\mathrm{e}^{-\alpha_2(f)x}\mathrm{e}^{-i(2\pi ft-k_2x)} \tag{1b}$$

$$\alpha_1 = \frac{\pi f}{Q_1V_1} \tag{1c}$$

$$\alpha_2 = \frac{\pi f}{Q_2V_2} \tag{1d}$$

where f is the frequency, $A_1(f)$ and $A_2(f)$ are the P-wave spectra, x is the propagation distance, t is time of propagation, $\alpha_1(f)$ and $\alpha_2(f)$ are frequency-dependent attenuation coefficients, and $G_1(x)$ and $G_2(x)$ are geometrical factors. k_1 and k_2 are the wavenumbers, Q_1 and Q_2 are the quality factors, and V_1 and V_2 are the P-wave velocities.

Then, the P-wave attenuation is computed with

$$\ln\left(\frac{A_1(f)}{A_2(f)}\right) = \left(\frac{\pi x}{Q_2V_2} - \frac{\pi x}{Q_1V_1}\right)f + \ln\frac{G_1(x)}{G_2(x)} \tag{1e}$$

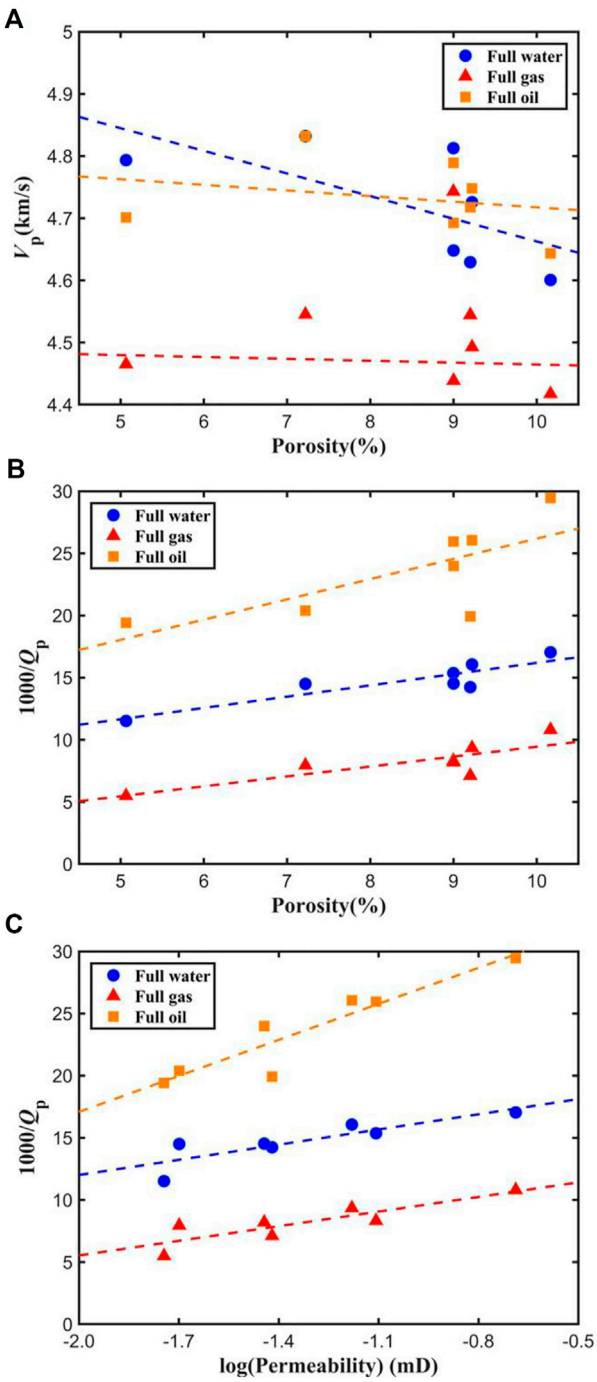

FIGURE 5
P-wave velocity versus porosity **(A)** and P-wave dissipation factor as a function of porosity **(B)** and permeability **(C)** at a confining pressure of 30 MPa and different full saturations.

Since the quality factor of aluminum is much higher than rocks, we assume

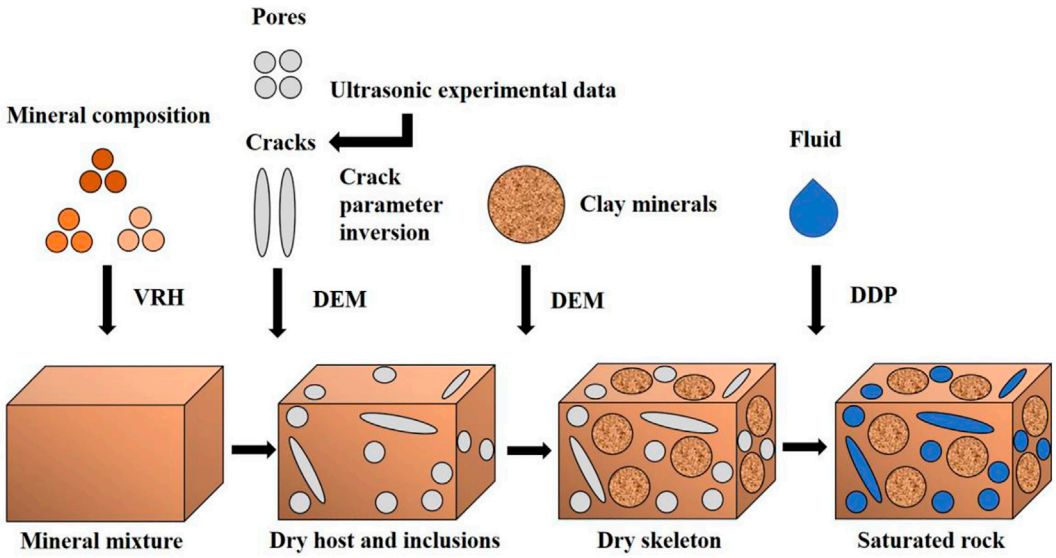

FIGURE 6
Modeling workflow to obtain wave velocity and attenuation.

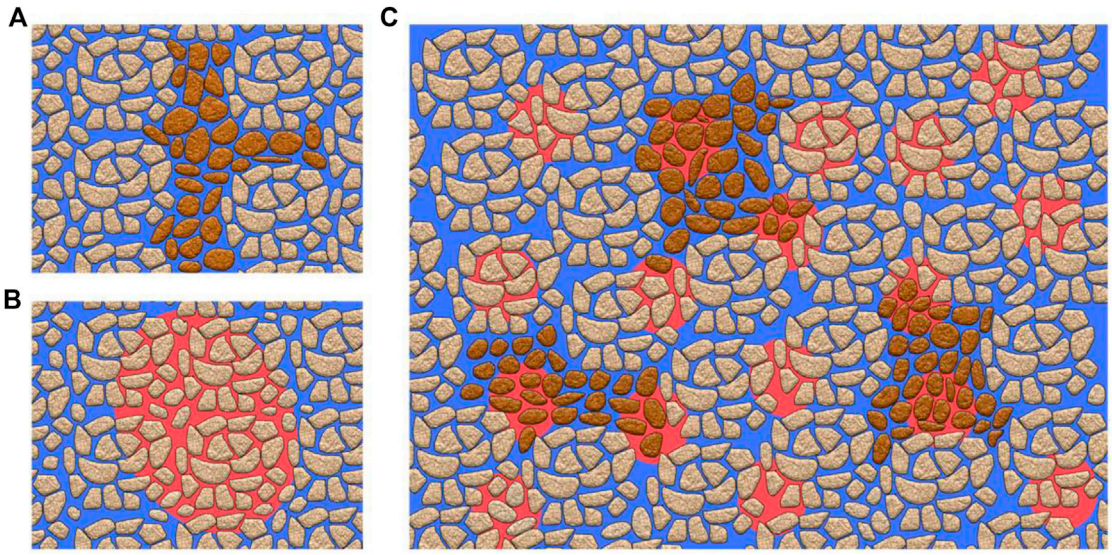

FIGURE 7
Double-porosity solid structure saturated with a single fluid **(A)**, patchy saturation with two immiscible fluid phases within a single-porosity solid **(B)** and combination of the two types of heterogeneity **(C)**. The blue and red zones represent the two immiscible fluids.

TABLE 2 Modeling parameters of sample 1–19.

Porosity (%)	ϕ_{20} (%)	Volume ratio of inclusions (%)	κ_1 (mD)	κ_2 (mD)
5.065	9	6	0.018	0.1

TABLE 3 Fluid properties.

Fluid	Density (g/cm^3)	Bulk modulus (GPa)	Viscosity (cP)
Gas (Nitrogen)	0.138	0.0291	0.0196
Water	1.004	2.273	0.981
Oil (Kerosene)	0.762	1.361	8

$$\ln\left(\frac{A_1(f)}{A_2(f)}\right) = -\frac{\pi x}{Q_1 V_1} f + \ln\frac{G_1(x)}{G_2(x)} \tag{1f}$$

and Q_1 can be obtained.

Due to the error caused by the choice of pulse window and frequency band (Zhubayev et al., 2016), we compute it by using the slope change of spectrum ratio at the fitting band,

$$\pm d\left(Q_1^{-1}\right) = \pm\frac{V_P}{\pi} d\frac{\pi}{Q_1 V_1} \pm \frac{1}{Q_1 V_1} dV_P \tag{1g}$$

where $d\frac{\pi}{Q_1 V_1}$ and dV_P are the errors of spectrum comparison curve slope estimation and P-wave velocity measurement, respectively. V_P is P-wave velocity.

3 Experimental results

Figure 1 shows the P-wave velocity with confining pressure for the seven samples at full gas, water and oil saturations, and Figure 2 shows the results at water saturations of 20%, 40%, 60%, and 80% (gas-water case). The velocity increases with confining pressure when the soft pores/cracks gradually tend to close, resulting in the increase of the dry-rock bulk shear moduli.

On the other hand, Figure 3 shows the P-wave dissipation factor as a function of confining pressure at different fluid saturations. In general, attenuation decreases with confining pressure, because as this increases, cracks tend to close, precluding local fluid flow between these cracks and intergranular pores (squirt flow). At the same pressure, the attenuation at water- and oil-saturation conditions is higher than that at gas saturation. This can be due to the viscous motion of the fluid and the variation of the contact surface energy between solid and liquid caused by the wave (Wang et al., 2006).

Figure 4 shows the P-wave dissipation factor as a function of water saturation (gas-water case) and different confining pressures. Generally, there is a maximum at 40% saturation, possibly related to the fluid distribution in the pores.

Figure 5 shows the P-wave velocity as a function of porosity (a) and the dissipation factor as a function of porosity (b) and permeability (c) for a confining pressure of 30 MPa. As expected, the velocities decrease with porosity, and attenuation increases. Indeed, with increasing porosity, the frame moduli decrease and the presence of more cracks results in higher local fluid flow and dissipation.

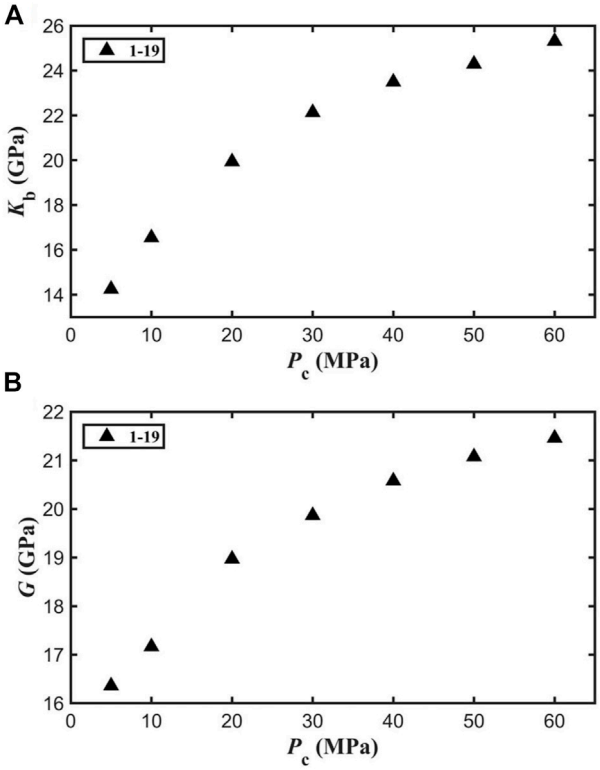

FIGURE 8
Estimated bulk **(A)** and shear **(B)** moduli of the dry rocks for sample 1–19.

4 Theory

4.1 Basic theory and modeling

The heterogeneity of the frame and the patchy saturation of the immiscible fluid mixture lead to the WIFF and P-wave dispersion and dissipation. The modeling workflow is shown in Figure 6. The mineral composition and crack porosity are obtained from the ultrasonic data and an inversion process (Zhang et al., 2019) and the fluid substitution is then performed with the DDP theory.

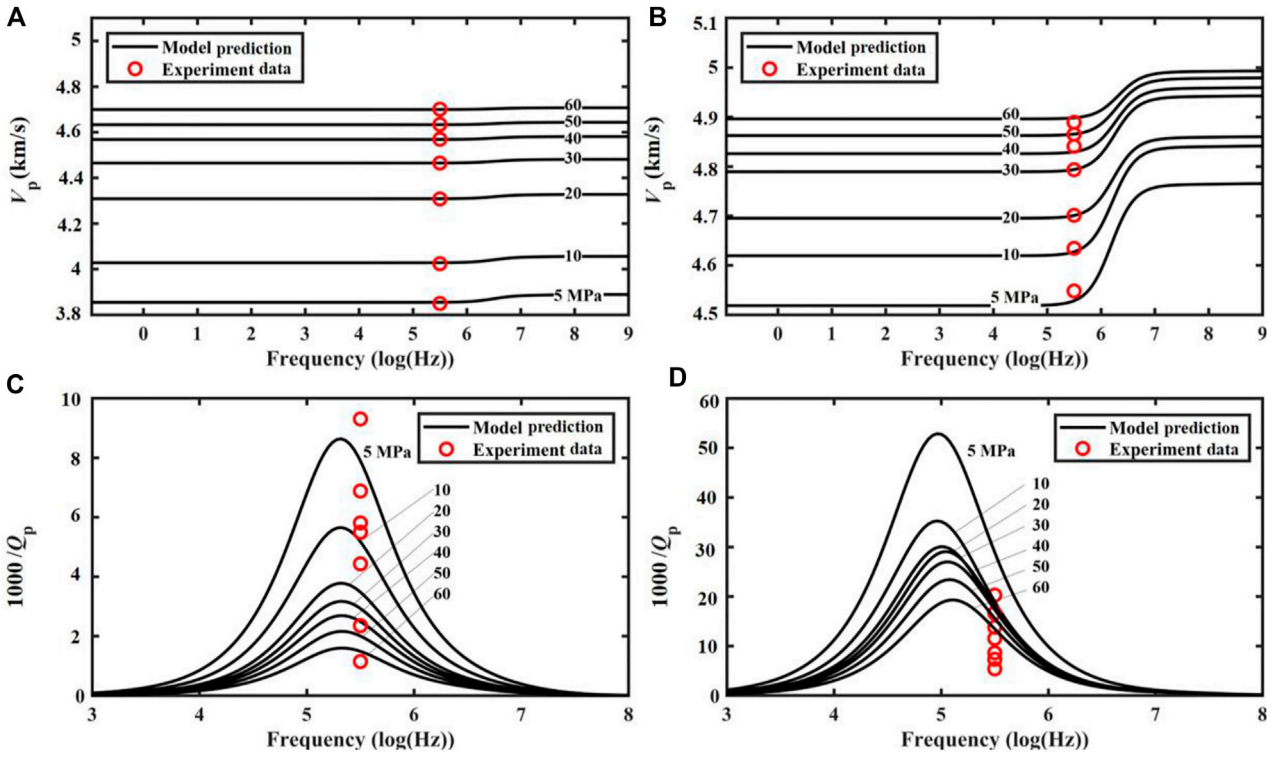

FIGURE 9
P-wave velocity frequency dependency for the gas- **(A)** and water- **(B)** saturated sample 1–19 at different confining pressures. The P-wave dissipation factors are shown in panels **(C,D)**, respectively, for gas and water. The experimental data are shown as red circles.

The mineral composition and pore structure of the samples are analyzed with X-ray diffraction and scanning electron microscopy tests. The mineral components are mainly quartz, feldspar, carbonate minerals and clay. Clay minerals are present within the host matrix, together with pores and cracks, constituting the skeleton of tight reservoirs (Deng et al., 2018). The mineral components except for clay minerals are considered as the mineral mixture, and the elastic moduli are computed with the VRH equation (Hill, 1952; Reuss, 1929). The crack properties are obtained from the ultrasonic measurements at different confining pressures and the frame moduli are computed with the DEM theory, by which clay minerals, pores (with an aspect ratio of 0.5) and cracks are added into the mineral mixture.

The DDP theory by Ba et al. (2015) considers two types of heterogeneities, i.e., the two porous components for the solid skeleton with different compressibilities (Figure 7A), and patchy-saturation of two immiscible fluids within the pores (Figure 7B), leading to WIFF and anelasticity. Figure 7C shows the combination of the two heterogeneities, where it is assumed that porous spherical inclusions are uniformly embedded in a porous host, and patch saturation occurs in both regions, the host and the inclusion skeletons.

It has been considered that the P-wave responses can be affected by the capillary pressure variations in rocks saturated with multi-phase fluids. At the high-frequency range, the P-wave velocity is shown to increase as capillary pressure increases, while the P-wave attenuation decreases (Shukla et al., 2019). In this work, two types of heterogeneities are incorporated in modeling, and due to the complexity of wave governing equations, the influence of capillary pressure is not considered yet, which can be analyzed in a future study. In the partial-saturation case, due to the hydrophilicity of the mineral surface and capillary tension, the flat contact between grains or within cracks is considered to be fully saturated with water, while the gas pockets are mainly distributed within the intergranular pores (Li et al., 2001).

Ba et al. (2017) DDP differential equations are

$$N\nabla^2\boldsymbol{u} + (A+N)\nabla e + Q_1\nabla\left(\xi_1 + \phi_{f2}\zeta_{12} + \phi_{f3}\zeta_{13}\right) + Q_2\nabla\left(\xi_2 - \phi_{f1}\zeta_{12} + \phi_{f4}\zeta_{24}\right) + Q_3\nabla\left(\xi_3 - \phi_{f1}\zeta_{13}\right) + Q_4\nabla\left(\xi_4 - \phi_{f2}\zeta_{24}\right) = \rho_{00}\ddot{\boldsymbol{u}} + \rho_{01}\ddot{\boldsymbol{U}}^{(1)} + \rho_{02}\ddot{\boldsymbol{U}}^{(2)} + \rho_{03}\ddot{\boldsymbol{U}}^{(3)} + \rho_{04}\ddot{\boldsymbol{U}}^{(4)} + b_1\left(\dot{\boldsymbol{u}} - \dot{\boldsymbol{U}}^{(1)}\right) + b_2\left(\dot{\boldsymbol{u}} - \dot{\boldsymbol{U}}^{(2)}\right) + b_3\left(\dot{\boldsymbol{u}} - \dot{\boldsymbol{U}}^{(3)}\right) + b_4\left(\dot{\boldsymbol{u}} - \dot{\boldsymbol{U}}^{(4)}\right) \tag{2a}$$

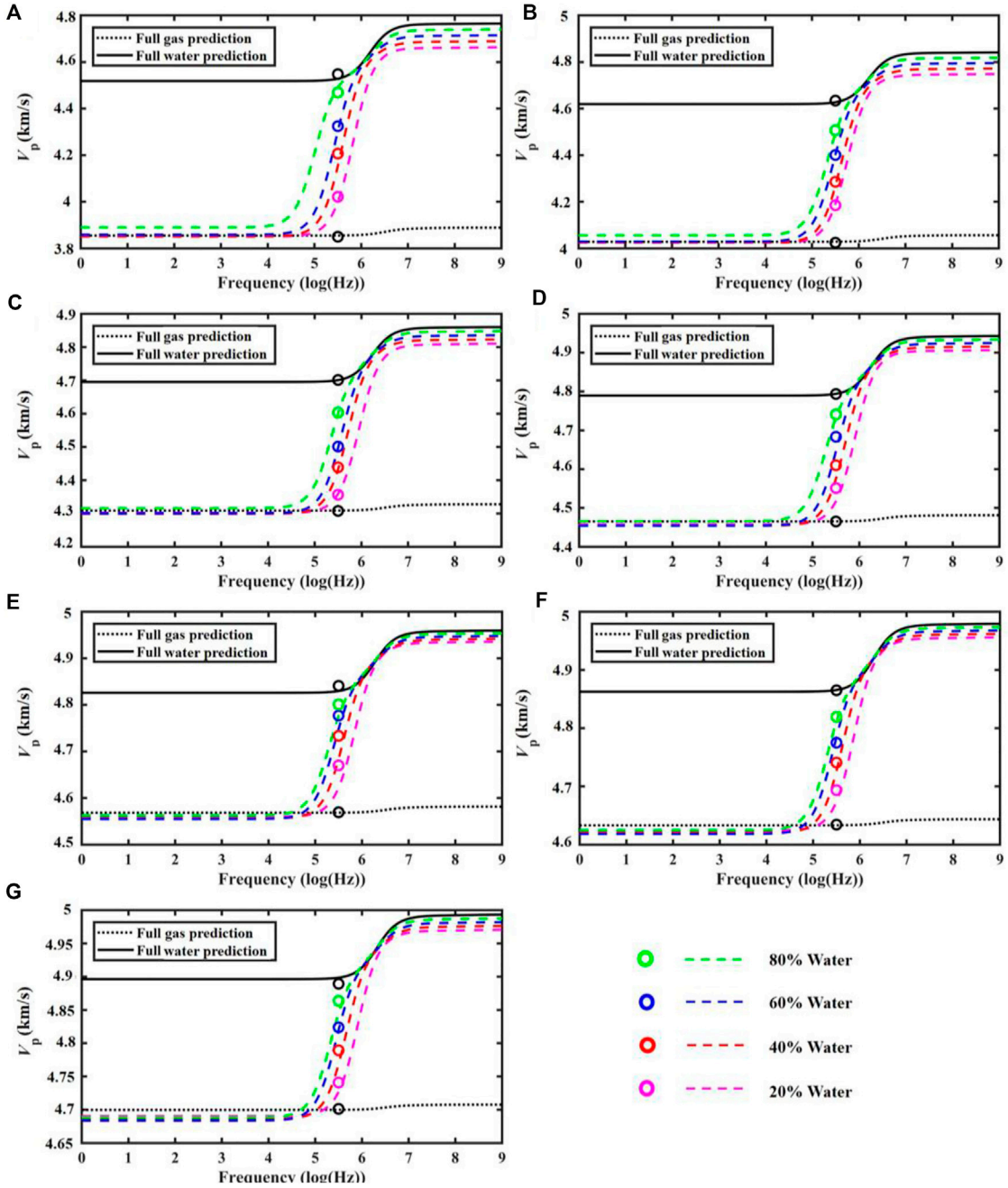

FIGURE 10
P-wave velocity frequency dependence for sample 1–19 at 5 MPa **(A)**, 10 MPa **(B)**, 20 MPa **(C)**, 30 MPa **(D)**, 40 MPa **(E)**, 50 MPa **(F)** and 60 MPa **(G)**. The experimental data are shown as circles.

$$Q_1\nabla e + R_1\nabla\left(\xi_1 + \phi_{f2}\zeta_{12} + \phi_{f3}\zeta_{13}\right) = \rho_{01}\ddot{\boldsymbol{u}} + \rho_{11}\ddot{\boldsymbol{U}}^{(1)} - b_1\left(\dot{\boldsymbol{u}} - \dot{\boldsymbol{U}}^{(1)}\right) \quad (2b)$$

$$Q_2\nabla e + R_2\nabla\left(\xi_2 - \phi_{f1}\zeta_{12} + \phi_{f4}\zeta_{24}\right) = \rho_{02}\ddot{\boldsymbol{u}} + \rho_{22}\ddot{\boldsymbol{U}}^{(2)} - b_2\left(\dot{\boldsymbol{u}} - \dot{\boldsymbol{U}}^{(2)}\right) \quad (2c)$$

$$Q_3\nabla e + R_3\nabla\left(\xi_3 - \phi_{f1}\zeta_{13}\right) = \rho_{03}\ddot{\boldsymbol{u}} + \rho_{33}\ddot{\boldsymbol{U}}^{(3)} - b_3\left(\dot{\boldsymbol{u}} - \dot{\boldsymbol{U}}^{(3)}\right) \quad (2d)$$

$$Q_4\nabla e + R_4\nabla\left(\xi_4 - \phi_{f2}\zeta_{24}\right) = \rho_{04}\ddot{\boldsymbol{u}} + \rho_{44}\ddot{\boldsymbol{U}}^{(4)} - b_4\left(\dot{\boldsymbol{u}} - \dot{\boldsymbol{U}}^{(4)}\right) \quad (2e)$$

$$\phi_{f2}\left(Q_1 e + R_1\left(\xi_1 + \phi_{f2}\zeta_{12} + \phi_{f3}\zeta_{13}\right)\right) - \phi_{f1}\left(Q_2 e + R_2\left(\xi_2 - \phi_{f1}\zeta_{12} + \phi_{f4}\zeta_{24}\right)\right) = \frac{1}{3}\rho_f{}^{(1)}\ddot{\zeta}_{12}R_{12}^2\frac{\phi_{f1}^2\phi_{f2}^2\phi_{20}}{\phi_{10}\left(\phi_{f2}+\phi_{f4}\right)} + \frac{1}{3}\dot{\zeta}_{12}R_{12}^2\frac{\eta_f^{(1)}\phi_{f1}^2\phi_{f2}^2\phi_{20}}{\kappa_1\left(\phi_{f2}+\phi_{f4}\right)} \quad (2f)$$

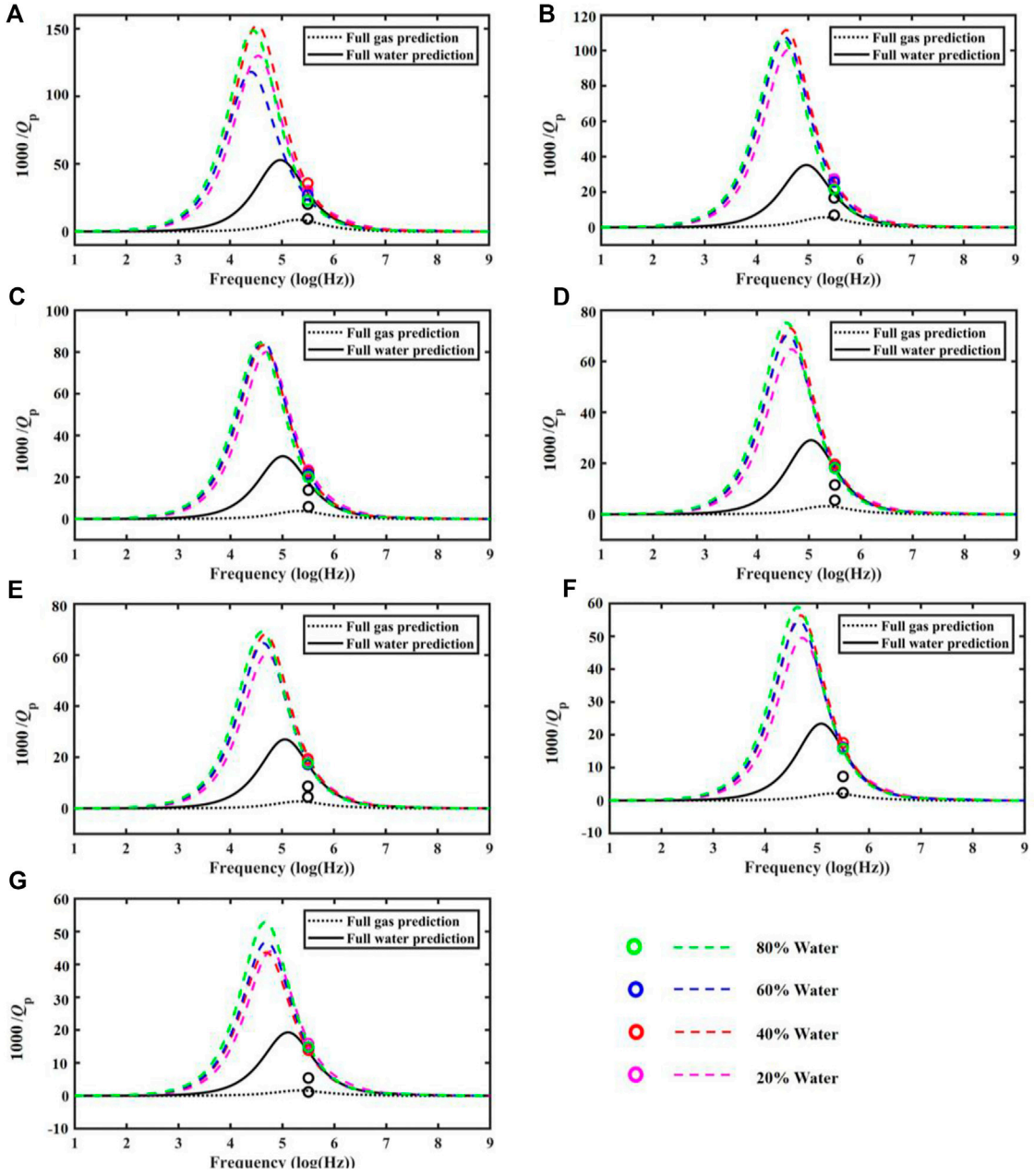

FIGURE 11
P-wave dissipation factor frequency dependence for sample 1–19 at 5 MPa **(A)**, 10 MPa **(B)**, 20 MPa **(C)**, 30 MPa **(D)**, 40 MPa **(E)**, 50 MPa **(F)** and 60 MPa **(G)**. The experimental data are shown as circles.

$$\phi_{f3}\left(Q_1 e + R_1\left(\xi_1 + \phi_{f2}\zeta_{12} + \phi_{f3}\zeta_{13}\right)\right) - \phi_{f1}\left(Q_3 e + R_3\left(\xi_2 - \phi_{f1}\zeta_{13}\right)\right)$$
$$= \frac{1}{3}\rho_f{}^{(1)}\ddot{\zeta}_{13}R_{13}^2\phi_{f1}^2\phi_{f3} + \frac{1}{3}\dot{\zeta}_{12}R_{13}^2\frac{\eta_f^{(1)}\phi_{f1}^2\phi_{f3}\phi_{10}}{\kappa_1} \quad (2g)$$

$$\phi_{f4}\left(Q_2 e + R_2\left(\xi_2 - \phi_{f1}\zeta_{12} + \phi_{f4}\zeta_{24}\right)\right) - \phi_{f2}\left(Q_4 e + R_4\left(\xi_4 - \phi_{f2}\zeta_{24}\right)\right)$$
$$= \frac{1}{3}\rho_f{}^{(1)}\ddot{\zeta}_{24}R_{24}^2\phi_{f2}^2\phi_{f4} + \frac{1}{3}\dot{\zeta}_{24}R_{24}^2\frac{\eta_f^{(1)}\phi_{f2}^2\phi_{f4}\phi_{20}}{\kappa_2} \quad (2h)$$

where $\boldsymbol{u}$, $\boldsymbol{U}^{(1)}$, $\boldsymbol{U}^{(2)}$, $\boldsymbol{U}^{(3)}$, $\boldsymbol{U}^{(4)}$ denote the average displacements of the frame, fluid phase 1 (host fluid in the host frame), fluid phase 2 (host fluid in the inclusions), fluid phase 3 (patch fluid in the host), and fluid phase 4 (patch fluid in the inclusions), respectively; e, ξ_1, ξ_2, ξ_3, ξ_4 are the corresponding displacement divergence fields of the solid and four fluid phases; ζ_{12}, ζ_{13}, ζ_{24} indicate the fluid changes due to local fluid flow; ϕ_{10}, ϕ_{20} are the local porosities of the host and inclusions, respectively; κ_1, κ_2 are the permeabilities of the host and inclusions, respectively; R_{12} is the radius of

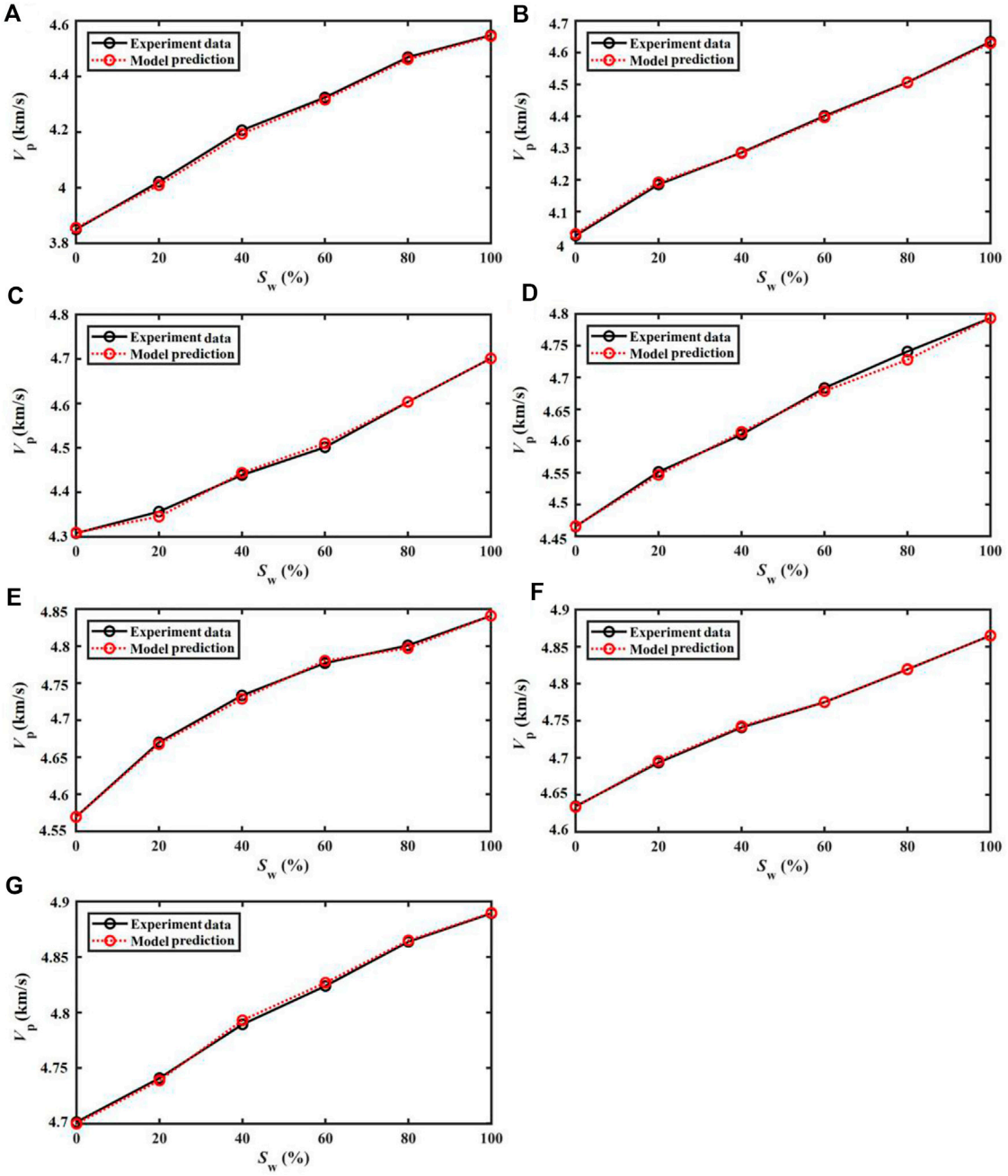

FIGURE 12
P-wave velocity as a function of water saturation compared to the experimental data for sample 1–19 at 5 MPa **(A)**, 10 MPa **(B)**, 20 MPa **(C)**, 30 MPa **(D)**, 40 MPa **(E)**, 50 MPa **(F)** and 60 MPa **(G)**.

inclusions; ϕ_{f1}, ϕ_{f2}, ϕ_{f3}, ϕ_{f4} are the absolute porosities related to the four fluid phases; $\rho_f^{(1)}$, $\eta_f^{(1)}$ are the density and viscosity of host fluid, respectively; R_{13}, R_{24} are the radius of pockets in the host skeleton and inclusions, respectively, b_1, b_2, b_3, b_4 are Biot dissipation coefficients. The density ρ_{00}, ρ_{01}, ρ_{02}, ρ_{03}, ρ_{04}, ρ_{11}, ρ_{22}, ρ_{33}, ρ_{44} and elastic parameters A, N, Q_1, Q_2, Q_3, Q_4, R_1, R_2, R_3, R_4 can be determined with the equations given in Appendix A. By substituting plane waves into these differential equations, the wave number can be obtained and then the P-wave velocity and attenuation can be computed (Guo et al., 2018).

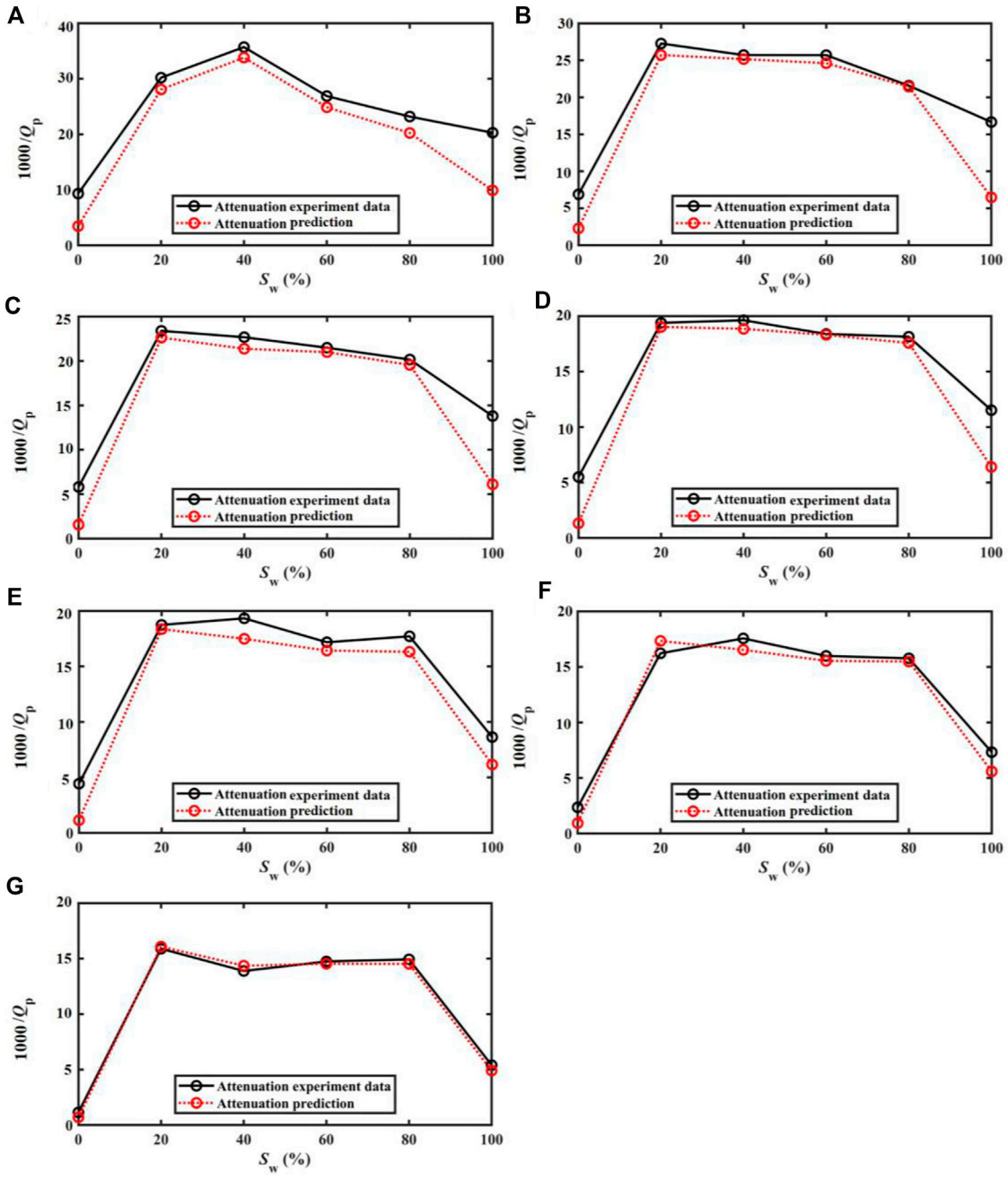

FIGURE 13
P-wave dissipation factor as a function of water saturation compared to the experimental data for sample 1–19 at 5 MPa **(A)**, 10 MPa **(B)**, 20 MPa **(C)**, 30 MPa **(D)**, 40 MPa **(E)**, 50 MPa **(F)** and 60 MPa **(G)**.

4.2 Results

We consider sample 1–19. The properties of gas, water and oil are obtained from the equations of Batzle and Wang (1992). The rock properties are given in Table 1, and the modeling parameters are given in Tables 2, 3.

Figure 8 shows the bulk (a) and shear (b) moduli of the dry rocks as a function of the confining pressure, showing the expected behavior.

Figure 9 compare the experimental and theoretical P-wave velocity dispersion and attenuation frequency dependence at different confining pressures, respectively, where we can see

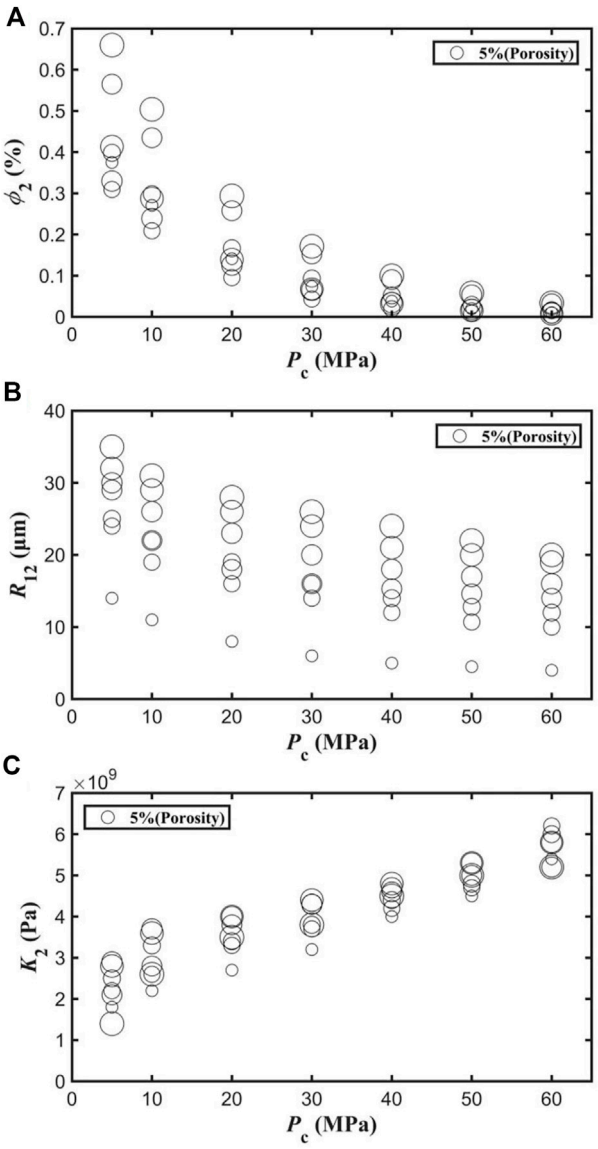

FIGURE 14
Crack porosity ϕ_2 **(A)**, inclusion radius R_{12} **(B)**, and inclusion bulk modulus K_2 **(C)** as a function of confining pressure for the seven rock samples (the size of the circles is proportional to porosity).

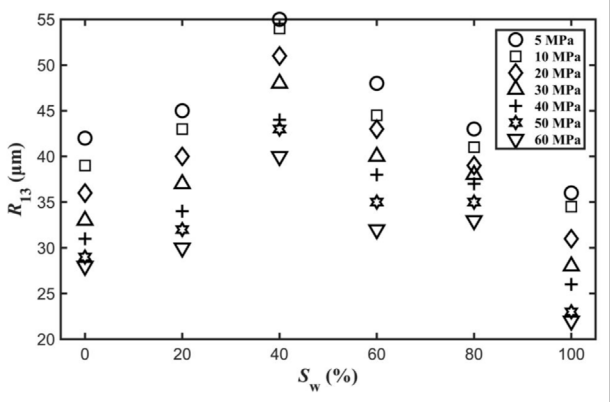

FIGURE 15
Radius of the gas pockets in the host skeleton R_{13} as a function of water saturation, corresponding to sample 1–19 at different confining pressures.

that the agreement is good. In the case of air, the anelasticity is very weak. In all cases, the anelasticity gradually decreases with confining pressure. For the saturated rocks, the P-wave attenuation is mainly caused by the heterogeneity of the frame and inclusions. With increasing pressure, cracks gradually tend to close. With the decrease of the inclusion (crack) radius and increase of bulk modulus, the WIFF effect is hindered, resulting in less dissipation.

Figures 10, 11 compare data and theory for sample 1–19 at different water saturations, for velocity and attenuation, respectively. The model results are consistent with the experimental data, and the anelasticity mainly occurs within the range of 10^3–10^7 Hz. The peaks move to low frequency with increasing water saturation. The lowest attenuation occurs in the full-gas saturation case. As mentioned above, when the rock is partially saturated, the P-wave dispersion and attenuation are caused by the two kinds of inhomogeneities, namely, fabric heterogeneity and patchy saturation. The anelasticity caused by the latter appears at lower frequencies, and is significantly stronger than that caused by the former inhomogeneity.

Results for partial saturation corresponding to sample 1–19, compared with the data, are shown in Figures 12, 13, where we can see that agreement is acceptable. Attenuation shows a maximum at medium saturations.

4.3 Inclusion properties

In this work, the inclusion is assumed to represent a crack or grain contact, with different porosity and compressibility as the host. The crack porosity ϕ_2 , inclusion radius R_{12}, and inclusion bulk modulus K_2, together with the radius of gas pockets in the host skeleton R_{13}, are set to analyze the effects of pressure on the observed wave responses.

Figure 14 shows the crack properties as a function of the confining pressure, obtained by inversion based on the experimental data. As expected, the crack porosity ϕ_2 decreases with the increase of confining pressure, and at the same confining pressure, the sample with a higher stiff porosity exhibits a higher crack (soft) porosity and inclusion radius. Moreover, K_2 increases with confining pressure, which is the result of the gradual closure of the cracks, and there is no apparent relationship with the rock porosity.

On the other hand, Figure 15 represents the radius of the gas pockets in the host R_{13} as a function of water saturation for sample 1–19 at different confining pressures.

The crack porosity ϕ_2, inclusion radius R_{12}, and inclusion bulk modulus K_2 as a function of confining pressure and

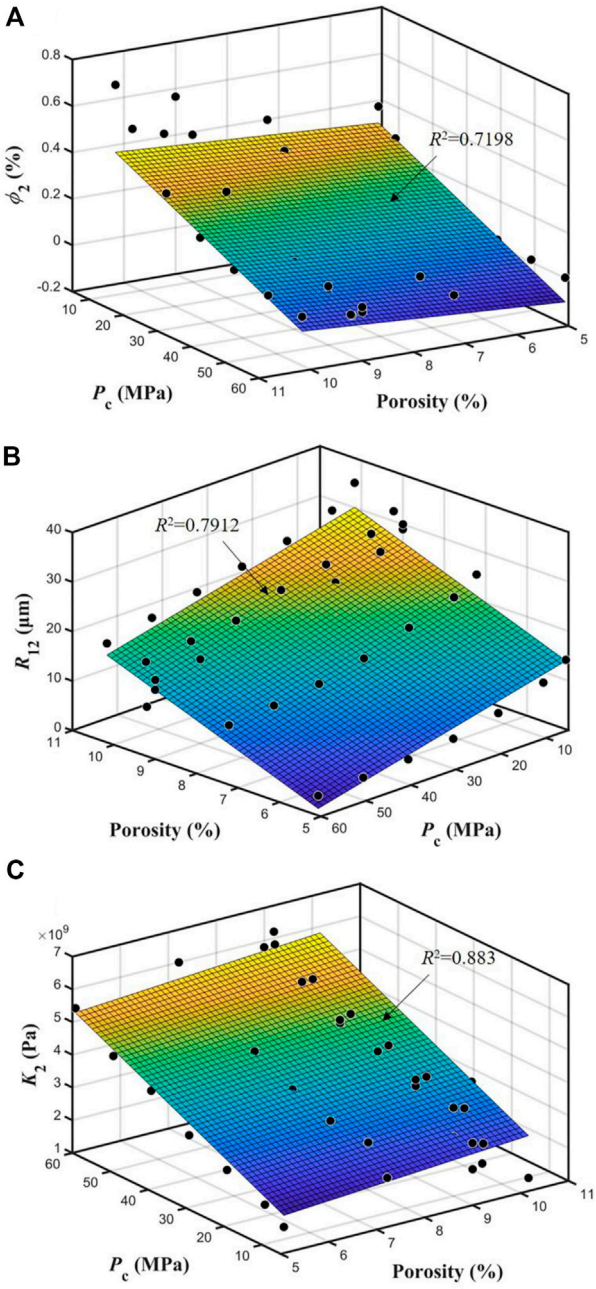

FIGURE 16
Crack porosity ϕ_2 **(A)**, inclusion radius R_{12} **(B)**, and inclusion bulk modulus K_2 **(C)** as a function of confining pressure and porosity, corresponding to the seven samples. The coefficient of determination (goodness of the fit) is given.

porosity, for all the samples, are given in Figure 16. ϕ_2 and K_2 are mainly affected by pressure and the effect of porosity is weak.

Finally, Figure 17 shows the radius of the gas pockets R_{13} as a function of water saturation and confining pressure for sample 1–19. R_{13} shows a maxium at

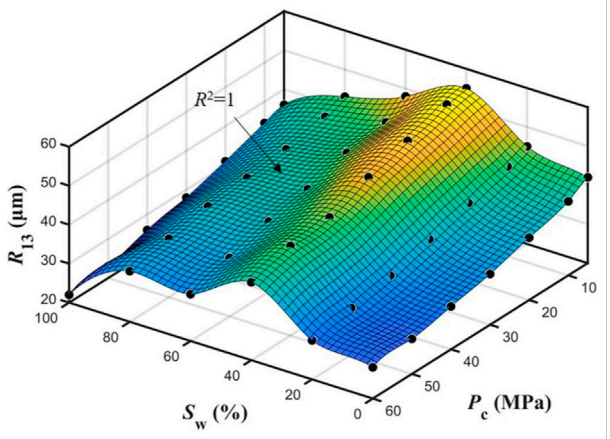

FIGURE 17
Radius of the gas pockets R_{13} as a function of water saturation and confining pressure for sample 1–19. The coefficient of determination (goodness of the fit) is given.

medium water saturations, and decreases with confining pressure. The effect of saturation decreases with pressure.

5 Conclusion

We have recorded ultrasonic waveforms and conducted X-ray diffraction tests on tight sandstones extracted from shale-oil strata. The properties of rock samples are measured. We have used the spectral-ratio method to obtain the P-wave attenuation at full and partial saturation conditions. The data has been interpreted with a double double-porosity theory that takes into account mesoscopic heterogeneities of the rock frame (inclusions) and gas pockets. A predictive theoretical model is proposed. P-wave velocity dispersion and attenuation are analyzed. The theoretical results show an acceptable agreement with the experimental data. The size, porosity and elastic modulus of the inclusions and size of the pockets are obtained as a function of porosity, saturation and confining pressure.

The experiments show that at full-saturation conditions, the P-wave velocity increases with confining pressure and attenuation decreases, and that the latter increases with increasing porosity and permeability. In the gas-water case, the P-wave velocity increases and attenuation shows a maximum at intermediate saturations. The theoretical results of P-wave anelasticity significantly decrease with the increase of confining pressure. The inclusion and gas-pocket properties are obtained by inversion with the theory, and it is shown that the crack (inclusion) porosity and radius decreases with confining pressure, while the inclusion bulk modulus increases, and the effect of rock porosity on them is weak. Moreover, the radius of the pockets shows a maximum at

intermediate saturations, and as pressure increases, the radius gradually decreases.

Data availability statement

The original contributions presented in the study are included in the article/Supplementary Material, further inquiries can be directed to the corresponding author.

Author contributions

JB and XP: Modeling and writing; RM: Modeling; JC: Interpretation and writing verification. All authors contributed to the article and approved the submitted version.

Funding

This work is supported by the National Natural Science Foundation of China (grant no. 41974123 and 42174161), and the Jiangsu Innovation and Entrepreneurship Plan.

Conflict of interest

The authors declare that the research was conducted in the absence of any commercial or financial relationships that could be construed as a potential conflict of interest.

Publisher's note

All claims expressed in this article are solely those of the authors and do not necessarily represent those of their affiliated organizations, or those of the publisher, the editors and the reviewers. Any product that may be evaluated in this article, or claim that may be made by its manufacturer, is not guaranteed or endorsed by the publisher.

Supplementary material

The Supplementary Material for this article can be found online at: https://www.frontiersin.org/articles/10.3389/feart.2022.1065630/full#supplementary-material

References

Ba, J., Carcione, J. M., and Nie, J. X. (2011). Biot-Rayleigh theory of wave propagation in double-porosity media. *J. Geophys. Res.* 116, B06202. doi:10.1029/2010jb008185

Ba, J., Carcione, J. M., and Sun, W. T. (2015). Seismic attenuation due to heterogeneities of rock fabric and fluid distribution. *Geophys. J. Int.* 202 (3), 1843–1847. doi:10.1093/gji/ggv255

Ba, J., Xu, W., Fu, L., Carcione, J. M., and Zhang, L. (2017). Rock anelasticity due to patchy saturation and fabric heterogeneity: A double double-porosity model of wave propagation. *J. Geophys. Res. Solid Earth* 122, 1949–1976. doi:10.1002/2016jb013882

Ba, J., Zhang, L., Wang, D., Yuan, Z., Cheng, W., Ma, R., et al. (2018). Experimental analysis on P-wave attenuation in carbonate rocks and reservoir identification. *J. Seismic Explor.* 27 (3), 371.

Ba, J., Zhao, J., Carcione, J. M., and Huang, X. (2016). Compressional wave dispersion due to rock matrix stiffening by clay squirt flow. *Geophys. Res. Lett.* 43, 6186–6195. doi:10.1002/2016gl069312

Batzle, M. L., and Wang, Z. (1992). Seismic properties of pore fluids. *Geophysics* 57, 1396–1408. doi:10.1190/1.1443207

Biot, M. A. (1962). Mechanics of deformation and acoustic propagation in porous media. *J. Appl. Phys.* 33 (4), 1482–1498. doi:10.1063/1.1728759

Born, W. T. (1941). The attenuation constant of Earth materials. *Geophysics* 6 (2), 132–148. doi:10.1190/1.1443714

Carcione, J. M. (2022). Wave fields in real media." in *Wave propagation in anisotropic, anelastic, porous and electromagnetic media*. 4th ed. Amsterdam, Netherlands: Elsevier. doi:10.1016/C2021-0-00938-X

Chapman, S., Quintal, B., Tisato, N., and Holliger, K. (2017). Frequency scaling of seismic attenuation in rocks saturated with two fluid phases. *Geophys. J. Int.* 208, 221–225. doi:10.1093/gji/ggw387

Chapman, S., Tisato, N., Quintal, B., and Holliger, K. (2016). Seismic attenuation in partially saturated Berea sandstone submitted to a range of confining pressures. *J. Geophys. Res. Solid Earth* 121 (3), 1664–1676. doi:10.1002/2015jb012575

Cheng, W., Ba, J., Ma, R. P., and Zhang, L. (2020). A study on the effects of pressure and fluid on rock pore structure and anelasticity: Theoretical model and experimental measurement. *Chin. J. Geophys.* 63 (12), 4517. doi:10.6038/cjg2020N0457

Deng, J., Tang, Z., Li, Y., Xie, J., Liu, H., and Guo, W. (2018). The influence of the diagenetic process on seismic rock physical properties of Wufeng and Longmaxi Formation shale. *Chin. J. Geophys.* 61 (2), 659. doi:10.6038/cjg2018L0062

Dvorkin, J., Mavko, G., and Nur, A. (1995). Squirt flow in fully saturated rocks. *Geophysics* 60 (1), 97–107. doi:10.1190/1.1443767

Dvorkin, J., Nolen-Hoeksema, R., and Nur, A. (1994). The Squirt-flow mechanism: Macroscopic description. *Geophysics* 59 (3), 428–438. doi:10.1190/1.1443605

Dvorkin, J., and Nur, A. (1993). Dynamic poroelasticity: A unified model with the squirt and the Biot mechanisms. *Geophysics* 58 (4), 524–533. doi:10.1190/1.1443435

Gao, F., Wei, J. X., and Di, B. R. (2019). Ultrasonic attenuation estimation based on time-frequency analysis. *Appl. Geophys.* 16, 414–426. doi:10.1007/s11770-019-0782-1

Guo, M. Q., Ba, J., Ma, R. P., et al. (2018). P-wave velocity dispersion and attenuation in fluid-saturated tight sandstones: Characteristics analysis based on a double double-porosity structure model description. *Chin. J. Geophys.* 61 (3), 1053. doi:10.6038/cjg2018L0678

Guo, M. Q., Fu, L. Y., and Ba, J. (2009). Comparison of stress-associated coda attenuation and intrinsic attenuation from ultrasonic measurements. *Geophys. J. Int.* 178 (1), 447–456. doi:10.1111/j.1365-246x.2009.04159.x

Hill, R. (1952). The elastic behaviour of a crystalline aggregate. *Proc. Phys. Soc. A* 65 (5), 349–354. doi:10.1088/0370-1298/65/5/307

Johnson, D. L. (1986). "Recent developments in the acoustic properties of porous media," in *Frontiers in physical acoustics XCIII*. Editor D. Sette (New York: Elsevier), 255

Johnston, D. H., Toksöz, M. N., and Timur, A. (1979). Attenuation of seismic waves in dry and saturated rocks: II. Mechanisms. *Geophysics* 44, 691–711. doi:10.1190/1.1440970

Johnston, D. H., and Toksöz, M. N. (1980). Ultrasonic P and S wave attenuation in dry and saturated rocks under pressure. *J. Geophys. Res.* 85, 925–936. doi:10.1029/jb085ib02p00925

Li, D. Q., Wei, J. X., Di, B. R., Ding, P. B., Huang, S. Q., and Shuai, D. (2018). Experimental study and theoretical interpretation of saturation effect on ultrasonic velocity in tight sandstones under different pressure conditions. *Geophys. J. Int.* 212 (3), 2226–2237. doi:10.1093/gji/ggx536

Li, X., Zhong, L. R., and Pyrak-Nolte, L. J. (2001). Physics of partially saturated porous media: Residual saturation and seismic-wavepropagation. *Annu. Rev. Earth Planet. Sci.* 29 (1), 419–460. doi:10.1146/annurev.earth.29.1.419

Ma, R. P., Ba, J., Carcione, J. M., Zhou, X., and Li, F. (2019). Dispersion and attenuation of compressional waves in tight oil reservoirs: Experiments and simulations. *Appl. Geophys.* 16, 33–45. doi:10.1007/s11770-019-0748-3

Ma, R. P., and Ba, J. (2020). Coda and intrinsic attenuations from ultrasonic measurements in tight siltstones. *J. Geophys. Res. Solid Earth* 125, e2019JB018825. doi:10.1029/2019jb018825

Mavko, G., and Mukerji, T. (1998). Bounds on low- frequency seismic velocities in partially saturated rocks. *Geophysics* 63 (3), 918–924. doi:10.1190/1.1444402

Pimienta, L., Fortin, J., and Guéguen, Y. (2016). Effect of fluids and frequencies on Poisson's ratio of sandstone samples. *Geophysics* 81 (2), D35–D47. doi:10.1190/geo-2015-0310.1

Pimienta, L., Fortin, J., and Guéguen, Y. (2015). Experimental study of Young's modulus dispersion and attenuation in fully saturated sandstones. *Geophysics* 80 (5), L57–L72. doi:10.1190/geo2014-0532.1

Pride, S. R., Berryman, J. G., and Harris, J. M. (2004). Seismic attenuation due to wave induced flow. *J. Geophys. Res.* 109 (B1), B01201. doi:10.1029/2003jb002639

Ren, S. B., Han, T. C., and Fu, L. Y. (2020). Theoretical and experimental study of P-wave attenuation in partially saturated sandstones under different pressures. *Chin. J. Geophys.* 63 (07), 2722. doi:10.6038/cjg2020O0021

Reuss, A. (1929). Berechnung der fliessgrenze von mischkristallen auf grund der Plastizitatsbedingungen Fur einkristalle. *Z. Angew. Math. Mech.* 9, 49–58. doi:10.1002/zamm.19290090104

Sams, M. S., Neep, J. P., Worthington, M. H., and King, M. S. (1997). The measurement of velocity dispersion and frequency-dependent intrinsic attenuation in sedimentary rocks. *Geophysics* 62, 1456–1464. doi:10.1190/1.1444249

Sharma, R., Prasad, M., Batzle, M., and Vega, S. (2013). Sensitivity of flow and elastic properties to fabric heterogeneity in carbonates. *Geophys. Prospect.* 61, 270–286. doi:10.1111/1365-2478.12030

Shukla, K., Carcione, J. M., Jaiswal, P., Santos, J., and Ba, J. (2019). Effect of capillary pressure on seismic velocities and attenuation. *J. Porous Media* 22 (4), 447–466. doi:10.1615/jpormedia.2018021864

Toksöz, M. N., Johnston, D. H., and Timur, A. (1979). Attenuation of seismic waves in dry and saturated rocks: i. Laboratory measurements. *Geophysics* 44, 681–690. doi:10.1190/1.1440969

Tutuncu, A. N., Podio, A. L., and Sharma, M. (1994). An experimental investigation of factors influencing compressional- and shear-wave velocities and attenuations in tight gas sandstones. *Geophysics* 59 (1), 77–86. doi:10.1190/1.1443536

Voigt, W. (1928). *Lehrbuch der kristallphysik*. Leipzig: Teubner, 739.

Wang, D. X., Xin, K. F., Li, M. Y., Gao, J. H., and Wu, X. Y. (2006). An experimental study of influence of water saturation on velocity and attenuation in sandstone under stratum conditions. *Chin. J. Geophys.* 49 (03), 908

Wei, Q., Wang, Y., Han, D., Sun, M., and Huang, Q. (2021). Combined effects of permeability and fluid saturation on seismic wave dispersion and attenuation in partially-saturated sandstone. *Adv. Geo-Energy Res.* 5 (2), 181–190. doi:10.46690/ager.2021.02.07

Wei, Y. J., Ba, J., Ma, R. P., Zhang, L., Carcione, J. M., and Guo, M. Q. (2020). Effect of effective pressure change on pore structure and elastic wave responses in tight sandstones. *Chin. J. Geophys.* 63 (07), 2810. doi:10.6038/cjg2019N0004

White, J. E., Mikhaylova, N. G., and Lyakhovitskiy, F. M. (1975). Low-frequency seismic waves in fluid saturated layered rocks. *J. Acoust. Soc. Am.* 57 (S30), S30–S659. doi:10.1121/1.1995164

Winkler, K. (1985). Dispersion analysis of velocity and attenuation in Berea sandstone. *J. Geophys. Res.* 90, 6793–6800. doi:10.1029/jb090ib08p06793

Yin, H., Zhao, J., Tang, G., Zhao, L., Ma, X., and Wang, S. (2017). Pressure and fluid effect on frequency-dependent elastic moduli in fully saturated tight sandstone. *J. Geophys. Res. Solid Earth* 122, 8925–8942. doi:10.1002/2017jb014244

Zhang, C. J., and Ulrych, T. J. (2002). Estimation of quality factors from CMP records. *Geophysics* 67, 1542–1547. doi:10.1190/1.1512799

Zhang, L., Ba, J., Fu, L., Carcione, J. M., and Cao, C. (2019). Estimation of pore microstructure by using the static and dynamic moduli. *Int. J. Rock Mech. Min. Sci.* 113, 24–30. doi:10.1016/j.ijrmms.2018.11.005

Zhang, L., Ba, J., Yin, W., Sun, W., and Tang, J. (2017). Seismic wave propagation equations of conglomerate reservoirs: A triple-porosity structure model. *Chin. J. Geophys.* 60 (3), 1073. doi:10.6038/cjg20170320

Zhao, L., Yuan, H., Yang, J., Han, D.-h., Geng, J., Zhou, R., et al. (2017). Mobility effect on poroelastic seismic signatures in partially saturated rocks with applications in time-lapse monitoring of a heavy oil reservoir. *J. Geophys. Res. Solid Earth* 122, 8872–8891. doi:10.1002/2017jb014303

Zhubayev, A., Houben, M. E., Smeulders, D. M. J., and Barnhoorn, A. (2016). Ultrasonic velocity and attenuation anisotropy of shales, Whitby, United Kingdom. *Geophysics* 81 (1), D45–D56. doi:10.1190/geo2015-0211.1

Zou, C. N., Yang, Z., Cui, J. W., Zhu, R. K., Hou, L. H., Tao, S. Z., et al. (2013). Formation mechanism, geological characteristics and development strategy of nonmarine shale oil in China. *Petroleum Explor. Dev.* 40 (01), 15–27. doi:10.1016/s1876-3804(13)60002-6

frontiers | Frontiers in Earth Science

TYPE Original Research
PUBLISHED 27 January 2023
DOI 10.3389/feart.2022.1098466

OPEN ACCESS

EDITED BY
Lidong Dai,
Institute of Geochemistry (CAS), China

REVIEWED BY
Genyang Tang,
China University of Petroleum, China
Junxin Guo,
Southern University of Science and Technology, China

*CORRESPONDENCE
Tongcheng Han,
hantc@upc.edu.cn

SPECIALTY SECTION
This article was submitted to Solid Earth Geophysics, a section of the journal Frontiers in Earth Science

RECEIVED 15 November 2022
ACCEPTED 09 December 2022
PUBLISHED 27 January 2023

CITATION
Wang P, Han T and Fu L-Y (2023), Elastic and electrical properties of calcite-cemented artificial sandstones based on a new manufacturing method. *Front. Earth Sci.* 10:1098466. doi: 10.3389/feart.2022.1098466

Elastic and electrical properties of calcite-cemented artificial sandstones based on a new manufacturing method

Pan Wang[1], Tongcheng Han[1,2]* and Li-Yun Fu[1,2]

[1]Shandong Provincial Key Laboratory of Deep Oil and Gas, School of Geosciences, China University of Petroleum (East China), Qingdao, China, [2]Laboratory for Marine Mineral Resources, Pilot National Laboratory for Marine Science and Technology (Qingdao), Qingdao, China

Calcite cement is widely existing in sandstones and can significantly affect the elastic and electrical properties of sandstones. Accordingly, understanding the effects of calcite cement on the elastic and electrical rock properties is of key importance for the accurate characterization of sandstone reservoirs through seismic and electromagnetic surveys. To obtain such knowledge, we design and implement dedicated laboratory experiments to investigate the effects of calcite cement and porosity on the P- and S-wave velocities and electrical resistivity of synthetic calcite-cemented sandstones made using a new recipe. The experimental results show that elastic velocities and electrical resistivity generally decrease with increasing porosity when the content of the calcite cement keeps constant, whereas the elastic and electrical rock properties exhibit complex variation with cement content in sandstones with approximately the same porosity. Analyses and interpretation of the experimental data indicate that the elastic and electrical rock properties are affected jointly by porosity, the content and distribution of the calcite cement, as well as the microstructure of the pore space resulting from the different axial stress employed for the consolidation of the rock samples. The results have revealed the mechanisms of how porosity and calcite cement affect the elastic and electrical properties of calcite-cemented sandstones, and provided a theoretical basis for the accurate characterization of sandstone reservoirs through seismic and electromagnetic surveys.

KEYWORDS

calcite-cemented artificial sandstones, porosity, cement, velocity, resistivity

1 Introduction

Sandstones are ideal hydrocarbon reservoirs and contain more than half of the conventional oil and gas found globally (Tanner et al., 1991). As an important cementation type of sandstones, calcite cement widely exists in sandstones formed in various depth and sedimentary environments (Morad et al., 2010; Ajdukiewicz and Larese, 2012; Wang et al., 2016). The content and distribution of calcite cement can significantly affect the elastic and electrical properties of calcite-cemented sandstones

(Jarrard et al., 2000; Tang et al., 2016), and therefore understanding how and why calcite cement affects the elastic and electrical rock properties is of key importance for the successful interpretation of the exploration data acquired by seismic and electromagnetic surveys, the most widely employed and most effective methods for the characterization of sandstone reservoirs (Wang, 2001; Constable, 2010).

Many experimental studies have been implemented to understand the effects of calcite cement on the elastic and electrical properties of sandstones, and most of the studies are based on natural sandstones (Jarrard et al., 2000; Tang et al., 2016; Wang et al., 2020). However, due to the fact that natural sandstones are with varying mineral compositions, porosity, cement type and distribution, and grain sizes (Wang, 2001; Al-Tahini et al., 2007), the use of natural sandstones makes it difficult to reveal the impact of a specific factor on the physical rock properties. As a result, the amount of calcite cement is only found to generally improve the rock velocity and resistivity, while the quantitative improvement of the elastic and electrical rock properties with the calcite cement content remains far from being reveled through the use of natural sandstones. Unlike natural sandstones, the rock parameters can be easily controlled in artificial rocks, and therefore artificial sandstones have been widely employed for the understanding of the effects of petrophysical parameters on the elastic and electrical rock properties (Sherlock and Siggins, 2004; Ding et al., 2015; Si et al., 2016).

In current experimental studies for the understanding of the effects of calcite cement on the physical properties of synthetic rocks, the artificial sandstones are manufactured predominantly using the calcite *in situ* precipitation system (CIPS, see Ismail et al., 2002a for more details) and the microbially induced carbonate precipitation (MICP) method (Konstantinou et al., 2021). CIPS depends on flushing a mixture of chemical solutions through a porous medium, leading to precipitation of calcite due to the reaction of the solution ingredients (Kucharski et al., 1997; Ismail et al., 2002a, b; Palmén et al., 2016). In a different way, bacteria are first introduced to the medium in MICP and then a cementation solution consisting of urea and a calcium source is supplied in the form of injections, and the bacterial urease activity builds up calcium carbonate cementation around the particles (Dejong et al., 2006; Harkes et al., 2010; Muynck et al., 2010; Qian et al., 2010; Konstantinou et al., 2021).

These methods can be applied to making calcite-cemented artificial rocks that are with customized petrophysical and physical properties, closely resembling those of natural sandstones (Kucharski et al., 1997; Ismail et al., 2002a; Sherlock and Siggins, 2004; Yasuhara et al., 2012; Konstantinou et al., 2021). However, it can be difficult to control precisely the porosity, and the content and distribution of the calcite cement in the samples made using these methods. Accordingly, the difference in the rock porosity, which can be dominant in some physical rock properties like electrical resistivity, has usually been ignored in the experimental investigations of the variation of physical properties with cement content (Sherlock and Siggins, 2004). Moreover, the calcite cement in current artificial sandstones is generally less than 10%, whereas natural calcite-cemented sandstones usually contain a wider cement range between 5% and 30% (Morad, 2009; Zhao et al., 2014; Wang et al., 2015, 2016), making synthetic sandstones not representative of natural rocks.

This work aims to investigate quantitatively the effects of calcite cement and porosity on the P- and S-wave velocities and electrical resistivity of synthetic calcite-cemented sandstones. We first present a new method for making calcite-cemented sandstones and prepare two groups of synthetic samples with cement content keeps constant and porosity varies in one group, and porosity is kept approximately the same and cement content is different in the other group. We then measure the P- and S-wave velocities and electrical resistivity of the samples with full brine saturation at bench-top conditions. The effects of varying cement content and porosity on the elastic and electrical properties of the artificial sandstones are finally analyzed in combination with their microstructures.

2 Preparation of artificial samples

2.1 A method for making calcite-cemented artificial sandstones

On basis of understanding the diagenesis of natural sandstones with calcite cement, we present a way to make calcite-cemented sandstone samples from simple inorganic ingredients (i.e., sand grains, $Ca(OH)_2$ powder and CO_2 gas) to best resemble natural sandstones in terms of mineral composition, and the type and content of cement. The manufacturing of the samples follows four main steps, i.e., pre-preparation of the raw materials, mixing of the ingredients, and consolidation and cementation of the mixture.

2.1.1 Pre-preparation of the raw materials

Different sized sand grains were employed to make the grain distribution of the synthetic samples better resemble that of natural rocks, and to make the porosity of the samples as low as possible. The sand grains were chosen with sizes of 0.3 mm, 0.18 mm, 0.135 mm, 0.075 mm, 0.038 mm and 0.013 mm, respectively. We washed the sand grains in 0.1 mol/L hydrochloric acid for 1 h to dissolve existing carbonate minerals and heated the washed grains in an oven at the temperature of 60 °C for about 8 h to make sure they were completely dry.

2.1.2 Mixing of the ingredients

We first mixed the washed and dried sand grains with weight ratio of 5:3.3:1.8:1.4:0.8:1 from large to small sizes, and then

added a small amount of distilled water to the grains (with a weight ratio of 1:25 to the sand grains) and mixed evenly to make sure the sand grains were evenly moisturized. The $Ca(OH)_2$ powder with a predetermined weight was finally added into and fully mixed with the sand-water mixture so as to form $Ca(OH)_2$ coated sand grains. The weight ratio of the different sized sand grains was chosen to mimic that of a tight sandstone acquired from the Ordos Basin, China. The sand to water weight ratio was determined as an optimal for the water to fully moisturize the sand grains so that the $Ca(OH)_2$ powder can evenly coat them, without leaving much water for the $Ca(OH)_2$ powder to agglomerate and hence most of the generated calcite is acting as cement.

2.1.3 Consolidation of the mixture

The mixture was packed into a cylindrical mould made of stainless steel with a diameter of 5 cm, and an axial stress of up to 70 MPa was applied for up to 4 h to compact and consolidate the mixture.

2.1.4 Cementation of the mixture

The consolidate mixture was placed into a sealed core-holder and CO_2 gas with the pressure of up to 0.9 MPa was added to react with $Ca(OH)_2$ to form the calcite cement. This process took up to 2 weeks to ensure all the $Ca(OH)_2$ powder has reacted so that the cement content has reached its predetermined value. During the cementation period, the sample was taken out of the core-holder every 24 h and heated at the temperature of 60 °C for 2 h to reduce the generated water. The reduction of the redundant water was to make sure it was not blocking the pore network so that the CO_2 gas could better get into the sample to react with Ca(OH)2.

2.2 Manufacturing of sandstones with varying cement content and porosity

Two groups of sandstones were made using the method above, each with a varying petrophysical parameter. Samples in Group A had the same cement content but with different porosity, and samples in Group B were with approximately the same porosity but their cement content varied. These samples were made to investigate respectively the effects of porosity and cement content on the elastic and electrical properties of the calcite-cemented sandstones. The content of calcite cement was controlled by adding different weights of $Ca(OH)_2$ powder into the sand grains, and the different porosity was achieved applying varying axis stresses during the consolidation of the sand-$Ca(OH)_2$ mixture.

The samples in Group A were made with calcite cement of 20 wt% (weight percentage of calcite in the whole dry sample). This cement content was reached by controlling 15.6 wt% of the $Ca(OH)_2$ powder in the sand-$Ca(OH)_2$ mixture, and by applying a consolidation stress of 15, 20, 30, 40 and 70 MPa, respectively, the porosity of the samples was varied. On the other hand, the calcite cement in the Group B samples was made to vary between 10 wt% to 30 wt% at an interval of 5 wt% (the corresponding weight percentage of $Ca(OH)_2$ powder in the sand-$Ca(OH)_2$ mixture is 7.6, 11.6, 15.6, 19.8 and 24.1 wt%, respectively). Since quartz and calcite are close in density, keeping the density of the final samples the same will guarantee the samples have approximately the same porosity, provided that the weight of the dry samples is not changing. Therefore, the same porosity of the samples in Group B was achieved by compressing to the same height of the sand-$Ca(OH)_2$ mixture, which was prepared to make sure the weight of the formed samples was the same.

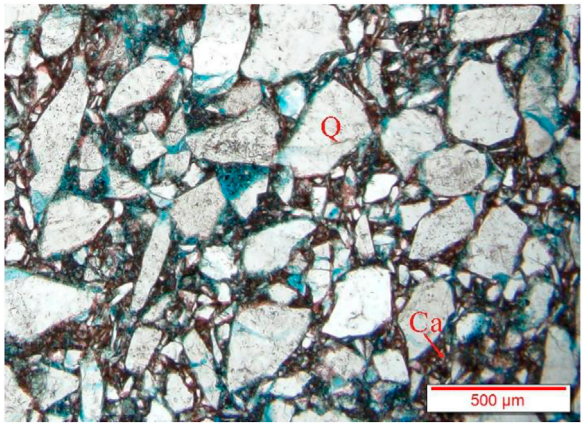

FIGURE 1
Microscopic characteristics of a typical manufactured calcite-cemented sandstone. The letters Ca and Q in the image stand for calcite and quartz, respectively. The pore space is filled with blue casting.

Typical thin section images (as illustrated in Figure 1) of the formed samples show that the sand grains are generally coated by the precipitated calcite, resembling the commonly existing distribution of calcite in natural calcite-cemented sandstones (Morad, 2009). The mineral composition, porosity and permeability of the samples are tabulated in Table 1, from which it can be seen that the porosity of the samples in Group A varies between 0.1519 and 0.2218, and the porosity difference in Group B is less than 0.01. The precise control of the cement content and porosity forms the basis for the following investigation of their impact on the elastic and electrical properties of the calcite-cemented sandstones.

3 Laboratory experiments

The artificial sandstone samples were cut into cylindrical cores with diameter of 1 inch and length of about 5 cm, with the two ends of each sample carefully polished to be parallel to

TABLE 1 Mineral composition, porosity and permeability of the artificial sandstones.

Group A				Group B			
Minerals (wt%)		Porosity	Permeability (mD)	Minerals (wt%)		Porosity	Permeability (mD)
Quartz	Calcite			Quartz	Calcite		
80.02	19.98	0.2218	2.91	90.00	10.00	0.1872	2.89
80.01	19.99	0.2002	2.25	85.03	14.97	0.1924	2.79
80.00	20.00	0.1912	1.78	79.90	20.10	0.1849	1.69
79.90	20.10	0.1719	1.13	75.20	24.80	0.1872	0.94
79.95	20.05	0.1519	0.77	69.90	30.10	0.1895	0.48

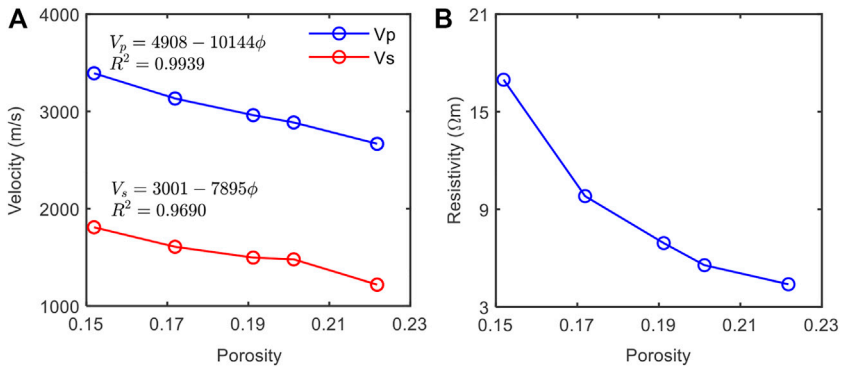

FIGURE 2
Effects of porosity on **(A)** the P- and S-wave velocities and **(B)** resistivity of the artificial samples with the same amount of calcite cement.

within ±0.01 mm, to reduce errors in the length measurements and to enhance the contact between the samples and the transducers. The core samples were dried in an oven at the temperature of 60 °C for 48 h, vacuumed to −0.1 MPa for more than 12 h, and then saturated with 35 g/L brine (made from distilled and deaired water and NaCl) at a pressure of 20 MPa for 12 h to make sure the samples are fully saturated with the brine.

After full brine saturation of the samples, they were loaded into the joint elastic-electrical rig described by Han et al. (2020a), where P- and S-wave velocities and electrical resistance were simultaneously measured at the confining pressure of 5 MPa and pore pressure of the atmosphere pressure. The measured resistance was employed to calculate the rock resistivity through the length and diameter of the samples. Frequencies of the elastic and electrical measurements were about 500 kHz and 1 kHz, respectively, with the errors estimated to be approximately ±0.8% and ±1.2% for P- and S-wave velocities, respectively, and approximately ±0.2% for electrical resistivity (Han et al., 2020a). The measurements were made in a laboratory with the temperature controlled at 22°C ± 1 °C to minimize the effects of varying temperature on the experimental results.

4 Results and discussion

4.1 Effects of porosity on the elastic and electrical properties

Figure 2 shows the effects of porosity on the P- and S-wave velocities and electrical resistivity of the samples with the same content of calcite cement in Group A. Both the velocities and the resistivity reduce with increasing porosity. This is expected because more brine is needed to saturate the samples with greater porosity, and since brine has lower elastic moduli and resistivity than the mineral grains have, greater amount of brine will lead to decreasing velocities and resistivity.

In addition to showing the decreasing velocities and resistivity with porosity, Figure 2 also illustrates that the decrease of the velocities tends to be linear, and can be best fitted by

$$V_p = 4908 - 10144\phi, \quad (1)$$

$$V_s = 3001 - 7895\phi, \quad (2)$$

where V_p and V_s are the P- and S-wave velocities in m/s, ϕ is the porosity, and the squared correlation coefficients for V_p and V_s

are R^2 = 0.9939, and R^2 = 0.9690, respectively. The linear dependence of velocities on porosity is similar with that found in natural sandstones (Han et al., 1986; Al-Tahini et al., 2007). However, the content of calcite cement in our samples keeps constant, which may be different from natural sandstones that are having varying types and content of cement. Therefore, although a similar linear variation of velocities with porosity is obtained in our artificial sandstones and in natural sandstones, the reasons that cause this linear variation can be different. A deep investigation of such reasons can help to better reveal how velocities are affected, but this is not the main focus of this work.

Unlike the linearly decreasing velocities, the reduction of electrical resistivity with porosity tends to show an exponential trend, as shown in Figure 2B. The exponentially decreasing resistivity with porosity is understandable because according to Archie's equation (Archie, 1942), the variation of resistivity with porosity is controlled by the cementation exponent, and if cementation exponent keeps unchanged, resistivity will show exponential dependence on porosity. Archie's equation is given as

$$\frac{R_0}{R_w} = \phi^{-m}. \tag{3}$$

where R_0 is the resistivity of a rock that is fully saturated with a brine of the resistivity R_w, ϕ is the rock porosity, and m is the cementation exponent, which implicitly represents the "connectedness" of the pore network for the transportation of hydraulic and electrical flow (Glover, 2009), and depends on the physical microstructural properties of fractal porous media (Wei et al., 2015; Cai et al., 2017). A greater m indicates a more complex pore structure of the rock.

It should be noted that the above explanation of the exponential dependency of resistivity on porosity is based on the assumption that the cementation exponent of the samples is not changing. This, however, may not be the case in our samples because different axial stresses are employed to consolidate the samples to achieve different porosity, and the difference in the applied stresses may lead to a variation in the microstructure and hence cementation exponent of the samples. Therefore, we will proceed to investigate whether the microstructure varies between the samples in Group A.

To obtain the microstructure, we invert from the measured velocities and resistivity to get the pore aspect ratio and the cementation exponent of the samples (Mavko et al., 2009; Han et al., 2021), through the employment of the differential effective medium (DEM) model (Berryman, 1995), and the equation of Archie (Archie, 1942), respectively. In the inversion, the bulk and shear moduli of quartz are taken to be 37 GPa and 44 GPa, respectively, and the elastic moduli of calcite are assumed to be 76.8 GPa and 32 GPa, respectively. Using these elastic parameters, the bulk and shear moduli of the mineral grains in the samples are determined to be 44.82 GPa and 41.64 GPa, respectively using the arithmetic average. The bulk modulus and resistivity of the brine saturating the samples are 2.25 GPa and 0.2132 Ω m, respectively. Densities are taken to be 2.65 g/cm^3 for the quartz, 2.71 g/cm^3 for the calcite and 1.035 g/cm^3 for the brine. The effective grain moduli obtained using the arithmetic average will not fully reflect the effects of calcite as the cement (Dvorkin et al., 1994; Han et al., 2013). However, because the samples in Group A have the same calcite content, neglecting their cement effects will still effectively convey the varying trend of the pore aspect ratio with porosity determined from the DEM model.

Figure 3 shows the obtained pore aspect ratio and cementation exponent with varying porosity of the samples, and the comparison between the measured velocities and those modeled using the inverted pore aspect ratio based on the DEM model is shown in Figure 4. It can be seen from Figure 3 that pore aspect ratio increases and cementation exponent decreases with increasing porosity, indicating the microstructure of the samples is changing with porosity resulting from the variation in the applied consolidation stress. In addition to showing the general trend of the varying microstructure, Figure 3 also illustrates the variation differs in different porosity ranges. In the low porosity range ($\phi < 0.1719$), the increase in the pore aspect ratio is relatively slow, whereas the cementation exponent that represents the "connectedness" of the pore network reduces dramatically. This may be due to the opening of the pore throats with lower consolidation stress (i.e., higher porosity). When porosity improves from 0.1719 to 0.2002, the pore aspect ratio increases significantly and the cementation exponent keeps dramatic decreasing. This might result from the rapid opening of the intergranular pores and the dilation of the pore throats with lowering consolidation stress. When porosity further increases, although the obtained pore aspect ratio still significantly increases, the reduction in the cementation exponent becomes slow. A possible cause of this microstructure variation can be that the lowering of the consolidation stress only enlarges the pore shape but does not generate new pore throats to connect the neighboring pores.

The variation in the pore structure offered above to explain the determined pore aspect ratio and cementation exponent with porosity can be confirmed from the thin section images of the samples with different porosity, as shown in Figure 5. In the sample with low porosity, the high consolidation stress compresses the grains to contact each in the way of line contact, and the pores are dominated by residual intergranular pores filled with the calcite cement. The pore throats that connect the residual intergranular pores are low in diameter and the coordination number (the number of pore throats connected to each pore) is low leading to poor connectivity of the pore network (Figure 5A). These characteristics result in the low aspect ratios of the pores and the complex microstructure (i.e., great cementation exponent) of the samples. With an increase in porosity, both the diameter of the bridging pore throats and the coordination number increase, improving the connectivity of the pore network (Figures 5B–D), and leading to increasing

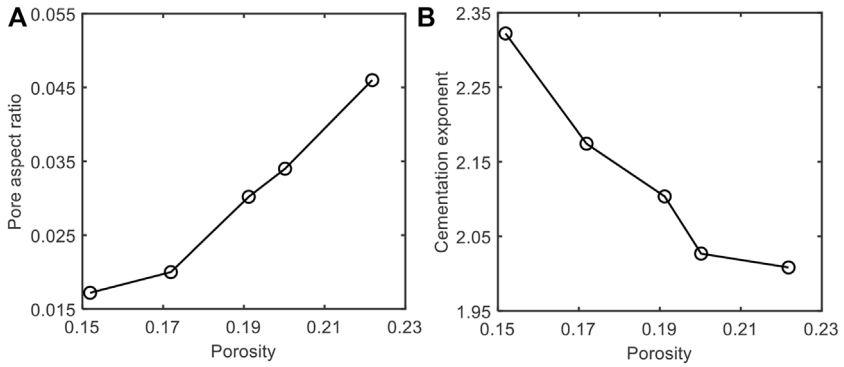

FIGURE 3
Variation of the **(A)** pore aspect ratio inverted from P- and S-wave velocities and **(B)** cementation exponent obtained from resistivity with porosity of the samples.

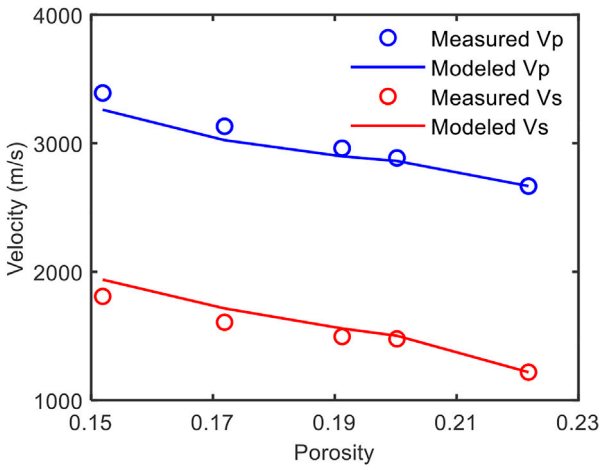

FIGURE 4
Comparison between the measured P- and S-wave velocities and those modeled using the inverted pore aspect ratio in Figure 3A based on the DEM model. The minor discrepancy between the measured and modeled velocities is possibly due to the averaged elastic moduli employed for the mineral grains.

effective pore aspect ratio and reducing complexity of the microstructure (i.e., decreasing cementation exponent). With further increase in porosity (Figures 5D,E), the decreasing consolidation stress weakly enlarges the diameter of the pore throats, and therefore the effective pore aspect ratio keeps increasing. However, the coordination number stabilizes at about 3, indicating the microstructure and the cementation exponent tend to be stable.

The quantitative and visual analyses of the microstructures not only reveal the difference in the samples apart from their porosity, but also help to better interpret the variation of the elastic and electrical properties with porosity. It is understandable that increasing porosity will lead to decreasing velocities and resistivity. However, to make the samples with increasing porosity, a lowering consolidation stress was applied, resulting in increasing pore aspect ratio and reducing cementation exponent. Since pores with higher aspect ratio will make a rock more resistive to compression, the increase in the pore aspect ratio alone will increase the velocities of the samples. Therefore, the observed decreasing velocities with porosity suggests that the effects of increasing porosity on reducing the rock velocities prevail over the effects of the increasing pore aspect ratio (as a result of the lowering consolidation stress) on improving the rock velocities. On the other hand, increasing porosity will reduce the rock resistivity, and the reducing cementation exponent with increasing porosity will further decrease the rock resistivity by enhancing the connectivity of the pore network. Therefore, the observed variation of the elastic and electrical rock properties with porosity in the Group A samples with the same content of calcite cement is a combined result of the varying porosity and the applied consolidation stress that causes the variation in the porosity.

4.2 Effects of cement content on the elastic and electrical properties

Having studied the effects of porosity on the elastic and electrical properties of the samples in Group A with the same amount of calcite cement, we proceed to investigate the effects of cement content on the elastic and electrical properties of the artificial samples with approximately the same porosity (varying between 0.1849 and 0.1924) in Group B.

The variation of the measured elastic and electrical properties with cement content of the samples is shown in Figure 6. When

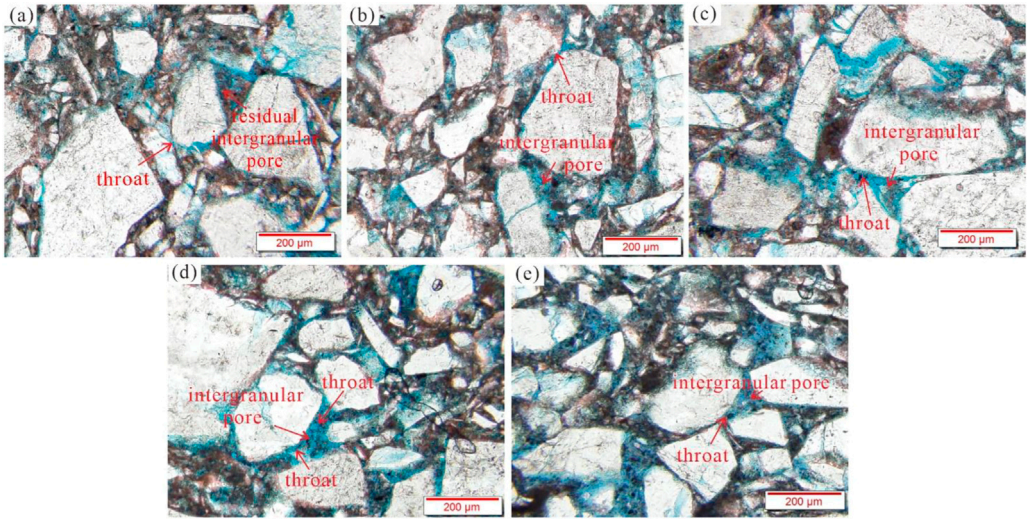

FIGURE 5
Typical thin section images of the samples with same cement content but with different porosity. Images **(A)** and **(B)** are respectively corresponding to the samples with porosity of 15.19% and 17.19%, and show that the majority of the pores are residual intergranular pores with poor connectivity. Images **(C)**, **(D)**, and **(E)** are for the samples with porosity of 19.12%, 20.02%, and 22.18%, respectively, illustrating the pores are dominantly intergranular pores with good connectivity.

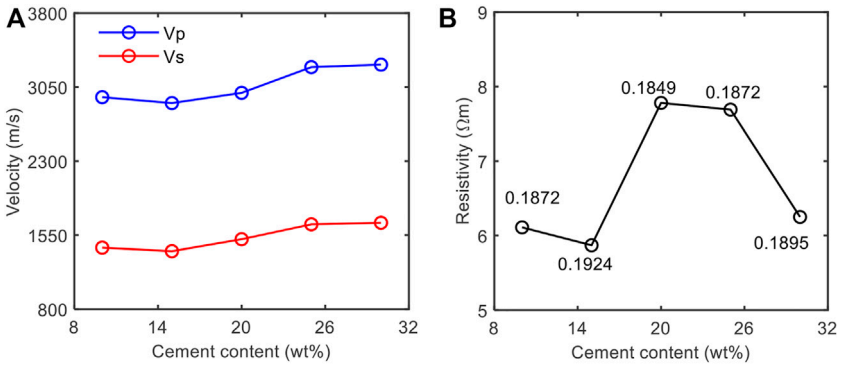

FIGURE 6
Effects of cement content on the **(A)** P- and S-wave velocities and **(B)** resistivity of the rock samples with approximately the same porosity.

porosity keeps almost the same, P- and S-wave velocities first weakly reduce and then gradually increase with increasing cement content until cement content reaches about 25 wt% when the increase in the velocities becomes weaker. In a different way, resistivity reduces first and decreases again after an increase in the middle range of cement content. The complex variation of the elastic and electrical properties with cement content is in great contrast with the expected increase of the physical properties with increasing cement content (Jarrard et al., 2000). A possible cause of the contrast is the difference in porosity of the samples, as indicated in Figure 6B. Although efforts have been made to confine the porosity difference to within 0.01, according to the effects of porosity on the elastic and electrical properties obtained in the previous section, such a small porosity difference may still impact significantly the physical and especially the electrical rock properties. Therefore, the small divergence in the porosity may cover up the effects on cement content on the measured rock properties.

We eliminate the impact of the different porosity by calculating, using Archie equation (Archie, 1942), the cementation exponent of the samples that is independent of porosity, as shown in Figure 7. The determined cementation exponent is not showing a monotonous variation with cement content, but instead first increases and then decreases, forming a

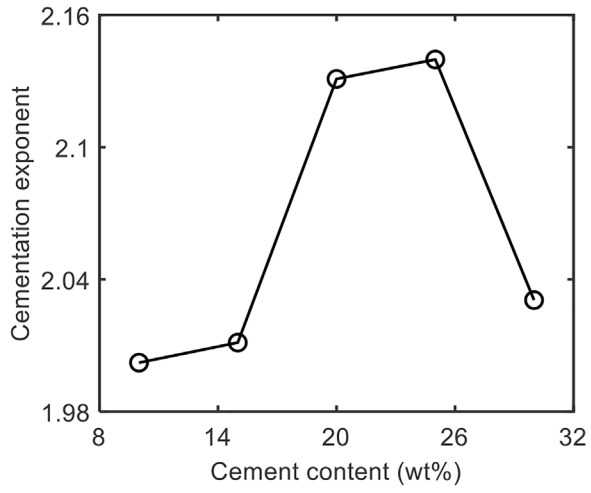

FIGURE 7
Relationship between cementation exponent and cement content of the samples with approximately the same porosity.

bell-shaped correlation with the increasing cement content. This obtained relationship is not consistent with previous studies that have found strong correlation between cementation exponent and the content of cement in sandstones (e.g., Glover, 2009). This inconsistency is possibly due to the fact that the microstructure (and hence cementation exponent) of our samples is not purely affected by the content of cement. Additional, the different consolidation stress employed to arrive at the same porosity of the samples (lower stresses are associated with the samples with greater content of calcite cement) may also contribute to the microstructure and cementation exponent of the samples. The increasing cementation exponent with cement content for the samples with cement content less than about 25 wt% indicates the impact of the increasing cement content that improves cementation exponent overwhelms the influence of the lowering consolidation stress that reduces cementation exponent. Similarly, the significant reduction of the cementation exponent when cement content exceeds about 25 wt% implies the effects of the lowering consolidation stress on simplifying the microstructure (reducing cementation exponent) prevail over that of the increasing cement content on complicating the microstructure (improving cementation exponent).

The variation in the microstructure of samples that can be jointly affected by the different cement content and consolidation stress can be observed from the thin section images, as illustrated in Figure 8. For the samples with cement content between 10 wt% and 20 wt% (Figures 8A–C), the rock structures are supported by the sand particles, and the calcite cement fills in the enlarging intergranular pores due to the lowering consolidation stress, forming the pores that are dominated by intergranular pores and residual intergranular pores. The pore throats in these samples become gradually narrowing due to the filling and blocking of the calcite cement, making the connectivity of the pores through the throats worse, and hence the microstructure becomes more and more complicated. When the cement content increases from 20 wt% to 25 wt% (Figure 8D), the rock structure turns from sand supporting to predominantly cement supporting with the sand grains floating in the calcite cement. The pores consist mainly of residual intergranular pores and micropores between the precipitated calcite grains, and the connectivity of the pore throats continues to reduce due to the uninterrupted filling and blocking of the calcite cement, making the pore structure increasingly complex. For the samples with cement content greater than about 25 wt% (Figures 8E,F), the rock structure is still supported by the calcite cement, but the pores are dominated by micropores between calcite grains. According the 'potential connectivity' theory proposed by Li (2013), the accumulation of the micropores will significantly improve the pore connectivity, leading to a dramatic reduction in the complexity of the pore structure.

It can be clear from the comprehensive analyses offered above that the variation in both porosity and microstructure (cementation exponent) of the samples will impact their elastic and electrical properties, and the microstructure is closely related to the cement content and the applied consolidation stress. Increasing porosity will reduce the elastic velocities and electrical resistivity, and on the other hand the increasing cement content and its associated reduction in the consolidation stress will respectively improve and reduce the cementation exponent, the increase in which shows strong positive correlation with the elastic and electrical rock properties (Glover, 2009; Han et al., 2020b). Since the above three parameters (i.e., porosity, cement content and cementation exponent) affect the physical properties in different ways, the obtained experimental results can be difficult to be explained directly from the variation in these parameters, but can help to infer their different contributions to the elastic and electrical properties.

Specifically, the weak reduction in the velocities and resistivity of the samples with calcite content increasing from 10 wt% to 15 wt% implies the contribution of the increasing porosity to reducing the elastic and electrical properties is dominant over the effects on increasing cementation exponent (for samples with calcite content less than about 25 wt%, the cementation exponent is dominated by the increasing cement content in comparison with the lowering consolidation stress) on improving the physical rock properties. When the cement content increases from 15 wt% to about 20 wt%, the improvement in the velocities and resistivity of the samples indicates the electrical properties are more subject to the porosity whereas the contribution of porosity to the elastic properties is less significant than that of the cementation exponent. For the samples with cement content increasing from 20 wt% to 25 wt%, their rapidly increasing velocities and

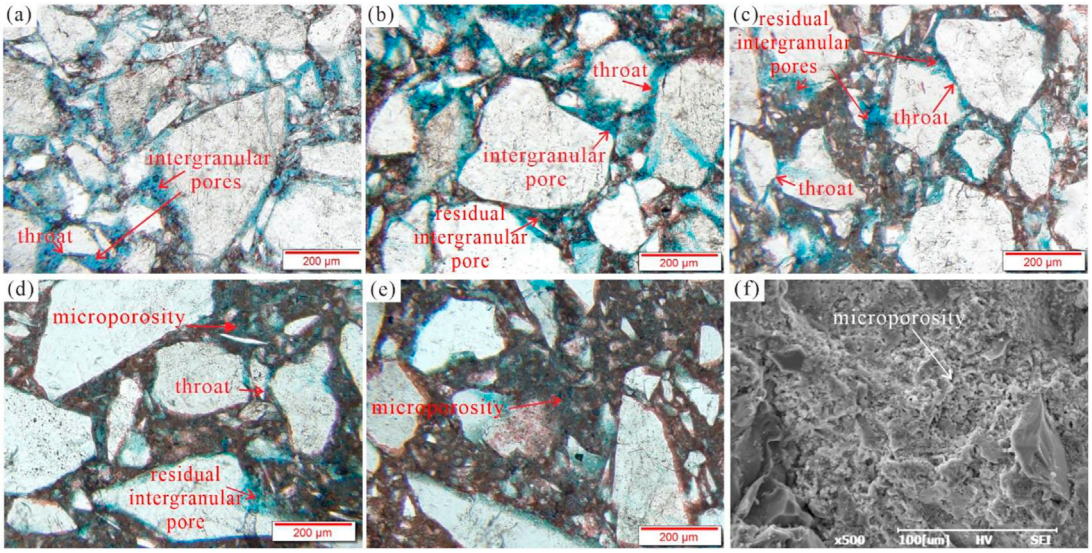

FIGURE 8
Typical thin section and scanning electron microscope (SEM) images of the samples with different cement content but with approximately the same porosity. Image **(A)**: cement content is 10 wt%, the structure is supported by the particles and the pores are dominated by intergranular pores. Image **(B)**: cement content is 15 wt%, the structure is supported by the particles and the pore system consists of intergranular pores and residual intergranular pores. Image **(C)**: cement content is 20 wt%, the structure is supported by the particles and the pore system mainly includes intergranular pores and residual intergranular pores. Image **(D)**: cement content is 25 wt%, the structure is supported by the cement and the pore system consists of residual intergranular pores and micropores. Image **(E)**: cement content is 30 wt%, the structure is supported by the cement. Image **(F)**: SEM image showing the development of micropores.

weakly decreasing resistivity suggests the impact of increasing cementation exponent on improving the velocities prevails over the influence of increasing porosity on reducing the velocities, whereas the impact of increasing cementation exponent on improving the resistivity is overwhelmed by the effects of the increasing porosity on reducing the resistivity. The porosity increases and the cementation exponent decreases in the samples with cement content exceeding about 25 wt% (as illustrated in Figure 6, Figure 7), and therefore their elastic and electrical properties should both reduce. The experimental results confirm the expected resistivity reduction, but show unexpected weak improvement in the elastic velocities. This might be possibly due to the fact that rock structure has changed from sand supporting to calcite supporting (as shown in Figure 8E). Since the elastic velocities of calcite are greater than that of sand, the increase in the calcite content may have covered up the combined effects of reducing consolidation stress and increasing porosity on decreasing the rock velocities.

5 Conclusion

We have studied quantitatively the effects of calcite cement and porosity on the P- and S-wave velocities and electrical resistivity of artificial calcite-cemented sandstones made using a new recipe. The experimental results demonstrate that the velocities reduce approximately linearly and the resistivity decreases exponentially with increasing porosity when the calcite cement content keeps constant in the samples. By contrast, the elastic and electrical properties are complexly affected by the cement content if porosity of the samples is roughly the same. Interpretation and analyses of the experimental results illustrate that the elastic and electrical rock properties are a combined result of porosity, the content and distribution of the calcite cement, as well as the microstructure of the samples caused by the variation in the applied consolidation stress. For the samples with cement content less than about 25 wt %, the calcite cement distributes mainly in the intergranular pores, and the elastic and electrical properties are affected predominantly by porosity, with the variation in the microstructure being the second order influencing parameter. On the other hand for the samples with greater content of calcite cement, the calcite turns to be the structure-supporting mineral, and therefore its impact on the microstructure becomes to play the dominant role over porosity in affecting the elastic and electrical properties. The results have revealed the mechanisms of how porosity and calcite cement affect the elastic and electrical properties of calcite cemented sandstones, and provided a theoretical basis for the accurate characterization of sandstone reservoirs through seismic and electromagnetic surveys.

Data availability statement

The raw data supporting the conclusion of this article will be made available by the authors, without undue reservation.

Author contributions

PW and TH conceive this research. PW implements the experiments, prepares the figures and writes the manuscript. TH reviews and supervises the manuscript. The co-author L-YF is involved in the discussion of the manuscript. All authors finally approve the manuscript and thus agree to be accountable for this work.

Funding

The research is supported by the National Natural Science Foundation of China (41821002, 42174136, 41874151), the Shandong Provincial Natural Science Foundation, China for distinguished young scientists (ZR2021JQ14), the Fundamental Research Funds for the Central Universities (22CX07004A), and the Science and Technology Fund Projects of PetroChina Company Limited (2021DJ1803).

Conflict of interest

The authors declare that the research was conducted in the absence of any commercial or financial relationships that could be construed as a potential conflict of interest.

Publisher's note

All claims expressed in this article are solely those of the authors and do not necessarily represent those of their affiliated organizations, or those of the publisher, the editors and the reviewers. Any product that may be evaluated in this article, or claim that may be made by its manufacturer, is not guaranteed or endorsed by the publisher.

References

Ajdukiewicz, J. M., and Larese, R. E. (2012). How clay grain coats inhibit quartz cement and preserve porosity in deeply buried sandstones: Observations and experiments. *AAPG Bull.* 96 (11), 2091–2119. doi:10.1306/02211211075

Al-Tahini, A. M., Sondergeld, C. H., and Rai, C. S. (2007). Effect of cementation on ultrasonic velocities in sandstones. *Geophysics* 72 (2), E53–E58. doi:10.1190/1.2431327

Archie, G. E. (1942). The electrical resistivity log as an aid in determining some reservoir characteristics. *Trans. AIME.* 146, 54–62. doi:10.2118/942054-G

Berryman, J. G. (1995). "Mixture theories for rock properties," in *Rock physics and phase relations*. Editor T. J. Ahrens (New York, NY, USA: Am. Geophys. U), 205–208. doi:10.1029/RF003p0205

Cai, J., Wei, W., Hu, X., and Wood, D. A. (2017). Electrical conductivity models in saturated porous media: A review. *Earth-Sci. Rev.* 171, 419–433. doi:10.1016/j.earscirev.2017.06.013

Constable, S. (2010). Ten years of marine CSEM for hydrocarbon exploration. *Geophysics* 75 (5), 75A67–75A81. doi:10.1190/1.3483451

Dejong, J. T., Fritzges, M. B., and Nüsslein, K. (2006). Microbially induced cementation to control sand response to undrained shear. *J. Geotech. Geoenviron. Eng.* 132 (11), 1381–1392. doi:10.1061/(asce)1090-0241

Ding, P., Di, B., Wei, J., Li, X., and Deng, Y. (2015). Experimental research on the effects of crack density based on synthetic sandstones contain controlled fractures. *Chin. J. Geophys.-Chinese Ed.* 58 (4), 1390–1399. doi:10.6038/cjg20150425

Dvorkin, J., Nur, A., and Yin, H. Z. (1994). Effective properties of cemented granular materials. *Mech. Mat.* 18 (4), 351–366. doi:10.1016/0167-6636(94)90044-2

Glover, P. (2009). What is the cementation exponent? A new interpretation. *Geophysics* 28 (1), 82–85. doi:10.1190/1.3064150

Han, D. H., Nur, A., and Morgan, D. (1986). Effects of porosity and clay content on wave velocities in sandstones. *Geophysics* 51 (11), 2093–2107. doi:10.1190/1.1442062

Han, T., Liu, S., Fu, L. Y., and Yan, H. (2021). Understanding how overpressure affects the physical properties of sandstones. *Geophysics* 86 (2), MR203–MR210. doi:10.1190/GEO2020-0776.1

Han, T., Liu, S., Xu, D., and Fu, L. Y. (2020a). Pressure-dependent cross-property relationships between elastic and electrical properties of partially saturated porous sandstones. *Geophysics* 85 (3), MR107–MR115. doi:10.1190/GEO2019-0477.1

Han, T., Wei, Z., and Fu, L. Y. (2020b). Cementation exponent as a geometric factor for the elastic properties of granular rocks. *Geophysics* 85 (6), MR341–MR349. doi:10.1190/geo2020-0250.1

Han, X., Guo, J., Li, F. B., Yang, L., and Tang, J. (2013). Modified acoustic velocity model for basal cemented loose sandstone based on contact cement theory. *J. China Univ. Pet. Ed. Nat. Sci.* 37 (04), 76–82. doi:10.3969/j.issn.1673-5005.2013.04.011

Harkes, M. P., Paassen, L., Booster, J. L., Whiffin, V. S., and Loosdrecht, M. C. M. V. (2010). Fixation and distribution of bacterial activity in sand to induce carbonate precipitation for ground reinforcement. *Ecol. Eng.* 36 (2), 112–117. doi:10.1016/j.ecoleng.2009.01.004

Ismail, M. A., Joer, H. A., Randolph, M. F., and Meritt, A. (2002a). Cementation of porous materials using calcite. *Géotechnique* 52 (5), 313–324. doi:10.1680/geot.52.5.313.38709

Ismail, M. A., Joer, H. A., Sim, W. H., and Randolph, M. F. (2002b). Effect of cement type on shear behavior of cemented calcareous soil. *J. Geotech. Geoenviron. Eng.* 128 (6), 520–529. doi:10.1061/(asce)1090-0241

Jarrard, R. D., Niessen, F., Brink, J. D., and Bücker, C. (2000). Effects of cementation on velocities of siliciclastic sediments. *Geophys. Res. Lett.* 27, 593–596. doi:10.1029/1999GL008429

Konstantinou, C., Biscontin, G., Jiang, N. J., and Soga, K. (2021). Application of microbially induced carbonate precipitation to form biocemented artificial sandstone. *J. Rock Mech. Geotech. Eng.* 13 (3), 579–592. doi:10.1016/j.jrmge.2021.01.010

Kucharski, E., Price, G., Li, H. Y., and Joer, H. A. (1997). Engineering properties of CIPS cemented calcareous sand. *Proc. 30th Int. Geol. Cong.* 23, 449–460. doi:10.1201/9780429087813-46

Li, N. (2013). *Introduction to logging interpretation of China marine carbonate rocks (in Chinese)*. Beijing, China: Science Press.

Mavko, G., Mukerji, T., and Dvorkin, J. (2009). *The rock physics handbook: Tools for seismic analysis of porous media*. 2nd ed. Cambridge, UK: Camb. Univ. Press. doi:10.1016/j.ijrmms.2011.08.002

Morad, S., Al-Ramadan, K., Ketzer, J. M., and Ros De, L. F. (2010). The impact of diagenesis on the heterogeneity of sandstone reservoirs: A review of the role of depositional facies and sequence stratigraphy. *AAPG Bull.* 94 (8), 1267–1309. doi:10.1306/04211009178

Morad, S. (2009). *Carbonate cementation in sandstones: Distribution patterns and geochemical evolution*. New jersey, NJ, USA: Blackwell Publishing Ltd. doi:10.1002/9781444304893.ch1

Muynck, W. D., Belie, N. D., and Verstraete, W. (2010). Microbial carbonate precipitation in construction materials: A review. *Ecol. Eng.* 36 (2), 118–136. doi:10.1016/j.ecoleng.2009.02.006

Palmén, A., Larsson, S., Axelsson, M., and Price, G. (2016). Low-temperature calcite precipitation in sand using CIPS. *Proc. ICEG. Ipv.* 169 (1), 1–6. doi:10.1680/grim.14.00009

Qian, C., Pan, Q., and Wang, R. (2010). Cementation of sand grains based on carbonate precipitation induced by microorganism. *Sci. China-Technol. Sci.* 53 (8), 2198–2206. doi:10.1007/s11431-009-3189-z

Sherlock, D. H., and Siggins, A. F. (2004). The development of synthetic CIPS sandstones for geophysical research. *ASEG Extend. Abs* 2003 (2), 1–5. doi:10.1071/aseg2003ab159

Si, W., Di, P., Wei, J., and Li, Q. (2016). Experimental study of water saturation effect on acoustic velocity of sandstones. *J. Nat. Gas. Sci. Eng.* 33, 37–43. doi:10.1016/j.jngse.2016.05.002

Tang, X., Song, Y., Fu, J., Li, Q., Fu, C., Xu, S., et al. (2016). Conductance mechanism and conduction model for tight shale-rich and calcite-rich sands. *Chin. J. Prog. Geophys.* 31 (4), 1660–1669. doi:10.6038/pg20160434

Tanner, R. S., Udegbunam, E. O., McInerney, M. J., and Knapp, R. M. (1991). Microbially enhanced oil recovery from carbonate reservoirs. *Geomicrobiol. J.* 9 (4), 169–195. doi:10.1080/01490459109385998

Wang, J., Cao, Y., Liu, K., Liu, J., Xue, X., and Xu, Q. (2016). Pore fluid evolution, distribution and water-rock interactions of carbonate cements in red-bed sandstone reservoirs in the Dongying Depression, China. *Mar. Pet. Geol.* 72, 279–294. doi:10.1016/j.marpetgeo.2016.02.018

Wang, B., Chen, X., Chen, J., Yao, J., and Tan, K. (2020). Elastic characteristics and petrophysical modeling of the Jurassic tight sandstone in Sichuan Basin. *Chin. J. Geophys.-Chinese Ed.* 63 (12), 4528–4539. doi:10.6038/cjg20200346

Wang, J., Cao, Y., Liu, H., and Gao, Y. (2015). Formation conditions and sedimentary model of over-flooding lake deltas within continental lake basins: An example from the paleogene in the jiyang subbasin, bohai bay basin. *Acta Geol. sin.-engl. Ed.* 89 (01), 270–284. doi:10.1111/1755-6724.12410

Wang, Z. (2001). Fundamentals of seismic rock physics. *Geophysics* 66 (2), 398–412. doi:10.1190/1.1444931

Wei, W., Cai, J., Hu, X., and Qi, H. (2015). An electrical conductivity model for fractal porous media. *Geophys. Res. Lett.* 42 (12), 4833–4840. doi:10.1002/2015GL064460

Yasuhara, H., Neupane, D., Hayashi, K., and Mitsu, O. (2012). Experiments and predictions of physical properties of sand cemented by enzymatically-induced carbonate precipitation. *Soils Found.* 52 (3), 539–549. doi:10.1016/j.sandf.2012.05.011

Zhao, X., Yang, S., Xiang, K., Chen, G., Zhu, C., and Wei, X. (2014). Oil-water inversion and its generation at top and bottom of the shallow sandstone reservoir in the Northern Chepaizi area, Junggar Basin, NW China. *Adv. Pet. Explor. Dev.* 41 (4), 485–491. doi:10.1016/s1876-3804(14)60055-0

frontiers | Frontiers in Earth Science

TYPE Methods
PUBLISHED 02 February 2023
DOI 10.3389/feart.2023.1126725

OPEN ACCESS

EDITED BY
Lidong Dai,
Institute of geochemistry (CAS), China

REVIEWED BY
Hongrui Xu,
Southwest Jiaotong University, China
Xiaozhou Yang,
China University of Geosciences Wuhan, China

*CORRESPONDENCE
Jinyan Zeng,
13903412202@163.com

SPECIALTY SECTION
This article was submitted to Geohazards and Georisks, a section of the journal Frontiers in Earth Science

RECEIVED 20 December 2022
ACCEPTED 13 January 2023
PUBLISHED 02 February 2023

CITATION
Guo M, Chen X and Zeng J (2023), Design method of frequency similarity relation for shaking table model test.
Front. Earth Sci. 11:1126725.
doi: 10.3389/feart.2023.1126725

Design method of frequency similarity relation for shaking table model test

Mingzhu Guo[1], Xudong Chen[1] and Jinyan Zeng[2]*

[1]Faculty of Urban Construction, Beijing University of Technology, Beijing, China, [2]Shanxi Earthquake Administration, Taiyuan, China

It is very important to determine the dynamic similarity relation in the shaking table model test. The accurate dynamic similarity relation can make the model reflect the dynamic characteristics of the prototype to the greatest extent. This paper describes the principle of similarity design for shaking table model test and reviews the related literature. According to the different research objects and purposes, four common similarity design methods including separation similarity method, artificial mass method, less artificial mass method and ignoring gravity method are summarized. Analysis of the shortcomings of the method of deriving frequency compression ratio from static factors in the design of seismic wave similarity relation. The Duhamel integral analytic expression of the structure motion equation under earthquake is analyzed. The seismic response of the structure is closely related to the natural vibration frequency of the structure. A design method using frequency as input seismic wave similarity design control quantity is proposed. The natural vibration frequencies of the prototype and the model are studied by means of the Gonza landslide field ground pulsation test and the model white noise excitation. A new frequency compression ratio design scheme is given from the perspective of dynamic similarity. It is of great reference significance to optimize the dynamic similarity design of shaking table model test and improve the accuracy of test results.

KEYWORDS

shaking table model test, principle of similitude, similarity solution, similarity design, rock slope

Introduction

Earthquake-induced building damage and secondary disasters such as landslide, collapse and mud-rock flow have attracted extensive attention because of their huge disaster causing force. China is a country with high-frequency earthquakes. In 1976, two strong earthquakes occurred in the area of Longling and Luxi of Yunnan Province, which caused serious surface damage, induced a large number of landslides and collapses. The resulting loss is far more than the earthquake itself. In 2008, a 8.0-magnitude earthquake occurred in Wenchuan, Sichuan Province. The number of earthquake-induced landslides investigated by the Ministry of Land and Resources was about 200, 000, causing huge economic losses and about 20,000 deaths (Kong et al., 2009; Xu et al., 2010). In 2010, the 7.1-magnitude Yushu earthquake triggered more than 2,000 landslides, debris flows and other geological disasters, with a total area of 1.194 km^2 (Xu et al., 2012). In 2013, a 7.0-magnitude earthquake hit Lushan, killing more than 100 people and triggering 1,678 geological disaster sites including landslides of varying degrees in Lushan and Baoxing counties, covering an area of 8.354 km^2 (Guo et al., 2014). Earthquakes and related geological disasters cause serious harm to people's lives and property. According to the existing earthquake damage data, researchers use different methods to explore the destruction mechanism of earthquake. Shaking table model test is widely used as a method to simulate

earthquake damage phenomenon and study dynamic response characteristics and failure law because of its intuitiveness and authenticity.

This paper expounds the principle of similarity design, reviews relevant previous studies, and analyzes four common similarity design methods. It is pointed out that most traditional methods derive the similarity ratio of each physical quantity only from static factors in the design of similar relation. Kinematic or dynamic factors are not sufficiently considered. In order to simulate the failure characteristic and response rule of prototype better and make the test results more in line with the actual situation. Therefore, it is necessary to optimize the design method of similarity relation. We propose that the method of determining the compression ratio of seismic wave is insufficient and give a new design scheme combined with shaking table test.

Three laws of similarity

The design of similarity relation is based on the three laws of similarity (Li et al., 2007).

The discipline of sibilism dates back to 1686, when Newton discussed similar conditions for fluid motion in his book *Philosophiae Naturalis Principia Mathematica.*

In 1822, French physicist Jean-Baptiste-Joseph Fourier put forward the concept of thermal similarity when studying heat conduction. It was not until 1848 that French scientist J. Bertrand elaborated the basic nature of similarity phenomenon based on the analysis of mechanical equations and put forward the first principle of similarity. The similar second theorem was later developed by Russian scholars αelman and American scholars E. Buckingham respectively. A similar third theorem was proposed by Soviet scientists M. B. Kirpichev and A. A. Guchman in 1930. So far, the first theorem of similarity and the second theorem of similarity give the necessary conditions of similarity, the third theorem of similarity gives the sufficient and necessary conditions of similarity, and the similarity theory forms a relatively complete theoretical system.

The first principle of similarity: For similar phenomena in mechanical systems, the similarity index is equal to 1, and the value of the similarity criterion is the same. There are two conditions for examining whether the phenomena occurring in two systems are similar: 1) The ratio of the corresponding physical quantity of similar phenomenon is constant, which is the concept of similar constant. 2) All the similar phenomena can be described by the same basic equation, so the similar constants such as C_L, C_V, C_a, C_t cannot be arbitrarily selected, and they will be restricted by the similarity index K. At the same time, the proportion relation between the corresponding physical quantities in the model and the prototype should be the same and equal to a constant π, which is called the similarity criterion. The second theorem of similarity: Basic physical equations that constrain two similar phenomena can be dimensionally analyzing, and the π equations of two similar systems must be identical. The π theorem is expressed as: There are n physical quantities describing a physical system, among which k physical quantities represent the basic quantities, and the other n−k physical quantities represent the derived quantities, and these quantities all have certain factors. Since the dimensions in any physical equation are homogeneous, the n quantities can be expressed as functional relationships between similar criteria.

The third theorem of similarity: For the same kind of physical phenomena, if the single valued quantities are similar, and the similar criteria composed of the single valued quantities are numerically equal, the phenomena are similar to each other. A single valued quantity refers to a physical quantity under a single valued condition, which separates an individual phenomenon from a similar phenomenon and turns the general solution of the phenomenon into a particular one. Single—valued conditions generally include: Geometric conditions, medium conditions, boundary conditions and initial conditions.

Similarity relation design method

Many scholars in this field have done a lot of work on the similarity relationship in shaking table model test (Lu and Chen, 2001; Song et al., 2004; Zhan et al., 2015; Zhao et al., 2015; Qian et al., 2016; Niu et al., 2017; Guo et al., 2021; Zhao et al., 2022). According to the different research objects and practical problems to be solved, a variety of methods to determine the similarity relationship are put forward (Lin et al., 2000; Lin and Wang et al., 2006; Li et al., 2020). Based on relevant literature, four common similar design methods in shaking table model tests are summarized and introduced as follows:

Wang et al. (2021a) and Wang et al. (2016) pointed out the shortcomings of the traditional dimensional analysis method in the design of similarity relation of shaking table model test for the interaction of multiple structures: It is not possible to distinguish the importance degree of different parameters of the test, the difference of similar relation design of different structures, or the importance degree of the same physical quantity to different structures of the model. Taking the shaking table test of slope reinforced by anchor cable and lattice beam as an example, the separation similarity design method is proposed. By separating the functional relation between each parameter, the key to the similar design of each structure is clarified, and the similarity relation of the key parameters of each part is solved. The importance of each research parameter to the similar material design is well distinguished. The method is also applied to the similar design process of shaking table model test for dynamic interaction of soil-underground pipeline corridor (Wang et al., 2021b). The similarity design is carried out according to the characteristics of soil mass, pipe corridor, contact surface and seismic wave respectively, and the similarity of the sub-subsystem of "contact interaction between media" is realized for the first time. Zhang et al. (2020) used the separation similarity design method to obtain the third-order characteristic equation when studying the interaction law of pile-soil-structure in the inclined site under earthquakes. The similarity ratio of key parameters, relevant parameters and irrelevant parameters of soil, structure and seismic wave is derived to directly guide the test design, which provides a theoretical basis for the similar design of shaking table of non-uniform soil-pile-structure system in the inclined site.

In the similar design of shaking table model test, such as large-span structure and high-rise building, due to the size of shaking table, most cases need to adopt the scaled model. It is extremely difficult to find high density materials that satisfy the density similarity relation: $S_\rho = S_E S_l^{-1}$. In the above expression, S_ρ, S_E and S_l are the similarity ratios of density, elastic modulus, and length, respectively. Therefore, many scholars in this field put forward a variety of test methods, among which the artificial mass similarity method is widely used.

Artificial mass similarity method is a special case based on the consistent similarity law (Zhang et al., 2003). This method changes the mass density of the model by artificially adding counterweights to the model to make it satisfy the similarity relation. Using length, elastic modulus and equivalent density as basic physical quantities, the similar relation of other parameters is derived by combining Π theorem and dimensionality analysis. Tian et al. (2017) carried out shaking table model test on a 220V large-span transmission line. Considering the large span of the pylon - line system, the design requirements of the scaled model cannot be realized under the existing test conditions, so the method of complete mass counterweight is used to balance the scaled model of the pylon - line system with large span. The proposed density similarity ratio of 1:1 is adjusted to the equivalent density similarity ratio of 20:1. Taking length, equivalent density and elastic modulus as control quantities, similar relationships of other physical quantities are derived. Several other scholars (Shi et al., 2006; Xie et al., 2014; Wei et al., 2018) also used the artificial mass method to guide the establishment of the model in the shaking table test of the large-span transmission tower-wire system.

In addition to using the above artificial mass model to solve the size and bearing capacity of the shaking table, some scholars also use the gravity ignoring similar design method to guide the experimental research. That is, the condition that the input acceleration similarity ratio is equal to the gravity acceleration similarity ratio is ignored to make the model meet the similarity requirement. Due to the lack of vertical stress, the error in the failure stage of the test is large and the gravity distortion effect is generated. Therefore, this method is only suitable for the elastic stage. Xie et al. (2019) carried out shaking table model test of steel-concrete frame structure with the ignored gravity model, and found that serious gravity distortion effect existed in the model test, leading to large errors in the test results. Wang and Li (2010) took the four-storey frame structure as an example and used the finite element software SAP2000 to carry out dynamic time-history analysis on the model ignoring gravity, and verified that the method could truly reflect the characteristics of the prototype in the elastic stage. Lu and Lu (2001) started from the Lame equation in solid mechanics and the Navier-stockes equation in Newton's viscous fluid mechanics. The dynamic similarity relation of shaking table model test of fluid-solid coupling system is deduced systematically, and a method of taking different values of three-dimensional direction of components is proposed to eliminate the gravity distortion effect.

The artificial mass model and the gravity ignoring model mentioned above solve the problems of limited size of the shaking table and difficulty in obtaining high-density materials. The former sets artificial mass to simulate the effect of total gravity and inertia force, while the latter does not set artificial mass and ignores the effect of gravity. Zhang (1997) have done a lot of research on the consistent similarity law, small-scale model similarity and nonlinear similarity, and proposed the less artificial mass method which can easily design the experimental model with arbitrary additional mass. In this method, the total weight of the model does not exceed the maximum bearing capacity of the shaking table by adding an appropriate amount of counterweight, and the method of ignoring gravity similarity design is avoided, which reduces the test error caused by gravity distortion effect. Huang et al. (1994) used two methods to deduce the dynamic similarity relationship between the model and prototype under different counterweight conditions, so as to provide a reliable quantitative method for correctly calculating the seismic performance of prototype under the condition of insufficient counterweight. Tao et al. (2010) established the equivalent density equation in order to solve the problem of structural counterweight in the shaking table test of subway structure, and studied the influence of different overlying soil thickness on the gravity effect by using the less artificial mass method. Under the premise of not changing the stiffness and mechanical properties of the structure, using the overlying soil layer and the artificial weight in the structure can improve the accuracy of the test results. Yang et al. (2007) took the three-story frame structure as an example, starting from the complete mass model, and considering the limitations of the bearing capacity of the shaking table, they adjusted the similarity relation, and derived the model similarity relation with incomplete counterweight. By comparing the derived values of the model and the calculated values of the prototype in the final test, it is concluded that under the less artificial mass method, the model and the prototype have a good similarity in the natural vibration period, the maximum acceleration of each layer, the lateral displacement, and the shear value of the structure base, which indicates that the less artificial mass model can also truly reflect the seismic behavior of the prototype in the elastic stage.

Frequency similarity ratio design

Shaking table model tests need to compress the duration of seismic waves, so the frequency of external loads and the strain rate of materials must be increased (Yin et al., 2010). However, with the increase of loading rate, the damage degree, failure mode, peak strength and deformation parameters of rock materials have nonlinear changes. Most of the similar relationships of dynamic parameters of current shaking table model tests (Zou et al., 2011; Yang et al., 2012; Ye et al., 2012a; Ye et al., 2012b; Huang et al., 2013; Hou, 2013; Li et al., 2014; Fan et al., 2015; Feng et al., 2018; Liu et al., 2019; Liu et al., 2020) are derived from static conditions of three basic physical quantities combined with dimensionality analysis and π determination, without sufficient consideration of dynamic factors.

At present, there are few studies on the dynamic response of the model under different frequency compression ratio of seismic waves. How to determine the frequency compression ratio more accurately is a problem to be further studied. Aiming at the dynamic response of slope under earthquakes, a new viewpoint on the determination of frequency similarity ratio is proposed.

Ground motion is a complex process that varies irregularly and rapidly over time. The earthquake acceleration time history is $\ddot{u}_g(t)$. The equation of structural motion under earthquake is $m\ddot{u} + c\dot{u} + ku = -m\ddot{u}_g$. The analytical expression of Duhamel integral can be used to solve the seismic response problem of linear elastic structures.The seismic equivalent load is $P_{eq}(t) = -m\ddot{u}_g(t)$. The displacement of structural seismic response is:

$$\begin{aligned} u(t) &= \int_0^t P_{eq}(\tau)h(t-\tau)d\tau \\ &= \frac{1}{m\omega_D}\int_0^t \left[-m\ddot{u}_g(\tau)\right]e^{-\xi\omega_n(t-\tau)}\,sin[\omega_D(t-\tau)]d\tau \\ &= -\frac{1}{\omega_D}\int_0^t \ddot{u}_g(\tau)e^{-\xi\omega_n(t-\tau)}\,sin[\omega_D(t-\tau)]d\tau \end{aligned}$$

In the above expression, $\omega_D = \omega_n\sqrt{1-\xi^2}$ is the natural vibration frequency of the damped system, ξ is the damping ratio of the structure, ω_n is the natural frequency of the structure.

By observing the above equation, we can see that for a given ground motion $\ddot{u}_g$, the seismic response of the structure is only related

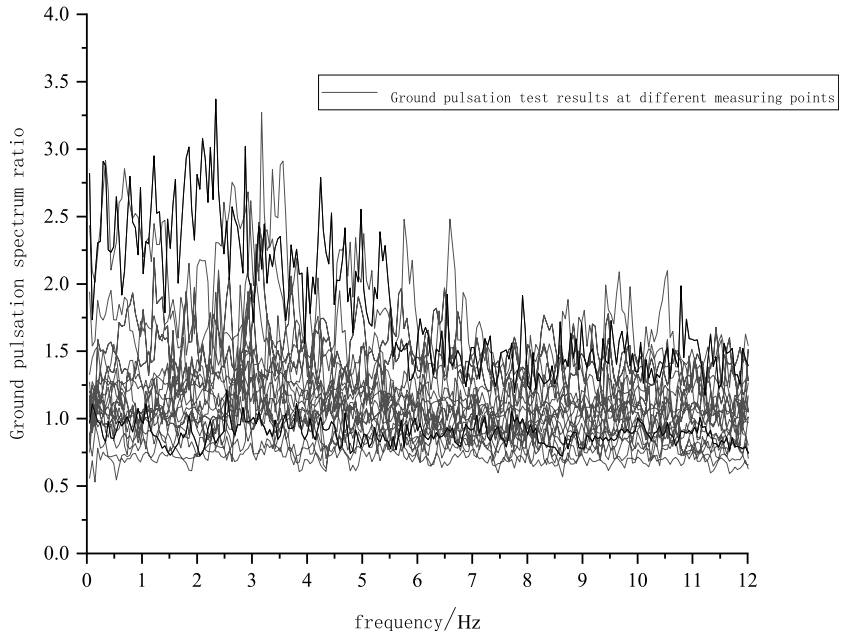

FIGURE 1
Ground pulsation test results.

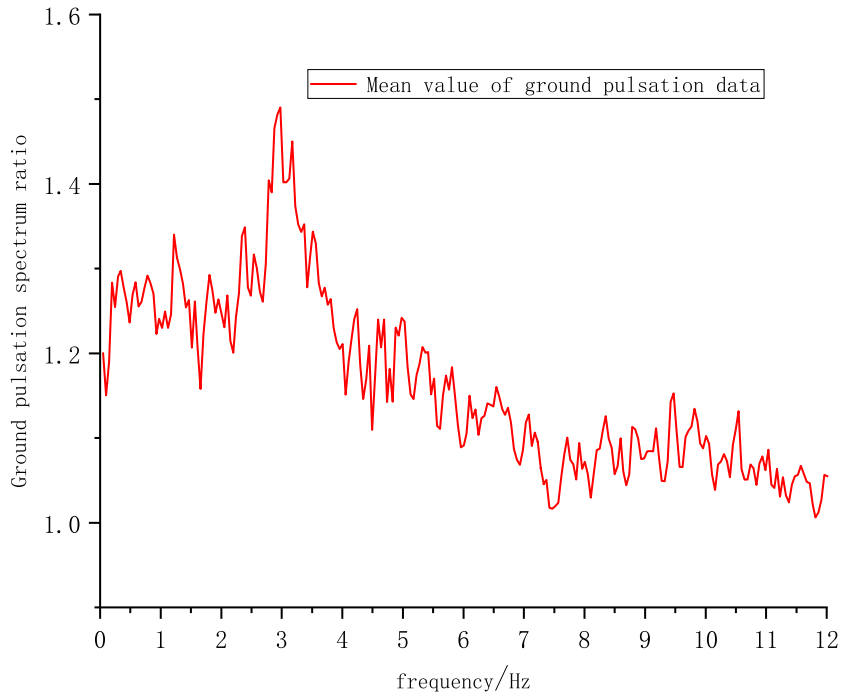

FIGURE 2
Mean value of ground pulsation test data.

to the damping ratio and the natural vibration frequency of the structure. That is, for different structures, when the damping ratio and natural vibration frequency of the structure are the same, the displacement response to the same earthquake is the same. Based on this, it is proposed that the damping similarity ratio between the model and the prototype in the shaking table test is 1 by the similarity of materials, the prototype natural vibration frequency is obtained by the field ground pulsation test or numerical simulation, and the natural vibration frequency of the model is obtained by the white noise scanning. The ratio of natural vibration frequency between the prototype and the model is taken as the frequency similarity ratio of seismic waves, and then the dynamic similarity relation of shaking

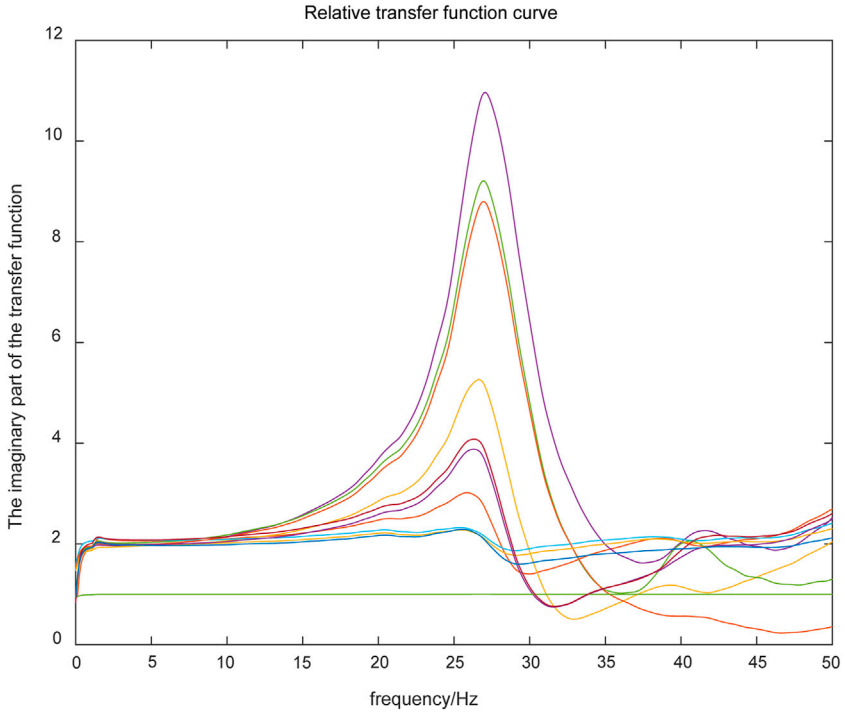

FIGURE 3
Relative transfer function curve.

TABLE 1 Similarity constants of similarity factor.

Name of physical quantity	Physical quantity symbol	Similarity factor
Length*(controlled quantity)	L	$C_L = 100$
Density	ρ	$C_\rho = C_\omega^{-2} C_L^{-1} = 0.83$
Gravitational acceleration* (controlled quantity)	g	$C_g = 1$
Duration	t	$C_t = C_\omega^{-1} = 9.09$
Amplitude	a	$C_a = 1$
Frequency	ω	$C_\omega = 0.11$

table model test is determined, which can reflect the dynamic response characteristics of the prototype under real earthquake more truly.

The author completed a shaking table model test with Gonza landslide in Soduoxi Township, Mangkang County, Qamdo Prefecture, Tibet Autonomous Region as the prototype. The author takes this landslide as the research object to carry out field measurement of ground pulsation, and uses Matlab program to carry out data extraction, separation, filtering and analytical calculation, so as to draw ground pulsation spectrum of the prototype of Gonza landslide, as shown in Figure 1. The average value of multiple ground pulsation data is obtained as shown in Figure 2. And according to the frequency corresponding to the maximum point, the natural vibration frequency of the landslide prototype is determined to be 2.97 Hz. The experiment was carried out in the structural mechanics Laboratory of Beijing University of Technology. The model was made, the measuring point was arranged and the ground motion input was completed. At the beginning of the experiment, we input 0.1g white noise to scan the model, test the dynamic characteristics of the model at the initial stage and use Matlab relative transfer function to process the data. As shown in Figure 3, the natural vibration frequency of the model after excitation is determined to be 27.1Hz according to the peak value of the curve. The ratio of natural vibration frequency between the prototype and the model is 0.11. In the processing stage of test results, the similarity design of seismic waves is carried out by combining the separation similarity design method. Length(L), gravity acceleration(g) and frequency(ω) are selected as basic physical quantities to derive the similarity relationship of other physical quantities. The specific values are shown in Table 1. The similarity relationship determined by this method provides a valuable reference for the follow-up experiment.

Conclusion

(1) This paper summarizes four common similarity design methods, separation similarity design method, artificial mass method, gravity ignoring similar design method and less artificial mass method. When determining the similarity ratio, the similarity

design method should be selected reasonably according to the research purpose and equipment condition. For the shaking table model test of the interaction of various structures, the separation similarity design method can be selected. For the large-span structure model or high-rise structure model, the artificial mass method can be selected when the shaking table bearing capacity is high, and the less artificial mass model can be selected when the shaking table bearing capacity is insufficient. For the shaking table test to study the seismic response of the elastic stage of the model, the gravity ignoring similar design method can be chosen.

(2) Based on the field ground pulsation test and shaking table model test data of Gonza slope, the frequency similarity ratio between the prototype and the model is determined to be 0.11. Length, gravity acceleration and frequency are selected as control quantities to satisfy geometric similarity, kinematic similarity and dynamic similarity, and the similarity ratio of each physical quantity of seismic wave determined by the new design method is derived. The new method makes up for the shortcomings of dynamic similarity design in shaking table model tests, provides a new idea for determining the frequency similarity ratio of seismic waves, and is of great significance for optimizing the similarity relationship and improving the accuracy of test result.

Data availability statement

The original contributions presented in the study are included in the article/Supplementary Material, further inquiries can be directed to the corresponding author.

Author contributions

Conceptualization, MG; investigation, XC; writing—original draft preparation, MG and XC; writing—review and editing, MG, XC, and JZ; supervision, JZ; and funding, JZ. All authors listed have made a substantial, direct, and intellectual contribution to the work and approved it for publication.

Funding

Funding for this work was supported by the National Key Research and Development Program (2018YFC1505001).

Conflict of interest

The authors declare that the research was conducted in the absence of any commercial or financial relationships that could be construed as a potential conflict of interest.

Publisher's note

All claims expressed in this article are solely those of the authors and do not necessarily represent those of their affiliated organizations, or those of the publisher, the editors and the reviewers. Any product that may be evaluated in this article, or claim that may be made by its manufacturer, is not guaranteed or endorsed by the publisher.

References

Fan, G., Zhang, J., and Fu, X. (2015). Large-scale shaking table test on dynamic response of anti-dip rock slope with argillated interlayer [J]. *J. Earthq. Eng.* 37 (02), 422–427. doi:10.3969/j.issn.1000-0844.2015.01.0422

Feng, X., Jiang, Q., Zhang, H., Jiang, J., Peng, Z., and Jiang, W. (2018). Shaking table test on seismic response of rock slope. Vibration. *J. Meas. Diagnosis* 38 (03), 575–582. doi:10.16450/j.cnki.issn.1004-6801.2018.03.022

Guo, M., Zou, Y., and Sun, H. (2021). Similarity theory analysis of shaking table model test [J]. *J. Shenyang Jianzhu Univ. Nat. Sci. Ed.* 37 (04), 594–601. doi:10.11717/j.issn:2095-1922.2021.04.03

Guo, Z., Tong, L., Zheng, X., Qi, J., and Wang, J. (2014). Remote sensing investigation and characteristics of post-earthquake geological disasters in Lushan, Sichuan Province [J]. *Remote Sens. Land Resour.* 26 (03), 99–105. doi:10.6046/gtzyyg.2014.03.16

Hou, H. J. (2013). *Shaking table test study on ground motion response characteristics of horizontal layered slope [D]*. Chengdu: Chengdu University of Technology.

Huang, R., Guo, L., and Ju, N. (2013). Shaking table test on strong seismic response of layered rock slope [J]. *Chin. J. Rock Mech. Eng.* 32 (05), 865–875.

Huang, W., Wu, R., and Zhang, Q. (1994). Discussion on the similar relationship between dynamic test model and prototype in case of insufficient counterweight [J]. *Earthq. Eng. Eng. Vib.* (04), 64–71. doi:10.13197/j.eeev.1994.04.008

Kong, J., Fa-You, A., and Wen-ping, W. U. (2009). Analysis of landslide types and typical cases in Wenchuan earthquake [J]. *J. Soil Water Conservation* 23 (06), 66–70. doi:10.13870/j.cnki.stbcxb.2009.06.006

Li, P., Liu, Y., Zhou, K., Zhu, S., and Li, Y. (2020). Review on similar design of shaking table model test [J]. *J. Disaster Prev. Sci. Technol. Inst.* 22 (04), 29–35.

Li, X. H., Lu, Y. Y., Kang, Y., et al. (2007). *Experimental simulation technology of rock mechanics*. Beijing: Science Press, 3–24.

Li, Y., Li, T., and Niu, Z. (2014). Shaking table test study on dynamic response characteristics and failure process of slope [J]. *Hydropower Energy Sci.* 32 (01), 93–95.

Lin, G., Zhu, T., and Lin, B. (2000). Similarity technique of structural dynamic model test [J]. *J. Dalian Univ. Technol.* (01), 1–8. doi:10.3321/j.issn:1000-8608.2000.01.001

Lin, M-L., and Wang, K. (2006). Seismic slope behavior in a large-scale shaking table model test. *Eng. Geol.* 86 (2–3), 118–133. doi:10.1016/j.enggeo.2006.02.011

Liu, H., Zheng, G., Wang, Z., Niu, L., and Xu, F. (2019). Study on dynamic response of anti-dip rock slope and influence of ground motion parameters [J]. *J. North China Univ. Water Resour. Electr. Power (Natural Sci. Ed.* 40 (04), 70–76. doi:10.19760/j.ncwu.zk.2019054

Liu, Y., Ma, S., Zhang, L., Guo, X., and Chen, W. (2020). Study on dynamic stability of bedding rock slope under earthquake [J]. *Railw. Constr.* 60 (12), 97–100. doi:10.3969/j.issn.1003-1995.2020.12.23

Lu, L., and Lu, X. (2001). Dynamic similarity relationship for eliminating gravity distortion effect in shaking table model test [J]. *Struct. Eng.* (04), 45–48. doi:10.15935/j.cnki.jggcs.2001.04.009

Lu, X., and Chen, Y. (2001). "Study on dynamic similarity relationship of structure-ground interaction system [J]," in *Earthquake engineering and engineering vibration*. Editors X. Z. Qi and G. C. Lee (Berlin: Springer) (03), 85–92. doi:10.13197/j.eeev.2001.03.016

Niu, L., Liu, H., Wang, Z., Yuan, F., and Ning, C. (2017). Dynamic Response and Deformation failure of slope shaking table model test review [A]. *Ind. Archit. Mag.*, 314–317. MAR - APR 2017.

Qian, D., Zhang, Z., Dai, Q., Yang, Y., Jiang, Y., and Qian, L. (2016). Research on the design of shaking table test model of overlimit high-rise building structure [J]. *Ind. Build.* 46 (02), 36–41. doi:10.13204/j.gyjz201602009

Shi, W., Li, H., and Jia, L. (2006). "Shaking table test of transmission pylon and conductor coupling system model [J]," in *Engineering mechanics*. Editors P. C. Dumir and S. Sengupta (Hyderabad: ORIENT BLACKSWAN), 89–93.

Song, Y., Zhang, G., and Dang, X. (2004). Expansion and analysis of similarity Theory [J]. *J. Lanzhou Univ. Technol.* (05), 123–125. doi:10.3969/j.issn.1673-5196.2004.05.034

Tao, L., Zhang, B., and Wang, W. (2010). "Underweight weight model for shaking table test of subway structure [C]," in Proceedings of the 8th National Conference on Earthquake Engineering (II), 314–315+332.

Tian, L., Niu, Y., Ma, R., Li, X., Yi, S., Xin, A., et al. (2017). Design and research of shaking table test model of long-span transmission tower-line coupling system [J]. *World Earthq. Eng.* 33 (03), 42–50.

Wang, B., and Li, X. (2010). Research on similarity relationship of shaking table test model with ignoring gravity influence [J]. *Shanxi Archit.* 36 (21), 77–78. doi:10.3969/j.issn.1009-6825.2010.21.048

Wang, Z., Fan, G., Cao, L., and Chang, J. (2021a). An isolated similarity design method for shaking table tests on reinforced slopes. *J. Mt. Sci.* 18 (9), 2460–2474. doi:10.1007/s11629-020-6398-3

Wang, Z., Li, S., He, X., Yin, T., and Wang, Z. (2021b). Similarity design method of model test system based on separation dimension analysis theory: Taking shaking table test of soil-underground pipeline corridor as an example [J]. *Chin. J. Rock Mech. Eng.* 40 (12), 2553–2569. doi:10.13722/j.cnki.jrme.2020.1166

Wang, Z., Zhang, J., Fu, X., Yan, K., Wang, M., and Peng, S. (2016). "Separation similarity design method for model test: A case study of slope reinforced by anchor cable lattice [J]," in *Rock and soil mechanics*. Editor W. Derski (Amsterdam: Elsevier), 2617–2623. doi:10.16285/j.rsm.2016.09.025

Wei, W., Liu, K., and Wang, H. (2018). Study on seismic effects of transmission tower line coupling system [J]. *J. Wuhan Univ. Technol.* 40 (08), 88–93.

Xie, J., Hu, Y., Bao, S., Ni, Y., Duan, L., and Zhang, H. (2019). Similarity ratio design of gravity distortion model for a steel-concrete frame structure [J]. *J. Hebei Inst. Civ. Eng. Archit.* 37 (02), 43–45+50. doi:10.3969/j.issn.1008-4185.2019.02.011

Xie, X., Tan, Y., Dan, L., and Long, H. (2014). Design and analysis of test model of pylon line system based on dynamic similarity [J]. *J. Hunan Univ. Sci. Technol. Nat. Sci. Ed.* 29 (04), 48–53. doi:10.13582/j.cnki.1672-9102.2014.04.010

Xu, C., Dai, F., and Xu, X. (2010). Wenchuan earthquake-induced landslides: An overview. *Geol. Rev.* 56 (06), 860–874.

Xu, C., Xu, X., and Yu, G. (2012). Investigation on distribution, characteristics and formation mechanism of Yushu earthquake landslide [J]. *Seismol. Geol.* 34 (01), 47–62. doi:10.3969/j.issn.0253-4967.2012.01.006

Yang, G., Wu, F., Dong, J., and Qi, S. (2012). Dynamic response characteristics and deformation failure mechanism of rock slope under earthquake [J]. *Chin. J. Rock Mech. Eng.* 31 (04), 696–702. doi:10.3969/j.issn.1000-6915.2012.04.007

Yang, S., Li, R., Liu, J., and Di, Q. (2007). Theoretical research on similarity relationship between shaking table test model and prototype [J]. *J. Hebei Univ. Technol. Nat. Sci. Ed.* (01), 8–11. doi:10.3969/j.issn.1673-9469.2007.01.003

Ye, H., Zheng, Y., Du, X., and Li, A. (2012b). Shaking table model test and Numerical Analysis of dynamic failure Characteristics of slope [J]. *J. Civ. Eng.* 45 (09), 128–135.

Ye, H., Zheng, Y., Li, A., and Du, X. (2012a). Shaking table test of prestressed anchor cable in slope under earthquake [J]. *Chin. J. Rock Mech. Eng.* 31 (S1), 2847–2854. doi:10.3969/j.issn.1000-6915.2012.z1.032

Yin, X., Ge, X., Li, C., and Wang, S. (2010). Influence of loading rate on mechanical behavior of rock materials [J]. *Chin. J. Rock Mech. Eng.* 29 (S1), 2610–2615. Available at: http://ir.casnw.net/handle/362004/20203.

Zhan, Z., Qi, S., Zheng, B., and Zou, Y. (2015). Simulation of slope shaking table model test [J]. *Geol. Rev.* 61 (S1), 127–128.

Zhang, L., Zhou, Y., Wang, Z., Yu, F., and Yan, K. (2020). "Shaking table Test and Numerical Analysis of non-uniform soil-pile-structure seismic interaction in inclined field [J]," in *Earthquake engineering and engineering vibration* (Berlin: Springer), 224–236. doi:10.13197/j.eeev.2020.05.224.zhanglm.024

Zhang, M., Meng, Q., and Liu, X. (2003). Experimental study on seismic simulation of building structures [J]. *J. Seismic Eng.* (04), 31–35. doi:10.3969/j.issn.1002-8412.2003.04.008

Zhang, M. (1997). Some problems on the application of similarity law in seismic simulation experiments [J]. *Earthq. Eng. Eng. Vib.* (02), 52–58.

Zhao, F., Yu, S., Bo, L., and Shi, Z. (2022). Research progress of large-scale shaking table test of rock slope under earthquake [J]. *Earth Sci.*, 1–13. doi:10.3799/dqkx.2022.317

Zhao, J., Wang, H., Liu, X., Chen, N., Liu, Q., Yang, Z., et al. (2015). Seismic response analysis and evaluation of high Earth rock dam under different input seismic waves [J]. *J. Hydroelectr. Power* 34 (01), 169–174+196.

Zou, W., Xu, Q., Liu, H., Chen, L., and Wang, L. (2011). Large shaking table test study on failure of understory rock slope under strong earthquake [J]. *Earthq. Eng. Vib.* 31 (04), 143–149. doi:10.13197/j.eeev.2011.04.006

frontiers | Frontiers in Earth Science

TYPE Original Research
PUBLISHED 15 February 2023
DOI 10.3389/feart.2023.1117193

OPEN ACCESS

EDITED BY
Qiaomu Qi,
Chengdu University of Technology, China

REVIEWED BY
Liang Wang,
Chengdu University of Technology, China
Wenlian Xiao,
Southwest Petroleum University, China

*CORRESPONDENCE
Guangzhi Liao,
liaoguangzhi@cup.edu.cn

SPECIALTY SECTION
This article was submitted to Solid Earth Geophysics, a section of the journal Frontiers in Earth Science

RECEIVED 06 December 2022
ACCEPTED 19 January 2023
PUBLISHED 15 February 2023

CITATION
Fan R, Liao G, Mao R, Luo X, Hou L, Zhang H, Tian H, Wang G, Qin Z and Xiao L (2023), Nuclear magnetic resonance response characteristics and quantitative evaluation method of fluid saturation of lacustrine shale oil.
Front. Earth Sci. 11:1117193.
doi: 10.3389/feart.2023.1117193

Nuclear magnetic resonance response characteristics and quantitative evaluation method of fluid saturation of lacustrine shale oil

Ruiqi Fan[1], Guangzhi Liao[1]*, Rui Mao[2], Xingping Luo[2], Lianhua Hou[3], Hao Zhang[2], Hua Tian[3], Gang Wang[2], Zhijun Qin[2] and Lizhi Xiao[1]

[1]State Key Laboratory of Petroleum Resources and Prospecting, China University of Petroleum, Beijing, China, [2]Research Institute of Exploration and Development, Xinjiang Oilfield Company, Karamay, Xinjiang, China, [3]PetroChina Research Institute of Petroleum Exploration and Development, Beijing, China

The quantitative evaluation of fluid saturation is important for formation evaluation of shale oil. However, there is currently no effective method to identify the fluid occurrence state and quantitative evaluate the fluid saturation of lacustrine shale oil because of the complexity of diagenetic minerals and pore types. In this paper, a method is proposed for the quantitative evaluation of fluid saturation based on nuclear magnetic resonance (NMR), X-ray diffraction (XRD) and scanning electron microscopy (SEM) measurements for shale samples of Fengcheng Formation, Mahu sag in Junggar Basin, China. These studies revealed that the shale oil rocks mainly contain quartz, feldspar, dolomite, calcite and clay minerals, both develop organic and inorganic pores. The fluids mainly occur in the form of bitumen, clay bound water, bound water, bound oil and movable oil in this study area. Based on the findings from these experiments, a mixed rock index (MI) and mud index (SI) were proposed to divide the shale oil formations into three types, including sand shale, dolomitic shale and mudstone. A T_1–T_2 2D NMR fluid occurrence state characterization map was established to identify the different fluids by the MI, SI and NMR characteristics. Furthermore, a method was proposed to quantitatively calculate the coefficient distribution of bound and movable fluids for shale oil in different formations. Finally, the proposed method was successfully applied into the lacustrine shale oil in the Fengcheng Formation to identify fluid occurrence state and evaluate fluid saturation quantitatively.

KEYWORDS

T_1-T_2 NMR, fluid occurrence state, fluid saturation, lacustrine shale oil, quantitative evaluation

1 Introduction

Lacustrine shale oil is widely distributed in lacustrine lake basins, such as Ordos Basin, Junggar Basin, China; Uinta Basin, America; Cooper Basin, Chad Bongor Basin, Australia; Sumatra Basin, Indonesia; Paris Basin, France; et al. (EIA, 2015; Zou et al., 2022) It has become an important field of petroleum resource exploration and development in current. However, due to the complexity diagenetic minerals and pore types, there is no effective method to quantitatively evaluate the fluid saturation and characterize fluid occurrence state of shale oil (Cao et al., 2020; Tang et al., 2020; Guan et al., 2022). Thus, the highlights of current research is

the diverse pore types and complex fluid occurrence states which are important to evaluate oil-bearing accurately for shale oil exploration.

NMR has emerged as a key measurement for characterizing the fluid components of shale oil in downhole logging and laboratory studies. Different fluids have different T_1/T_2 ratio and T_2 relaxation time, and different T_2 relaxation time reflect different size of the pores. Thus, T_1-T_2 NMR can obtain more information on the fluid composition and pore types in shale oil. It can identify the fluid component of kerogen, bitumen, light/heavy oils, gases and brine in the formations and characterize the pore types of shale oil (Ge et al., 2015; Jia et al., 2017; Song and Kausik, 2019; Guo et al., 2020; Jin et al., 2021).

Researchers have done a lot of work in the two-dimensional NMR evaluation methods of shale oil. First, many NMR T_1-T_2 interpretation maps have been proposed to distinguish fluid occurrence states and quantitative evaluate the fluids volume for shale oil and gas, such as the universal NMR T_1-T_2 map for all the different constituents of gas and tight-oil shale at 2 MHz for US shales (Kausik et al., 2016), T_1-T_2 pattern of oil-bearing shale fluid or protons (Zhang et al., 2020b), the illustration of the low-field T_1-T_2 map for all the components in gas-shale (Zhou et al., 2020), the time-elapsed NMR T_1-T_2 map for shale oil core at 22 MHz (Li et al., 2022). Moreover, blind source separation (BBS) algorithm and non-negative matrix factorization (NMF) have been employed to determine free oil saturation in recent studies (Venkataramanan et al., 2018). Base on blind source separation (BBS) algorithm, the volume fractions of shale oil can be computed by hierarchical clustering; a method of fast independent component analysis (FastICA) was proposed for the inverted NMR spectrums to obtain the fluid components of shale oil; a method of two-dimensional (2D) principal component analysis (PCA) was proposed to quantitative evaluate the T_1-T_2 signatures of different fluids (Zhang H. et al., 2020; Gu et al., 2021; Gu et al., 2022). However, none of these studies dealt with the influence of complex lithology on the 2D NMR evaluation model for shale oil.

In this paper, aiming at the influence of complex lithology on shale oil, we use mixed rock index (MI) and mud index (SI) to divide the shale oil formations. A T_1-T_2 map of fluid occurrence state of shale oil was proposed by the NMR characteristics and MI value. Based the T_1-T_2 map, a 2D T_1-T_2 NMR quantitative calculation method was proposed to evaluate the movable oil saturation. The results show that the proposed method can be used to identify the fluid occurrence state and to evaluate shale oil-bearing quantitatively.

2 Geological setting

Mahu Sag is located on the northwestern edge of Junggar Basin in west China. It is mainly composed of Wuxia fault zone and part of the western slope, with an area of about 2039 km^2 (Zou et al., 2022). Fengcheng Formation (P_1f) is the main source rock reservoir of Mahu Sag. From top to bottom, Fengcheng Formation can be divided into Feng 3 (P_1f_3), Feng 2 (P_1f_2) and Feng 1 (P_1f_1), which mainly sand shale and dolomitic shale (Figure 1). The Fengcheng Formation shows a complex lithological assemblage, which belongs to the mixed rock. It is the main target of shale oil exploration and development in Mahu Sag (Hu et al., 2020). There are 3 sets of sweet spots in Fengcheng Formation, which are characterized by scattered sweet spots and thin oil layers (Li et al., 2020) The porosity of the reservoir is 1% ~ 13%, with an average of 4.4%, and the permeability is mostly less than 0.1mD.

3 Experiments and method

3.1 Experiments

Shale oil rock samples were cut and prepared from Well W1 and Well W2 in Fengcheng Formation. Each sample was divided into 3 parts. Part 1 crushed for X-ray diffraction (XRD) analysis. Part 2 was made into thin slices for rock slice analysis and FE-SEM experiments. Part 3 was for the analysis of T_2 and T_1-T_2 NMR experiments. The experiment results are shown in Table A1 (Appendix A).

NMR experiments were performed on NMR rock analyzer (2 MHz, Magritek). The instrument was operated at 30°C with a magnetic field strength of 0.05T and a frequency of 2 MHz. These experiments used CPMG and IR-CPMG pulse sequences to obtain T_2 and T_1-T_2 maps (Hürlimann, 2001). The testing parameters for T_2 were 100 us echo spacing time, 2 s waiting time, 128 scans, and 4,000 echoes. The testing parameters for 2D T_1-T_2 were 100 us T_2 echo spacing time, 2 s waiting time, 64 scans, 4,000 echoes, 0.1 ms T_1 editing start time, 2000 ms T_1 editing stop time.

(1) Original shale samples were subjected to NMR T_2 distribution and T_1-T_2 map testing.
(2) After saturation, the mass of the saturated oil shales was measured.
(3) After oil washing, the mass of the dry shales was measured. Before the NMR T2 distribution and T1-T2 map tests, the shales were heated at 80°C for 24 hours. The organic solvent used in shale core washing experiment is a mixed solution of dichloromethane and methanol.
(4) After saturation, the mass of the re-saturated oil shales was measured. The fluids used in shale oil core saturation experiments are all crude oil taken from Fengcheng Formation, Mahu.

3.2 Method

This paper aims to evaluate fluid occurrence state and fluid saturation of lacustrine shale oil in Fengcheng Formation. We proposed a reservoir classification method [mixed rock index (MI) and mud index (SI)] to divide formations to eliminate the influence of complex lithology for shale oil. And a formation classification method was proposed to divide the shale oil formations into three types, including sand shale, dolomitic shale, and mudstone by the MI and SI. Based on the 2D T_1-T_2 NMR experiments and formation classification results, a characterization model of fluid occurrence state was established to identify fluids component and quantitative evaluate fluids saturation. Finally, a workflow of the proposed method for the quantitative evaluation of fluid saturation of lacustrine shale oil was established (Figure 2).

4 Results

4.1 Composition and structural characteristics of shale oil

The results of the mineral compositions of shale samples are listed in Table A1 (Appendix A). Mineral compositions are dominated by quartz, feldspar, clay minerals, dolomite, calcite and pyrite. Carbonate minerals

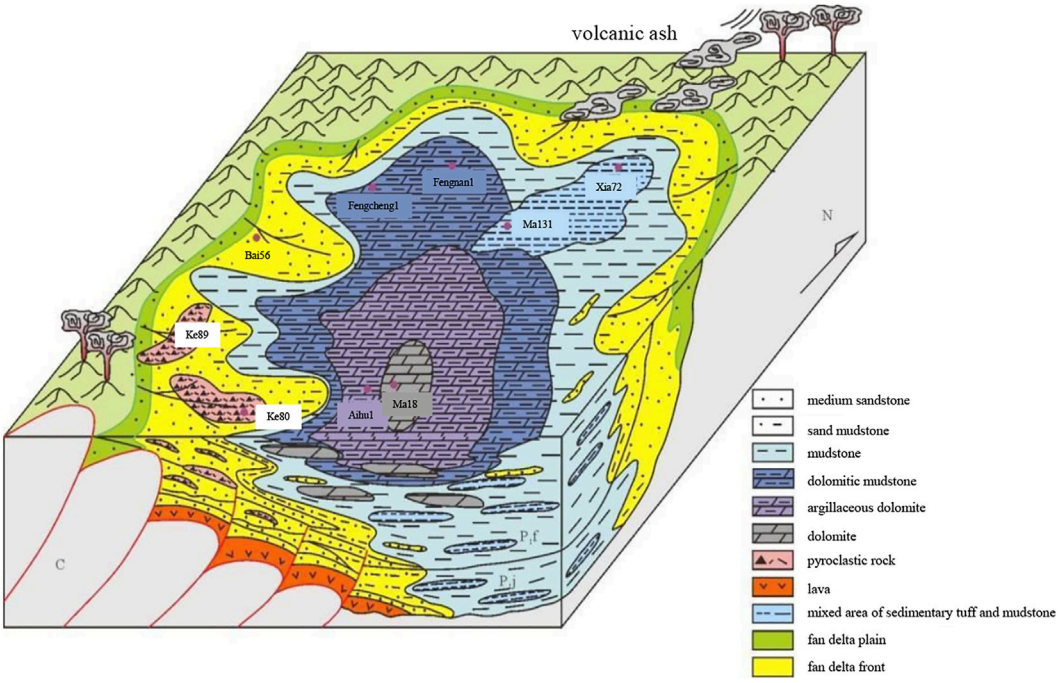

FIGURE 1
Alkaline-lake mixed sedimentary model in Mahu Sag (Kuang et al., 2012).

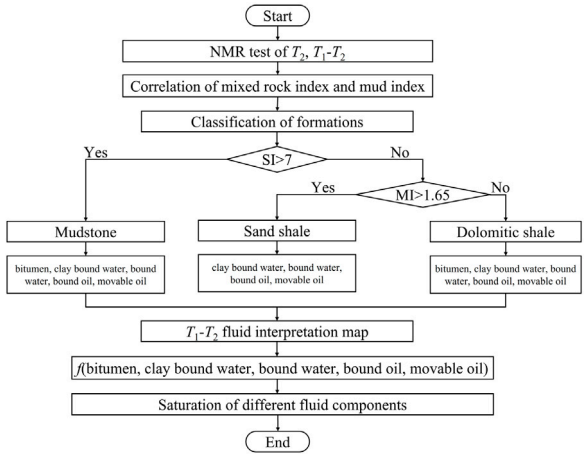

FIGURE 2
Workflow of the proposed method for the quantitative evaluation of fluid saturation of lacustrine shale oil.

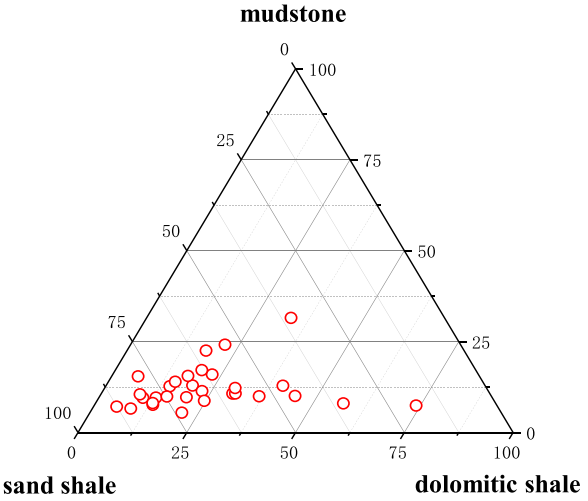

FIGURE 3
The rock type of Fengcheng Formation includes carbonate rocks, tight sandstones, sedimentary tuffs and mixed sedimentary rock.

(dolomite and calcite) ranges from 8.5% to 70.9%, with an average of 22.89%. Clay minerals content is low which ranges from 5.4% to 24.1%, with an average value of 11.85%. The main clay minerals types are montmorillonite, illite montmorillonite mixed layer, chlorite montmorillonite mixed layer and illite. Montmorillonite content is 5% ~ 88%, with an average of 31.8%. Illite montmorillonite mixed layer is between 18% and 85%, with an average of 26.37%. Chlorite montmorillonite mixed layer is between 11% and 77%, with an average of 15.6%. Illite content is 6% to 30%, with an average value of 17.2%. The TOC content ranges from 0.01 wt% to 1.07 wt%, with an average value of 0.38 wt%, shows a low organic matter content.

Based on the findings from these experiments, the rock type of Fengcheng Formation includes carbonate rocks, tight sandstones, and mixed sedimentary rock (Figure 3). Moreover, the Feng 3 (P_1f_3) mainly sand shale, the content of felsic minerals is the highest, followed by carbonate minerals. And the Feng 2 (P_1f_2) mainly dolomitic shale, the content of carbonate minerals is the

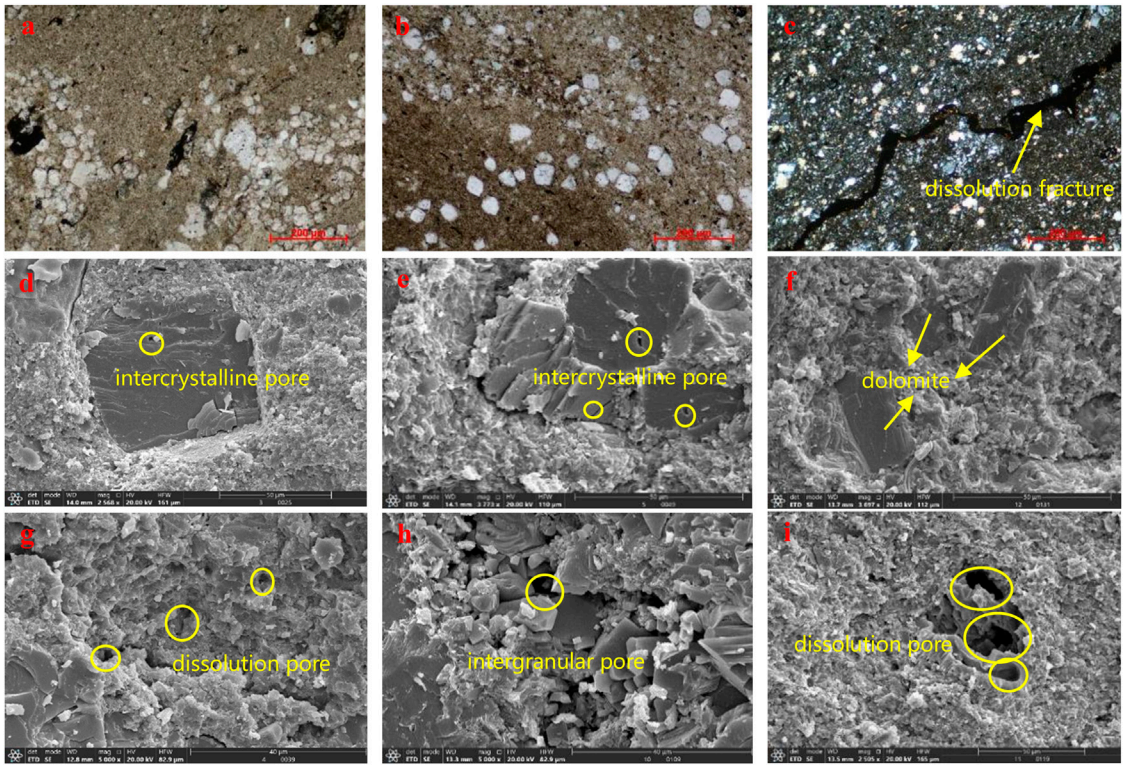

FIGURE 4
Microscopic characteristics of Fengcheng Formation. **(A)** Dolomite argillaceous anisotropic sandstone with a small amount of organic residues; **(B)** Dolomite-bearing mudstone, dust-spot-like, silk-like organic matter residues; few dissolved pores; **(C)** Dolomite sandy mudstone, 3 dissolution fractures, the fracture width is 0.01–0.04 mm; **(D)** Microcrystalline dolomite, intercrystalline pores (SEM); **(E)** Intercrystalline pores (SEM); **(F)** Dolomite and feldspar crystals (SEM); **(G)** Dissolved pores (SEM); **(H)** Intercrystalline pores and intergranular pores (SEM); dissolved pores (SEM).

TABLE 1 Classification of shale oil reservoirs in Fengcheng Formation.

Type	Mixed rock index	Felsic minerals, %	Mud index
Sand shale	>1.65	>50	<7
Dolomitic shale	<1.65	<50	<7
Mudstone	-	-	>7

highest, followed by felsic minerals. The clay mineral content is low throughout the Fengcheng Formation. The main clay minerals of Feng 2 (P_1f_2) are chlorite montmorillonite mixed layer, montmorillonite and illite; the main clay mineral components of Feng 3 (P_1f_3) are montmorillonite, chlorite montmorillonite mixed layer, illite montmorillonite mixed layer and illite.

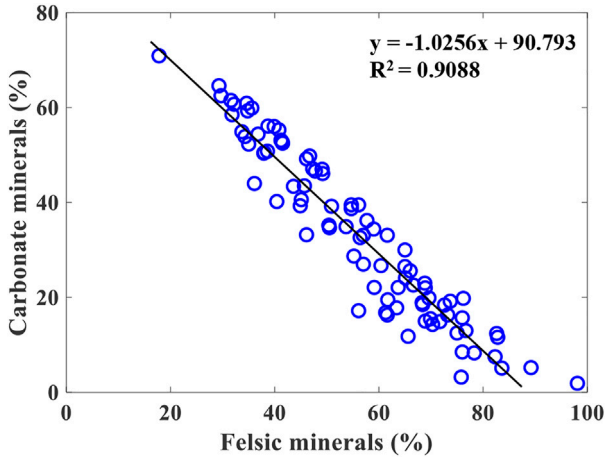

FIGURE 5
The plot of felsic minerals and carbonate mineral.

4.2 Pore structure features

The SEM measurement shows that shale oil mainly develops pores and micro-fractures in Fengcheng Formation. The pores include intergranular pores, dissolution pores, intercrystalline pores and organic pores, which mainly composed of nanopores and micropores (Figure 4). Intercrystalline and dissolution pores are commonly found in dolomite and calcite. Intergranular pores are commonly found in clay minerals and detrital minerals such as quartz and feldspar. Organic pores are pore spaces created in organic matter and often showing hydrophobicity. The micro-

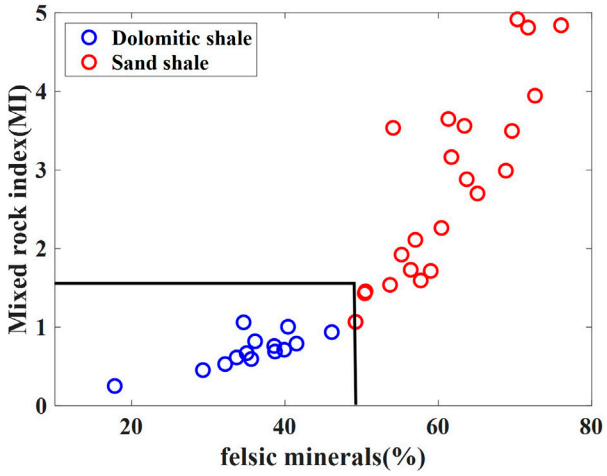

FIGURE 6
The relationship plot between MI and felsic minerals content.

fractures mainly bedding fractures and structural fractures (Figure 4).

4.3 Reservoir classification method

Mixed sedimentary rock is formed by terrigenous clastic and carbonate components. The types of mixed sedimentary rock mainly include calcareous sandstone, silty marl, dolomitic sandy shale, dolomitic siltstone and lithic sandstone (Mount, 1984; Mount, 1985). The Fengcheng Formation in Mahu Sag is a typical mixed sedimentary rock shale oil. In this work, we studied the mineral composition and lithology of the Fengcheng Formation mixed rocks by casting thin sections and SEM. The results show that shale reservoirs were mixed with many sandstones, dolomite and terrigenous clasts. The carbonate minerals (dolomite and calcite) ranges from 8.5% to 70.9%. And felsic minerals (quartz and feldspar) ranges from 30% to 90% (Figure 5). Thus, based on the previous method of calculating brittleness index according to the content of quartz, feldspar and carbonate minerals (Eq. 4.1) (Lai et al., 2015), we propose the mixed rock index (MI) based on the content of felsic minerals and carbonate minerals to evaluate the oil-bearing of shale oil reservoirs (Eq. 4.2). Moreover, in order to calculate the mudstone content, we propose a mud index (SI), using the difference between CNL and NMR porosity to calculate the shale mudstone of shale oil reservoir.

$$BI = \frac{W_{qz} + W_{car}}{W_{qz} + W_{fels} + W_{car} + W_{clay}} \quad \text{(Eq.4.1)}$$

among them, BI is the brittleness index, W_{qz}, W_{fels}, W_{car}, and W_{clay} are the percentages of quartz, feldspar, calcite and dolomite, clay respectively, %.

$$MI = \frac{w_{quarz} + w_{fledspar}}{w_{calcite} + w_{dolomite}} \quad \text{(Eq.4.2)}$$

among them, MI is the mixed rock index, w_{quarz}, $w_{fledspar}$, $w_{calcite}$, and $w_{dolomite}$ are the percentages of quartz, feldspar, calcite and dolomite respectively, %.

The shale oil formation in study area can be divided into three types based on the petrological classification standard, including sand shale, dolomitic shale and mudstone (listed in Table 1). Sand shale is rich in felsic minerals and organic matters, with higher MI. The main lithology is siltstone. Dolomitic shale is rich in dolomite and calcite, with lower MI and felsic minerals. The main lithology is carbonate (Figure 6). And mudstone with higher mud index (Figure 7).

4.4 NMR response characteristics of shale oil

4.4.1 NMR relaxation characteristics of shale

Different T_2 response characteristics have different lithology and MI, which have great influence on the NMR response characteristics of shale oil. The NMR T_2 relaxation time distribution of Fengcheng Formation is narrow, about 0.03 ms ~ 200 ms. The components of crude oil are complex, mainly medium and high viscosity crude oil. The comparison between original shale and saturated oil shale shows that the shale oil samples have good storage space. The saturation T_2 spectrum is three peaks or two peaks, including bitumen, clay bound water, bound water, bound oil, and movable oil. Bitumen exists in organic pores, which is adsorbed oil. Clay bound water exists in clay mineral, which is adsorbed water. Bound water develops in inorganic pores, and the pore size is about several nanometers, which is capillary bound water. Bound oil develops in both organic and inorganic pores, and the pore size is about several nanometers, which is adsorbed oil. Movable oil mostly develops in organic pores and inorganic pores of micropore, which is free oil. Crude oil with fluidity not only exists in micropores, but also has good fluidity in nanopores. The T_2 signal is mainly concentrated in the short relaxation part, and the T_2 signal in the long relaxation part is low. The overall relaxation time is short, not exceeding 700 ms. By analyzing the results of the T_2 NMR experiments (Figure 8), we find that the NMR T_2 spectrum of shale cores are mainly divided into three types.

Sand shale: The fluid signal is distributed in the long transverse relaxation time component, the main peak is around 10 ms, and the movable oil signal and the bound oil signal overlap (Figure 8, core 1, core 2).

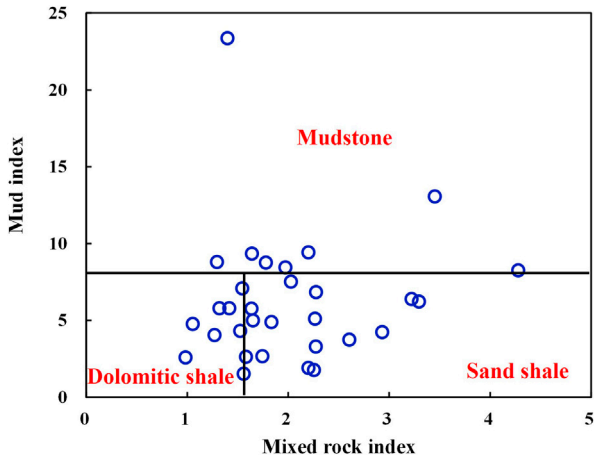

FIGURE 7
Shale oil reservoir type classification results.

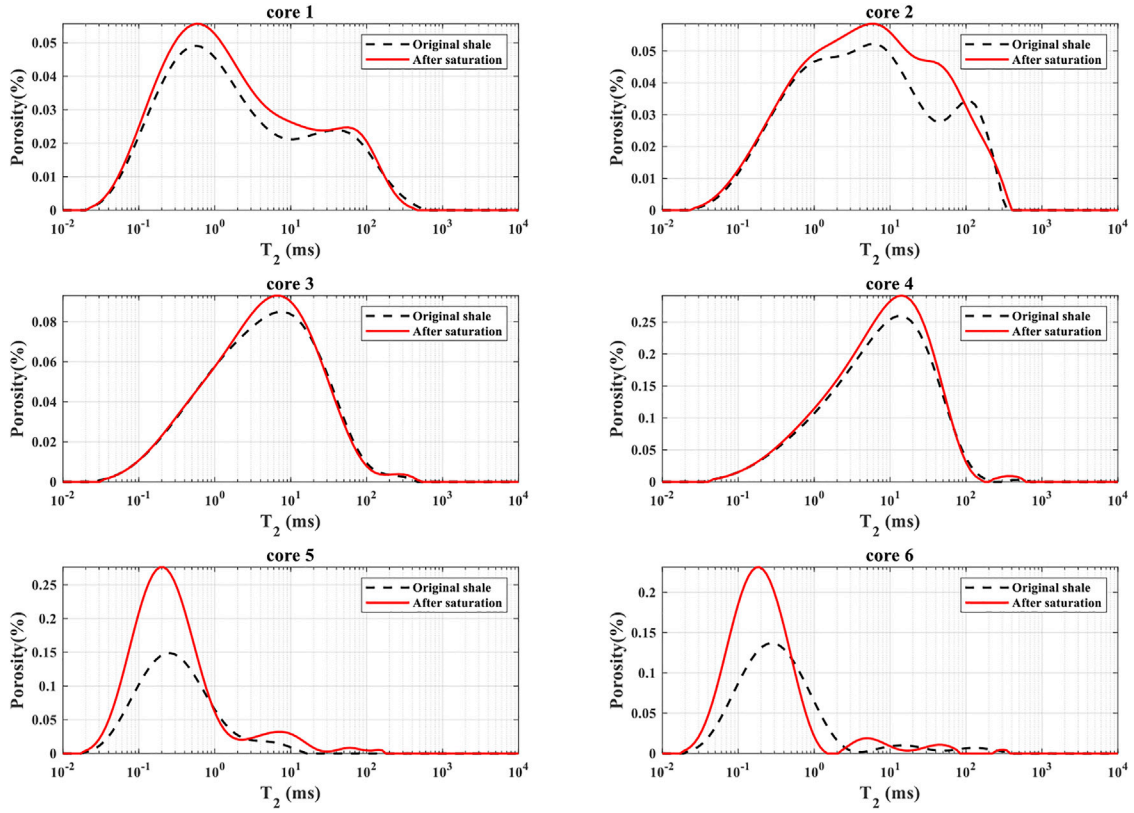

FIGURE 8
T_2 NMR experiment results of shale cores.

Dolomitic shale: The fluid signal is mainly distributed in the short and medium transverse relaxation components, the main peak is around 1 ms, and the movable oil signal overlaps with the irreducible water signal and the irreducible oil signal (Figure 8, core 3, core 4).

Mudstone: The fluid signal is mainly distributed in the short transverse relaxation component, the main peak is around 0.2 ms, the movable oil signal overlaps with the irreducible water signal (Figure 8, core 5, core 6).

4.4.2 T_1-T_2 experiments

The experimental results of the 2D NMR T_1-T_2 maps are shown in Figure 9. The shale T_1-T_2 map can mainly divided into three types and consistent with T_2 results. Fluids are mainly present in shale in the form of movable oil, bound oil, bound water, clay-bound water and bitumen. The T_1/T_2 of movable oil is about 7 ~ 15, and the signal of movable oil is distributed in the whole relaxation spectrum. It shows that the crude oil with fluidity not only exists in the micropores, but also has good fluidity in the nanopores. The T_1/T_2 of the bound oil is about 5 ~ 10, and the fluid signal is mainly concentrated in the short relaxation component, which occurs in organic pores and nano-scale inorganic pores. The T_1/T_2 of the bound water is about 2 ~ 5, and the fluid signal is mainly concentrated in the short relaxation component, which occurs in nano-scale inorganic pores. The T_1/T_2 of clay bound water is about 1, and the fluid signal is concentrated at 0.05 ms ~ 1 ms. The T_1/T_2 of bitumen is about 3~300, the fluid signal is distributed in a very short relaxation time period, and the signal decays rapidly.

Discussion

5.1 2D NMR T_1-T_2 interpretation modal of shale oil

By comparing two-dimensional T_1-T_2 spectra of shale oil cores under different states (Figure 9), a 2D NMR logging interpretation map was established to identify the fluid occurrence state for shale oil (Figure 10). Based on T_1/T_2 ratios and T_2 cutoff values of fluid signals as the classification basis, the fluids types of shale oil include movable oil, bound oil, bound water, clay-bound water, and bitumen. The T_1/T_2 of movable oil is about 7~15, and the T_2 signal of movable oil is 30~300 ms. The T_1/T_2 of the bound oil is about 5~10, and the T_2 fluid signal is 0.3~30 ms. The T_1/T_2 of the bound water is about 2~5, and the T_2 fluid signal is 0.3~30 ms. The T_1/T_2 of clay-bound water is about 1, and the T_2 fluid signal is 0.01 ms~0.3 ms. The T_1/T_2 of bitumen is about 3~300, the T_2 fluid signal is 0.01~0.3 ms. The T_1-T_2 interpretation map of shale oil was consistent with that obtained by NMR T_1-T_2 experiments (Figures 11–13). Results show that the T_1-T_2 interpretation map can be used to determine the porosity, movable oil and bound oil contents, and saturations of shale oil.

Based on the established NMR T_1-T_2 fluid identification map, we divide the T_1-T_2 distribution map into five areas. The NMR T_1-T_2 spectral area coefficients of different fluid component were obtained from NMR measurements. Using the method of 2D area spectrum coefficient, we establish a fluid saturation calculation model for shale oil.

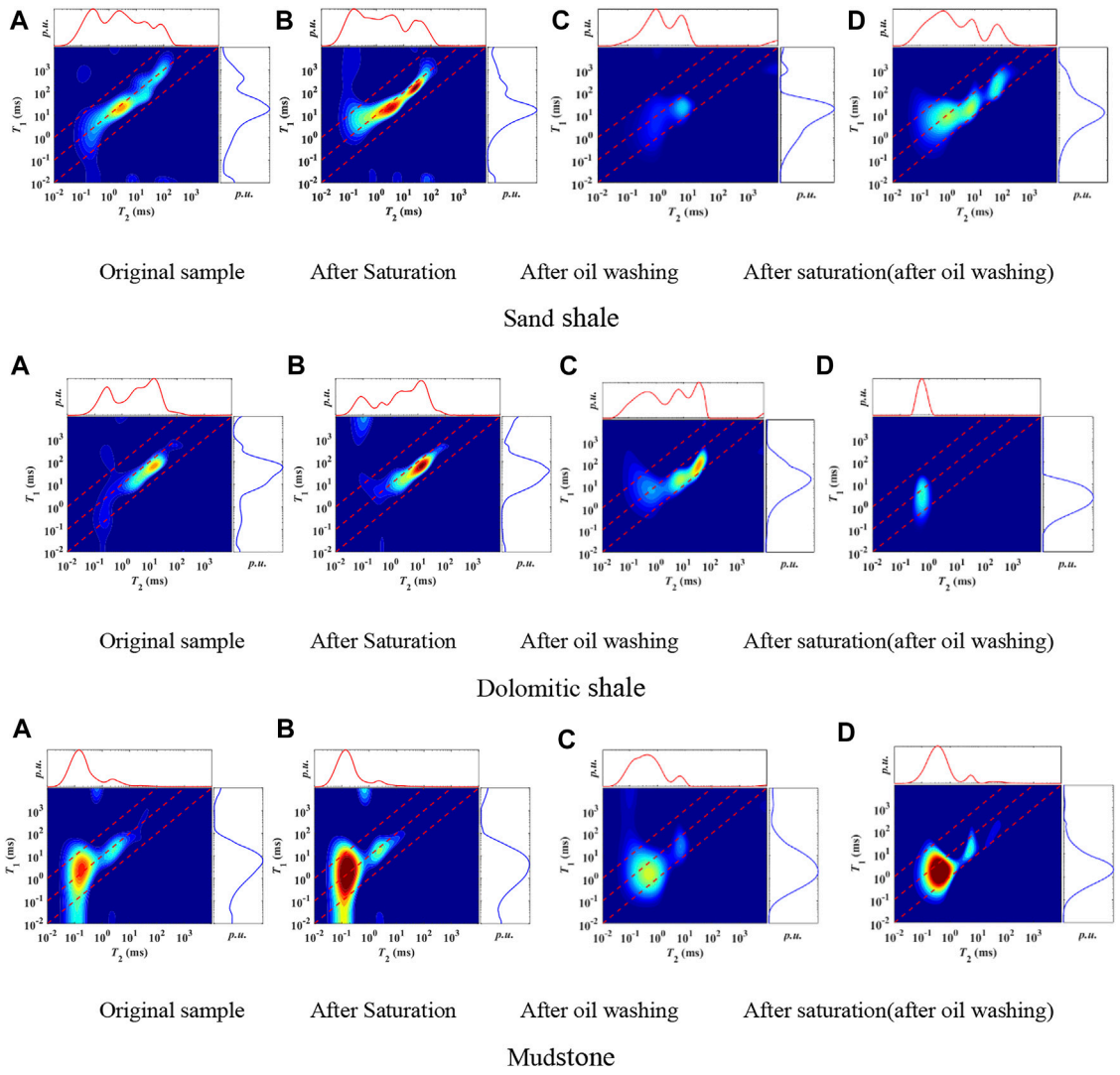

FIGURE 9
2D T_1/T_2 NMR experiment results of shale cores. **(A)** Original sample; **(B)** After saturation sample; **(C)** After oil washing sample; **(D)** After saturation (after oil washing) sample.

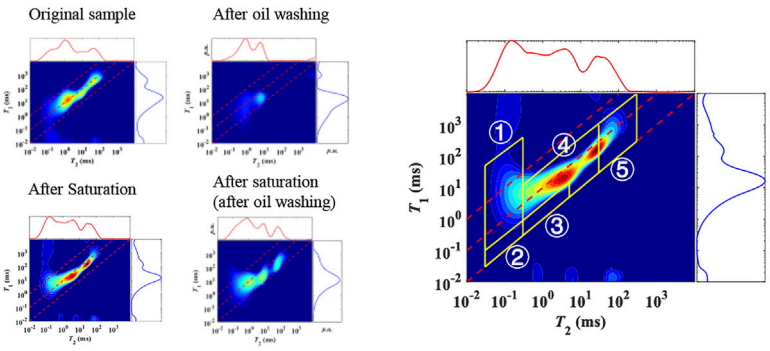

	Fluid	T_1/T_2	T_2
①	Bitumen	3-100	0.05-0.3
②	Clay bound water	1	0.05-0.3
③	Capillary bound water	2	0.5-5
④	Bound oil	2-50	0.3-30
⑤	Movable oil	5-30	30-300

FIGURE 10
Sand shale.

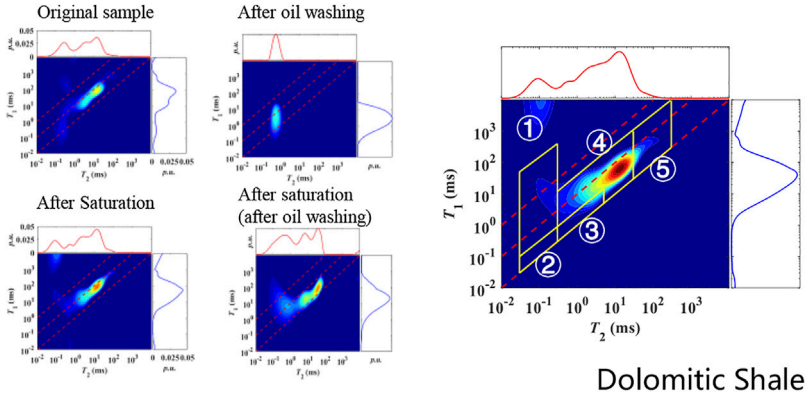

	Fluid	T_1/T_2	T_2
①	Bitumen	3-100	0.1-0.3
②	Clay bound water	1	0.1-0.3
③	Capillary bound water	2	0.5-5
④	Bound water	2-50	0.3-30
⑤	Movable oil	5-30	30-200

FIGURE 11
Dolomitic Shale.

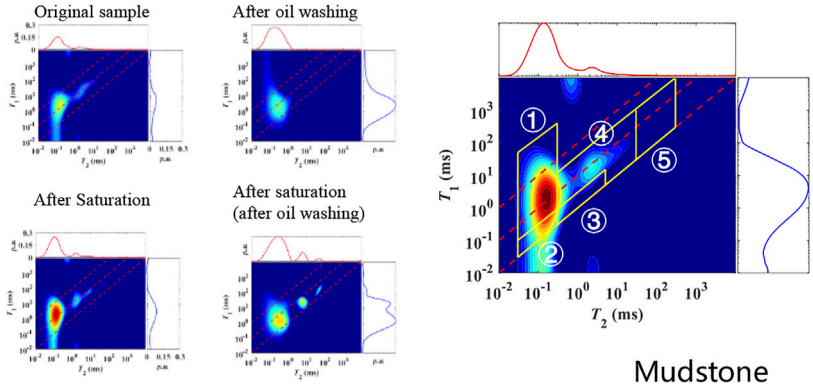

	Fluid	T_1/T_2	T_2
①	Bitumen	3-100	0.03-0.3
②	Clay bound water	1	0.03-0.3
③	Capillary bound water	2	0.3-3
④	Bound water	2-50	0.3-30
⑤	Movable oil	5-30	30-100

FIGURE 12
Mudstone.

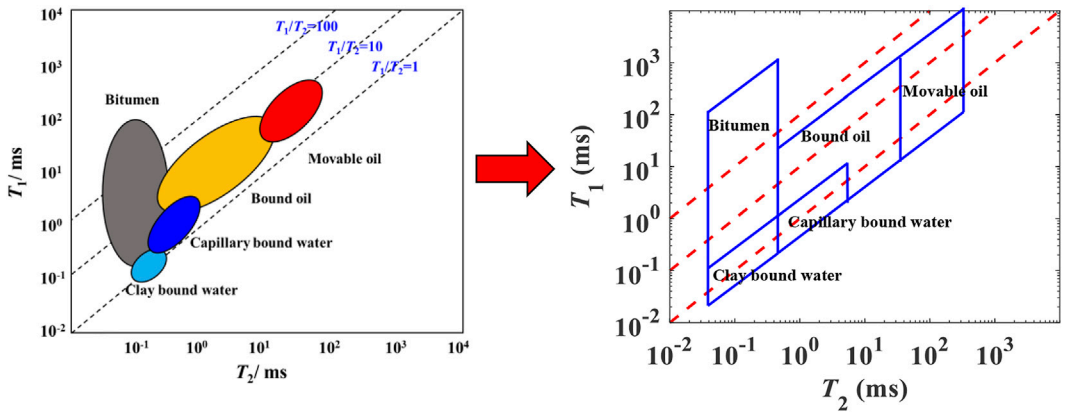

FIGURE 13
T_1-T_2 2D NMR fluid identification map at 2MHz for Fengcheng Formation.

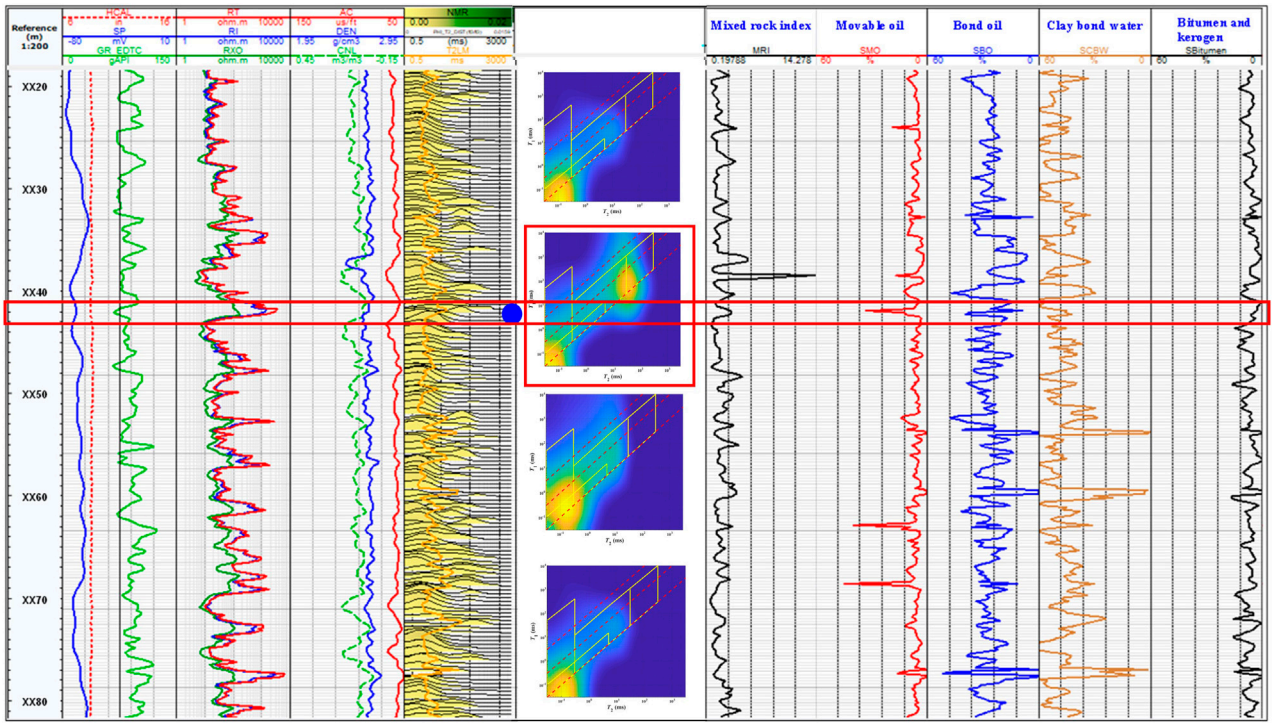

FIGURE 14
NMR logging evaluation results of Well W2. The first track is depth. The second track includes the gamma (GR), SP, and caliper (CAL) logs. The third track includes the deep, medium, and shallow resistivity logs. The fourth track includes the acoustic (AC), density (DEN), and compensated neutron logging (CNL) logs. The fifth track shows the T2 distributions (T2_DIST). The sixth track gives the mixed rock index. Tracks 7, 8, 9, and 10 are the NMR fluid saturation from the method we established.

5.2 Application

We apply the 2D NMR logging interpretation map and effective porosity calculation for the actual logging data to identify the occurrence state of downhole fluids, calculate the movable oil saturation and effective porosity. The higher MI value, and the higher movable oil saturation of shale oil in the Fengcheng Formation. Figure 14 is the 2D NMR logging curve of Well W2 in the Mahu Sag. From the logging interpretation results, we find that the XX44m position is sand shale formation, with high mixed rock index, and high movable oil content, which is consistent with the actual logging.

6 Conclusion

This paper aims to evaluate fluid occurrence state and fluid saturation of lacustrine shale oil in Fengcheng Formation. We use mixed rock index (MI) and mud index (SI) to divide formations to eliminate the influence of complex lithology. Furthermore, based on the 2D T_1-T_2 NMR experiments and formation classification results, a characterization model of fluid occurrence state was established. The characterization model was successfully applied to the lacustrine shale oil in the Fengcheng Formation, Mahu sag, Junggar Basin, China.

(1) A formation classification method was proposed by the MI value, SI value and the felsic minerals content to eliminate the influence of complex lithology on the fluid occurrence state of shale oil. The shale oil of Fengcheng Formation was divided into three types, including sand shale, dolomitic shale and mudstone.
(2) A model of NMR 2D T_1-T_2 logging interpretation map was established for shale oil through the T_1/T_2 ratio and T_2 cutoff value. The shale oil fluids are differentiated into movable oil, bound oil, bound water, clay bound water and bitumen. Based on 2D NMR T_1-T_2 map, a quantitative calculation method of fluid saturation was proposed for shale oil. It has implications for understanding fluid occurrence state and evaluating fluid saturation in shale oil with similar geological settings.

Data availability statement

The original contributions presented in the study are included in the article/supplementary material, further inquiries can be directed to the corresponding author.

Author contributions

RF is mainly responsible for the writing and modification of the article, as well as the experiments, data processing and analysis required for article writing; GL is mainly responsible for guiding the revision of the article and data analysis and processing, to provide technical support; RM, XL, LH, HZ, HT, GW, ZQ, and LX provided financial support and technical support in the writing and

preparation of articles. All authors participated in the revision and agreed to submit the published version.

Funding

This work was supported by National Key Research and Development Program (2019YFA0708301), National Natural Science Foundation of China (51974337), the Strategic Cooperation Technology Projects of CNPC and CUPB (ZLZX 2020-03), Strategic Priority Research Program (A) of Chinese Academy of Sciences (XDA14020405).

Acknowledgments

The authors also thank for assistance and data supports from China National Petroleum Corporation, China National Offshore Oil Corporation. Thanks to the hard work of many colleagues, collaborators, doctoral and master students in the China University of Petroleum. Thanks to Harvard University and the Weitz's Lab for providing visiting opportunities.

Conflict of interest

Authors RM, XL, HZ, GW, and ZQ were employed by Xinjiang Oilfield Company. Authors LH and HT were employed by PetroChina.

The remaining authors declare that the research was conducted in the absence of any commercial or financial relationships that could be construed as a potential conflict of interest.

Publisher's note

References

Althaus, S., Chen, J.-H., Jacobi, D., and Brothers, J. (2019) "NMR Signature and quantification of bitumen in unconventional source Rocks," in SPE/AAPG/SEG Unconventional Resources Technology Conference.

Cao, J., Xia, L., Wang, T., Zhi, D., Tang, Y., and Li, W. (2020). An alkaline lake in the late paleozoic ice age (lpia): A review and new insights into paleoenvironment and petroleum geology. *Earth-Science Rev.* 202, 103091.

Cudjoe, S. E., Barati, R., Tsau, J.-S., Zhang, C., Nicoud, B., Bradford, K., et al. (2021). Assessing the efficiency of saturating shale oil cores and evaluating hydrocarbon gas huff 'n' puff using nuclear magnetic resonance. *SPE Reserv. Eval. Eng.* 24, 429–439.

EIA (2015). *Technically recoverable shale oil and shale gas resources[EB/OL].* (2015 -09-24). https://www.eia.gov/analysis/studies/worldshale gas/pdf/Oman_2014.pdf.

Ge, X., Fan, Y., Chen, H., Deng, S., Cao, Y., and Zahid, M. A. (2015). Probing the influential factors of NMR T1–T2 spectra in the characterization of the kerogen by numerical simulation. *J. Magnetic Reson.* 260, 54–66.

Gu, M., Xie, R., and Jin, G. (2022). A new quantitative evaluation method for fluid constituents with NMR T1-T2 spectra in shale reservoirs. *J. Nat. Gas Sci. Eng.* 99, 104412.

Gu, M., Xie, R., Jin, G., Xu, C., Wang, S., Liu, J., et al. (2021). Quantitative evaluation for fluid components on 2D NMR spectrum using Blind Source Separation. *J. Magnetic Reson.* 332, 107079.

Guan, M., Liu, X., Jin, Z., Lai, J., Liu, J., Sun, B., et al. (2022). Quantitative characterization of various oil contents and spatial distribution in lacustrine shales: Insight from petroleum compositional characteristics derived from programed pyrolysis. *Mar. Petroleum Geol.* 138, 105522.

Guo, J., Xie, R., and Xiao, L. (2020). Pore-fluid characterizations and microscopic mechanisms of sedimentary rocks with three-dimensional NMR: Tight sandstone as an example. *J. Nat. Gas Sci. Eng.* 80, 103392.

Hu, S., Jianzhong, L., Tongshan, W., Zecheng, W., Tao, Y., Zin, L., et al. (2020). CNPC oil and gas resource potential and exploration target selection. *Petroleum Geol. Exp.* 42, 813–823.

Hürlimann, M. D. (2001). Carr–purcell sequences with composite pulses. *J. Magnetic Reson.* 152, 109–123.

Jia, Z. J., Xiao, L. Z., Zhizhan, W. Z., Liao, G. Z., Zhang, Y., Liang, C., et al. (2017). Magic echo for nuclear magnetic resonance characterization of shales. *ENERGY & FUELS* 31, 7824–7830.

Jin, G., Xie, R., Xiao, L., Wu, B., Xu, C., Wang, X., et al. (2021). Quantitative characterization of bound and movable fluid microdistribution in porous rocks using nuclear magnetic resonance. *J. Petroleum Sci. Eng.* 196, 107677.

Kausik, R., Fellah, K., Rylander, E., Singer, P. M., Lewis, R. E., and Sinclair, S. M. (2016). NMR relaxometry in shale and implications for logging. *Petrophysics - SPWLA J. Form. Eval. Reserv. Descr.* 57, 339–350.

Kuang, L., Yong, T., Dewen, L., Qiusheng, C., Min, O., Lianhau, H., et al. (2012). Formation conditions and exploration potential of tight oil in the Permian saline lacustrine dolomitic rock, Junggar Basin, NW China. *PETROLEUM Explor. Dev.* 39, 657–667.

Lai, J., Wang, G., Huang, L., Li, W., Ran, Y., Wang, D., et al. (2015). Brittleness index estimation in a tight shaly sandstone reservoir using well logs. *J. Nat. Gas Sci. Eng.* 27, 1536–1545.

Li, J., Wang, M., Fei, J., Xu, L., Shao, H., Li, M., et al. (2022). Determination of *in situ* hydrocarbon contents in shale oil plays. Part 2: Two-dimensional nuclear magnetic resonance (2D NMR) as a potential approach to characterize preserved cores. *Mar. Petroleum Geol.* 145, 105890.

Li, J., Wang, M., Lu, S., Chen, G., Tian, W., Jiang, C., et al. (2020). A new method for predicting sweet spots of shale oil using conventional well logs. *Mar. Petroleum Geol.* 113, 104097.

Mount, J. F. (1984). Mixing of siliciclastic and carbonate sediments in shallow shelf environments. *Geology* 12, 432–435.

Mount, J. (1985). Mixed siliciclastic and carbonate sediments: A proposed first-order textural and compositional classification. *Sedimentology* 32, 435–442.

Song, Y.-Q., and Kausik, R. (2019). NMR application in unconventional shale reservoirs – a new porous media research frontier. *Prog. Nucl. Magnetic Reson. Spectrosc.* 112-113, 17–33.

Tang, W., Zhang, Y., Pe-Piper, G., Piper, D. J. W., Guo, Z., and Li, W. (2020). Soft-sediment deformation structures in alkaline lake deposits of Lower Permian Fengcheng Formation, Junggar Basin, NW China: Implications for syn-sedimentary tectonic activity. *Sediment. Geol.* 406, 105719.

Venkataramanan, L., Evirgen, N., Allen, D. F., Mutina, A., Cai, Q., Johnson, A. C., et al. (2018). An unsupervised learning algorithm to compute fluid volumes from NMR T1-T2 logs in unconventional reservoirs. *Petrophysics - SPWLA J. Form. Eval. Reserv. Descr.* 59, 617–632.

Zhang, H., Wang, Y., Fang, T., Wang, W., Zhao, X. R., Zhao, H. P., et al. (2020a). "First application of new generation NMR T1-T2 logging and interpretation in unconventional reservoirs in China," in SPE Asia Pacific Oil & Gas Conference and Exhibition.

Zhang, P., Lu, S., Li, J., and Chang, X. (2020b). 1D and 2D Nuclear magnetic resonance (NMR) relaxation behaviors of protons in clay, kerogen and oil-bearing shale rocks. *Mar. Petroleum Geol.* 114, 104210.

Zhou, G., Gu, Z., Hu, Z., Chang, J., Duan, X., Liu, X., et al. (2020). Characterization and interpretation of organic matter, clay minerals, and gas shale rocks with low-field NMR. *J. Petroleum Sci. Eng.* 195, 107926.

Zou, C., Feng, M., Songqi, P., Xinshun, Z., Songtao, W., Guoyou, F., et al. (2022). Formation and distribution potential of global shale oil and the theoretical and technological progress of continental shale oil in China. *Earth Sci. Front.*, 1–16.

10.3389/feart.2023.1117193

Appendix

TABLE A1 Mineral composition and TOC content of shale samples from Fengcheng formation in Mahu Sag, Junggar Basin.

Number	Mineral type and content (%)								
	Quartz	Potassium feldspar	Plagioclase	Calcite	Dolomite	Pyrite	Iron dolomite	Clay minerals	TOC
W1-1-4	39.5	2.4	17.2	22.1	—	3.4	—	15.4	0.18
W1-1-10	32.2	3.9	20.0	17.2	—	5.4	—	21.3	0.01
W1-1-43	55.3	1.7	4.7	19.5	—	2	—	16.8	0.22
W1-2-12	26.9	3.9	3.8	32.6	—	1.9	—	30.9	0.43
W1-2-15	27.2	3.2	14.5	39.3	—	3.5	—	12.4	0.34
W1-2-22	58.8	2.6	20.9	7.5	—	2.5	1.1	6.4	0.61
W1-2-32	59.8	3.6	14.9	8.3	—	2.5	1.6	9.3	0.59
W1-2-63	11.7	2.6	51.3	11.8	—	2.4	7.6	12.6	0.30
W1-2-75	47.2	3.8	24.8	3.2	—	3.3	2.7	14.9	0.11
W1-2-100	25.6	5.8	25.6	27.0	—	3.7	2.1	10.3	0.47
W2-2-30	65.3	1.2	3.1	19.9	—	0.8	—	9.6	0.64
W2-4-14	63.5	2.3	6.8	18.4	—	1.3	2.5	5.4	0.57
W2-4-30	48.9	1.3	7.1	17.2	—	2.1	13	10.5	0.59
W2-4-31	29.8	5.3	19.0	15.3	—	—	6.4	24.1	0.39
W2-4-58	16.4	7.5	48.5	0.8	—	6.3	11.5	9.0	0.18
W2-4-68	37.8	11.4	14.5	0.6	21.5	3.2	—	11	0.27
W2-5-6	55.7	4.1	10.5	3.1	11.2	3.0	—	12.3	0.26
W2-8-7	49.0	6.2	13.7	2.5	12.5	2.6	—	13.6	0.39
W2-8-18	52.3	5.1	19.3	1.5	11.5	2.9	—	7.4	0.80
W2-9-19	30.2	3.0	10.4	1.6	41.8	3.2	—	9.7	0.17
W2-9-38	30.0	3.9	49.7	1.5	3.6	3.5	—	6.8	0.42
W2-10-35	26.7	5.3	44	1.1	7.4	4.3	—	9.9	1.07
W2-11-73	19.9	5.5	36.2	—	—	5.7	16.1	14.3	0.29
W2-12-31	19.4	5.0	30.8	1.4	27.3	4.5	—	11.7	0.19
W2-12-39	34.5	7.8	29.4	1	13.9	4.0	—	9.5	0.14
W2-12-40	23.5	6.0	21.0	15.4	19.3	5.5	—	9.4	0.23
W2-12-61	44.8	6.0	14.3	15.5	8.6	2.3	—	8.5	0.64
W2-12-63	8.4	2.2	7.2	57	13.9	1.9	—	7.1	0.36
W2-12-68	30.2	12.7	32.1	1.3	11.2	4.7	—	7.7	0.56
W2-12-98	20.2	4.9	8.6	3.1	51.8	3.7	—	7.7	0.43

frontiers | Frontiers in Earth Science

TYPE Original Research
PUBLISHED 08 March 2023
DOI 10.3389/feart.2023.1132882

OPEN ACCESS

EDITED BY
Qiaomu Qi,
Chengdu University of Technology,
China

REVIEWED BY
Chao Tang,
Chengdu University of Technology,
China
Xiaobin Li,
China National Petroleum Corporation,
China

*CORRESPONDENCE
Lingli Zheng,
478109107@qq.com

SPECIALTY SECTION
This article was submitted to Solid Earth Geophysics,
a section of the journal
Frontiers in Earth Science

RECEIVED 28 December 2022
ACCEPTED 17 February 2023
PUBLISHED 08 March 2023

CITATION
Zheng L, Chen M, Li T, He J, Li Y and Xiao W (2023), Apparent permeability in tight gas reservoirs combining rarefied gas flow in a microtube.
Front. Earth Sci. 11:1132882.
doi: 10.3389/feart.2023.1132882

Apparent permeability in tight gas reservoirs combining rarefied gas flow in a microtube

Lingli Zheng[1]*, Muyao Chen[1], Tao Li[2], Jiahuan He[2], Yongming Li[1] and Wenlian Xiao[1]

[1]State Key Laboratory of Oil and Gas Reservoir Geology and Exploitation, Southwest Petroleum University, Chengdu, China, [2]Exploration and Development Research Institute, PetroChina Southwest Oil and Gasfield Company, Chengdu, China

In tight gas reservoirs, the major flow channels are composed of micro/nanopores in which the rarefaction effect is prominent and the traditional Darcy law is not appropriate for gas flow. By combining the Maxwell first-order slip boundary condition and Navier–Stokes equations, a three-dimensional (3D) analysis of compressible gas slip flow in a microtube was presented, and the flux rate and pressure variation in the flow direction were discussed. Subsequently, by superimposing the Knudsen diffusion, a gas flux formula applicable to a larger Knudsen number was further proposed and satisfactorily verified by two groups of published experimental data in microtubes or microchannels in the membrane. The results indicate that slip flow and Knudsen diffusion make an important contribution to the total gas flow in the microtube, and their weight increases with an increase in the Knudsen number. By substituting the gas flux formula into Darcy's law for compressible gas, a new apparent permeability model for tight gas reservoirs was proposed, in which the slippage effect and Knudsen diffusion were synthetically considered. The results indicate that the apparent permeability of tight reservoirs strongly depends on the reservoir pressure and pore-throat radius, and an underestimation value may be predicted by the previously published models. This study provides a case study for evaluating these apparent permeability models, which remains a challenging task in the laboratory.

KEYWORDS

microtube, apparent permeability model, slippage effect, Knudsen diffusion, tight gas

1 Introduction

Tight sandstone gas is an important energy source. A sound understanding of reservoir properties and gas flow mechanisms is required to effectively develop these natural gas resources (Gensterblum et al., 1995; Sander et al., 2017; Rutter et al., 2022). Gas molecules generally move without rules; this movement is commonly described by the molecule mean free path. The Knudsen number (K_n), defined as the ratio of the mean free path and the characteristic length of the microchannels, is applied to determine whether the gas flow meets the continuity assumption (Freeman et al., 2011). As the characteristic length of microchannels approaches the mean free path, the rarefaction effect is significant, resulting in the breakdown of the continuity assumption (Javadpour et al., 2007; Civan, 2010). Based

Abbreviations: app, apparent; avg, average; D, Darcy; d, diffusion; i, the inlet of the microtube; o, the outlet of the microtube.

on K_n, gas flow regimes can be divided into continuum flow (K_n <10^{-3}), slip flow (10^{-3} <K_n <10^{-1}), transition regime (10^{-1} <K_n <10), and free molecular regime (K_n >10) (Roy et al., 2003; Civan, 2010; Sakhaee-Pour and Bryant, 2011; Swami et al., 2012; Kim et al., 2016).

The Navier–Stokes equations and Darcy's law are suitable for continuum flow. For slip flow, two approaches have been proposed to describe the gas flow. One approach combines the Navier–Stokes equations with different slip boundary conditions (Shen et al., 2007), and the other uses a molecular-based model (Fukui and Kaneko, 1988). Compared with molecular-based models, slip boundary models are simpler and more efficient because they can be applied with a continuum description (Shen et al., 2007). Maxwell (1878) first proposed the slip model and expected two kinds of reflections existing as gas molecules to collide with the wall, a part of (σ_v) the diffuse reflection, and the remaining part of (1-σ_v) the specular reflection. σ_v depends on the surface material, surface roughness, incident angles of gas molecules, gas types, temperature, and pressure (Arkilic and Schmidt, 1997). Although the derivation process of the slip model was not strictly physical, it correctly reflected the dependence of the slip velocity on the reflection and sectional velocity gradient. Subsequently, the 1.5-order and second-order slip boundaries were proposed based on kinetic theory (Kennard, 1938; Mitsuya, 1993; Wu and Bogy, 2001; Hadjiconstantinou, 2003). These models usually act for K_n < 0.1, and the second-order slip model is likely to overestimate the flow rate at large K_n. Meanwhile, the legitimacy of 1.5-order and second-order slip models has also been debated (Shen et al., 2007). A general slip boundary condition declared to be appropriate for the entire Knudsen range was developed by Beskok and Karniadakis (1999). However, the slip coefficient needs to be determined using either experimental or DSMC data. Simultaneously, a similar slippage effect was obtained by employing the effective viscosity near the wall or applying the extended Navier–Stokes equations with no-slip boundary conditions (Beskok and Karniadakis, 1999; Chakraborty and Durst, 2007; Roy and Chakraborty, 2007; Arlemark et al., 2010; Michalis et al., 2010; Agrawal, 2011). For the transition and free molecular regimes, the collision between the gas molecules and the wall is more prominent. The Navier–Stokes equations have to be substituted by Boltzmann or Burnett equations (Agarwal et al., 2001; Freeman et al., 2011; Rahmanian et al., 2012), but it is difficult to obtain analytical solutions. Subsequently, some authors have attempted to estimate the total gas flux in microchannels by superimposing the slip flow with Knudsen diffusion (Javadpour, 2009; Zhang et al., 2015), which shows a reasonable match with experimental data (Javadpour, 2009). In addition, many experiments focusing on gas flow at different scales and shapes of microchannels have been conducted (Arkilic and Schmidt, 1997; Maurer et al., 2003; Hsieh et al., 2004; Ewart et al., 2006; Velasco et al., 2012), which have been reviewed in detail by Morini et al. (2011).

Unlike the Darcy permeability, the apparent permeability for gas transport in tight reservoirs results from the joint effects of rock properties and gas flow regimes, which makes a big difference in the production characteristics of natural gas. Pores and throats are small in tight gas reservoirs. As the gas reservoir pressure decreases, the apparent permeability becomes as much as 10 times larger than the Darcy permeability (Darabi et al., 2012; Kalarakis et al., 2012). Klinkenberg (1941) first developed a famous formula that considers the slippage effect based on the kinetic theory, but it is not appropriate for flows at high K_n (Sakhaee-Pour and Bryant, 2011).

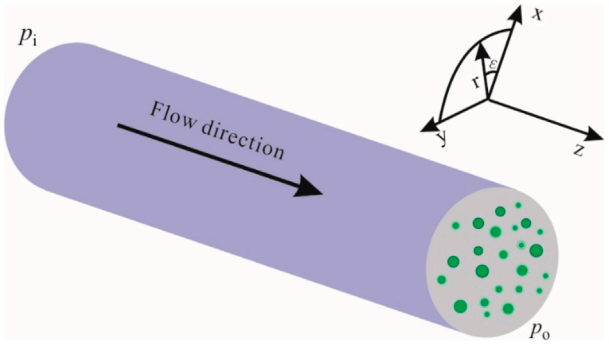

FIGURE 1
Schematic diagram of the 3D microtube.

By adopting the lattice Boltzmann method, Tang et al. (2005) confirmed the Klinkenberg equation and concluded that the second-order term of K_n needed to be added for gas flow at high K_n. Meanwhile, experimental results have shown that the gas slippage factor is a power function of the Darcy permeability versus porosity (Jones and Owens, 1980; Florence et al., 2007), but it might not hold for tight gas reservoirs (Swami et al., 2012). Michel et al. (2011) proposed a dynamic slippage factor considering the Knudsen diffusion coefficients, but the slippage effect was not accounted for (Swami et al., 2012). Moreover, by combining the Beskok–Karniadakis model (1999), Civan et al. (2011), and Sakhaee-Pour and Bryant et al. (2012) introduced apparent permeability as a function of K_n. As the total gas flux in micro- and nanopores consists of viscous flow driven by the pressure gradient and Knudsen diffusion under the action of a gas concentration gradient, an accurate apparent permeability model may need to consider the aforementioned two parts in the meantime (Harley et al., 1995; Rushing et al., 2003; Javadpour, 2009). It is closely related to rock properties, gas types, and environmental conditions (Javadpour, 2009; Chen et al., 2015; Zhang et al., 2015).

This study theoretically analyzed the gas slip flow in a 3D microtube by combining the Navier–Stokes equations and first-order slip boundary condition. A gas flux formula in the microtube was proposed by superimposing the Knudsen diffusion, which was suitable for a higher K_n. Subsequently, a new apparent permeability model for tight gas reservoirs, including the slippage effect and Knudsen diffusion, was proposed, which contributes to a further understanding of the gas flow mechanism and production characteristics in tight reservoirs.

2 Theoretical gas flow formula in a microtube

2.1 The derivation of the theoretical gas flow formula

As gas flows in a 3D microtube (Figure 1), ignoring the mass force and temperature variation and assuming that viscosity is

constant and the second viscosity coefficient μ' equals 0, the Navier–Stokes equations for compressible gas under steady-state conditions are written as follows (Chen, 2017):

$$\frac{\mu}{3}\nabla\left(\nabla\cdot\vec{V}\right)+\mu\nabla^2\vec{V}=\nabla p \tag{1}$$

where fluid pressure is denoted as p, Pa; gas viscosity μ, Pa s; and velocity $\vec{V}$, m/s. By ignoring the changes in radial velocity (v) and angular velocity (w) over angle (θ) (Eq. 1), the continuity equation for steady-state and compressible gas flow was expanded in cylindrical coordinates:

$$\frac{\mu}{3}\left(\frac{\partial^2 v}{\partial r^2}+\frac{\partial^2 u}{\partial r\partial z}+\frac{1}{r}\frac{\partial v}{\partial r}-\frac{v}{r^2}\right)+\mu\left(\frac{1}{r}\frac{\partial v}{\partial r}+\frac{\partial^2 v}{\partial r^2}+\frac{\partial^2 v}{\partial z^2}-\frac{v}{r^2}\right)=\frac{\partial p}{\partial r} \tag{2}$$

$$\frac{\mu}{3}\left(\frac{\partial^2 v}{\partial r\partial z}+\frac{\partial^2 u}{\partial z^2}+\frac{1}{r}\frac{\partial v}{\partial z}\right)+\mu\left(\frac{1}{r}\frac{\partial u}{\partial r}+\frac{\partial^2 u}{\partial r^2}+\frac{\partial^2 u}{\partial z^2}\right)=\frac{\partial p}{\partial z} \tag{3}$$

$$\rho\frac{\partial v}{\partial r}+\rho\frac{\partial u}{\partial z}+v\frac{\partial \rho}{\partial r}+u\frac{\partial \rho}{\partial z}+\rho\frac{v}{r}=0 \tag{4}$$

For ideal gases, $p=\rho R_a T/M$, where M represents the molar mass (kg/kmol); R_a refers to the gas constant, 0.008314 (Pam^3)/(kmolK); ρ is the density, kg/m^3; and T is the temperature (K). The non-dimensionalization of these variables is as follows: streamwise velocity (u) and radial velocity (v) are normalized by the area-averaged velocity at the outlet, the streamwise coordinate (z) by the length of the microtube (L), radial coordinate (r) by the radius of the microtube (R), and p and ρ are the pressure and density at the outlet, respectively. Meanwhile, $\varepsilon = R/L$ <<1 and $\delta p = p_i$-p_o. With these assumptions, Eqs. 2–4 were expressed in a non-dimensional form as follows:

$$\frac{4}{3}\left(\frac{\delta p}{8\mu L}\frac{\partial^2\tilde{v}}{\partial\tilde{r}^2}+\frac{\delta p}{8\mu L}\frac{1}{\tilde{r}}\frac{\partial\tilde{v}}{\partial\tilde{r}}-\frac{\delta p}{8\mu L}\frac{\tilde{v}}{\tilde{r}^2}\right)+\frac{R^2\delta p}{8\mu L^3}\frac{\partial^2\tilde{v}}{\partial\tilde{z}^2}+\frac{1}{3}\frac{R\delta p}{8\mu L^2}\frac{\partial^2\tilde{u}}{\partial\tilde{z}\partial\tilde{r}}=\frac{1}{\mu}\frac{p_o\partial\tilde{p}}{R\partial\tilde{r}} \tag{5}$$

$$\frac{4}{3}\frac{R^2\delta p}{8\mu L^3}\frac{\partial^2\tilde{u}}{\partial\tilde{z}^2}+\frac{\delta p}{8\mu L}\frac{\partial^2\tilde{u}}{\partial\tilde{r}^2}+\frac{\delta p}{8\mu L}\frac{1}{\tilde{r}}\frac{\partial\tilde{u}}{\partial\tilde{r}}+\frac{1}{3}\left(\frac{R\delta p}{8\mu L^2}\frac{1}{\tilde{r}}\frac{\partial\tilde{v}}{\partial\tilde{z}}+\frac{R\delta p}{8\mu L^2}\frac{\partial^2\tilde{v}}{\partial\tilde{z}\partial\tilde{r}}\right)=\frac{1}{\mu}\frac{p_o\partial\tilde{p}}{L\partial\tilde{z}} \tag{6}$$

$$\frac{R^2\delta p}{8\mu L^2}\tilde{\rho}\frac{\partial\tilde{u}}{\partial\tilde{z}}+\frac{R\delta p}{8\mu L}\tilde{\rho}\frac{\partial\tilde{v}}{\partial\tilde{r}}+\frac{R\delta p}{8\mu L}\tilde{\rho}\frac{\tilde{v}}{\tilde{r}}+\frac{R^2\delta p}{8\mu L^2}\tilde{u}\frac{\partial\tilde{\rho}}{\partial\tilde{z}}+\frac{R\delta p}{8\mu L}\tilde{v}\frac{\partial\tilde{\rho}}{\partial\tilde{r}}=0 \tag{7}$$

It is clear that the radial velocity equals 0 at the wall of the microtube, where the streamwise velocity is expressed by the Maxwell first-order slip velocity (Eq. 8). Meanwhile, K_n was replaced by the ratio of K_n at the outlet (denoted by K_o) and the non-dimensional pressure to obtain the non-dimensional boundary condition:

$$\tilde{u}(1,\tilde{z})=-\frac{\sigma K_o}{\tilde{p}(\tilde{z})}\left.\frac{\partial\tilde{u}}{\partial\tilde{r}}\right|_{\tilde{r}=1},\ \tilde{v}(1,\tilde{z})=0 \tag{8}$$

After expanding $\tilde{p}$, $\tilde{u}$, and $\tilde{v}$ in powers of ε Eqs. 9 10, we found that the 0th-order radial velocity was not included according to (Eq. 7):

$$\tilde{p}(\tilde{r},\tilde{z})=\tilde{p}_0(\tilde{r},\tilde{z})+\varepsilon\tilde{p}_1(\tilde{r},\tilde{z})+\varepsilon^2\tilde{p}_2(\tilde{r},\tilde{z})\ldots \tag{9}$$

$$\tilde{u}(\tilde{r},\tilde{z})=\tilde{u}_0(\tilde{r},\tilde{z})+\varepsilon\tilde{u}_1(\tilde{r},\tilde{z})+\varepsilon^2\ldots \tag{10}$$

$$\tilde{v}(\tilde{r},\tilde{z})=\varepsilon\tilde{v}_1(\tilde{r},\tilde{z})+\varepsilon^2\ldots \tag{11}$$

Subsequently, based on Eqs 9, 11 and solving Eq. 6 with the boundary conditions (Eq. 8), the non-dimensional 0th-order streamwise velocity is written as (Eq. 12)

$$\tilde{u}_0(\tilde{r},\tilde{z})=-\frac{2}{\alpha}\tilde{p}_0'\left(1-\tilde{r}^2+\frac{2\sigma K_o}{\tilde{p}_0}\right) \tag{12}$$

By substituting Eq. 12 into Eq. 7 and integrating it once in the non-dimensional microtube radius, the expression of the non-dimensional first-order radial velocity (Eq. 13) can be obtained:

$$\tilde{v}_1=\frac{1}{\alpha\tilde{p}_0}\left(\frac{d^2\left(\tilde{p}_0^{\,2}\right)}{d\tilde{z}^2}\right)\left(\frac{\tilde{r}}{2}-\frac{\tilde{r}^3}{4}\right)+2\sigma K_o\tilde{r}_0\tilde{p}_0'' \tag{13}$$

Combining Eq. 8, Eq. 13 was simplified to $(\tilde{p}_0')^2+\tilde{p}_0\tilde{p}_0''+4\sigma K_o\tilde{p}_0''=0$. It was expanded in a second-order polynomial of the non-dimensional pressure (Eq. 14), which contributes to solving the non-dimensional pressure (Eq. 15). Note that the non-dimensional pressure is positive and equal to 1 at the outlet of the microtube:

$$\frac{\tilde{p}_0^2}{2}+4\sigma K_o\tilde{p}_0-\left[\left(\frac{1}{2}+4\sigma K_o\right)\tilde{z}+\left(\frac{1}{2}\left(\frac{p_i}{p_o}\right)^2+4\sigma K_o\frac{p_i}{p_o}\right)(1|-\tilde{z})\right]=0 \tag{14}$$

$$\tilde{p}_0=-4\sigma K_o+\sqrt{(4\sigma K_o)^2+(1|+8\sigma K_o)\tilde{z}+\left(\left(\frac{p_i}{p_o}\right)^2+8\sigma K_o\frac{p_i}{p_o}\right)(1|-\tilde{z})} \tag{15}$$

The outlet flow rate is $q_o=\pi R^2\bar{u}_0|_{z=L}=\frac{\pi R^4 p_o}{8\mu L}\left(-\tilde{p}_0'-\frac{4\sigma K_o}{\tilde{p}_0}\tilde{p}_0'\right)$. Then, by substituting Eq. 14 into it, the gas rate at the outlet is written as Eq. 16, and the outlet mass flux is derived as shown in Eq. 17:

$$q_o=\frac{\pi R^4\left[p_i^2-p_o^2+8\sigma K_o p_o(p_i-p_o)\right]}{16\mu L p_o} \tag{16}$$

$$J_o=\frac{\left[p_i^2-p_o^2+8\sigma K_o p_o(p_i-p_o)\right]\rho_o R^2}{16\mu L p_o} \tag{17}$$

where J_o denotes the mass flux at the outlet, kg/s/m^2; and q refers to the flow rate at the outlet, m^3/s. In addition, the mass flux brought about by the Knudsen diffusion can be described by the Knudsen diffusion model (Eq. 18) (Javadpour, 2009). The total mass flux at the outlet of the microtube, including viscous flow, slip flow, and the Knudsen diffusion, is presented by a combination of Eq. 17 and Eq. 18, which is theoretically valid for slip and transition flow regimes ($P=p_i/p_o$) (Javadpour, 2009; Swami et al., 2012; Zhang et al., 2015). R_b is the gas constant [8.314 J/(mol K)]:

$$J_d=\frac{2R}{3\times10^3}\left(\frac{8\times10^3 M}{\pi R_b T}\right)^{0.5}\frac{p_i-p_o}{L} \tag{18}$$

$$J=\left[\frac{(P+1+8\sigma K_o)\rho_o R^2}{16\mu}+\frac{2R}{3\times10^3}\left(\frac{8\times10^3 M}{\pi R_b T}\right)^{0.5}\right]\frac{p_i-p_o}{L} \tag{19}$$

2.2 Model verification

Ewart et al. (2006) conducted an experimental investigation of the gas mass rate for an isothermal steady flow in cylindrical

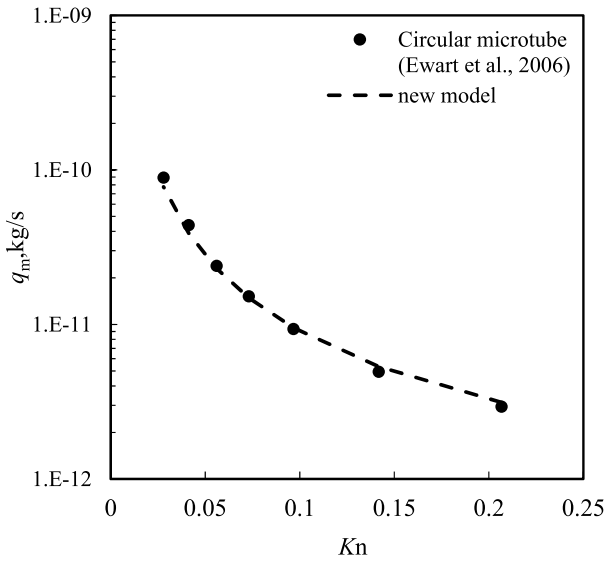

FIGURE 2
Comparison of the gas mass rate and Knudsen number calculated by a new model (Eq. 18) (dashed line) multiplied by the cross-section area to the experimental data of nitrogen flow in microchannel (black dots) by Ewart et al. (2006).

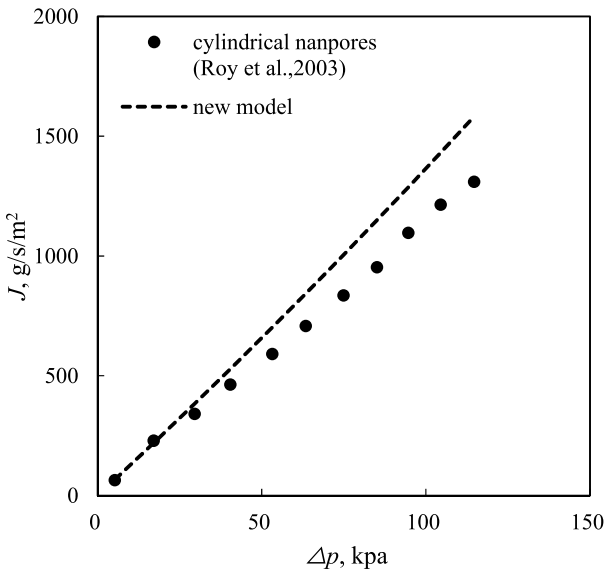

FIGURE 3
Comparison of the mass flux and pressure drop calculated by the new model (Eq. 18) (dashed line) to the experimental data in the cylindrical nanopores of the membrane by Roy et al. (2003).

microchannels. The diameter of the microchannel is 25.2 ± 0.35 μm, and the length is 5.30 cm. The resolution of the pressure gauge is 0.019 Pa. During the experiments, the calculated Reynolds numbers varied in the range of 1.8×10^{-3}~2.5. The experimental data on the gas mass rate *versus* the Knudsen number are shown in Figure 2 (black dots). The gas mass flux model proposed in this study (Eq. 19) was used to model the experiment (σ_v = 0.8) (Javadpour, 2009),

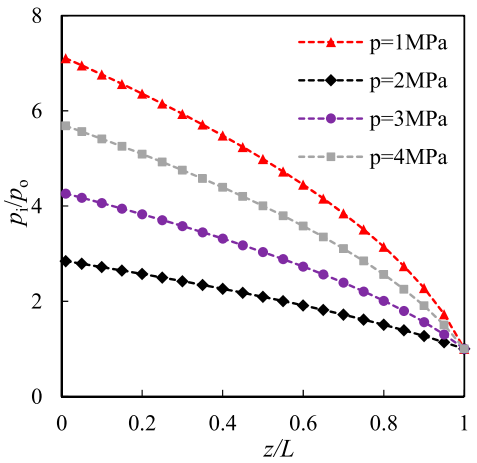

FIGURE 4
Pressure variation *versus* microtube coordinate at different inlet pressure.

which showed good agreement with the experimental results, and the relative error was less than 5%. In addition, Roy et al. (2003) used a membrane with a pore size of 200 nm and thickness of 60 μm to study the gas micro-flow. Figure 3 shows the mass flux *versus* pressure drop during this experiment, with an exit K_n of 7.36. The results calculated by Eq. 19 were simultaneously depicted in Figure 3 with an exit K_n of 14.66. K_n was expressed as the ratio of the mean free path to the microtube diameter in Roy's study. Based on Figure 3, the model results based on Eq. 19 approach the experimental results well at small pressure drops but deviate from the experimental results as the pressure drop increases. This is mainly because of the irregular shape of the microchannels in the membrane, which may lead to a smaller transport capacity than that of the regular microtube used in the model.

2.3 Model results

According to the models in Section 2.1, the gas flow characteristics, including the pressure distribution, gas mass flux, and mass flow ratio for different flow regimes in the microtube, will be further discussed. Nitrogen was selected as the gas source, the temperature was set to 300 K, and σ_v = 0.8 in the models.

Pressure distribution in the microtube for slip flow. Based on Eq. 15, the pressure distribution in the microtube at different inlet pressures is shown in Figure 4. The inlet pressures were 1, 2, 3, and 4 MPa (the outlet pressure was 0.7 MPa), and the average K_n values were 0.083, 0.052, 0.038, and 0.03, respectively. At the same time, the length and diameter (d) of the microtube were 1 cm and 200 nm, respectively. When gas flows into the microtube, the flow rate increases, whereas the pressure decreases, which results in a change in the gas density in the flow direction. As shown in Figure 4, there was a non-linear variation in the pressure along the flow direction. The non-linearity of the pressure distribution in this microtube should be caused by gas compression, whereas the rarefaction effect should be the opposite. With a larger ratio of the inlet and outlet pressures, the curvature of the pressure curve is

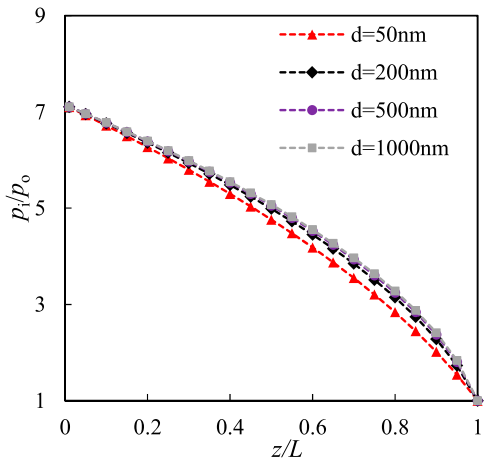

FIGURE 5
Pressure variation *versus* microtube coordinate at different microtube diameters.

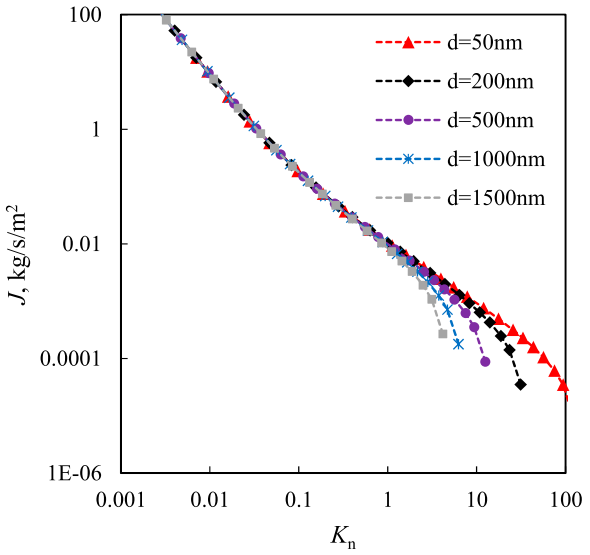

FIGURE 6
Gas mass flux *versus* K_n at different diameters of microtubes.

smaller, which can also be speculated from Eq. 15. In addition, the curvature was slightly smaller for the larger microtube at the same pressure ratio (Figure 5), and the influence of the gas type was almost negligible.

Gas mass flux *versus* K_n for different microtubes. Figure 6 shows the gas mass flux in microtubes of different scales with variational K_n. The microchannel length was 1 cm, and the diameter of the microtube ranged from 50 to 1,500 nm. Simultaneously, the outlet pressure was set to 0.002 MPa. Figure 6 shows that the gas mass flux in the microtubes gradually decreases with an increase in K_n. The gas mass flux for different microtubes is in accordance with K_n smaller than 1, and the absolute slope of the coincident curves continues to

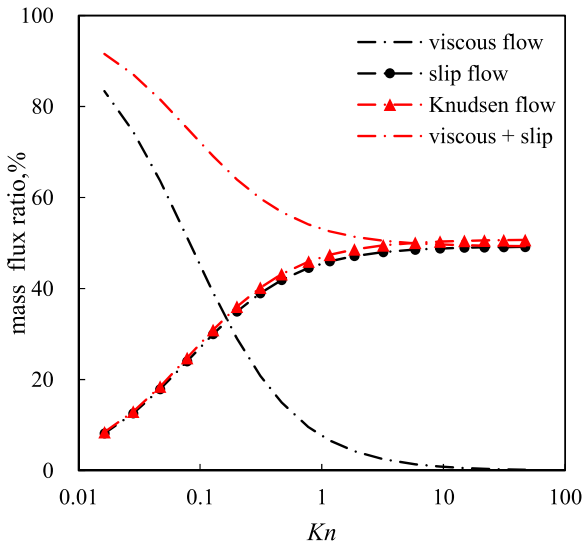

FIGURE 7
Dynamic mass flux ratio by different flow parts with K_n variations.

decrease with an increase in K_n. However, for K_n >1, a slower decrease occurred in the smaller microtubes, resulting in the mass flux curves beginning to diverge between the different microtubes. Additionally, the slippage effect and Knudsen diffusion were more significant in smaller microtubes. However, the average pressure was higher for smaller microtubes to achieve the same K_n.

Mass flow ratio *versus* K_n. During gas flow in a microtube, the flow regimes include viscous flow, slip flow, and Knudsen diffusion, which are mixed in different proportions (Zhang et al., 2015). According to Eqs 17–19, the gas mass flux ratios in different regimes with variations in K_n are shown in Figure 7. The length and diameter of the microtubes were 1 cm and 200 nm, respectively. As shown in Figure 7, the viscous flow is dominant, and the Knudsen diffusion is almost neglected when K_n is smaller than 0.1. As K_n increases, the slip flow and Knudsen diffusion play a more important role in the gas flow. At the later stage of the transition flow, the Knudsen diffusion accounts for almost 50% of the total gas mass flux, which approaches the sum of viscous and slip flows. The ratio of Knudsen diffusion is constant in the free molecular flow regime and shows a slight increase with an increase in the microtube diameter. In brief, slip flow and Knudsen diffusion must be considered for the rarefied gas flow in the microchannels.

3 Apparent permeability

At present, gas production in tight gas reservoirs presents a tendency for rapid growth. To a great extent, it is determined by the apparent permeability of gas transport in porous media. The gas flow mechanism in the microtubes can be used to promote the understanding of gas flow in tight reservoirs. Based on Darcy's law for compressible gas, the apparent permeability for tight porous media (Eq. 20) can be calculated (Javadpour, 2009; Zhang et al., 2015):

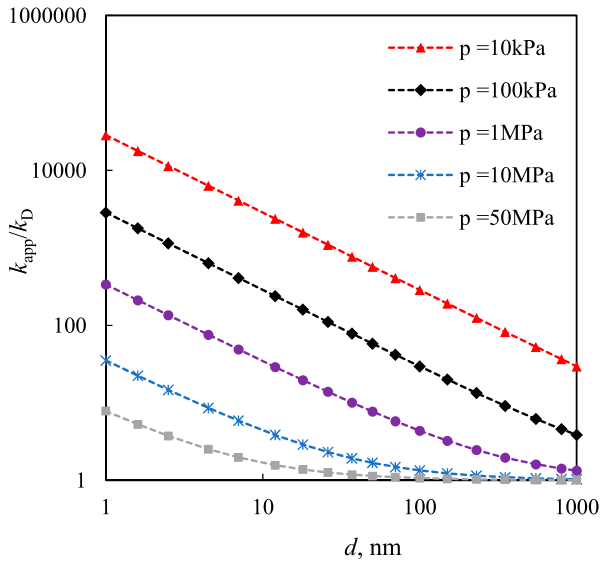

FIGURE 8
Effect of pressure and microchannel diameter on the k_{app}/k_D ratio.

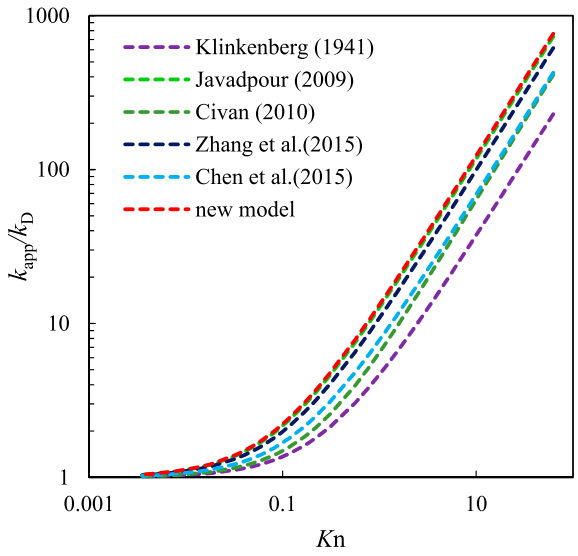

FIGURE 9
Comparison of the new apparent permeability model and the previously published models.

$$k_g = \frac{q_m \mu L}{A(p_i - p_o)\rho_{avg}} \tag{20}$$

where k_g denotes the permeability, m^2; and q_m refers to the gas mass rate (kg/s). By combining the new gas flux formula in the microtube presented in Section 2.1 (Eq. 19), a new apparent permeability model (Eq. 21) was derived, which includes viscous flow, slip flow, and Knudsen diffusion. Meanwhile, the ratio of apparent permeability and Darcy's permeability in porous media was written as Eq. 22. This indicates that the difference between the apparent permeability and the Darcy permeability depends primarily on the pore radius and pressure. The apparent permeability of tight reservoirs significantly depends on pressure and pore radius (Roy et al., 2003; Freeman et al., 2011):

$$k_{app} = \frac{(p + 1 + 8\sigma K_o)\rho_o R^2}{16\rho_{avg}} + \frac{2R\mu}{3 \times 10^3 \rho_{avg}} \left(\frac{8 \times 10^3 M}{\pi R_b T}\right)^{0.5} \tag{21}$$

$$\frac{k_{app}}{k_D} = \frac{(p + 1 + 8\sigma K_o)\rho_o}{2\rho_{avg}} + \frac{16\mu}{3 \times 10^3 \rho_{avg} R} \left(\frac{8 \times 10^3 M}{\pi R_b T}\right)^{0.5} \tag{22}$$

The correlation of the k_{app}/k_D ratio with pressure and pore diameter is shown in Figure 8. The outlet pressure was 0.002 MPa, and the pore diameter ranged from 1 to 6,000 nm. As shown in Figure 8, the ratio is largest at the smallest inlet pressure of 0.01 MPa. In addition, the ratio decreased with increasing pressure, which indicates that in tight reservoirs, the viscous flow was dominant at high pressure, whereas the production gas was mainly driven by slip and Knudsen diffusion at low pressure.

A comparison of the new apparent permeability model and the previously published models is shown in Figure 9. The k_{app}/k_D ratio based on Klinkenberg's (1941) model is the smallest, especially for K_n >0.1 because only the slippage effect was considered. In the model of Chen et al. (2015), the Knudsen diffusion was considered, but slippage was excluded. The k_{app}/k_D ratio of Chen et al.'s model is in good agreement with that of Civan's model (2010), which introduced Beskok and Kaniadakis's (1999) correction factor and is slightly larger than that in Klinkenberg's model. Zhang et al. (2015) combined the Klinkenberg model (1941) with the Knudsen diffusion. Javadpour (2009) combined slip flow using the theoretical dimensionless coefficient (F) introduced by Brown et al. (1946) with the Knudsen diffusion. The ratio predicted by the models of Zhang et al. and Javadpour is approximate while being larger than that of the models proposed by Klinkenberg, Chen et al., and Civan. The results of the new model most approximate those of Javadpour's model and are slightly larger than those of Chen et al.'s model because of the different slippage factors considered. It can be concluded that these apparent permeability models are all more or less equivalent in the slip flow regime and differ in the transition and free molecular regimes because the different gas flow mechanisms and theoretical models were accounted for.

4 Discussion

Pores and throat spaces in tight gas reservoirs are complex pore network systems. According to Zou et al. (2012), the pore diameter of tight gas reservoirs is in the range of 5–700 nm. When the pore diameter is less than 10 nm, surface diffusion occurs on the surface of the pores (Yang et al., 2016). Therefore, surface diffusion was not considered in this study because the vast majority of pores in reservoirs are larger than 10 nm. The range of K_n in tight gas reservoirs as the reservoir pressure decreases from 35 MPa to 1 MPa, as shown in Figure 10. Figure 10 suggests that K_n decreases with an increase in reservoir pressure and pore diameter, whereas the main flow

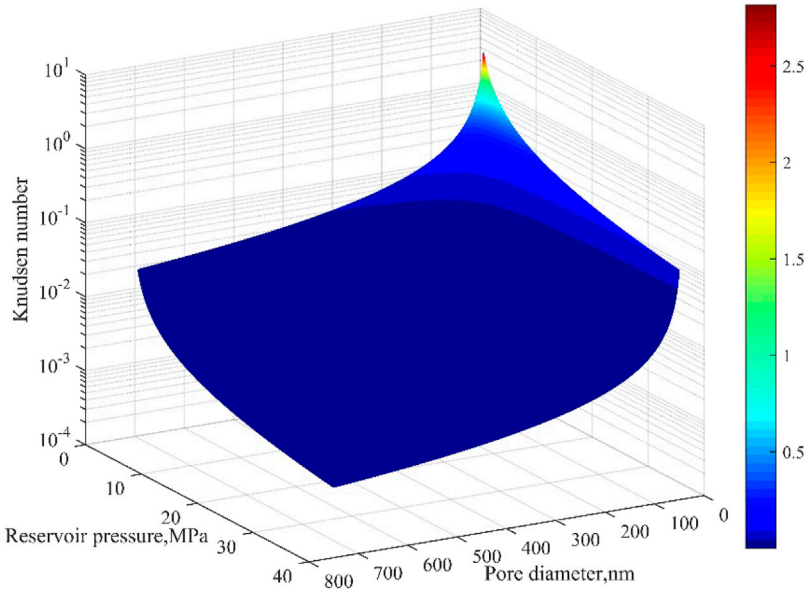

FIGURE 10
Range of K_n in tight gas reservoirs as p = 1–35 MPa.

regimes are the slip flow and transition regime (K_n <10). Darcy's law is not appropriate, and the new apparent permeability model is theoretically valid for tight gas reservoirs. However, it may be impractical to test the validity of these models in a laboratory study of reservoir rocks. As gas flows in true reservoir rocks, the variation in apparent permeability comes from two parts: the changes in gas flow regimes and the stress sensitivity of rocks (i.e., the pore space changes in rocks). For a high K_n, it is very difficult to weigh the contribution of the rock stress sensitivity because of the complicated variation in the gas flow regimes. Some authors excluded the slippage effect in tight sandstones by conducting experiments at high pressure (Li et al., 2009) or directly neglected the effect of effective stress on apparent permeability (Yuan et al., 2016). Therefore, it may be better to directly include the effective stress in the apparent permeability model together with the transport mechanism. Some researchers have attempted to do some work and have obtained apparent permeability models based on the linear effective stress law (Cao et al., 2016; Xiao et al., 2019). However, effective non-linear stress is common in tight rocks (Li et al., 2014; Xiao et al., 2019), and the apparent model needs to be improved in future work.

Moreover, based on network simulations, Bernabé et al. (2010) found that the matrix permeability in 3D simple cubic, FCC, and BCC networks obeyed the "universal" power laws, $k \propto (z\text{-}z_c)\beta$, where β is a function of the standard deviation of the pore radius distribution and z_c is the percolation threshold in terms of the coordination number (z). Permeability can be further expressed as a combination of scale-invariant parameters (Bernabé et al., 2010):

$$k = w\frac{\pi}{8}\left(\frac{r_H}{l}\right)^2 (z-1.5)^{\beta} r_H^2 \tag{23}$$

where r_H is the mean pore radius, l is the mean pore separation distance, and w is a function of the standard deviation of the pore radius distribution. Our results showed that rock permeability is related to the pore structure. Thus, it may be beneficial to considering the pore structure parameters in different apparent permeability models.

5 Conclusion

A 3D analysis of the Navier–Stokes equations for compressible gas flow in a microtube was presented by combining the first-order slip boundary condition. The non-linear pressure variation was analyzed for the gas slip flow. Subsequently, a new gas flux formula in the microtube, including viscous flow, slip flow, and Knudsen diffusion, was proposed, which is in good agreement with the published experimental data.

According to the calculated Knudsen number range, it can be concluded that slip and transition flow are the main flow regimes in tight gas reservoirs. The gas mass flux driven by slip and Knudsen diffusion significantly contributes to the total gas mass flux in the micropores and nanopores, and their weight increases with an increase in the Knudsen number.

A new apparent permeability model for tight gas reservoirs, considering the slippage effect and Knudsen diffusion, is presented based on the new gas flux formula and Darcy's law. By comparing the new model with previous models, the results of the new model were close to those of Javadpour's model, and other previous models may underestimate the apparent permeability of tight reservoirs. The results show that the apparent permeability strongly depends on the reservoir pressure and pore-throat radius.

Data availability statement

The original contributions presented in the study are included in the article/Supplementary Material. Further inquiries can be directed to the corresponding author.

Author contributions

LL was mainly responsible for the writing and modification of the article, as well as data processing and analysis required for article writing; MY and LT were mainly responsible for guiding the revision of the article and data analysis and processing to provide technical support; JH, YM, and WL provided financial and technical support in the writing and preparation of articles. All authors participated in the revision and agreed to submit the published version.

Funding

This research was financially supported by the National Natural Science Foundation Project of China (nos 51874248 and U19A2043) and the Youth Science and Technology Innovation Team of Southwest Petroleum University (no. 2018CXTD10).

Acknowledgments

We would like to show our deepest appreciation to all of them who supported and helped in this research.

Conflict of interest

TL and JH were employed by PetroChina Southwest Oil and Gasfield Company.

The remaining authors declare that the research was conducted in the absence of any commercial or financial relationships that could be construed as a potential conflict of interest.

Publisher's note

References

Agarwal, R. K., Yun, K. Y., and Balakrishnan, R. (2001). Beyond Navier–Stokes: Burnett equations for flows in the continuum–transition regime. *Phys. Fluids* 13 (10), 3061–3085. doi:10.1063/1.1397256

Agrawal, A. (2011). A comprehensive review on gas flow in microchannels. *Int. J. Micro-Nano Scale Transp.* 2 (1), 1–40. doi:10.1260/1759-3093.2.1.1

Arkilic, E. B., Schmidt, M. A., and Breuer, K. (1997). Gaseous slip flow in long microchannels. *J. Microelectromechanical Syst.* 6 (2), 167–178. doi:10.1109/84.585795

Arlemark, E. J., Dadzie, S. K., and Reese, J. M. (2010). An extension to the Navier–Stokes equations to incorporate gas molecular collisions with boundaries. *J. Heat Transf.* 132 (4), 041006. doi:10.1115/1.4000877

Bernabé, Y., Li, M., and Maineult, A. (2010). Permeability and pore connectivity: A new model based on network simulations. J. Geophys. Res. *Solid Earth* 115 (B10203), B10203. doi:10.1029/2010JB007444

Beskok, A., and Karniadakis, G. E. (1999). Report: A model for flows in channels, pipes, and ducts at micro and nano scales. *Microscale Thermophys. Eng.* 3 (1), 43–77. doi:10.1080/108939599199864

Beskok, A., and Karniadakis, G. E. (1994). Simulation of heat and momentum transfer in complex microgeometries. *J. Thermophys. Heat Transf.* 8 (4), 647–655. doi:10.2514/3.594

Brown, G. P., DiNardo, A., Cheng, G. K., and Sherwood, T. K. (1946). The flow of gases in pipes at low pressures. *J. Appl. Phys.* 17 (10), 802–813. doi:10.1063/1.1707647

Cao, P., Liu, J., and Leong, Y. K. (2016). General gas permeability model for porous media: Bridging the gaps between conventional and unconventional natural gas reservoirs. *Energ & Fuels* 30 (7), 5492–5505. doi:10.1021/acs.energyfuels.6b00683

Chakraborty, S., and Durst, F. (2007). Derivations of extended Navier-Stokes equations from upscaled molecular transport considerations for compressible ideal gas flows: Towards extended constitutive forms. *Phys. Fluids* 19 (8), 088104. doi:10.1063/1.2759531

Chen, L., Zhang, L., Kang, Q., Viswanathan, H. S., Yao, J., Tao, W. Q., et al. (2015). Nanoscale simulation of shale transport properties using the lattice Boltzmann method: Permeability and diffusivity. *Sci. Rep.* 5, 8089. doi:10.1038/srep08089

Chen, X. Y. (2017). *Advanced fluid mechanics (in Chinese)*. Beijing: Petroleum Industry Press.

Civan, F. (2010). Effective correlation of apparent gas permeability in tight porous media. *Transp. Porous Media* 82, 375–384. doi:10.1007/s11242-009-9432-z

Civan, F., Rai, C. S., and Sondergeld, C. H. (2011). Shale-gas permeability and diffusivity inferred by improved formulation of relevant retention and transport mechanisms. *Transp. Porous Media* 86 (3), 925–944. doi:10.1007/s11242-010-9665-x

Darabi, H., Ettehad, A., Javadpour, F., and Sepehrnoori, K. (2012). Gas flow in ultra-tight shale strata. *J. Fluid Mech.* 710 (1), 641–658. doi:10.1017/jfm.2012.424

Doyen, P. M. (1988). Permeability, conductivity, and pore geometry of sandstone. *J. Geophys. Res. Solid Earth* 93 (B7), 7729–7740. doi:10.1029/JB093iB07p07729

Ewart, T., Perrier, P., Graur, I., and Gilbert Meolans, J. (2006). Mass flow rate measurements in gas micro flows. *Exp. fluids* 41 (3), 487–498. doi:10.1007/s00348-006-0176-z

Florence, F. A., Rushing, J., Newsham, K. E., and Blasingame, T. A. (2007). *Presented at the Rocky mountain oil & gas technology symposium*. Denver, Colorado, USA: Society of Petroleum Engineers, 16–18. doi:10.2118/107954-MSImproved permeability prediction relations for low permeability sands

Fredrich, J. T., Greaves, K. H., and Martin, J. W. (1993). Pore geometry and transport properties of Fontainebleau sandstone. *Int. J. Rock Mech. Min. Sci. Geomechanics Abstr.* 30 (7), 691–697. doi:10.1016/0148-9062(93)90007-z

Freeman, M. C., Moridis, G. J., and Blasingame, T. A. (2011). A numerical study of microscale flow behavior in tight gas and shale gas reservoir systems. *Transp. Porous Media* 90 (1), 253–268. doi:10.1007/s11242-011-9761-6

Fukui, S., and Kaneko, R. (1988). Analysis of ultra-thin gas film lubrication based on linearized Boltzmann equation: First report—derivation of a generalized lubrication equation including thermal creep flow. *J. Tribology-transactions Asme* 110 (2), 253–261. doi:10.1115/1.3261594

Gensterblum, Y., Ghanizadeh, A., Cuss, R. J., Amann-Hildenbrand, A., Krooss, B. M., Clarkson, C. R., et al. (1995). Gas transport and storage capacity in shale gas reservoirs - a review. Part A: Transport processes. *J. Unconv. Oil Gas Resour.* 12, 87–122. doi:10.1016/j.juogr.2015.08.001

Hadjiconstantinou, N. G. (2003). Comment on Cercignani's second-order slip coefficient. *Phys. Fluids* 15 (8), 2352–2354. doi:10.1063/1.1587155

Harley, J. C., Huang, Y., Bau, H. H., and Zemel, J. N. (1995). Gas flow in micro-channels. *J. Fluid Mech.* 284, 257–274. doi:10.1017/S0022112095000358

Hsieh, S. S., Tsai, H. H., Lin, C. Y., Huang, C. F., and Chien, C. M. (2004). Gas flow in a long microchannel. *Int. J. Heat Mass Transf.* 47 (17-18), 3877–3887. doi:10.1016/j.ijheatmasstransfer.2004.03.027

Javadpour, F., Fisher, D., and Unsworth, M. (2007). Nanoscale gas flow in shale gas sediments. *J. Can. Petroleum Technol.* 46 (10), 55–61. doi:10.2118/07-10-06

Javadpour, F. (2009). Nanopores and apparent permeability of gas flow in mudrocks (shales and siltstone). *J. Can. Petroleum Technol.* 48 (08), 16–21. doi:10.2118/09-08-16-DA

Jones, F. O., and Owens, W. W. (1980). A laboratory study of low-permeability gas sands. *J. Petroleum Technol.* 32 (09), 1631–1640. doi:10.2118/7551-PA

Kalarakis, N., Michalis, V. K., Skouras, E. D., and Burganos, V. N. (2012). Mesoscopic simulation of rarefied flow in narrow channels and porous media. *Transp. Porous Media* 94, 385–398. doi:10.1007/s11242-012-0010-4

Kennard, E. H. (1938). *Kinetic theory of gases*. McGraw-Hill.

Kim, C., Jang, H., Lee, Y., and Lee, J. (2016). Diffusion characteristics of nanoscale gas flow in shale matrix from Haenam basin, Korea. *Environmational Earth Sci.* 75 (4), 350–358. doi:10.1007/s12665-016-5267-4

Klinkenberg, L. J. (1941). The permeability of porous media to liquids and gases. *Drill. Prod. Pract.*, 57–73. doi:10.5510/OGP20120200114

Li, M., Xiao, W. L., Bernabé, Y., and Zhao, J. Z. (2014). Nonlinear effective pressure law for permeability. *J. Geophys. Res. Solid Earth* 119, 119:302–318. doi:10.1002/2013JB010485

Li, M., Bernabé, Y., Xiao, W. I., Chen, Z. Y., and Liu, Z. Q. (2009). Effective pressure law for permeability of E-bei sandstones. *J. Geophys. Res.* 114 (B7), B07205. doi:10.1029/2009JB006373

Lindquist, W. B., Venkatarangan, A., Dunsmuir, J., and Wong, T. f. (2000). Pore and throat size distributions measured from synchrotron X-ray tomographic images of Fontainebleau sandstones. *J. Geophys. Res.* 105 (B9), 21509–21527. doi:10.1029/2000JB900208

Maurer, J., Tabeling, P., Joseph, P., and Willaime, H. (2003). Second-order slip laws in microchannels for helium and nitrogen. *Phys. Fluids* 15 (9), 2613–2621. doi:10.1063/1.1599355

Maxwell, J. C. (1878)., 1. Appendix.*Phil. Trans. R. Soc.*

Maxwell, J. C. (1867). *On the dynamical theory of gases*, A157. London: Philosophical Transactions of the Royal Society of London, 49–88. doi:10.1098/rstl.1867.0004

Michalis, V. K., Kalarakis, A. N., Skouras, E. D., and Burganos, V. N. (2010). Rarefaction effects on gas viscosity in the Knudsen transition regime. *Microfluid. Nanofluidics* 9 (4-5), 847–853. doi:10.1007/s10404-010-0606-3

Michel, G. G., Sigal, R. F., Civan, F., and Devegowda, D. (2011). *Parametric investigation of shale gas production considering nano-scale pore size distribution, formation factor, and non-Darcy flow mechanisms*. Denver, Colorado, USA: Presented at the SPE Annual Technical Conference and Exhibition. doi:10.2118/147438-MS

Mitsuya, Y. (1993). Modified Reynolds equation for ultra-thin film gas lubrication using 1.5-order slip-flow model and considering surface accommodation coefficient. *J. Tribology-transactions Asme* 115 (2), 289–294. doi:10.1115/1.2921004

Morini, G. L., Yang, Y., Chalabi, H., and Lorenzini, M. (2011). A critical review of the measurement techniques for the analysis of gas microflows through microchannels. *Exp. Therm. Fluid Sci.* 35 (6), 849–865. doi:10.1016/j.expthermflusci.2011.02.005

Rahmanian, M., Aguilera, R., and Kantzas, A. (2012). A new unified diffusion-viscous-flow model based on pore-level studies of tight gas formations. *SPE J.* 18 (01), 38–49. doi:10.2118/149223-PA

Roy, S., and Chakraborty, S. (2007). Near-wall effects in micro scale Couette flow and heat transfer in the Maxwell-slip regimes. *Microfluid. Nanofluidics* 3 (4), 437–449. doi:10.1007/s10404-006-0132-5

Roy, S., Raju, R., Chuang, H. F., Cruden, B. A., and Meyyappan, M. (2003). Modeling gas flow through microchannels and nanopores. *J. Appl. Phys.* 93 (8), 4870–4879. doi:10.1063/1.1559936

Rushing, J. A., Newsham, K. E., and Van Fraassen, K. C. (2003). "Measurement of the two-phase gas slippage phenomenon and its effect on gas relative permeability in tight sands," in *Presented at the 2003 SPE annual technical conference and exhibition held in denver* (Colorado, USA, 5–8. doi:10.2118/84297-MS

Rutter, E., Mecklenburgh, J., and Bashir, Y. (2022). Matrix gas flow through "impermeable" rocks – shales and tight sandstone. *Solid earth.* 13 (3), 725–743. doi:10.5194/se-13-725-2022

Sakhaee-Pour, A., and Bryant, S. (2012). Gas permeability of shale. *SPE Reserv. Eval. Eng.* 15 (04), 401–409. doi:10.2118/146944-PA

Sakhaee-Pour, A., and Bryant, S. L. (2011). *Gas permeability of shale*. Denver, Colorado,USA: Presented at the SPE Annual Technical Conference and Exhibition. doi:10.2118/146944-MS

Sander, R., Pan, Z., and Connell, L. D. (2017). Laboratory measurement of low permeability unconventional gas reservoir rocks: A review of experimental methods. *J. Nat. Gas Sci. Eng.* 37, 248–279. doi:10.1016/j.jngse.2016.11.041

Shen, S., Chen, G., Crone, R. M., and Anaya-Dufresne, M. (2007). A kinetic-theory based first order slip boundary condition for gas flow. *Phys. Fluids* 19 (8), 086101. doi:10.1063/1.2754373

Swami, V., Clarkson, C. R., and Settari, A. (2012). "Non-Darcy flow in shale nanopores: Do we have a final answer?," in *Presented at the SPE Canadian unconventional resources conference* (Alberta, Canada: Calgary). doi:10.2118/162665-MS

Tang, G. H., Tao, W. Q., and He, Y. L. (2005). Gas slippage effect on microscale porous flow using the lattice Boltzmann method. *Phys. Rev. E* 72 (5), 056301. doi:10.1103/PhysRevE.72.056301

Velasco, A. E., Friedman, S. G., Pevarnik, M., Siwy, Z. S., and Taborek, P. (2012). Pressure-driven flow through a single nanopore. *Phys. Rev. E* 86 (2), 025302. doi:10.1103/PhysRevE.86.025302

Wu, L., and Bogy, D. B. (2001). A generalized compressible Reynolds lubrication equation with bounded contact pressure. *Phys. Fluids* 13 (8), 2237–2244. doi:10.1063/1.1384867

Xiao, W. L., Bernabé, Y., Evans, B., Mok, U., Zhao, J., Ren, X., et al. (2019). Klinkenberg effect and effective pressure for gas permeability of tight sandstones. *J. Geophys. Res. Solid Earth* 124 (2), 1412–1429. doi:10.1029/2018JB016686

Yang, B., Kang, Y., You, L., Li, X., and Chen, Q. (2016). Measurement of the surface diffusion coefficient for adsorbed gas in the fine mesopores and micropores of shale organic matter. *Fuel* 181, 793–804. doi:10.1016/j.fuel.2016.05.069

Yuan, Y. D., Doonechaly, N. G., and Rahman, S. (2016). An analytical model of apparent gas permeability for tight porous media. *Transp. Porous Media* 111 (1), 193–214. doi:10.1007/s11242-015-0589-3

Zhang, P., Hu, L., Meegoda, J. N., and Gao, S. (2015). Micro/nano-pore network analysis of gas flow in shale matrix. *Sci. Rep.* 5, 13501. doi:10.1038/srep13501

Zou, C. N., Zhu, R. K., Wu, S. T., Yang, Z., Tao, S. Z., Yuan, X. J., et al. (2012). Types, characteristics, Genesis and prospects of conventional and unconventional hydrocarbon accumulations: Taking tight oil and tight gas in China as an instance. *Acta Pet. Sin.* 33 (2), 173–187.

frontiers | Frontiers in Earth Science

TYPE Original Research
PUBLISHED 17 March 2023
DOI 10.3389/feart.2023.1131298

OPEN ACCESS

EDITED BY
Giovanni Martinelli,
National Institute of Geophysics and Volcanology, Italy

REVIEWED BY
Jiafei Zhao,
Dalian University of Technology, China
Yang Mingjun,
Dalian University of Technology, China

*CORRESPONDENCE
Mingming Zheng,
mingming.zheng@hotmail.com

SPECIALTY SECTION
This article was submitted to Solid Earth Geophysics,
a section of the journal
Frontiers in Earth Science

RECEIVED 24 December 2022
ACCEPTED 09 March 2023
PUBLISHED 17 March 2023

CITATION
Wang X, Zheng M, Zhou K, Qi Q, Wu Z, Yan S, Zeng G and Ma T (2023), Physical property response of peri-well sediments during cementing of gas hydrate-bearing sediments in conventional oil-gas wells in the South China Sea.
Front. Earth Sci. 11:1131298.
doi: 10.3389/feart.2023.1131298

Physical property response of peri-well sediments during cementing of gas hydrate-bearing sediments in conventional oil-gas wells in the South China Sea

Xiaoyu Wang[1,2], Mingming Zheng[2,3]*, Kerui Zhou[2], Qiaomu Qi[2], Zurui Wu[2], Shichun Yan[2], Guoao Zeng[2] and Ting Ma[1]

[1]School of Civil Engineering, Henan Vocational University of Science and Technology, Zhoukou, China, [2]State Key Laboratory of Geohazard Prevention and Geoenvironment Protection, Chengdu University of Technology, Chengdu, China, [3]Engineering Research Center of Rock-Soil Drilling and Excavation and Protection, Ministry of Education, China University of Geosciences (Wuhan), Wuhan, China

In order to investigate the effect of cement slurry penetration during cementing in gas hydrate-bearing sediments. In this study, gas hydrate bearing sediments in Shenhu Area of the South China Sea is taken as the research object, numerical simulation software TOUGH+HYDRATE is used to realistically reproduce the process of cement slurry exothermic and penetration by "continuous segmental simulation." The physical properties response of sediments near the well wall during cementing under different cementing process parameters and sediment geological parameters are well studied. Results show that the hydration exothermic rate of cement slurry has significant influence on the decomposition degree of hydrate in the penetration area, when it is higher than 0.21 $J\cdot(g\cdot s)^{-1}$, the hydrate in the penetration range is completely decomposed. The cementing pressure difference affects the cement slurry penetration depth, the extent of sediment pressurization and heat-up, which in turn affects the range of the decomposition zones. In addition, it is helpful to increase pore pressure and hydrate phase equilibrium, but it should be strictly controlled within the window of sediment fracture pressure. Extending the holding time of cementing pressure difference expands the heat-up and decomposition zones, but also delays the onset of hydrate decomposition. Higher saturation prevents the penetration of cement slurry and weakens the diffusion of pore pressure, which causes the shrinkage of the heat-up and decomposition zones, and makes higher pressure in the decomposition zone. The hydrate phase equilibrium environment directly determines the resistance of hydrate sediments to perturbation, with insignificant changes in physical properties in stable sediments. The permeability affects the transport efficiency of pore fluid and expands the heat-up zone and decomposition zone, but also weakens the pore pressure peak of sediment, the increase of permeability from 1 to 100 mD expands the decomposition zone from 1 to 10 cm. The porosity has a less significant effects on the extent of sediment physical properties. This study is a valuable guide and reference for hydrate sediment cementing operations.

KEYWORDS

natural gas hydrate, deep-water oil-gas cementing, physical properties response, dynamic exothermic source, continuous segmental simulation, cementing process and geological conditions

1 Introduction

With the gradual depletion of continental oil-gas resources and the maturity of marine oil-gas development technology, marine areas have become the most desirable resource replacement areas for some countries (Wang J. Q., 2021). In China, the South China Sea region has been proven to contain large amounts of oil-gas resources and natural gas hydrate resources, which are predicted to reach a total of 29 billion tons of oil and gas (Lu, 2013). Due to the characteristics of the marine sedimentary environment, most marine oil, gas and hydrate resources are located in the marine basin area (Zhang et al., 2009; Pang, 2012), which has a high overlap with the geographic location of oil-gas resources and gas hydrate resources in the South China Sea (Figure 1) (Sun et al., 2011; Weng et al., 2013; Wang D. D., 2021). Since hydrates can only exist stably in low-temperature and high-pressure environments (Sloan and Koh, 2008), they are generally located in the shallow surface area of the seafloor, while oil-gas resources are usually buried at depths of several kilometers. Therefore, during the drilling of oil-gas wells, gas hydrate bearing sediments (GHBS) are often encountered in the shallow surface layer.

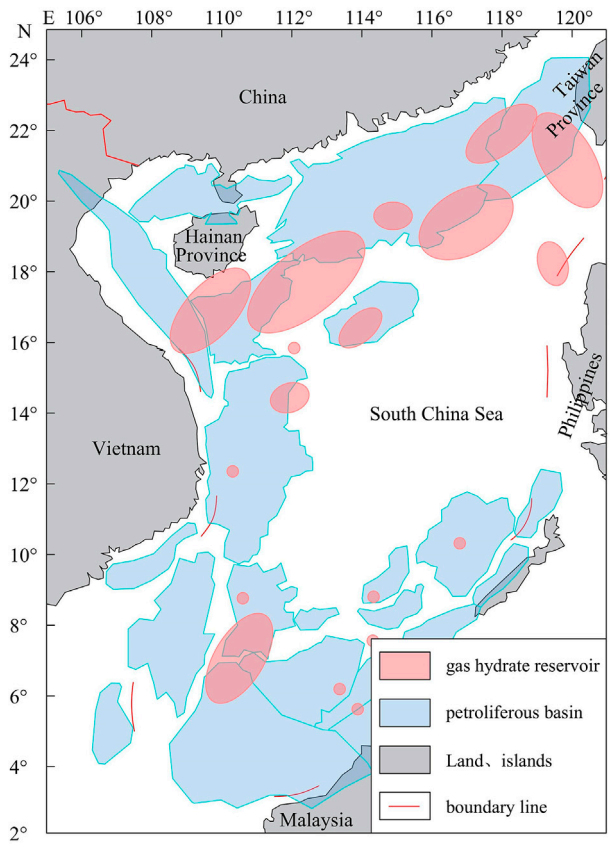

FIGURE 1
Distribution of hydrocarbon-bearing basins and gas hydrate reservoirs in the South China Sea (adapted from Wang D. D., 2021; Weng et al., 2013; Sun et al., 2011).

In the Shenhu Area of the South China Sea, the GHBS are complex, mainly powdery sands and clays, and the mechanical strength is low in the sediments. The hydrate reservoir environment is close to its phase equilibrium, so slight changes in temperature and pressure can lead to its decomposition (Ning et al., 2010). In deepwater drilling, the entire well is usually cemented, and the cement hydration exotherm during cementing will inevitably cause the sediment to heat up, which will cause the decomposition of the hydrate near the wellbore wall and reduce the density of the sediment. Meanwhile, the high-pressure free gas and water generated by decomposition can further disturb the stability of GHBS and even cause sediment rupture, which will seriously affect the quality of cementing. Therefore, it is crucial to investigate the effect of the cementing process on GHBS, which will provide a theoretical basis for the design and optimization of the cementing process to ensure the safety of the wellbore.

To address the cementing problem of GHBS, Li. (2018) established a calculation method for the cement slurry penetration distance and penetration volume in the sediments around a well and studied the effect of cement slurry penetration into GHBS by using indoor tests and numerical simulations together. The results showed that it would lead to wellbore wall destabilization and affect the quality of cementing under the effect of cement slurry penetration. Yang et al. (2022) developed a phase change microencapsulated low-heat cement slurry. It was shown that the thermal adjustment of the microencapsulation suppressed the heat-up rate of the cement slurry and significantly reduced the damage to hydrates. Xu et al. (2014) proposed a silicate cement slurry system for use in GHBS environments to address the problems of low temperatures, fragile sediments, and gas hydrate intercalation in cementing wells for deepwater drilling. Xi et al. (2020) developed a cement slurry for cementing GHBS in the sea at temperatures ranging from 4°C to 30°C. The above scholars have mainly studied the optimization of cementing process, but the effect of cement slurry penetration on GHBS has not been systematically investigated.

Cement slurry penetration into sediments is essentially a mass and heat transfer process, which is very similar to that of drilling fluids, and the drilling process of GHBS has been studied for quite a long time. Zheng et al. (2022, Zheng et al. (2021), Zheng et al. (2020), Zheng et al. (2017) conducted a large space-scale indoor simulation experiment for the process of drilling fluid penetration into GHBS using an artificial rock core preparation device and an integrated simulation system for seepage and exploitation in GHBS. The study demonstrated the physical property response rule of sediments in this process and noted that temperature is the most important influencing factor of hydrate decomposition. Then, TOUGH+HYDRATE was used to conduct a preliminary numerical simulation of cement slurry penetration into GHBS and to obtain the physical property response of the sediment in this process. Tinku and Vikas. (2018) analyzed the effect of hydrate

inhibitors in subsea GHBS on the rheological behavior of drilling fluids and optimized drilling fluid formulations. Zhang et al. (2018) used ultrasonic testing to investigate the process of two types of hydrate thermodynamic inhibitor drilling fluids, specifically NaCl and ethylene glycol, penetrating into GHBS, which explored the effect rule of hydrate thermodynamic inhibitors on hydrate decomposition. Merey (2019) evaluated and analyzed follow-up logging and other drilling data from gas hydrate drilling campaigns around the world, finding that the risks in drilling are more manageable and concluding that the key to drilling safety is proper wellbore design. Ning et al. (2013) used TOUGH+HYDRATE numerical simulation software to observe the dynamic behavior of drilling fluid penetration into GHBS, which proved that heat transfer phenomena caused by temperature differences between drilling fluid and sediment can lead to hydrate decomposition and thus affect sediment stability, followed by a systematic study of the sensitivity of sediment properties and drilling process parameters. Tu et al. (2010) studied the decomposition of hydrates in the pores of porous media, thus identifying the main influencing factors in this process, and finally proposed a new model of drilling fluid penetration. The above studies have well revealed the effect of drilling fluid penetration on GHBS, and the results are important references for this study due to the similarity of the two scenarios.

The above studies are a guide to analyze the physical property response rules of GHBS during cementing, but the unique difficulty in the cementing problem is that the cement slurry not only continuously penetrates GHBS during cementing but is also continuously exothermic as a new heat source, making the process more variable and significantly more complex. Based on this, the authors take the SH2 station exploration well in the hydrate drilling project GMGS-1 in the Shenhu Area of the South China Sea as the research object, using the numerical simulation software TOUGH+HYDRATE developed by Lawrence Berkeley National Laboratory to simulate the penetration process of the cement slurry as a dynamic exothermic source into the sediment during the cementing process. Then, we study the influence of the cementing process on the physical properties of GHBS near the wellbore wall under *in situ* sediment conditions and cementing process conditions. Furthermore, we analyze the influence of different cementing process parameters and sediment properties on this process to provide some guidance and reference for GHBS cementing operations.

2 Simulation methods

2.1 Simulation objects

Due to the superiority of the reservoir conditions, hydrate reservoirs in the Shenhu Area in the middle part of the northern land slope of the South China Sea have become a popular research area for hydrate exploration and development (Wu et al., 2007b; Wang et al., 2011a, 2011b; Yang et al., 2017; Li et al., 2022). In 2007, China conducted a gas hydrate drilling project GMGS-1 in this area, and the location of the study area in this study is shown in Figure 2. The drilling project drilled eight scientific drilling holes (SH1~SH8), and satisfactory test hydrate samples were recovered from three

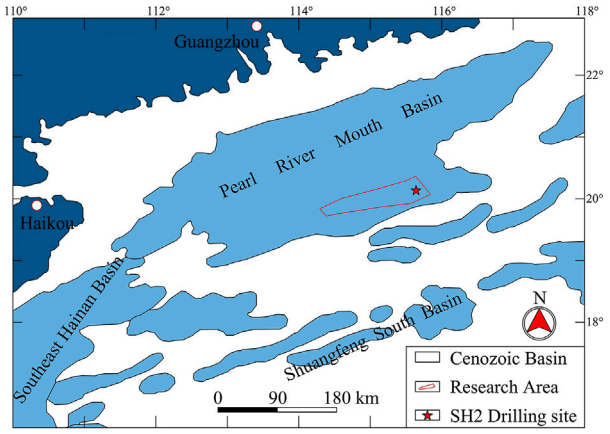

FIGURE 2
Location map of the GMGS-1 project in the Shenhu Area of the South China Sea (adapted from Wu et al., 2007b).

holes, SH2, SH3, and SH7 (Wu et al., 2007a; Zhang et al., 2007). In particular, the SH2 hole is extremely rich in both field data and sediment data, so it is an important object for research on hydrates. For example, Zhu et al. (2020) used these hole data to predict the accumulation of gas hydrates in marine sediments. Sun (2018) used these data to simulate and analyze the influence pattern of the drilling construction process on GHBS. Shen et al. (2019) used it to build a model to quantitatively explain the source of gas production in extraction wells.

This study also relies on field data from the SH2 of the GMGS-1 project for the simulation study. Based on logging data and sample analysis results (Nakai et al., 2007; Wang et al., 2011a, Wang et al., 2011b), the water depth at this site is approximately 1,235 m. The hydrate reservoir is stored in the sediment from approximately 185–229 m below the seafloor, and the longitudinal depth of the sediment is approximately 44 m. The sediment mainly consists of powdery clay with a porosity of approximately 0.40. *In situ* logging data indicate that the seafloor temperature is approximately 4°C. The hydrate saturation is high, up to 0.47. The geothermal gradient is approximately 47°C/km.

2.2 Numerical model and parameters

The cement slurry penetration process in cementing is shown in Figure 3, based on which a numerical model is developed. Since cement slurry penetration is radially dispersed from the wellbore to the surrounding area, the two-dimensional cylindrical coordinate system is the most suitable to describe the process. In addition, the cementation process is usually homogeneous in long sections of sediments, and the GHBS can be considered homogeneous within a certain range, so the penetration process can be assumed to be homogeneous in any section in the direction of the wellbore axis. Therefore, this three-dimensional model can be reduced to a one-dimensional problem in a two-dimensional coordinate system. As shown in Figure 4, a thin layer of 0.1 m thickness in the GHBS is taken as the object of study, which is used to establish the numerical

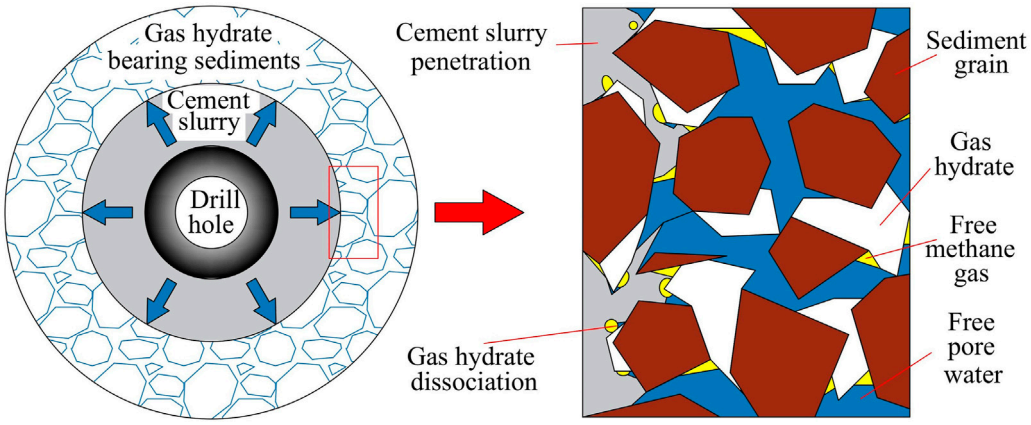

FIGURE 3
Schematic diagram of cement slurry for cementing penetrating into GHBS.

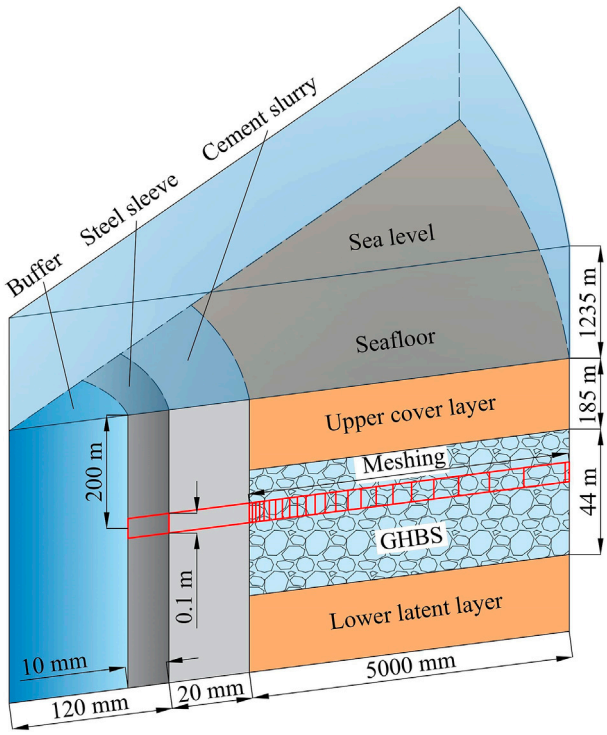

FIGURE 4
Schematic diagram of the wellbore-sediment numerical model for GHBS cementing.

model. The model is an axisymmetric cylinder of 0.1 m thick, the wellbore is at the center, the diameter of the wellbore is taken as 280 mm, the steel casing of 240 mm outer diameter and 10 mm thickness is chosen, and the annular space between the outer wall of the casing and the sediment is 20 mm thick. Outside the wellbore is the GHBS. Combined with previous studies on related issues (Liu, 2018; Sun, 2018), the radial depth was taken as 5 m for a conservative estimate. The mesh is divided into one layer in the axial direction of the wellbore, with a thickness of 0.1 m. The mesh is divided into 113 cells in the radial direction, which are dense near the wellbore wall and sparse at the far side. The cell closest to the center is the casing cell, the outer cell is the annulus cell, and the further outer cells are all GHBS cells.

The sediments 200 m below the seafloor were used as the target study layer in the simulation, and the values taken were based on the available logging and drilling coring data from the SH2 station (Wu et al., 2007b; Nakai et al., 2007; Wang et al., 2011a, Wang et al., 2011b). The sediment density is 2,600 kg/m^3, the wet thermal conductivity is 3.1 W/(m°C), the dry thermal conductivity is 1.0 W/(m°C), the specific heat of grains is taken as 1,000 J/(kg°C), the sediment compression coefficient is taken as 1.0×10^{-8} Pa^{-1}, the porosity is taken as 0.4, and the absolute permeability is taken as 1.0×10^{-14} m^2. The sediment temperature is 13.4°C, and the pore pressure is 14.5 MPa. The sediment pore water salinity is 3.05%, which is basically the same as that of the overlying seawater. The gas hydrate phase stability temperature in this environment is calculated to be 15.4°C. The pore space is almost filled with hydrate and water, the hydrate saturation is taken as 33%, and the free gas saturation is approximately 1%~1.2%. To avoid interference, the original gas phase material of the sediment is neglected.

In cementing operations, to ensure the cementing strength and sealing performance of the second interface, the annular cement slurry is usually kept under pressure in a safety pressure window for a period of time after cement injection so that the cement slurry penetrates into the sediment. During this process, the cement slurry leading edge position and exothermic rate are constantly changing; that is, there is the problem of a "dynamic exothermic source." To fully recreate this process, "continuous segmental simulation" is used. During the holding pressure phase, the cement slurry cell is set as a constant pressure cell and held for the required time, and at the end of the holding pressure, it is changed to a time-varying cell. The whole process is divided into several segments for simulation (segment length can be freely set according to the accuracy requirements, this paper uses 2 min) until the initial setting of cement slurry, and the initial setting time is taken as 28 min. During the experiment, the amount of cement slurry penetration

TABLE 1 Segmented values of the cement hydration exothermic rate during simulation.

Time period/s	Value/J·(g·s)$^{-1}$
0–120	0.20
120–240	0.28
240–360	0.40
360–480	0.36
480–600	0.32
600–720	0.24
720–1,680	0.16

at the end of each simulation is recorded to determine the distribution range of cement slurry at the beginning of the next simulation, based on which the exothermic cells are set at the corresponding positions in the model. Additionally, according to the measured data, the exothermic rate of hydration is adjusted so that the cement slurry penetration process can be accurately recreated. In addition, the SH2 station well sediments are mostly weakly cemented and uncemented, and the safety pressure window is narrow, so the designed cementing pressure difference needs to be within the range of sediment fracture pressure.

The cementing parameters in the simulation were selected based on the cementing technology schemes of previous studies (Xu et al., 2014; Liu, 2018; Liu et al., 2018; Zhang et al., 2020; Yang et al., 2021a; Yang et al., 2021b). The cementing pressure difference is taken as 1 MPa, and the holding time of cementing pressure difference is taken as 7 min. The cement slurry adopts a low-temperature low-density cement slurry system, and the density is taken as 1,050 kg/m^3. The average exothermic rate during the simulation is taken as 0.28 J/(g·s), and its specific segmental values are shown in Table 1. The initial temperature of the cement slurry is usually somewhat higher than the sediment temperature, which is taken as 14.4°C. The parameters required in the simulation are summarized in Table 2.

3 Main characteristics of the cement slurry penetration into the GHBS process

Figure 5 illustrates the penetration of the cement slurry during the cementing process. It can be seen in the figure that cement slurry penetration into the sediment mainly occurs during the holding pressure phase, which is obviously due to the presence of the cementing pressure differential providing a strong driving force for the penetration process. It can also be seen that the cement slurry penetration is not linear during the pressure-holding period but gradually slows down with time. The reason for this is that the high-pressure fluid penetrating into the sediment in the early stage raises the sediment pore pressure and reduces the pressure difference, making the driving force of the penetration gradually weaker. After the maintenance pressure is removed, the cement slurry penetration comes to a standstill and hardly changes significantly in the subsequent time. Therefore, it can be assumed that cement slurry penetration occurs mainly during the holding pressure period, with a penetration depth of approximately 2.5 cm, after which the penetration is negligible.

Figures 6A, B show the distribution of pressure in the sediment at various time points. During the holding pressure period (before 420 s), the pore pressure increased sharply near the wellbore wall, and the leading edge of the pressure increase area gradually moved deeper into the sediment as the holding pressure process continued. This is because the high-pressure fluid (cement slurry) continuously penetrated into the sediment under the pressure differential during the holding pressure, which raised the sediment pore pressure, and the continuous pressurization caused the high-pressure range to spread to the greater depth. After the removal of the cementing pressure differential (after 420 s), the pressure near the wellbore wall first experienced a sharp drop and then continued to slowly decrease with time. However, the high-pressure impact zone gradually penetrated deeper into the sediment and finally reached approximately 2.5 m. This is because the removal of the cementing pressure differential caused the high-pressure fluid accumulated at the wellbore wall to be released instantaneously, resulting in a sharp pressure drop, and then the high-pressure fluid gradually moved deeper due to the pressure differential. There are two points worth noting here: 1) the pressure rose near the wellbore wall after 900 s; 2) the highest pressure point in the sediment was initially at the wellbore but deepened to a distance from the wellbore wall at the later stage. This is due to the decomposition of the hydrate near the wellbore wall at the later stage, which made the pressure rise at the decomposition site and a local pressure peak when the pressure at the decomposition was higher than that at the wellbore wall.

Figure 6C shows the distribution of temperature in the sediment at various time points. As seen in the figure, the region of large temperature variation occurs mainly within the cement slurry penetration zone, with the leading edge of the region being approximately 2.5 cm. Before 900 s, the temperature variation in the region is extremely small, after which it starts to increase rapidly. Combined with Figures 6D–F, it is easy to see that this is because when the temperature rises to a certain extent before 900 s, the temperature increase is hindered by the heat absorption due to the decomposition of hydrate in the region, and only after that the hydrate is consumed does the temperature start to rise rapidly. At deeper depths, due to the absence of cement slurry, the temperature increase relies mainly on heat conduction, which changes very little, and the leading edge of the region is approximately 10 cm.

Figures 6D–F show the distribution of hydrate, liquid and gas saturation at various time points. Combined analysis shows that the decomposition behavior of hydrate in the range of cement slurry penetration starts at approximately 480 s, which is due to the time required to warm up the sediment to disrupt the hydrate phase equilibrium environment. After that, the hydrate decomposition deepened in this range, after that, the hydrate decomposition deepened and accelerated in this range, which is because the lower the hydrate saturation, the faster the decomposition rate (Chen et al., 2020). It is noteworthy that the hydrate saturation increased instead in the deep area immediately adjacent to the hydrate decomposition zone. This is because the hydrate decomposition produced high-pressure

TABLE 2 Main parameter values of the numerical simulation.

Parameters	Value	Parameters	Value
Depth of burial (below seafloor)/m	200	Pore pressure/MPa	14.5
Sediment density/kg·m^{-3}	2,600	Salinity/%	3.05
Wet thermal conductivity/W·(m°C)$^{-1}$	3.1	Phase equilibrium temperature Difference/°C	2
Dry thermal conductivity/W·(m°C)$^{-1}$	1.0	Hydrate saturation/%	33.0
Specific heat of grains/J·(kg°C)$^{-1}$	1,000	Cementing pressure difference/MPa	1
Compression coefficient/Pa^{-1}	1.0×10^{-8}	Holding time of cementing pressure difference/min	7
Porosity/1	0.4	Cement slurry density/kg·m^{-3}	1,050
Absolute permeability/m^2	1.0×10^{-14} (=10 mD)	Average cement slurry exothermic rate/J·(g·s)$^{-1}$	0.28
Temperature/°C	13.4	Cement slurry initial temperature/°C	14.4
Composite thermal conductivity model Moridis et al. (2005)	$\lambda_c = \lambda_{Hs} + (\sqrt{S_A} + \sqrt{S_H})(\lambda_s - \lambda_{Hs}) + \varphi S_I \lambda_I$ Including: $S_I = 0$		
Capillary pressure model Van. (1980)	$P_{cap} = -P_0[(S^*)^{-1/\lambda} - 1]^{1-\lambda}$; $S^* = \frac{(S_A - S_{irA})}{(S_{mxA} - S_{irA})}$; $-P_{max} \le P_{cap} \le 0$ Including: $\lambda = 0.45$, $S_{irA} = 0.11$, $S_{mxA} = 1.0$, $P_{max} = 10^6$ Pa		
Relative permeability model Stone. (1970)	$k_{rA} = \max\{0, \min[(\frac{S_A - S_{irA}}{1 - S_{irA}})^n, 1]\}$; $k_{rG} = \max\{0, \min[(\frac{S_G - S_{irG}}{1 - S_{irA}})^{nG}, 1]\}$; $k_{rH} = 0$ Including: $S_{irA} = 0.12$, $S_{irG} = 0.02$, n=nG=3.0		

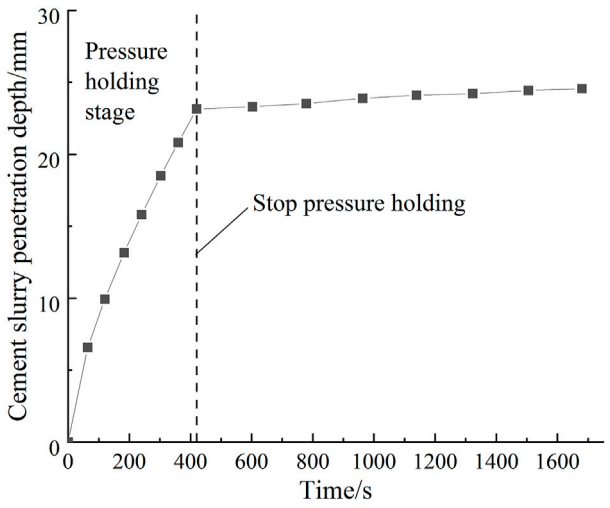

FIGURE 5
Variation in cement slurry penetration depth with time.

gas and water and absorbed heat. These high-pressure fluids flowed to both sides under the effect of the pressure difference, which increased the sediment pore pressure immediately adjacent to the decomposition area. In contrast, the warming due to heat conduction is not significant, and together with the heat absorption of hydrate decomposition, led to no significant change in temperature in the zone of pressure increase. This high-pressure and low-temperature environment, together with the methane gas brought by the freshly decomposed hydrate, contributes to the secondary generation of hydrate, forming a high-saturation zone of hydrate at the periphery of the decomposition zone around the well (Figure 7). As the temperature of the decomposition zone gradually increases and the heat conduction slowly spreads, this early formed high saturation zone will decompose again, and a new high saturation zone will be formed at its periphery. The process can be imagined such that when the high saturation zone is formed at the periphery of the decomposition zone, it moves outward with the expansion of the decomposition zone, which is eventually stabilized with the cessation of the exothermic hydration of cement. This is consistent with the conclusion of Yang et al. (2023) that the nucleation and growth of hydrates would preferentially proceed towards a low temperature region. It can also be seen in Figure 6D that the total amount of hydrate generated in 1,200–1,500 s is significantly higher than that in 900–1,200 s for the same time interval. This is because the fluid flow rate is relatively slower at a distance from the wellbore wall, while it is known that lower flow rate promotes hydrate generation according to Sun et al. (2023).

4 Discussion

During cement slurry penetration, the main characteristic of this process in GHBS compared to conventional hydrocarbon-bearing sediments is that hydrate decomposition and reorganization will occur when cement slurry penetration disrupts the hydrate phase equilibrium. The characteristics of cement slurry penetration in conventional hydrocarbon-bearing sediments are influenced by several factors, such as the depth and extent of penetration controlled by the cementing process and formation properties. Based on the data from station SH2, we further explore the influence of cementing process parameters and sediment properties on the process to clarify the influencing factors of cement slurry penetration in GHBS and then provide guidance for drilling and logging in the field.

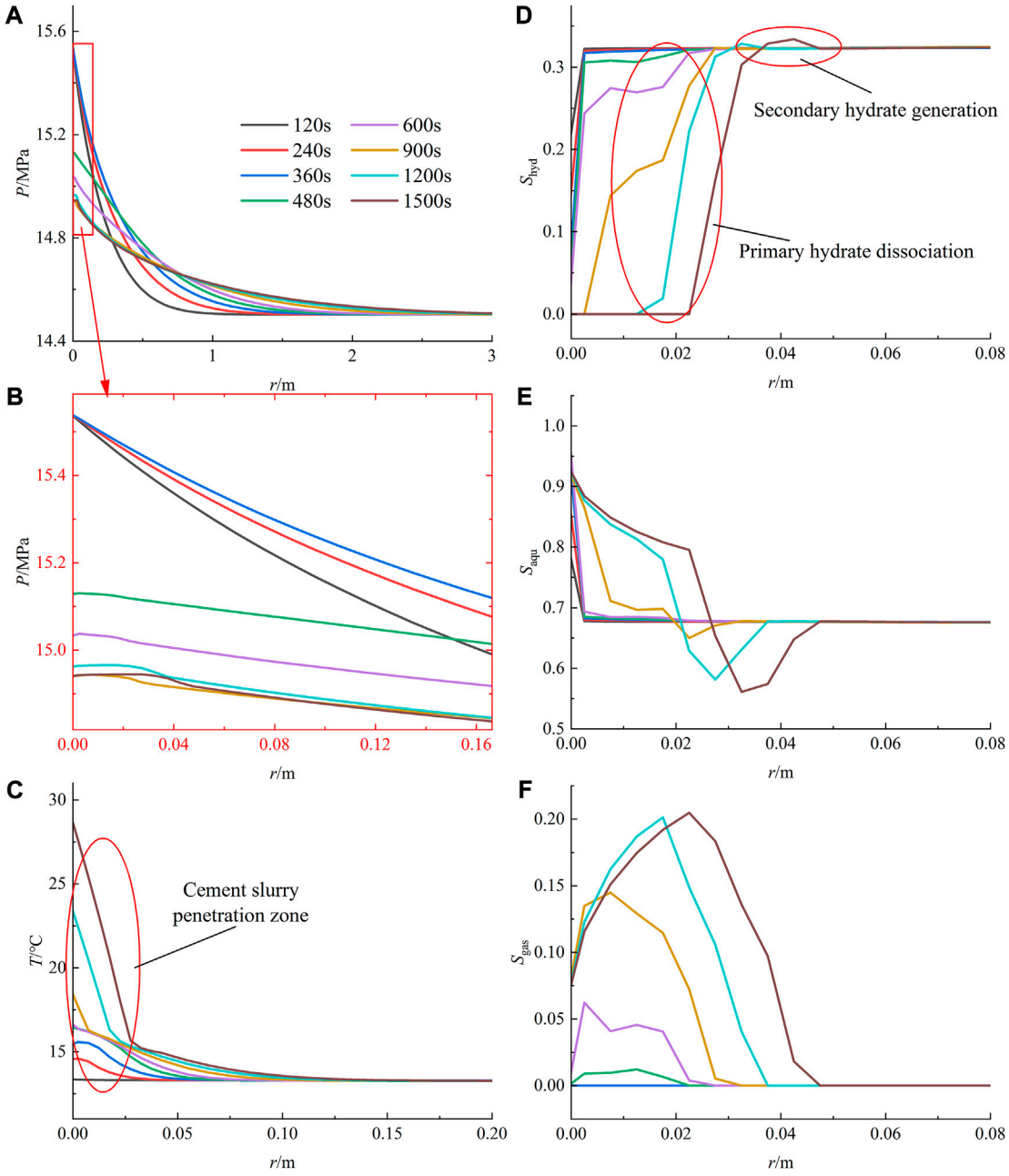

FIGURE 6
Changes in the main physical properties of the sediment at different times during cement slurry penetration. **(A)** Pressure. **(B)** Pressure local amplification. **(C)** Temperature. **(D)** Hydrate saturation. **(E)** Liquid saturation. **(F)** Gas saturation.

4.1 Effect of cementing process parameters on the cement slurry penetration process

4.1.1 Hydration heat of cement slurry

During cementation of GHBS, the hydration exothermic rate of the cement slurry directly determines the exothermic heat of the cement slurry. Figure 8A shows the pressure distribution in the late sediment at different exothermic rates. It is obvious that there is an increase in pore pressure over a large zone in the sediment as the exothermic rate is increased. This is because as the exothermic heat increases, more hydrates are decomposed in the sediment, which generates more methane gas and further raises the pore pressure in the sediment.

Figure 8B shows the temperature distribution of the sediment after stabilization at the late stage (25 min) under different exothermic rates. As the exothermic rate becomes faster, the sediment temperature increase at the near wellbore wall within the cement slurry penetration range elevates significantly, and the sediment heat-up at the near wellbore wall within the change range is as much as 20°C as the range of significant temperature increase also has a significant expansion. The former is due to the increase in the exotherm, which drives the sediment to heat up more. The latter

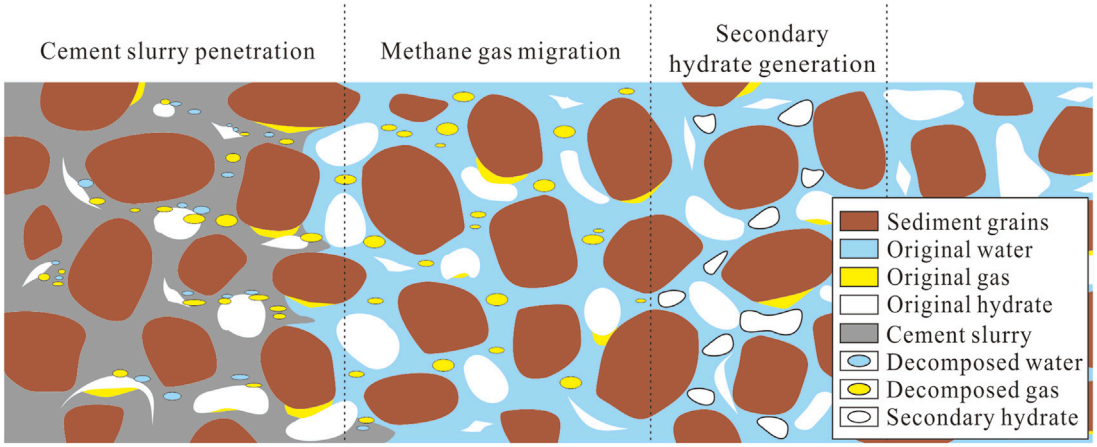

FIGURE 7
Schematic diagram of Secondary hydrate generation.

is because the process of heat absorption and decomposition of hydrate can neutralize the rapid elevation of sediment temperature, and the sediment temperature will again increase sharply after the range of complete decomposition of hydrate by heat, while the increase in exotherm leads to a larger range of complete decomposition of hydrate, so the range of dramatic temperature increase is also expanded.

Figure 8C shows the distribution of hydrate saturation in the late sediments at different exothermic rates. The range of hydrate decomposition in the sediment increases significantly and more completely with the increasing exothermic rate, while the formation of secondary hydrates also increases. This is because the amount of hydrate decomposition increases with increasing exotherm, and the hydrate decomposes completely in the penetration zone when it is higher than 0.21 $J\cdot(g\cdot s)^{-1}$. After that, it gradually starts to decompose deeper hydrate, which generates higher pore pressure and more high-pressure gas-water, which causes the hydrate synthesis zone to have greater synthesis power.

The impact of the cement slurry hydration exothermic rate on sediment physical properties is mainly in the increase of sediment temperature, which largely determines the degree of hydrate decomposition in the penetration zone, which in turn will bring elevated effects on sediment pressure. In conclusion, excessive hydration heat has a very drastic disturbance on the stability of GHBS, which will have a large impact on the quality of cementing; therefore, low hydration heat cement slurry should be selected whenever possible in actual projects.

4.1.2 Cementing pressure difference

The cementing pressure difference is the source force of cement slurry penetration into the sediment, and its magnitude directly affects the amount and depth of cement slurry penetration. The degree of cement slurry penetration in turn brings about differences in the range and amount of exotherms. Figure 9A shows the pressure distribution in the late sediment under different cementing pressure differences. The effect of this parameter on the sediment pressure is more significant. Although the range of the pressure rise zone does not change much, the pressure rise near the wellbore wall is obvious. This may be caused by two factors: 1) the increase in cementing pressure difference makes the both mass transfer and the pressure rise on the sediment more obvious; 2) the deepening of cement penetration also causes the amount of hydrate decomposition to increase, which generates more high-pressure gas-water to raise the sediment pressure.

Figure 9B shows the temperature distribution in the late sediment under different cementing pressure differences. The temperature increase near the wellbore wall is not obvious, but the range of the heat-up zone is significantly expanded. This is highly related to the depth of cement slurry penetration, which leads to the results in the figure due to the expansion of the cement slurry penetration and its exothermic influence. Based on the same principle, it can be seen from Figure 9C that the range of hydrate decomposition also expands significantly with increasing cementing pressure difference, and the decomposition zone increases from 2 to 6 cm in the studied range.

The effect of the cementing pressure difference on the sediment physical properties mainly presents in two aspects: 1) the sediment pressure increase and 2) the cement slurry penetration range expansion. Although the sediment pressure increase helps to stabilize the hydrate phase equilibrium, considering that GHBS are usually weakly cemented, excessive sediment pressure easily breaks the sediments. At the same time, the expansion of the cement slurry penetration zone is not conducive to the stability of GHBS, so the cementing pressure difference should not be too high in actual engineering.

4.1.3 Holding time of cementing pressure difference

The holding time of cementing pressure difference (HTPD) is the time when the cementing pressure difference exists and determines the duration of the cement slurry penetration process. Figure 10A shows the pressure distribution in the late sediment under different HTPDs. It can be seen that its effect on the sediment pressure is not significant, and the increase in the HTPD only slightly raises the sediment pressure. This is the result of two factors offsetting each other: 1) the longer HTPD causes more cement slurry to enter the sediment, which raises the sediment pressure and causes the thermal field to affect a larger zone; 2) it slows down the decomposition time of hydrate and delays the whole decomposition process of hydrate.

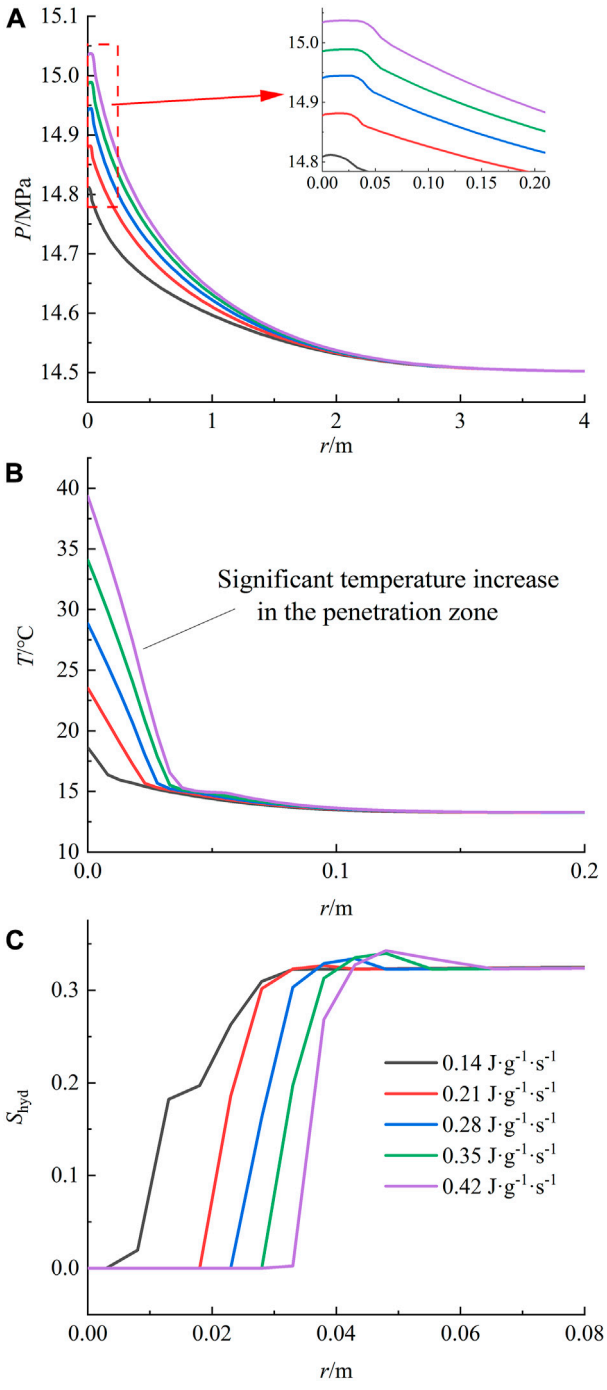

FIGURE 8
Changes in the main physical properties of the sediment around the wellbore at 25 min under different exothermic rates. **(A)** Pressure. **(B)** Temperature. **(C)** Hydrate saturation.

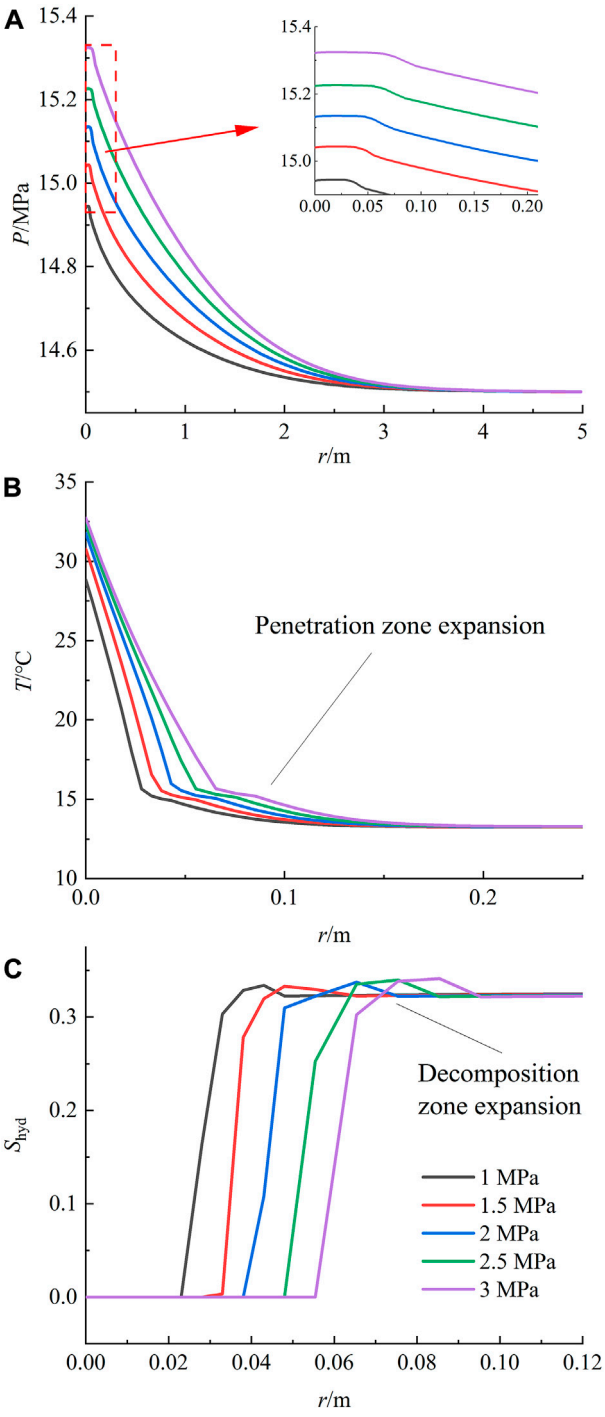

FIGURE 9
Changes in the main physical properties of the sediment around the wellbore at 25 min under varying cementing pressure differences. **(A)** Pressure. **(B)** Temperature. **(C)** Hydrate saturation.

Figures 10B, C show the temperature and hydrate saturation distributions in the late sediments under different HTPDs. As the HTPD increases, the range of the temperature field and hydrate saturation distribution in the sediment does not change significantly due to the hindering effect of the holding pressure process on hydrate decomposition.

The effect of HTPD on sediment physical properties is mainly due to its influence on the duration of the cement slurry penetration process, which causes two contradictory effects: 1) the amount and depth of cement slurry penetration increases with time, which promotes hydrate decomposition; 2) high pore pressure is

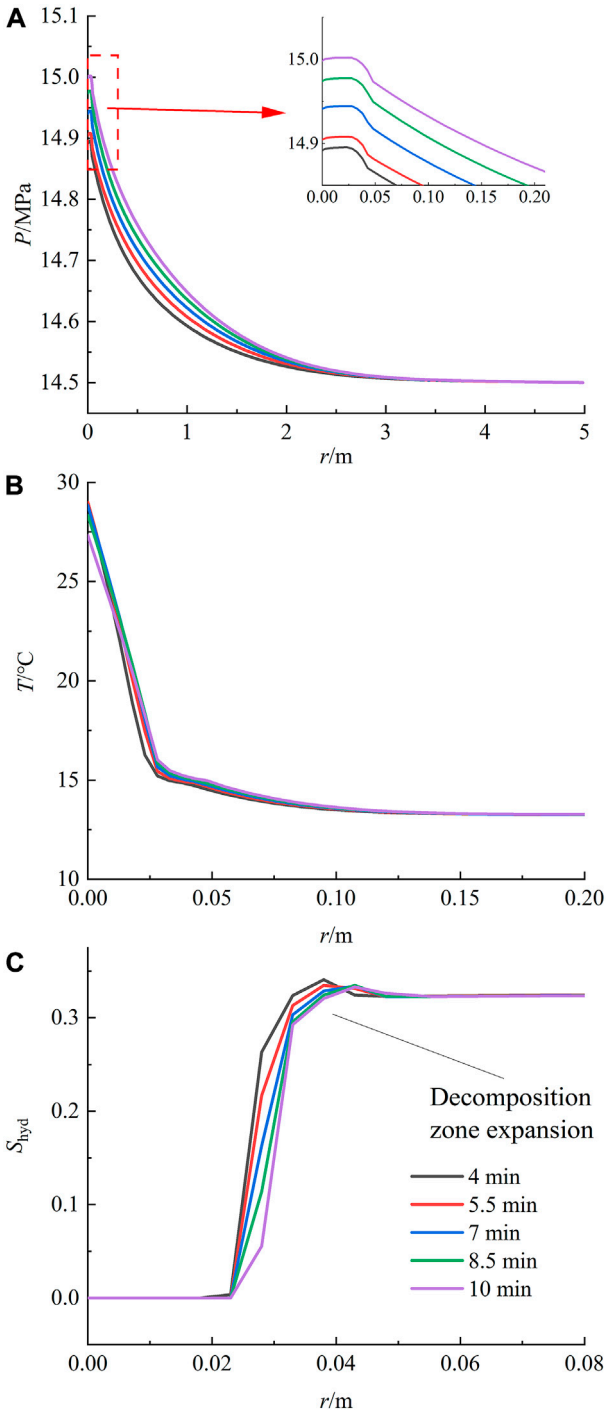

FIGURE 10
Changes in the main physical properties of the sediment around the wellbore at 25 min under different HTPDs. **(A)** Pressure. **(B)** Temperature. **(C)** Hydrate saturation.

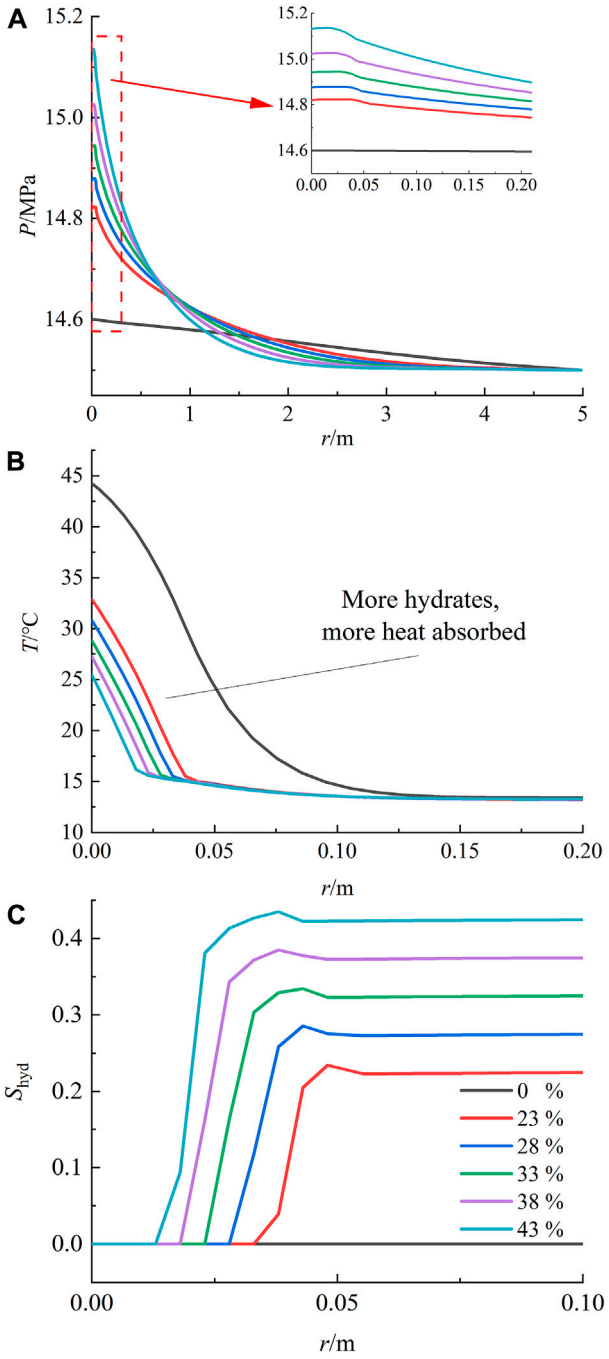

FIGURE 11
Changes in the main physical properties of the sediment around the wellbore at 25 min at different hydrate saturations. **(A)** Pressure. **(B)** Temperature. **(C)** Hydrate saturation.

maintained during holding pressure, which hinders hydrate decomposition and delays the start of hydrate decomposition. The effects of these are not significant in terms of the distribution of the physical properties of the sediment. However, in terms of cementing quality, it delays the decomposition of hydrate and increases time for cement hardening.

4.2 Influence of sediment physical properties on cement slurry penetration

4.2.1 Hydrate saturation

Hydrate saturation is one of the most important parameters of GHBS and directly determines the hydrate content in the pore space. Figure 11A shows the pressure distribution in the late sediment under different hydrate saturations. It can be seen that, on the one

hand, with the increase in hydrate saturation, the pressure at the near wellbore wall increases subsequently, and on the other hand, the influence range of high pressure decreases. The former is because more hydrate can be decomposed in the range of cement slurry penetration, and more methane gas is produced by its complete decomposition, which increases the pressure at the near wellbore wall. The latter is due to the decrease in sediment permeability caused by the increase in hydrate saturation, which makes it difficult for the high-pressure fluid to dissipate to greater depth.

Figure 11B illustrates the temperature distribution in the late sediments under different hydrate saturations. The image shows that the magnitude and extent of heat-up in the sediment decrease as the hydrate saturation increases. Both factors combine to cause this phenomenon due to the reduced extent of cement slurry penetration and more hydrate near the wellbore wall that can be used to mitigate the heat-up. Based on the same principle, it can be seen from Figure 11C that the extent of hydrate decomposition decreases as the initial hydrate saturation increases. Within the study area, the decomposition zone was reduced from 4 to 1 cm.

In summary, hydrate saturation affects GHBS mainly because 1) it determines the total amount of hydrate available for decomposition per unit volume of pore space, which in turn determines the degree of pressure increase due to methane gas production and the ability of the sediment to resist warming; 2) the hydrate occupies pore channels and reduces the permeability of pore spaces, which can impede fluid flow in them. Although the affected area in the sediment is smaller at higher hydrate saturation, the high pressure near the wellbore wall may be harmful to the quality of cementing, and the influence of this property should be taken into account in practical engineering.

4.2.2 Hydrate phase equilibrium temperature difference

The hydrate phase equilibrium temperature difference is the difference between the ambient temperature of the sediment and the hydrate phase equilibrium temperature at pore pressure, which indicates the degree of hydrate stability. Different hydrate phase equilibrium environments often imply differences in the initial pressure and temperature conditions of the sediment. For comparison purposes, the impact of sediment pressure increments and temperature increments on this parameter was used for evaluation. Figure 12A shows the distribution of pressure increments in the late sediments under varying hydrate phase equilibrium temperature differences. The picture shows that as the hydrate phase equilibrium temperature difference increases, the pressure increment in the whole sediment decreases. This is a direct effect due to the decrease in hydrate decomposition. The pressure increment at the wellbore wall was reduced from 0.5 to 0.2 MPa over the study area.

Figure 12B shows the distribution of temperature increments in the late sediment under different hydrate phase equilibrium temperature differences. The picture shows that with an increasing difference in hydrate phase equilibrium temperature, the temperature of the sediment near the wellbore wall does not change much, while the temperature slightly farther away increases significantly. This is because the hydrates near the wellbore wall are all completely decomposed, the heat absorbed is of the same value, and the heat up of the sediment at this location is consistent due to the constant total heat of cement decomposition. The hydrates slightly farther away are not completely decomposed. At this time, the total amount of hydrates decomposed in the sediments with high phase stability is less; thus, the heat absorbed by them is also less, which makes the temperature higher.

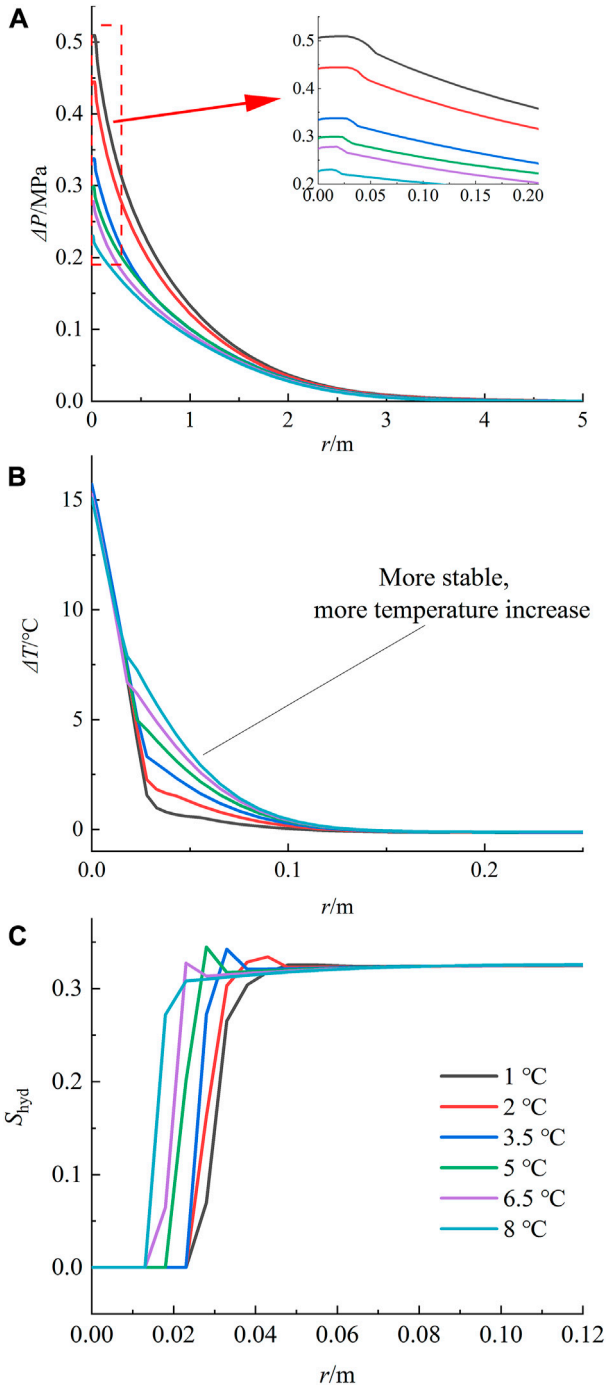

FIGURE 12
Changes in the main physical properties of the sediment around the wellbore at 25 min under different phase equilibrium temperature differences. **(A)** Pressure. **(B)** Temperature. **(C)** Hydrate saturation.

Figure 12C shows the distribution of hydrate saturation in the late sediment under different hydrate phase equilibrium

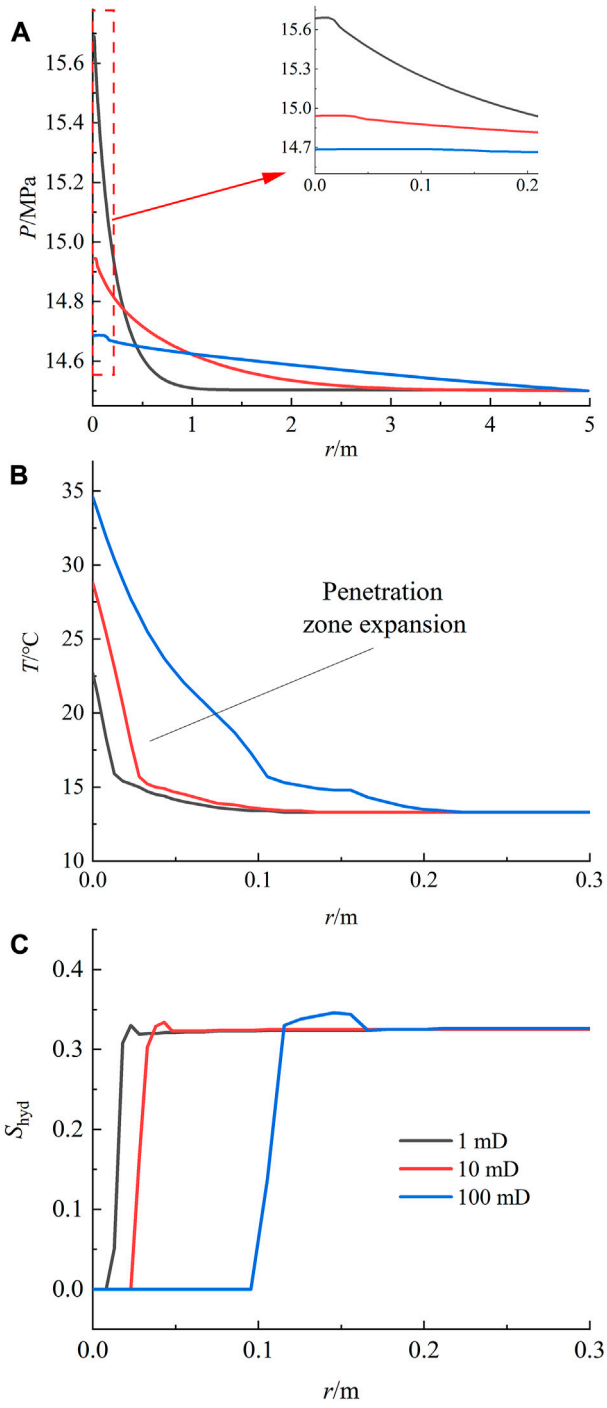

FIGURE 13
Changes in the main physical properties of the sediment around the wellbore at 25 min at different absolute permeabilities. **(A)** Pressure. **(B)** Temperature. **(C)** Hydrate saturation.

temperature differences. With an increase in the difference, the decomposition range of the hydrate is obviously reduced.

The hydrate phase equilibrium temperature difference mainly affects the degree of hydrate decomposition; the more stable sediment decomposes less and produces less methane gas. Therefore, more attention should be given to sediments with poor phase stability in production.

4.2.3 Absolute permeability

Absolute permeability is an inherent property of porous media, and in conventional oil-gas sediment systems, it has a significant influence on the dynamic process of cement slurry penetration. In GHBS, this property depends mainly on the pore structure of the sediment, without considering the reservoir of hydrate it contains, and the absolute permeability of GHBS deposited in different environments varies greatly. Figure 13A shows the pressure distribution in the later sediments under different absolute permeabilities. The greater the permeability, the larger the influence range of the sediment pressure, while the pressure accumulated near the wellbore wall is smaller. This is because in the well permeable sediments, the high pressure near the wellbore wall dissipates rapidly to depth and cannot accumulate at the original location; thus, its pressure influence zone is wider, but the peak is lower.

Figures 13B, C show the distributions of temperature and hydrate saturation in the late sediments under different absolute permeabilities. The heat-up and decomposition zones increase in the more permeable sediments, and the increase in permeability causes the decomposition zone to expand from 1 to 10 cm in the study. This is because better permeability facilitates the penetration behavior of cement slurry, leading to a wider area of cement slurry penetration, which in turn leads to a larger area of thermal radiation influence and a larger hydrate decomposition zone.

The absolute permeability mainly affects the efficiency of pore fluid flow, including the transport of cement slurry and decomposition products. The expansion of the cement slurry penetration zone causes the expansion of the heat-up and decomposition zones, which increases the amount of hydrate decomposition. However, it also effectively attenuates the pore pressure build-up and protects the sediments from fracturing.

4.2.4 Porosity

Porosity represents the effective porosity when hydrate saturation is zero. Porosity is a fundamental geophysical property of GHBS, and it also varies greatly in different depositional environments. Figure 14A illustrates the pressure distribution in late sediments under different porosities. The figure shows that the pore pressure hardly changes as the porosity increases. This is due to the pore environment being increased equiproportionally as the porosity increases while other parameters remain constant; that is, the volume of space in the environment, the hydrate content, the total amount of penetrating cement slurry, and the decomposed gases are all increased equiproportionally. These react to the surface to provide the results in the figure.

Figures 14B, C show the distribution of temperature and hydrate saturation in the late sediment under different porosities. It can be seen that with the increase in porosity, the decomposition range of hydrate does not change much because the change in the penetration range of cement slurry is not very significant. Although the increase in the total amount of cement slurry penetration brings an increase in the exothermic heat, the increase in the total amount of hydrate hinders the increase in the temperature of the sediment, and the

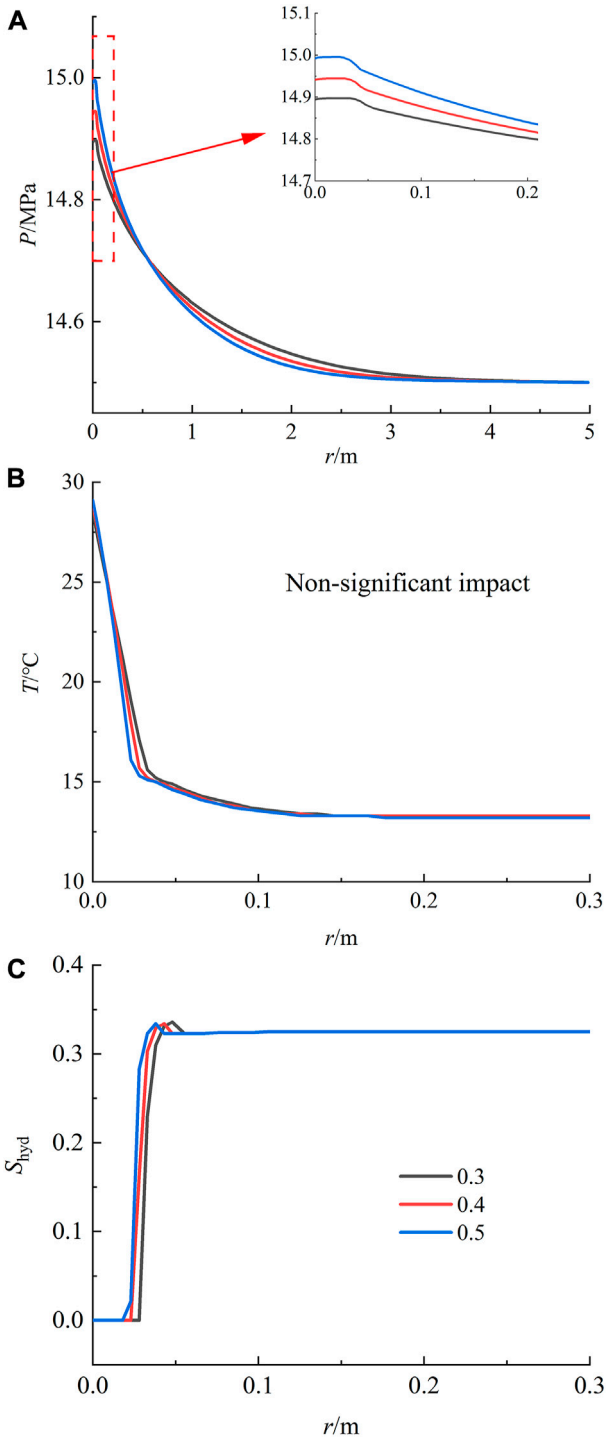

FIGURE 14
Changes in the main physical properties of the sediment around the wellbore at 25 min under different porosities. **(A)** Pressure. **(B)** Temperature. **(C)** Hydrate saturation.

changes in the temperature field are not significant when the two factors cancel each other.

The increase in porosity facilitates the flow of pore fluid and increases the penetration of cement slurry. However, at the same time, the increase in its pore space indicates an equal increase in the material content in the pore space, and the volume of fluid that can be accommodated also increases, which is reflected as its effect on the physical properties of the sediment is less obvious. However, this is only for the sediment, and its increased fluid volume will certainly have a significant effect on the cement ring.

5 Conclusion

In this study, the GHBS explored at the SH2 station of GMGS-1, a gas hydrate drilling project in the Shenhu Area in the South China Sea, were the object of study. A numerical model of casing-annulus-sediment was constructed using TOUGH+HYDRATE, realistically reproducing the cement slurry exothermic and penetration processes by "continuous segmental simulation," and the physical properties of GHBS around the wellbore during cementing were investigated. Then, single-factor controlled variable studies were conducted to investigate the changes in the physical properties of sediments under different cementing process parameters and sediment properties, which led to the following conclusions and insights.

(1) The main reasons for the increase in GHBS pressure during the cementing process include the reliance of the initial stage on the squeezing effect of cement slurry penetration on the sediment pores triggered by the cementing pressure difference, and the later stage generates high-pressure gas from hydrate decomposition to further increase the sediment pressure. In the early stage, the pressure distribution in the sediment is highest at the wellbore wall and gradually decreases deeper in the sediment. In the later stage, the high pressure brought by hydrate decomposition will make the pressure in the decomposition zone higher than the pressure near the wellbore wall. The main role of sediment heat-up comes from the hydration exotherm of the cement slurry, so the heat-up zone of the GHBS and the penetration zone of the cement slurry are highly coincident; thus, the decomposition of hydrate mainly occurs in the penetration zone of the cement slurry. In addition, because the decomposition of hydrate produces a large amount of methane gas and raises the pressure of the surrounding sediment, secondary hydrate will be formed in the annular space outside the decomposition zone. With the expansion of the decomposition zone, this hydrate high-saturation zone will also subsequently expand.

(2) Among the cementing process parameters, the hydration exothermic rate of the cement slurry determines the degree of sediment heating and has a drastic effect on the degree of hydrate decomposition in the penetration zone, which is completely decomposed when it is higher than 0.21 $J\cdot(g\cdot s)^{-1}$ in the zone; therefore, low hydration heat cement slurry should be selected whenever possible in the actual project. The effects of increasing the cementing pressure difference on the physical properties of the sediment mainly include the increase in sediment pressure and the expansion of the cement slurry penetration zone. The former inhibits hydrate decomposition, while the latter increases the range of the heat-up zone and decomposition zone. The leading edge of decomposition in the study went from 2 to 6 cm in depth.

Considering that GHBS are usually weakly cemented, the value of this parameter is not very large. The increase in HTPD increases the amount and depth of cement slurry penetration with time, so that the range of heat-up and decomposition zones increases. On the other hand, the extension of the HTPD delays the onset of hydrate decomposition. The combined effect on the physical properties of the sediment is not significant.

(3) Among the physical properties of the sediment, the effects of increased hydrate saturation mainly include increasing the total amount of hydrate per unit volume of pore space and decreasing the permeability of the pore space. It hinders the penetration of cement slurry, affects the diffusion of pore pressure, and reduces the influence of the heat-up and decomposition zones. Within the study area, the decomposition zone was reduced from 4 to 1 cm. At the same time, the pressure in the decomposition zone increases due to the increase in the total hydrate volume in this zone. The hydrate phase equilibrium temperature difference mainly affects the decomposition degree of hydrate in the heat-up zone, and the more stable sediment decomposes less and produces less methane gas. This results in a reduction of the pressure increment in the sediment, from 0.5 to 0.2 MPa at the wellbore wall over the study area. The absolute permeability mainly affects the pore fluid circulation efficiency, and a better permeability will increase the cement slurry penetration into the sediment, causing the expansion of the heat-up and decomposition zone, which changes from 1 to 10 cm in the study. However, it also effectively reduces the pore pressure accumulation and protects the sediment from fracturing. Porosity affects the pore volume of the sediment and the permeable volume of the cement slurry, and has a less pronounced effect on the physical properties of the sediment.

In summary, cement slurry penetration into hydrated sediments is a very complex process. Both the cementing process and the physical properties of the sediment significantly impact the process. At present, cementing GHBS in deep-water oil-gas drilling is still a difficult problem. The work in this paper lays the foundation for analyzing the effect of cement slurry penetration, which is important for the application of appropriate drilling techniques, accurate logging interpretation, wellbore stability evaluation and effective GHBS protection in engineering.

Data availability statement

The original contributions presented in the study are included in the article/supplementary material, further inquiries can be directed to the corresponding author.

Author contributions

XW: contributed to analysis, writing, experiment design, and data collection; MZ: contributed to conceptualization, methodology, analysis, writing, supervision, resources, and funding acquisition; KZ: contributed to experiment design, and data collection; QQ: contributed to investigation resources, and funding acquisition; ZW, SY, GZ, and TM: contributed to data collection, analysis, and writing. All authors have read and agreed to the published version of the manuscript.

Funding

This work was sponsored by the National Natural Science Foundation of China (No. 42272363), the National Natural Science Foundation of Sichuan Province (No. 23NSFSC1511).

Conflict of interest

The authors declare that the research was conducted in the absence of any commercial or financial relationships that could be construed as a potential conflict of interest.

Publisher's note

All claims expressed in this article are solely those of the authors and do not necessarily represent those of their affiliated organizations, or those of the publisher, the editors and the reviewers. Any product that may be evaluated in this article, or claim that may be made by its manufacturer, is not guaranteed or endorsed by the publisher.

References

Chen, B. B., Sun, H. R., Zheng, J. J., and Yang, M. J. (2020). New insights on water-gas flow and hydrate decomposition behaviors in natural gas hydrates deposits with various saturations. *Appl. Energy* 259, 114185. doi:10.1016/j.apenergy.2019.114185

Li, Y., Cheng, Y. F., Yan, C. L., Wang, Z. Y., Zhang, Q. X., et al. (2022). Multi-physical field coupling model of hydrate formation and analysis of wellbore collapse law in Shenhu area of South China Sea. *J. Central South Univ. Sci. Technol.* 53 (3), 976–990.

Liu, T. L. (2018). *Discussion on cementing technology scheme and problems of hydrate formation encountered in XX pre exploration well on northern slope of South China Sea*. Wuhan): China University of Geosciences, 3–6.

Liu, T. L., Zheng, S. J., Wang, R., Sun, J. X., Jiang, G. S., Zhang, L., et al. (2018). Negative effect of cementing slurry invasion on gas hydrate stability around borehole wall. *Acta Pet. Sin.* 39 (8), 937–946.

Lu, F. (2013). *Analysis of the impact of South China Sea energy on China's future energy security*. Beijing: China Foreign Affairs University, 1–3.

Merey, Ş. (2019). Evaluation of drilling parameters in gas hydrate exploration wells. *J. Petroleum Sci. Eng.* 172, 855–877. doi:10.1016/j.petrol.2018.08.079

Moridis, G. J., Kowalsky, M. B., and Pruess, K. (2005). *HydrateResSim users' manual: A numerical simulator for modeling the behavior of hydrates in geologic media*. Berkeley: Lawrence Berkeley National Laboratory.

Nakai, T., Tjok, K., and Humphrey, G. (2007). *Deepwater gas hydrate investigation Shenhu survey area south South China Sea, offshore China*. Guangzhou: Guangzhou Marine Geological Survey.

Ning, F. L., Wu, N. Y., Jiang, G. S., Zhang, L., Guan, J. A., Yu, Y. B., et al. (2010). A method to use solar energy for the production of gas from marine hydrate-bearing sediments: A case study on the Shenhu area. *Energies* 3, 1861–1879. doi:10.3390/en3121861

Ning, F. L., Zhang, K. N., Wu, N. Y., Zhang, L., Li, G., Jiang, G. S., et al. (2013). Invasion of drilling mud into gas-hydrate-bearing sediments. Part I: Effect of drilling mud properties. *Geophys. J. Int.* 193 (3), 1370–1384. doi:10.1093/gji/ggt015

Pang, L. Y. (2012). *The characteristics and extension of depositional system and their relationship with hydrocarbon distribution in paleogene in north margin basins, south China sea*. Beijing: China University of Geosciences.

Shen, Z. C., Wang, D., and Jia, Y. G. (2019). Analysis on gas hydrate exploitation response between the horizontal and vertical wells at SH 2 site in the Shenhu area of the South China Sea. *Ocean Eng.* 37 (4), 107–116.

Sloan, E. D., and Koh, C. (2008). *Clathrate hydrates of natural gases*. London: CRC Press.

Stone, H. (1970). Probability model for estimating three-phase relative permeability. *J. Petroleum Technol.* 22 (2), 214–218. doi:10.2118/2116-pa

Sun, H. R., Chen, B. B., Li, K. H., Song, Y. C., Yang, M. J., Jiang, L. L., et al. (2023). Methane hydrate re-formation and blockage mechanism in a pore-level water-gas flow process. *Energy* 263, 125851. doi:10.1016/j.energy.2022.125851

Sun, J. X. (2018). *Characteristics of reservoir response to drilling and production in gas hydrate-bearing sediments in the South China Sea. Wuhan*. Wuhan): China University of Geosciences, 48–52.

Sun, Z., Zhang, C. M., Wang, X., Li, P. C., Sun, L. T., Zhang, Y. F., et al. (2011). *China's offshore oil and gas industry*. Guangzhou: Guangdong Economic Publisher, 14–16.

Tinku, S., and Vikas, M. (2018). Experimental investigations and optimizations of rheological behavior of drilling fluids using RSM and CCD for gas hydrate-bearing formation. *Arabian J. Sci. Eng.* 43, 6541–6554. doi:10.1007/s13369-018-3292-1

Tu, Y. Z., Ning, F. L., Jiang, G. S., Wu, N. Y., and Zhang, L. (2010). Mechanism and characteristics of invasion of drilling fluid in gas hydrates-bearing formation. *Geol. Sci. Technol. Inf.* 29 (3), 110–113.

Van, G. M. T. (1980). A closed-form equation for predicting the hydraulic conductivity of unsaturated soils. *Soil Sci. Soc. Am. J.* 44 (5), 892–898. doi:10.2136/sssaj1980.03615995004400050002x

Wang, D. D. (2021). *Geological characteristics and physical properties of low permeability and weakly consolidated hydrate reservoirs in the South China Sea*. Wuhan: China University of Geosciences.

Wang, J. Q. (2021). The way to explore marine oil and gas resources. *Nat. Resour. Sci. Cult.* (4), 20–23.

Wang, X. J., Hutchinson, D. R., Wu, S. G., Yang, S. X., and Guo, Y. Q. (2011a). Elevated gas hydrate saturation within silt and silty clay sediments in the Shenhu area, South China Sea. *J. Geophys. Res. Solid Earth* 116 (5), B05102. doi:10.1029/2010JB007944

Wang, X. J., Wu, S. G., Lee, M., Guo, Y. Q., Yang, S. X., and Liang, J. Q. (2011b). Gas hydrate saturation from acoustic impedance and resistivity logs in the Shenhu area, South China Sea. *Mar. Petroleum Geol.* 28 (9), 1625–1633. doi:10.1016/j.marpetgeo.2011.07.002

Weng, T. W., Lo, S. C., Huang, J. H., and Li, C. F. (2013). The general situation of the distribution and potential volume of gas hydrate in the south China sea. *Min. Metallurgy* (222), 56–70.

Wu, N. Y., Zhang, H. Q., Su, X., Yang, S. X., Zhang, G. X., Liang, J. Q., et al. (2007a). High concentrations of hydrate in disseminated forms found in very fine-grained sediments of Shenhu area, South China Sea. *Terra Nostra* 1 (2), 236–237.

Wu, N. Y., Zhang, H. Q., Yang, S. X., Liang, J. Q., and Wang, H. B. (2007b). Preliminary discussion on natural gas hydrate (NGH) reservoir system of Shenhu area, north slope of South ChinabSea. *Nat. Gas. Ind.* 27 (9), 1–6.

Xi, F. Z., Sun, F. Q., Yang, K. P., Liu, A. P., Wang, Y. H., Song, B. L., et al. (2020). *Cement slurry for hydrate well cementation and preparation method thereof*. China, CN111056784A.

Xu, M. B., Wang, X. L., Zhou, J. L., Jiang, S. Q., Wang, Y. Q., Zhu, R. D., et al. (2014). The research of low-heat slurry for cementing in the natural gas hydrate formation. *J. Oil Gas Technol.* 36 (11), 134–137.

Yang, G. K., Jiang, G. S., Liu, T. L., Qin, X., and Yu, Y. F. (2021a). Analysis on preparation of temperature controlled self-repairing microcapsules and its application in cement slurry for hydrate formation. *Mater. Rep.* 35 (2), 2032–2038.

Yang, G. K., Liu, T. L., Zhu, H., Zhang, Z. H., Feng, Y. T., Leusheva, E., et al. (2022). Heat control effect of phase change microcapsules upon cement slurry applied to hydrate-bearing sediment. *Energies* 15 (12), 4197. doi:10.3390/en15124197

Yang, G. K., Wang, A. M., Yin, S. T., Dai, T., Liu, T. L., and Jiang, G. S. (2021b). Preparation and application of phase change microcapsules for low heat cement slurry for well cementing in hydrate formation. *Drill. Eng.* 48 (3), 118–124.

Yang, L., Guan, D. W., Qu, A. X., Li, Q. P., Ge, Y., Liang, H. Y., et al. (2023). Thermotactic habit of gas hydrate growth enables a fast transformation of melting ice. *Appl. Energy* 331, 120372. doi:10.1016/j.apenergy.2022.120372

Yang, S. X., Liang, J. Q., Lu, J. A., Qu, C. W., and Liu, B. (2017). New understandings on the characteristics and controlling factors of gas hydrate reservoirs in the Shenhu area on the northern slope of the South China Sea. *Earth Sci. Front.* 24 (4), 1–14.

Zhang, H. Q., Yang, S. X., Wu, N. Y., Su, X., and Holland, M. (2007). Successful and surprising results for China's first gas hydrate drilling expedition. *Fire Ice Newsl.* 9.

Zhang, H. W., Cheng, Y. F., Li, L. D., Shi, J. H., Jiang, L., and Han, X. T. (2018). Perturbation simulation of invasion of drilling fluid containing thermodynamic hydrate inhibitors into natural gas hydrate formation. *Sci. Technol. Eng.* 18 (6), 93–98.

Zhang, J. B., Li, B., Jin, H., Chen, Y., Lu, Y. W., and Wang, L. (2020). Study and application of a low hydration heat cement slurry system for the cementing of deepwater hydrate layer. *China Offshore Oil Gas* 32 (1), 119–124.

Zhang, J. H., Wei, W., and Wang, H. Y. (2009). Research on gas hydrate and its development techniques. *Nat. Gas. Technol.* 3 (2), 67–69+80.

Zheng, M. M., Jiang, G. S., Liu, T. L., Peng, L., Ning, F. L., Liu, L., et al. (2017). Physical properties response of hydrate bearing sediments near wellbore during drilling fluid invasion. *Earth Sci.* 42 (3), 453–461.

Zheng, M. M., Liu, T. L., Jiang, G. S., Wei, M., Huo, Y. X., and Liu, L. (2020). Large-scale and high-similarity experimental study of the effect of drilling fluid penetration on physical properties of gas hydrate-bearing sediments in the Gulf of Mexico. *J. Petroleum Sci. Eng.* 187, 106832. doi:10.1016/j.petrol.2019.106832

Zheng, M. M., Wang, X. Y., Zhou, K. R., Wang, K., Wu, Z. R., Jiang, G. S., et al. (2022). Critical conditions identification of generated high-pressure gas and water reverse penetration during cementing in hydrate reservoirs in the South China Sea. *J. Central South Univ. Sci. Technol.* 53 (3), 963–975.

Zheng, M. M., Wang, X. Y., Zhou, K. R., Wang, K., Wang, Z. L., Dong, G., et al. (2021). Hydrate reservoir physical properties response and high-pressure gas-water reverse penetration during deepwater oil and gas cementing. *Coal Geol. Explor.* 49 (3), 118–127.

Zhu, H. X., Xu, T. F., Zhu, Z. Y., Yuan, Y. L., and Tian, H. L. (2020). Numerical modeling of methane hydrate accumulation with mixed sources in marine sediments: Case study of Shenhu Area, South China Sea. *Mar. Geol.* 423, 106142. doi:10.1016/j.margeo.2020.106142

Frontiers in Earth Science

Investigates the processes operating within the major spheres of our planet

Advances our understanding across the earth sciences, providing a theoretical background for better use of our planet's resources and equipping us to face major environmental challenges.

Discover the latest Research Topics

See more →

Frontiers

Avenue du Tribunal-Fédéral 34
1005 Lausanne, Switzerland
frontiersin.org

Contact us

+41 (0)21 510 17 00
frontiersin.org/about/contact